Microdevices for High-Throughput
Screening of Single Catalyst Particles

Alessia Broccoli

MICRODEVICES FOR HIGH-THROUGHPUT SCREENING OF SINGLE CATALYST PARTICLES

Alessia Broccoli

MICRODEVICES FOR HIGH-THROUGHPUT SCREENING OF SINGLE CATALYST PARTICLES

DISSERTATION

to obtain
the degree of doctor at the University of Twente,
on the authority of the rector magnificus,
prof. dr. ir. A. Veldkamp,
on account of the decision of the Doctorate Board
to be publicly defended
on Friday 10 November 2023 at 12.45 hours

by

Alessia Broccoli

born on the 16th of July, 1993
in Caserta, Italy

This dissertation has been approved by:

Promotors
Prof. dr. ir. M. Odijk
Prof. dr. ir. A. van den Berg

Co-promotors
Dr. F. Meirer
Prof. dr. G. Mul

Graduation Committee

Table of Contents

Chapter 3

Nanoparticle Printing for Microfluidic Applications: Bipolar Electrochemistry and Localized Raman Sensing Spots

Chapter 4

Accessibility Study of Porous Materials at the Single Particle Level as Evaluated within a Multiplexed Microfluidic Chip with Fluorescence Microscopy

Chapter 5

High-Throughput Device for *In Situ* Studies and at Millisecond Spatiotemporal Resolution of Heterogeneous Catalytic Reactions at the Single Particle Level with Fluorescence Microscopy

Chapter 6

In Situ Study of Mass Transfer Limitations in Plastic Waste Conversion over a Single Catalyst Particle using a MEMS-based Microreactor for High-Resolution X-ray Microscopy

Chapter 7

Summary and Outlook

Chapter 1

General Introduction

Heterogeneous catalysis has a vital role in advancing energy- and material-efficient chemical reactions, aiming for a cleaner and more sustainable chemical industry. The improvement of catalyst performance requires multiscale studies; microdevices provide unique advantages for studying catalytic processes, especially at the single particle level. This chapter provides the motivation and background of this thesis, with an introduction to the implementation of microfluidic technology for catalyst particle screening. Finally, the outline of the thesis is presented, and each chapter will be described briefly.

1.1 Heterogeneous catalysis

At the heart of catalysis science, heterogeneous catalysis drives many of the chemical reactions that underpin essential industrial processes, ranging from the production of fuels and polymers to the manufacturing of pharmaceuticals and specialty chemicals. Furthermore, it plays an integral role in the development of sustainable energy solutions such as hydrogen production[1] and carbon dioxide conversion[2], underlining its vital contribution to addressing global environmental challenges. The widespread use of heterogeneous catalysts relies on their ability to provide an alternative reaction pathway with lower activation energy (without altering the thermodynamic equilibrium), which accelerates the reaction rate, and to direct a reaction towards a specific product, minimizing the formation of undesired byproducts (i.e., high selectivity).

Heterogeneous catalysis is an extremely dynamic field with a continuous focus on improving and developing more efficient, robust, and sustainable catalysts. Solid catalysts can exhibit different sizes and shapes. They are often structured porous particles with large surface areas to obtain a high density of active sites and to maximize the reactant contact, enhancing the overall catalyst efficiency. The structural features of catalysts cover length scales from nanometers to centimeters, as they include sub-nanometer active catalytic sites, nanometer-scale metal clusters or nanoparticles, as well as multiscale networks comprising micro- (<2 nm), meso- (2–50 nm), and macropores (>50 nm)[3,4]. Furthermore, particle dimensions range from micrometers to centimeters. This range of structural features highlights the complexity of solid catalysts, with each component and hierarchical arrangement playing a significant role in their catalytic functions, namely activity, accessibility, and stability. Therefore, understanding and characterizing these materials is crucial for elucidating structure-activity relationships and developing catalysts with improved performance.

1.2 Multiscale Catalytic Energy Conversion (MCEC) consortium

To optimize catalytic reactions, it is important to gain information across multiple length scales, spanning from the atomic level of the catalyst active sites to tens of meters when moving the catalytic process on an industrial

1

level (Figure 1). This approach allows researchers to understand the intricate details of catalysts' active sites, mass transfer phenomena, reaction kinetics, and deactivation dynamics. Additionally, reactor design, and catalyst regeneration strategies are critical aspects that need to be considered for successful industrial implementation. Therefore, different expertise in various fields needs to be combined to face both scientific and technological challenges in heterogeneous catalysis. In this context, the Multiscale Catalytic Energy Conversion (MCEC) consortium brings together researchers with chemistry, engineering, and physics expertise to collaborate on multiscale and multidisciplinary projects for sustainable energy conversion. More information about MCEC, including details about individual projects, researchers, and various outreach programs, can be found at: https://mcec-researchcenter.nl/. The consortium encompasses research groups from the University of Utrecht (UU), the Technical University of Eindhoven (TU/e), and the University of Twente (UT).
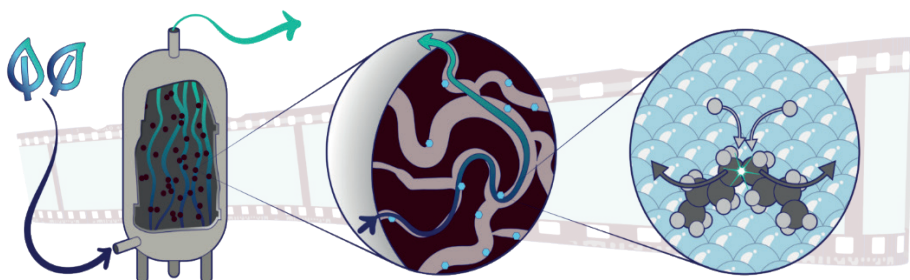
Figure 1: Illustration showcasing the multiscale approach in heterogeneous catalysis, ranging from the industrial to the atomic scale. Figure reprinted from the MCEC website: https://mcec-researchcenter.nl/education/demonstrator-project-visualizing-multiscale-catalysis/

The research project described in this thesis is part of the MCEC Gravitation program from the Netherlands Organization for Scientific Research (NWO). It has been carried out at the BIOS Lab-on-a-Chip group (UT) in collaboration with the Inorganic Chemistry and Catalysis (ICC) group (UU), combining expertise in microfluidics and microfabrication with catalysis and spectroscopy.

1.3 From bulk to individual catalyst characterization

The optimization of catalysts and the development of new materials and processes for novel applications rely on an in-depth assessment of their properties. Traditionally characterization of catalyst particles is done in bulk, providing individual features of catalysts, such as concentration of active sites or accessibility, as an ensemble average over millions or billions of catalyst particles. Using that information for interpreting performance as well as enhancing the design of the catalyst requires the underlying assumption of uniformity in the properties across the **individual particles** in a catalyst batch. This assumption, however, may not always hold true given the variability that can exist at multiple scales (intra- and inter-particle **heterogeneity**[5,6]). Slight differences in the composition of individual catalyst particles, or even in simple model systems, can greatly affect their overall reactivity and efficiency. For instance, in the characterization of cobalt-based catalysts, which are commonly used in Fischer-Tropsch synthesis, techniques like Inductively Coupled Plasma Optical Emission or Mass Spectrometry (ICP-OES, ICP-MS) are often employed to estimate the average cobalt content within the sample volume. However, they offer no insight into the distribution of cobalt on the scale of individual particles. Such lack of detailed information can mask important variations, such as clustering of cobalt atoms[7] or uneven distribution[8] across the catalyst surface, that can significantly impact the catalyst's activity and durability. In addition to compositional and structural characterization, catalyst performance (e.g., activity, accessibility) is also usually assessed via bulk catalytic experiments. Much like the process of catalyst characterization, the activity assessments often operate under the assumption of particle homogeneity within the tested population. However, this conventional approach in catalysis research may neglect the potential for heterogeneous distribution of catalytic activity both between different particles and within a single catalyst particle, leading to an oversimplification of their complex nature. Moving towards the use of devices and techniques allowing for focusing on the individual catalyst particles is beneficial in recognizing the structure-performance relationship, ultimately guiding the design of more effective and efficient catalysts for specific applications.

1.4 Microfluidic approach

Microfluidic devices have emerged as powerful tools for accelerating catalyst development and characterization at the single-particle level[9–12]. Their potential lies in the ability to explore the microscale domain offering distinctive advantages over traditional macroscale techniques. For instance, microfluidic systems have channels with sizes ranging from tens of nanometers to hundreds of micrometers, which implies small sample or reagent volumes (fL to µL) consumption. Additionally, the enhanced mass and heat transfer due to the high surface-to-volume ratio leads to high reaction rates and high sensitivity. The key advantages of their use in catalyst research stem from their ability to isolate and examine individual particles under controlled temperature and pressure conditions, pioneering innovative methods for *in situ* and *operando* imaging, and analysis of catalysts[13] for a direct study of catalyst structure-function relations. Specifically, *in situ* refers to studies under model or true reaction conditions, while *operando* analysis involves studying a catalyst under true reaction conditions with the simultaneous online evaluation of its performance.

The miniaturization offered by microfluidics also allows for **high-throughput** screening of catalysts. This can be obtained by e.g. encapsulating individual particles in droplets[14], analyzing spatially resolved particles in flow, or having parallel channels loaded with a different catalyst or the same catalyst under different conditions, allowing simultaneous testing of a multitude of scenarios.

The high-throughput screening approach not only accelerates catalyst development with rapid testing of multiple particles or conditions, but it also resolves particle heterogeneities. The resulting datasets pave the way for improving both the depth of analysis for bulk characterization and the statistical significance of single particles, contributing to more accurate predictions of catalyst performance and more effective catalyst design.

The insights presented in this chapter lay the motivation for the multidisciplinary research carried out in this thesis.

1.5 Thesis Aim

The thesis objective is to develop microdevices that enable the (high throughput) characterization of individual catalytic particles. By doing so, we aim to provide methods able to capture the distinct behaviors and properties of these catalyst particles, beyond what conventional bulk analysis methods can offer.

1.6 Thesis Outline

Chapter 2 provides an introduction to the subject of this thesis, discussing new opportunities and benefits for catalyst testing offered by microfabrication technology. Furthermore, we report the current state of the art of selected spectroscopy and microscopy techniques frequently coupled with microfluidic systems in the realm of catalyst screening. Finally, future directions and challenges in this field are discussed.

Chapter 3 reports the fabrication of a functional device for high-throughput screening or sensing applications consisting of a multiplexed polydimethylsiloxane (PDMS) chip with Pt or Ag nanoparticle films deposited on its chambers. Its originality lies in a new (cleanroom-free) aerosol-based direct-write method in which patterns of metal nanoparticles generated via spark ablation are locally printed inside microfluidic structures.

Chapter 4 discusses a new chemically sensitive method to evaluate the accessibility and surface properties of porous particles at the single-particle level in a high-throughput fashion. The approach consists of the use of a multiplexed microfluidic device (as reported in Chapter 3) which allows screening the uptake of fluorescent molecules in SiO_2 particles and capturing the interparticle heterogeneities, which could not have been resolved with traditional bulk methods.

Chapter 5 describes the fabrication of a device and setup for *in situ* analysis of individual catalyst particles at high throughput with millisecond timescale resolution. The method aims to capture the lifetime and progressive catalyst deactivation due to the formation of (fluorescent) carbonaceous byproducts on its surface by using fluorescence microscopy.

1

Chapter 6 presents the combination of hard X-ray holotomography with an innovative micro-electromechanical system (MEMS)-based microreactor developed by L. Carnevale[15] for *in situ/operando* studies at the single particle level. The approach aims for the direct observation of polymer melting and pyrolysis over a single catalyst particle, with the potential to provide spatially resolved information on the polymer intrusion and changes in the catalyst pore space.

Chapter 7 provides a summary of the results and conclusions presented in the thesis, together with possible improvements and future perspectives on the presented microdevices for catalytic applications.

1.7 References

1. Tanksale, A., Beltramini, J. N. & Lu, G. Q. M. A review of catalytic hydrogen production processes from biomass. *Renew. Sustain. Energy Rev.* **14**, 166–182 (2010).

2. Whang, H. S., Lim, J., Choi, M. S., Lee, J. & Lee, H. Heterogeneous catalysts for catalytic CO2 conversion into value-added chemicals. *BMC Chem. Eng.* **1**, 1–19 (2019).

3. *Handbook of Heterogeneous Catalysis*. (Wiley-VCH Verlag GmbH & Co. KGaA, 2008).

4. Moulijn, Jacob A., Freek Kapteijn, and A. S. *Structured Catalysts and Reactors: A Contribution to Process Intensification*. (CRC Press, 2018).

5. Nieuwelink, A. E. *et al.* Single Particle Assays to Determine Heterogeneities within Fluid Catalytic Cracking Catalysts. *Chem. Eur. J.* **26**, 8546–8554 (2020).

6. Buurmans, I. L. C. & Weckhuysen, B. M. Heterogeneities of individual catalyst particles in space and time as monitored by spectroscopy. *Nat. Chem.* **4**, 873–886 (2012).

7. Jacobs, G. *et al.* Fischer-Tropsch synthesis: Support, loading, and promoter effects on the reducibility of cobalt catalysts. *Appl. Catal. A Gen.* **233**, 263–281 (2002).

8. Munnik, P., De Jongh, P. E. & De Jong, K. P. Control and impact of the nanoscale distribution of supported cobalt particles used in fischer-tropsch catalysis. *J. Am. Chem. Soc.* **136**, 7333–7340 (2014).

9. Solsona, M., Papadimitriou, V. A., Olthuis, W., Van Den Berg, A. & Eijkel, J. C. T. Ion Concentration Polarization for Microparticle Mesoporosity Differentiation. *Langmuir* **35**, 9704–9712 (2019).

10. Solsona, M. *et al.* Magnetophoretic Sorting of Single Catalyst Particles. *Angew. Chemie - Int. Ed.* **57**, 10589–10594 (2018).

11. Vollenbroek, J. C. *et al.* Droplet microreactor for high-throughput fluorescence-based measurements of single catalyst particle acidity. *Microsystems Nanoeng.* **9**, 39 (2023).

12. Nieuwelink, A. E. *et al.* Single catalyst particle diagnostics in a microreactor for performing multiphase hydrogenation reactions. *Faraday Discuss.* **229**, 267–280 (2021).

13. Tsakoumis, N. E., York, A. P. E., Chen, D. & Rønning, M. Catalyst characterisation techniques and reaction cells operating at realistic conditions; towards acquisition of kinetically relevant information. *Catal. Sci. Technol.* **5**, 4859–4883 (2015).

14.   Nieuwelink, A. E. *et al.* High-throughput activity screening and sorting of single catalyst particles with a droplet microreactor using dielectrophoresis. *Nat. Catal.* **4**, 1070–1079 (2021).
15.   Carnevale, L. Microreactors for In Situ Single Catalyst Particle Characterization Using Advanced Imaging Techniques. (University of Twente, 2023).

1
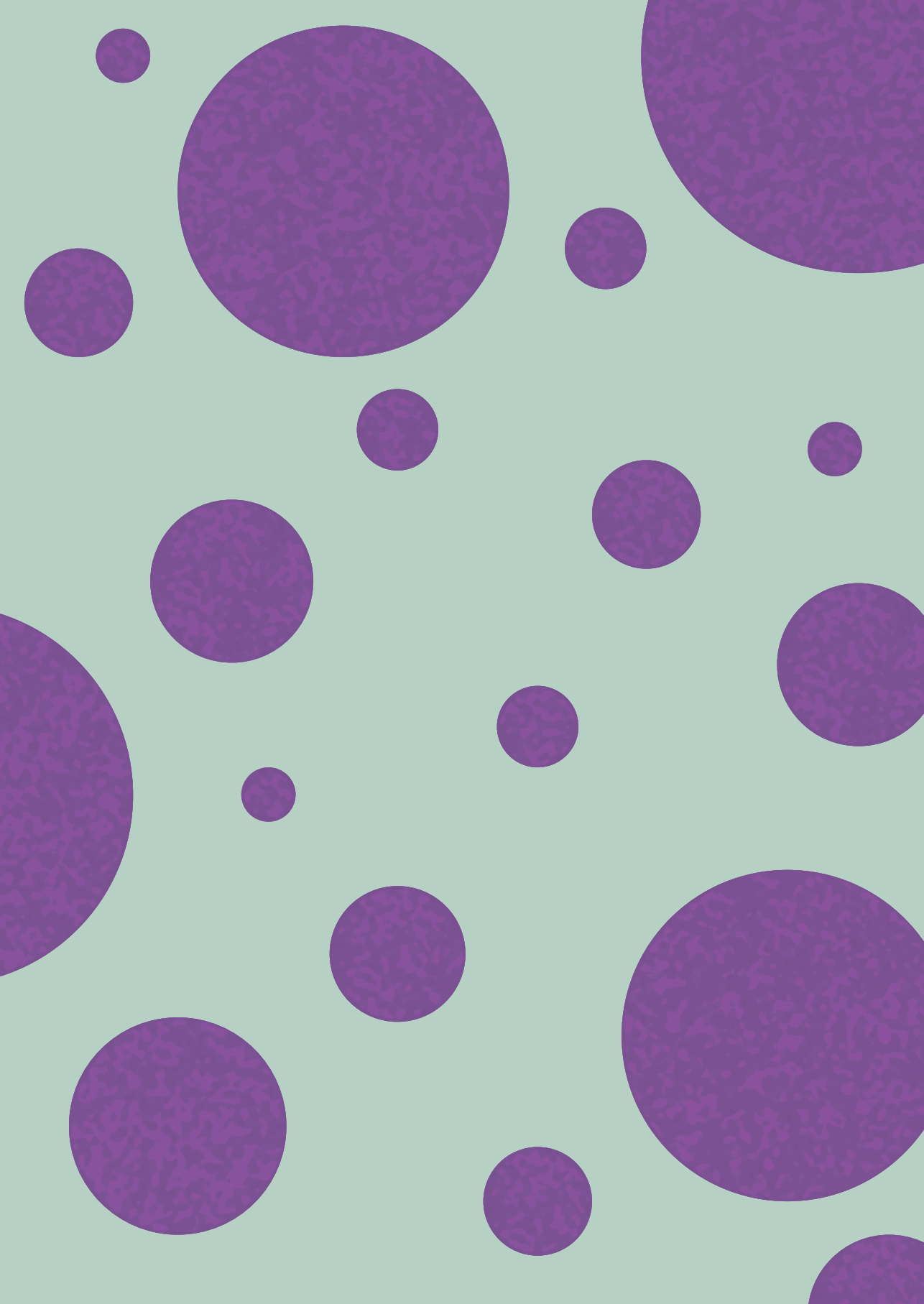
Chapter 2

Heterogeneous Catalyst Characterization in Microfluidics

This chapter reviews technological advancements in microfluidic devices for heterogeneous catalyst characterization. As miniaturized laboratories, these systems offer new opportunities for catalyst testing due to their high-throughput and efficient heat and mass transfer.

The use of these systems for catalyst characterization is a promising approach that can enhance our understanding of catalytic processes and significantly shorten development times. Here we give an overview of the current state of the art of the most used spectroscopy and microscopy techniques coupled with microfluidic technology for catalyst analysis and future directions in this rapidly growing field.

2.1 Introduction

Heterogeneous catalysis plays a fundamental role in many industrial chemical processes, including the production of (solar) fuels, pharmaceuticals, and chemicals. Improving the overall yield and sustainability of chemical processes is a key objective for environmental, economic, and societal considerations in present times. As such, the development of new and improved catalysts represents a significant scientific and technological challenge. Particularly, catalyst optimization strives to increase the selectivity of reactions, thereby decreasing the production of unwanted by-products and minimizing waste production, and to operate under milder conditions, reducing the energy requirements. To design efficient and stable catalysts, understanding their operational mechanisms and exploring the reasons for their deactivation is essential.

Recently, microfluidic devices have emerged as innovative tools to accelerate the process of catalyst development and characterization[1,2]. Although the application potential of microfluidic devices has been demonstrated as an efficient tool for chemical synthesis[3-6], there is a continuous requirement for their use as analytical tools. The key advantages of microfluidics for catalyst characterization include precise control of experimental conditions, such as well-defined flow patterns, high temporal and spatial resolution, and the ability to conduct parallel experiments in a single device. Furthermore, the small scale of microfluidic systems (nL to µL in volume) can significantly reduce the consumption of reactants and catalysts, making it a cost-effective approach for catalyst screening. Perhaps the most impactful aspect of miniaturization lies in its potential to offer innovative approaches to image and analyze catalysts *in situ* and/or *operando*[7,8]. *In situ* (from Latin ''on site'') refers to the direct observation of a process, either under model or true reaction conditions, while *operando* (from Latin ''working/operating'') means studying the catalyst under the true reaction conditions and analyzing its performance by measuring the product concentration[9]. This enables the gaining of a more comprehensive understanding of the functioning of solid catalysts, their properties, and dynamic changes finally assessing structural and functional correlations in

the material. The fraction of heterogeneous catalysis papers involving "microfluidics" is constantly increasing over the last 10 years (Figure 1). Moreover, most of the heterogeneous catalyst publications include characterization studies. Of the reported characterization studies, more than 50% use *in situ* methodologies, and among those, *operando* studies have increased exponentially with time, representing at the moment ~10% of total characterization studies.
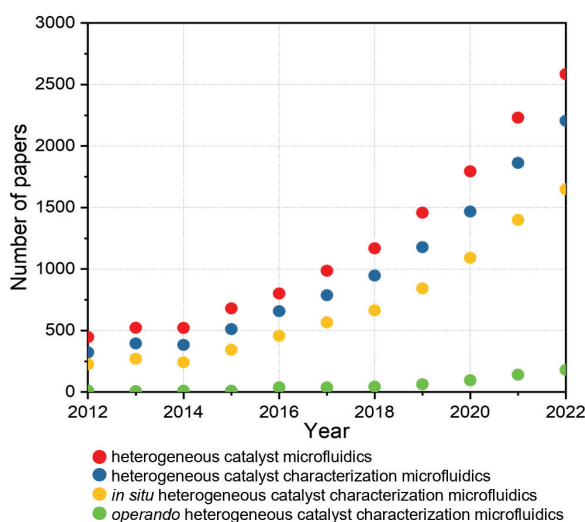
Figure 1: Number of papers with the terms "heterogeneous catalyst microfluidics" (red) from 2012; among these, those referring to "characterization" (in blue) and those using *in situ* (yellow) and *operando* (green). (Source: app.dimensions.ai (May 2022)).

The trend toward miniaturization in analytical chemistry[10] and perspectives[11] on the use of microreactor technology to support catalytic process development has been comprehensively reviewed, finally underlining the interdisciplinary and multidisciplinary nature of research in heterogeneous catalysis. Characterization of solid catalysts involves a broad spectrum of parameters, focusing on material properties and catalytic activity. These parameters can include the number of active sites, their spatial distribution, the particle's porosity, and characteristics of the support structure, such as composition and stability. Moreover, the mass transfer of reactant molecules to the active surface and overall particle accessibility determine the catalyst activity and are therefore important properties to

assess. To be able to obtain this information, specialized techniques and equipment are needed for measuring the catalytic properties of the materials, which can be based on the use of (fluorescent) probe molecules, electromagnetic radiation, photons, mechanical forces, or others. The detection methods mostly rely on spectroscopic and microscopic analyses, with a broad spectrum of electromagnetic radiation being utilized to probe solid catalysts at different scales including radio frequencies (e.g. nuclear magnetic resonance- NMR), microwaves (e.g. electron Paramagnetic Resonance- EPR), infrared (e.g. IR), UV and visible (UV-vis or fluorescence), X-rays (e.g. X-ray Absorption Spectroscopy- XAS, X-ray diffraction, XRD)[12]. Consequently, when integrating these techniques with microfluidic cells, it is essential to use materials that do not interfere with the measurement, allowing the penetration of the radiation through the cell material to ensure the optimal limits of detection. Moreover, the device should also be compatible with the experimental conditions (temperature, pressure, chemicals) needed for the reaction. Traditional chip materials include polydimethylsiloxane (PDMS)[13], glass, quartz, and silicon. In academia, PDMS is the most utilized material for device fabrication due to its cost-effectiveness and straightforward prototyping, but it lacks compatibility with organic solvents. On the other hand, while glass or silicon substrates offer high chemical resistance, their fabrication processes are relatively complex and expensive. Additionally, small fluidic volumes dictate that low Reynolds number (generally below 250) regimes are the norm. To ensure homogeneity in the probe solution or temperature in the device, or to extract inherent reaction kinetics it is necessary to include features like micromixers to enhance the mass transport in the system. Therefore, the final device material and design need to be tailored to suit the specific experimental conditions, the critical length scales of the phenomena under study, the related time scales, and material transparency for the specific techniques.

2.2 Traditional characterization techniques used in catalysis

Traditional characterization techniques in catalysis include a broad spectrum of methods, both spectroscopic and microscopic in nature. Spectroscopic methods include techniques such as Infrared (IR) or Raman

spectroscopy, Ultraviolet-Visible (UV-Vis) spectroscopy, and X-ray photoelectron spectroscopy (XPS), among others. These techniques analyze the interaction between matter and radiated energy, thereby providing detailed information about the chemical composition and molecular structure of catalysts. They can reveal information on the active sites, metal-support interactions, and the nature of reaction intermediates. Microscopic methods, on the other hand, offer direct visualization of the catalyst structure. Although distinct in their approach, often complement each other in providing a complete understanding of the catalytic material, ultimately guiding the optimization of catalyst design. In this chapter, we will provide an overview of commonly used techniques in heterogenous catalyst characterization, briefly discussing their basic principles and selected examples of their integration with microfluidics.

2.2.1 Vibrational spectroscopy: Infrared and Raman spectroscopy

Among the most frequently used methods for (*in situ*) catalyst characterization, vibrational spectroscopy stands out, comprising both Infrared (IR) and Raman spectroscopic techniques. The chemical information that can be extracted from these methods include the nature of chemical bonds, allowing for the determination of the chemical structure of reaction intermediates and products[14]. Additionally, the catalyst's chemical composition, hydration level, and redox state can be examined under *in situ* conditions[12]. Furthermore, both IR and Raman spectra exhibit distinct features related to the presence of carbonaceous deposits, which are among the most common causes of catalyst deactivation and are of critical interest in numerous industrial processes.

IR and Raman spectroscopy involve the study of the interaction of radiation with molecular vibrations but differ in the manner in which photon energy is transferred to the molecule by changing its vibrational state[15]. Both Raman and Infrared (IR) spectroscopy are classified as vibrational spectroscopy techniques as they provide essential information about the vibrational properties of molecules. However, even when evaluating the same sample, they often yield distinct vibrational spectra. This variance can be attributed to the difference in how the incident light interacts with the

sample in each technique. In IR spectroscopy, a molecule absorbs infrared light which matches the energy of a specific vibrational mode, resulting in an excited state. The intensity of a spectral peak in IR spectroscopy is determined by the degree of change in the molecular dipole moment relative to the equilibrium position during that particular vibration[16]. In simple terms, vibrations that cause significant changes in the molecule's dipole moment, - which represents the distribution of electric charge within the molecule, are most effectively observed using IR spectroscopy.

Raman spectroscopy, on the other hand, operates on the principle of inelastic scattering or the Raman effect. When light interacts with a molecule, most photons are elastically scattered, meaning they retain their initial energy upon scattering. However, a small fraction of light is scattered inelastically, either gaining or losing energy in the interaction. This change in energy corresponds to shifts into different vibrational or rotational states within the molecule. The intensity of a peak in a Raman spectrum is determined by how much the polarizability of the molecule changes during a vibration. In simpler terms, vibrations that cause significant changes in the shape of the molecule's electron cloud are most effectively observed using Raman spectroscopy. One of the key limitations of traditional Raman spectroscopy is its relatively weak signal related to the rare inelastic (Raman) scattering, and Surface Enhanced Raman Spectroscopy (SERS) was developed to address this issue amplifying the Raman scattering signal due to the localized surface plasmon resonance effect. For further reading on the basics of vibrational spectroscopy, the following work is recommended: *IR and Raman Spectroscopy, Principles and Spectral Interpretation* by Peter Larkin[15].

2.2.1.1   FTIR

Infrared spectroscopy (IR) is a valuable technique used to analyze the vibrations occurring in the skeletal region of catalysts. The field of IR spectroscopy has evolved significantly over time, leading to a variety of configurations (e.g., transmission, reflection) and methods (e.g., dispersive or time-resolved IR spectroscopy) available nowadays. Particularly, Fourier-transform infrared (FTIR) spectroscopy is the most commonly used method

due to its high acquisition speed and sensitivity. Furthermore, FTIR provides versatility in handling different types of samples, in the form of gases, liquids, or solids, by coupling it with different sampling techniques.

The primary application of IR spectroscopy lies in the investigation of solid catalyst surfaces, enabling researchers to gather detailed molecular-level insights about various surface features such as hydroxyls, M=O bonds, adsorbed molecules, reaction intermediates, and kinetics. For example, real-time analysis of catalytic hydroprocessing of triglycerides with FTIR spectroscopy in a tubular microreactor elucidated the reaction mechanism and pathway[17], while in the context of surface analysis of the catalyst, microcells were used to perform surface analysis of adsorbates on the Pt catalyst and/or support in the ethylene hydrogenation reaction[18]. Similarly, CO oxidation kinetic over Pt/Al_2O_3 and $Pt/CeO_2–Al_2O_3$ catalysts[19] and CO adsorption and oxidation over Pt/SiO_2[20] were monitored by coupling microreactors with IR spectroscopy. FTIR is used in several configurations namely transmission, reflection, and attenuated total reflection (ATR) as reported in Figure 2.
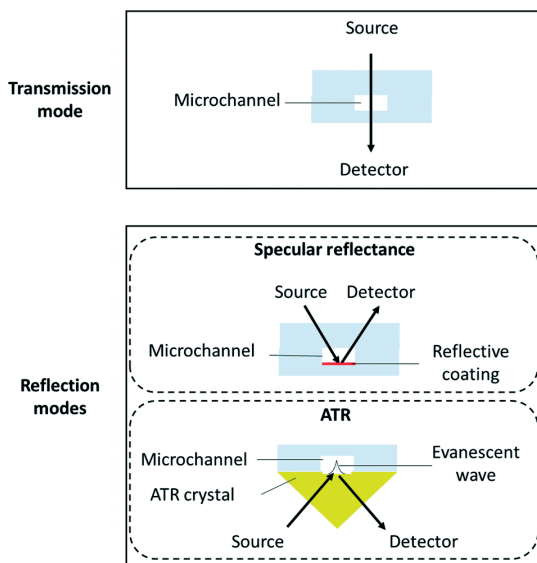
Figure 2: Schematic representation of microdevices coupled with transmission and reflection modes of FTIR spectroscopy.

In transmission mode, the IR beam passes through the microfluidic channel containing the sample. The amount of light absorbed at specific wavelengths, deduced from the recorded transmittance, provides information about the sample. In reflection mode, the IR beam is directed onto the surface of the sample within the microfluidic channel, and the light that is reflected back is measured. This technique is particularly useful for studying surface reactions on a catalytic surface within the channel, even though difficulties are associated with quantitative analysis and interference effects. A more convenient configuration is Attenuated Total Reflectance (ATR) FTIR in which an IR-transparent crystal is positioned beyond the critical internal reflection angle. This arrangement causes the IR light to reflect within the crystal, generating an evanescent wave that penetrates the surface (up to several μm)[21], resulting in an interesting approach for studying e.g. liquid-solid interface processes. ATR has found promising applications in the realm of microfluidics to study the surface and bulk characteristics of catalytic materials, as well as the dynamics of catalytic reactions. Some examples will be reported in the next paragraphs to showcase the ATR-FTIR approach for heterogeneous catalysis.

2.1.1.1.1 Chip material for FTIR spectroscopy compatibility

As already mentioned, to make use of these spectroscopic methods for on-chip measurements, it is essential to have an IR-compatible microfluidic platform. However, this presents a significant challenge since conventional materials commonly employed for microfluidics, such as polymers and glass, exhibit strong absorption of mid-IR light. In the context of FTIR, silicon and calcium fluoride (CaF_2) are generally considered construction materials for their transparency (see Figure 3). in the conventional wavelength range of FTIR spectra, i.e., from 1667 to 25000 nm.
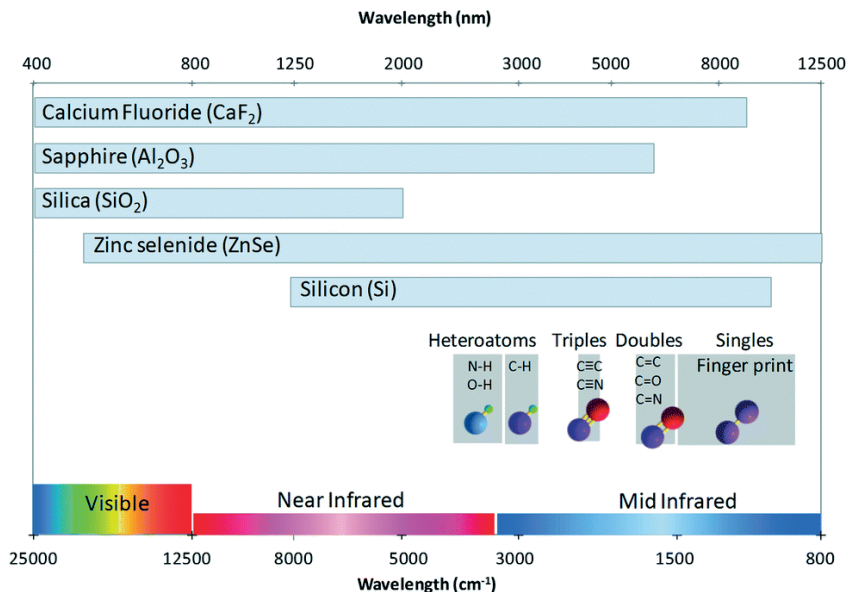
Figure 3: Guide for material compatibility for FTIR analysis. The most common materials used for the fabrication of microfluidic devices and their transparency to the IR radiation are reported in the chart, together with the major region of some conventional spectra of bond stretching. Reproduced from Ref. [22] with permission from the Royal Society of Chemistry.

While Si cannot be used in the visible spectrum, thus limiting the range of reactions that could be studied on chip, CaF_2 is an ideal candidate material for such experiments because it has a transmission range of 170–7800 nm. Therefore, infrared-compatible microfluidic devices have been obtained via etching IR transparent CaF_2 windows[23], by patterning photoresist onto CaF_2 windows[24], or by printing paraffin wax on CaF_2 windows to pattern the microchannels[25]. Polymer-based devices have also been developed for interfacing with IR light[26,27] resulting in an easier and cheaper fabrication. Thin PDMS layers (from 25 to 400 µm) were fabricated to attenuate its IR absorption, allowing for IR measurements. The typical design of IR-compatible devices includes fluidic inlets and outlets, a microfluidic chamber or channel with a length depending upon the desired residence time, and eventual micro-mixers to shorten diffusion lengths and obtain time-resolved measurements[28].

2.1.1.1.2 Examples of FTIR in Microfluidics and Catalysis

In the context of microfluidic devices used for heterogeneous catalysis studies, transmission FTIR is particularly popular due to its simplicity. However, it may pose challenges when dealing with thick or strongly absorbent samples or solvents (e.g. water), which could prevent the transmission of the infrared beam. Attenuated Total Reflectance (ATR) FTIR is advantageous when dealing with liquid samples or samples that strongly absorb IR, and it is very well adapted to microfluidic experiments. In this configuration, catalysts are usually deposited on the internal reflection elements (IRE) as films (e.g. metal film) or as layers of powders, and they are exposed to the reactants[29]. Time-resolved ATR-FTIR spectra can lead to the characterization of transport dynamics, as demonstrated in the CO adsorption on a thin film of platinum[29], or to the catalyst activity screening[17]. To ensure effective functionality, the chip design must facilitate close contact between the channels and the ATR-IR crystal. Usually, the microfluidic devices are directly integrated with polished/commercial IREs, and examples in the literature include e.g. the use of poly(methyl methacrylate) PMMA[30], and PDMS[31,32,] which results in a versatile fabrication, although precise bonding and leaking represent potential limitations together with chemical compatibility.

One of the major challenges faced by these methods is their limited sensitivity, which can impact the detection of subtle changes. Additionally, IR techniques suffer from low signal-to-noise (S/N) levels, resulting in long signal acquisition times often leading to inadequate time resolution. Quantum cascade lasers and synchrotron-sourced IR light provide a substantial advantage for catalysis research[33] due to their significantly brighter nature (>100 times[34]) compared to laboratory IR sources. This enhanced brightness leads to improved signal-to-noise levels, enabling faster (sub-second) measurement of IR spectra and thus contributing to a deeper understanding of the catalytic processes occurring in the microenvironment. A second approach to enhance the signal would be the on-chip integration of nanostructured metal film or an array of nanofabricated metal structures. These components can improve and amplify the interaction between the electromagnetic radiation and the

sample, leading to the so-called Surface Enhanced Infrared Spectroscopy (SEIRS)[35].

Further, utilizing plasmonic nanostructures made from catalytically active metals as enhancement substrates could potentially facilitate *in situ* investigations of catalytic reactions at these interfaces.

2.2.1.2 (Surface-Enhanced) Raman Spectroscopy

As mentioned above, Raman spectroscopy represents a complementary technique to IR and provides fingerprints of molecules and/or crystal structures by probing their inelastic scattering of incident light. This scattering produces a spectrum with distinct frequency differences, revealing the molecule's characteristic fundamental vibrations[36]. While IR spectroscopy is based on molecules' dipole moment change, Raman relies on polarizability and can be applied for the identification and quantification of organic and inorganic compounds. However, conventional Raman spectroscopy often exhibits low sensitivity due to the weak scattering effect, unless enhancement techniques are employed. Indeed, in the case of low-concentrated samples (nanomolar or picomolar concentrations) the obtained Raman signal is weak, and therefore Surface-Enhanced Raman Spectroscopy (SERS) is widely employed[37]. In this case, the signal from the target molecule can be significantly enhanced when it adsorbs onto metallic nanostructures smaller than the wavelength of the incident laser light[38]. Surface enhancement occurs when target molecules are in close proximity to nanostructures that exhibit plasmonic resonance, and the interaction between the compounds and the local surface plasmon resonance field leads to enhanced Raman scattering.

2.2.1.2.1 Chip Material Considerations

Raman spectra can be recorded over a range of 4000–10 cm^{-1} [39], and Raman active normal modes of vibration of organic molecules occur in the range of 4000–400 cm^{-1}. As for the material suitable for constructing microfluidic devices for Raman spectroscopy, it should have low Raman scattering itself, to avoid overwhelming the signal from the sample. Additionally, the material should be transparent to the laser light used for Raman excitation (typically 532, 633, and 785 nm lasers are used) and the

resulting scattered light. Glass and PDMS are the most common materials used for the fabrication of devices for Raman spectroscopy due to their optical transparency, ease of fabrication, and low cost. The potential of the technique in the catalysis field relies on acquiring information on the state of the catalyst (chemical composition, hydration) and monitoring chemical reactions in microdevices, which allows the establishment of structure-activity/selectivity relationships.

2.2.1.2.2 Examples of SERS in microfluidics and catalysis

Many authors have combined SERS with microfluidics, leading to the development of microfluidic-based SERS chips[40,41,42] used for both static and dynamic (in-flow) conditions. Examples of such devices are reported in Figure 4. SERS-active substrates can be synthesized using various methods[43], including bottom-up approaches (e.g. chemical reduction of metal precursors) for obtaining metal colloids or core-shell nanoparticles in the microfluidic channels. Additionally, self-assembly or template-assisted methods can be employed, as well as top-down processes (nanolithography). As an example, Xu et al.[44] demonstrated the on-chip fabrication of silver microflower arrays made by upright nanoplates and attached nanoparticles via femtosecond laser-induced photo-reduction of a silver precursor. The deposited metal patterns showed both high catalytic activity in the reduction of 4-nitrophenol to 4-aminophenol as well as high SERS enhancement (10^8), which allowed *in situ* monitoring of the reaction. Similarly, Pt-catalyzed reduction of 4-nitrothiophenol to 4-aminothiophenol was also performed and monitored in a SERS- chip[45], as bifunctional Au–Pt–Au hybrid NPs were used as colloidal metal catalysts and SERS-active substrates. In this case, the microfluidic approach allowed for the required time resolution to monitor the fast Pt-catalyzed reduction reaction. By recording the spectra at different positions along the microfluidic reactor's channel or by adjusting the flow rate, the time intervals for kinetic monitoring could be easily modified[46], offering flexibility in capturing the reaction dynamics.
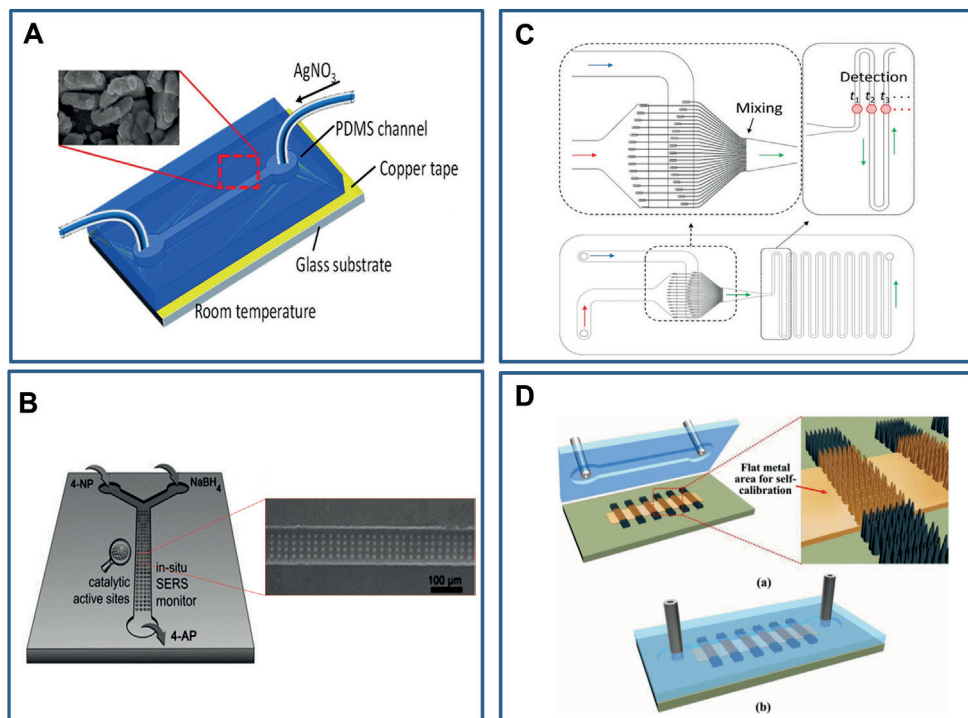
Figure 4: Examples of SERS-active substrates integrated in microfluidic systems. **A)** Ag nanostructures obtained in a PDMS channel via a one-step electroless galvanic replacement reaction. An AgNO$_3$ solution is injected into the channel and the Cu base reduces Ag ions to Ag nanoparticles. (Figure reproduced with permission from Wen et al.[47]) **B)** Ag-micro flower-equipped microreactor obtained with femtosecond laser direct writing. The process consists of two-photon absorption-induced photoreduction of a silver precursor. (Figure reproduced with permission from Sun et al.[44]) **C)** Microfluidic device used to study the kinetics of a Pt-catalyzed surface reaction using sodium borohydride in aqueous media. Time-resolved SERS spectra were obtained by recording measurements at various positions along the meander-shaped flow channel (top right in the figure). The red data points represent specific instances of SERS detection at different reaction times. (Figure reproduced with permission from Schlücker et al.[45]) **D)** Microfluidic device including a PDMS layer bonded on a silicon substrate composed of noble-metal covered silicon nanopillar forests obtained via photolithography. (Figure reproduced with permission from Zhang et al.[48])

The same concept was recently applied for Pickering emulsion catalysis with a continuous flow droplet microfluidic approach[49], in which acid-catalyzed deacetalization reaction was followed *in situ* with Raman spectroscopy over different device positions, representative of different residence times. The examples demonstrate the potential of the

microfluidics-based Raman analysis in monitoring heterogeneous catalysis with SERS methods being widely employed. In this context, challenges persist in the preparation of SERS-active substrates for microfluidic chips, particularly in achieving cheap, ordered, easy-to-reproduce, and highly enhanced factors (EFs) fabrication.

2.2.2 Fluorescence Microscopy

Fluorescence microscopy techniques provide a versatile approach for studying catalyst particles in microdevices, offering real-time monitoring capabilities and compatibility with various labeling and imaging strategies. By incorporating fluorescent tags or probes onto the catalyst particles, these techniques enable the visualization and tracking of probes over individual particles with high spatial resolution[50].

Fluorescence microscopy employs near-infrared (NIR), UV, and visible light to illuminate and study the sample under investigation. These wavelengths correspond to the typical energies required to electronically excite fluorescent molecules with polycyclic aromatic cores[50]. Briefly, the fluorescence emission from a fluorophore consists of the absorption of a photon carrying sufficient energy to excite an electron to a higher electronic state. This excited state is unstable, and the electron tends to return to its original state, releasing the absorbed energy. The release of energy manifests as a photon emission process known as fluorescence[51]. Since a portion of the initially absorbed energy dissipates during vibrational relaxation, the emitted photon's energy and corresponding color differ from the absorbed one. The fluorescence microscope takes advantage of this color disparity between the absorbed and emitted photons to construct an almost noise-free image of the target object.

The two main fluorescence microscopy configurations that are used nowadays are wide-field fluorescence microscopy (WFM) and confocal laser scanning microscopy (CLSM). The latter provides exceptional spatial resolution by using a pinhole to eliminate out-of-focus light. This enables optical 3D sectioning of the sample under study, producing slices with a thickness of about 500 nm[52]. On the other hand, CLSM results 70-fold

slower than WFM are obtained, making it less suited for capturing images of fast-evolving phenomena.

2.2.2.1 Chip Material Considerations

To achieve optimal detection limits when using microfluidic devices, it is beneficial to use materials with a low fluorescence background at the investigated wavelengths. Glass and quartz are suitable choices, although they necessitate an expensive fabrication procedure. Low-cost alternatives like PMMA and PDMS produce considerable autofluorescence when exposed to UV or even visible radiation to a limited extent. Despite this drawback, the fluorescence background interference originating from these materials can be reduced through the implementation of improved optics or by marking analytes with fluorophores that can be excited at longer wavelengths.[53]

2.2.2.2 Examples of on-chip catalytic studies via fluorescence microscopy

As most of the heterogeneous catalyst materials exhibit sufficient optical transparency and lack of fluorescence, it is possible to observe fluorophores even inside the (porous) catalyst volume. Thus, fluorescence microscopy has often been employed to ascertain functional attributes such as the distribution of catalytic sites and porosity and to address variations in reactivity[54], both within individual catalyst particles (intraparticle variations) and among distinct catalyst particles (interparticle variations). To identify the positions of catalytically active or accessible sites, fluorogenic reactions are often employed. For this approach, non-fluorescent probes diffuse and react on the catalyst active sites leading to the formation of fluorescent products, thus highlighting the location of catalytic activity. This strategy has been used to explore the reactivity in zeolites. Non-fluorescent probes such as furfuryl alcohol, styrene, and thiophene can undergo an oligomerization reaction upon reaching the acid sites, leading to the formation of fluorescent products. This results in the mapping of zeolite acid sites[55,56]. Recently, this approach has also been used on-chip to screen the activity of fluid catalytic cracking (FCC) particles[57], which is linked to the availability of (Brønsted) acid sites in the

zeolite domains. The particles were pre-stained in 4-methoxy styrene, used as a probe molecule, and captured in paraffin oil droplets in the microfluidic device. By increasing the temperature to 95°C, the oligomerization reaction was induced, and it was possible to measure on-chip the mean fluorescence intensity from the particles, directly related to the availability of the active sites in the particle[54].
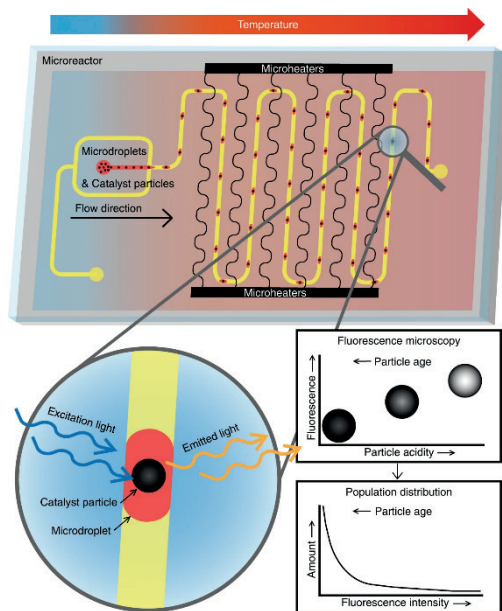
Figure 5: Microfluidic chip that enables high-throughput screening of individual fluid catalytic cracking (FCC) equilibrium catalyst (ECAT) particles activity evaluated using a fluorescent reaction product as an indicator of catalyst acidity. The chip is equipped with built-in heaters and temperature sensors, facilitating the adjustment of reaction parameters and enhancing the efficiency of the screening process. (Figure reproduced with permission from Vollenbroek et al.[57])

Furthermore, a similar approach coupling a droplet-based microreactor with dielectrophoresis (DEP) allowed for the individual analysis of FCC particles at high throughput and their sorting based on the activity[58]. Upon detecting the fluorescent light from catalyst particles encapsulated in droplets, DEP was triggered and allowed for the manipulation of the most intense ones into a sorted outlet for further (*ex situ*) analysis. Fluorescence microscopy was also used to enable the visualization of ion concentration

polarization phenomena to characterize particles' (meso) porosity in a PDMS microfluidic device[59].

A direct way to study the pore space of catalyst materials is the selective staining of fluorescent dyes with different sizes and shapes to provide information on the accessible pore volume[60,61] and eventual spatial heterogeneities. On the other hand, the dynamic imaging of the uptake of fluorescent dyes can be used to follow the mass transport[62,63,64,65,66] through the pore network of catalyst particles, providing information on their accessibility i.e., how easily molecules enter the porous host. In this context, microfluidic technology proves to be an efficient tool for studying mass transfer phenomena, as extensively demonstrated through its application in biological systems. With the approach, it is possible to gain precise control over the experimental conditions and investigate individual catalyst particles potentially in a high-throughput fashion.

Single-molecule tracking constitutes an even more direct approach to visualizing molecular motion and determining diffusion constants and pore accessibility[67,68,69]. The positions of individual molecules (obtained in highly dilute conditions) can be determined with a precision of nanometers[52] by analyzing time-lapse recordings obtained through super-resolution fluorescence microscopy techniques. Then, diffusion rates can be calculated based on the displacement of a molecule along its trajectory. Such methods have been used to assess diffusion pathways in porous materials[70], to get physicochemical information on their pore network[69]. However, the pore space of each catalyst is extremely complex, making it particularly challenging to correlate tracks to the diffusion properties of a probe and the local pore geometries, especially in nanopores. To address this issue, one approach could involve developing optically transparent micro/nanofluidic-based model systems. These systems, with well-defined structures and known compositions and geometries, would allow for a high signal-to-noise ratio. This in turn would facilitate high-resolution imaging and mass transfer evaluation. This approach can facilitate the identification of the diffusion characteristics of the probes employed which can help to quantitatively and precisely investigate more intricate pore space configurations.

2.2.3 X-ray Microscopy

X-ray microscopy (XRM) is a powerful imaging technique used to investigate the structure and composition of materials through X-ray excitation. When coupled with spectroscopy, it becomes a powerful tool that can create detailed 2D and 3D maps of elemental distributions and for chemical imaging. X-ray radiation exhibits a wavelength that is three orders of magnitude shorter than visible light, thus allowing for the imaging of comparatively thick samples at a high spatial resolution (sub-micron). Moreover, X-ray imaging methods are non-destructive and, compared to electron microscopy, measurements do not require high-vacuum conditions and can be performed for instance, in air or at elevated pressures and temperatures thus allowing for their use for *in situ* solid catalyst characterization in specially designed devices.

When a material is exposed to a beam of monochromatic X-ray radiation, the interaction of the radiation with the electrons bound within the atoms of the sample leads to either absorption or scattering of the X-rays. This interaction can occur through processes such as electronic transitions or elastic collisions between electrons and X-ray photons, which is typically followed by the emission of an X-ray photon (fluorescence X-rays). Based on the energy of the incident X-ray radiation, it is possible to classify the soft X-ray region, which extends from ~250 eV to several keV, while hard X-rays extend up to ~100 keV[71]; resulting in depth of focus in the range of 10 μm or higher. As a result, despite the higher spatial resolution achievable in the case of soft X-rays (10 nm[72]), penetration depth into the reactor and catalyst material may be an important limitation for *in situ/operando* studies. Nevertheless, hard X-rays are better suited to get detailed information about the internal structure and composition of catalysts, reducing absorption and scattering effects and allowing for imaging materials with high atomic numbers, such as metals and inorganic compounds.

In general, X-ray microscopes can be categorized into full-field and scanning microscopes (examples of various configurations are reported in Figure 6). In the first case, the sample imaging is obtained by capturing a simple projection through a single exposure, (e.g. in holotomography[73])

leading to a short measurement time. In the scanning mode, the sample is scanned (pixel by pixel) via a focused X-ray beam (e.g. in scanning Transmission X-ray Microscopy STXM[74] and X-ray fluorescence microscopy, XRF) resulting slower than the full-field approach but allowing for high-resolution local structural information and elemental composition[75]. Scanning microscopes enable the application of multiple contrast methods, like X-ray diffraction (XRD)[76] in both wide-angle (WAXS) and small-angle (SAXS) modes, X-ray fluorescence[77], and absorption spectroscopy[78] allowing for local structural and compositional information on the atomic and mesoscopic scale. Therefore, the choice of a particular technique and X-ray regime mostly depends on the research question and length scales involved.

2
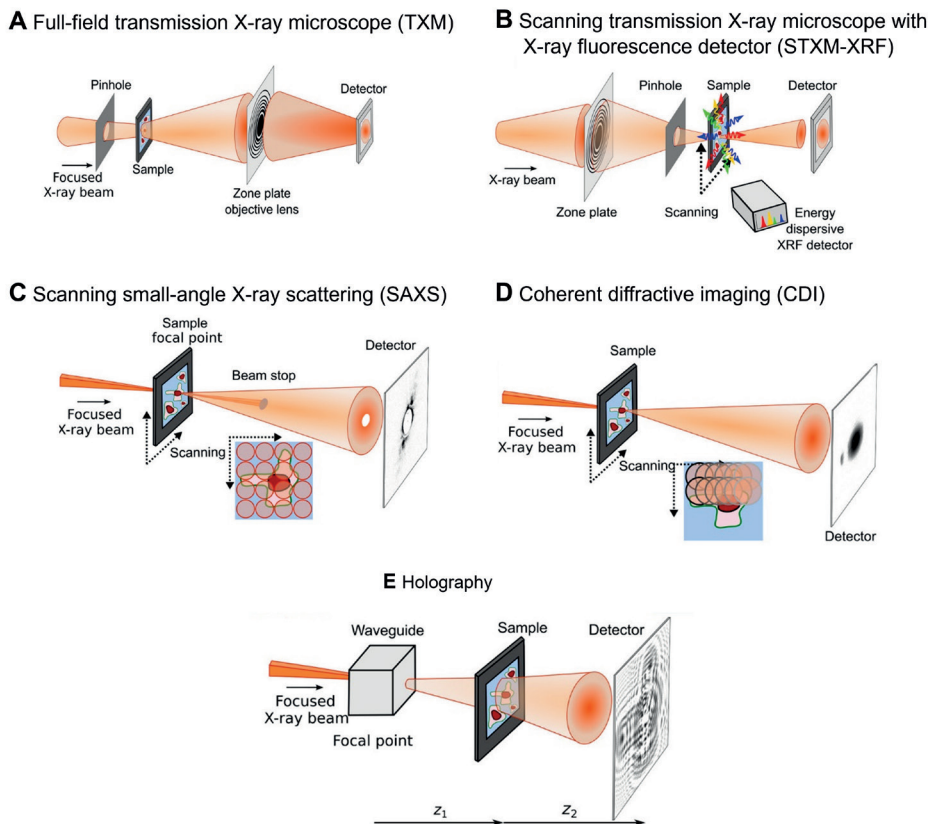
Figure 6: Different setups for X-ray imaging techniques. **A)** A full-field transmission X-ray microscope (TXM) where the sample is positioned outside the focal plane. **B)** A scanning transmission X-ray microscope (STXM) equipped with an X-ray fluorescence (XRF) detector. **C)** A scanning nano diffraction/scanning small-angle X-ray scattering (SAXS) setup. **D)** Coherent diffractive imaging (CDI) setup, specifically ptychtography. **E)** In-line holography setup that utilizes waveguides emitting spherical waves. Figure reproduced with permission from Köster[79].

Synchrotron radiation sources[80,81] have been extremely useful in the development of *in situ* and *operando* studies of catalytic materials. The radiation, especially that from modern third or fourth-generation synchrotron facilities[82], provides highly focused and brilliant X-ray beams, which enable a resolution to the nanometer scale and high-temporal resolution. On the other hand, the high intensity of these radiation sources

can cause significant radiation damage, which has to be taken into account when planning experiments involving the use of synchrotron radiation.

The integration and continuous improvement of synchrotron radiation facilities have significantly enhanced the capabilities of hard X-ray microscopy, leading to achievable spatial resolution approaching those of soft X-ray microscopy (tens of nm[83] with field of views of a few ten micrometers). This favored its use in the heterogeneous catalysis field[84], with major applications in microscopy and tomography to probe their 2D and 3D structure and chemistry. Image acquisition under *in situ* or *operando* conditions requires devices that allow for the control over temperature and pressure and that are optically freely accessible to nearly 180° allowing for 3D image acquisition by rotation. Microdevices can address those requirements, representing a valuable solution for the reaction performance as well as compatibility with the desired imaging technique.

2.2.3.1 Chip Material Considerations

The use of microdevices for X-ray imaging methods requires several considerations concerning the interaction between the beam and the material used for its fabrication, such as transparency and surface smoothness. If the material tends to strongly absorb photons, this invariably reduces both the incident and emitted beam strengths, resulting in beam attenuation. Secondly, the scattering from the device material is influenced by various aspects such as surface and wall textures, and the material's thickness.

Microreactors for X-ray analysis are frequently designed with inspection windows made from materials like polyimides (e.g. Kapton), due to their relatively low X-ray absorption properties and resilience to the high-intensity X-ray beams produced by synchrotrons. On the other hand, other materials commonly employed in microreactor manufacturing, such as silicon and glass, demonstrate substantial radiation absorption, especially at low X-ray energies. This typically necessitates the use of exceptionally thin (few µm) inspection windows for performing X-ray measurements in these devices.

2.2.3.2   Examples of microdevices coupled with X-ray Imaging

In the context of hard X-rays, microdevices have been developed to investigate catalysts *in situ/operando* using XRM techniques. For instance, a quartz capillary reactor (100 mm in diameter and 10 mm of wall thickness) has been used to perform *operando* transmission X-ray microscopy (TXM) of a Fe-based Fischer-Tropsch synthesis (FTS) catalyst of tens of micrometers in size at ~30 nm 2D resolution[85]. The approach was used to obtain information on structural changes of the catalyst over time (7h). In a transmission configuration, the detected X-ray intensity is measured behind the sample, providing information on the spatial changes in the sample's absorption coefficient. The glass capillary was placed onto a specifically designed adaptor to allow gas reactant supply and optical access and mounted on the sample stage. The reaction was performed at 10 bar and 350°C, obtained by external heating via a heater gun, and it was possible to obtain information on the composition of the catalyst active sites. An improved device version was used to study Co/TiO_2 FTS catalyst particles[86,87] which allowed for spatial and chemical mapping of Co during the reaction at 10 bar and 250°C, induced and controlled using a thermocouple near the sample location. From the reported studies one can conclude that TXM results in a powerful tool to understand the activity and deactivation of catalyst particles, as also reported via *ex situ* analysis of FCC particles[88,89]. In this case, full-field TXM allowed the 3D mapping of the catalyst pore structure at different reaction stages and the deactivation of the catalyst due to metal deposition. It was possible to obtain a direct measure of the (2D or 3D) elemental concentration distribution within the sample as the imaging contrast is directly related to the elemental composition of the absorbing material (specific X-ray attenuation coefficient). Performing the study on chip has the potential to investigate the process under realistic reaction conditions and to provide its timescale, which is a topic of particular interest for the understanding of the mechanisms and rate of catalyst deactivation. Hard X-ray holotomography has been recently used to investigate (*ex situ)* the effect of carbon deposits (reaction byproduct) on the macro-pore network of the FCC catalyst[90]. Unlike TXM in which the contrast in the images comes from differences in

the X-ray absorption of different parts of the sample, X-ray holotomography is a phase contrast imaging technique, that is suitable for low adsorbing X-ray species (''soft'' materials). Its coupling with microreactors holds a big potential in the field of heterogeneous catalysis for e.g., the understanding of catalyst deactivation via coke deposition, which represents among the most common causes of their activity decrease[91].

2.2.4 Challenges and Future Directions

In recent years, significant advancements have been made in the fabrication of microreactors and on-chip catalytic testing. The reported findings demonstrate the new and potential approaches in heterogeneous catalyst characterization, with advantages such as reduced reaction time, ease of handling, high throughput, and low consumption, resulting in highly efficient experimental platforms. By integrating advanced characterization techniques with microfluidic systems, we can gain a deeper understanding of the structure-performance relationships of heterogeneous catalysts, ultimately guiding the design of more efficient and sustainable catalytic processes. Accurate prediction of catalyst behavior is desirable for every reaction before embarking on the journey toward commercialization. In the context of catalyst characterization, microfluidic systems can offer enhanced spatial resolution for studying catalysts, as the confinement allows for a better focus of the radiation, whether from microscopic or spectroscopic techniques, on specific regions of interest on the catalyst thus allowing for more detailed analysis of localized phenomena taking place on the catalyst, surface features, and reaction intermediates in the case of *in situ/operando* experiments. This can be obtained thanks to the advanced micro-nanofabrication techniques and a variety of materials that can be used to make the device compatible with specific (ideally multiple) characterization techniques.

As our understanding of the structure, composition, and operation of solid catalysts deepens, we have come to recognize these intricate, multi-component, and hierarchical materials for their inherent (spatiotemporal) heterogeneity[92]. Traditionally, solid catalysts are fixed in microchips either by being coated on a wall or by being packed in a bed. In most experiments

information about the structure and function of the catalyst is obtained in an integral manner, i.e., averaging the information over the whole population of catalytic sites. This approach relies on the assumption that the structure of the active site is homogeneously distributed throughout the catalyst particle, the formed pellet, or the entire catalyst bed. However, fundamental studies in surface science have demonstrated that distinct areas of the catalytic particles, for instance, crystalline faces of different orientations can exhibit varying catalytic activities and/or selectivity[92]. This heterogeneity, existing both within and between particles, poses significant challenges to the thorough analysis of the catalyst material as they cannot be directly correlated to the averaged performance information derived by a bulk characterization. It restricts the effectiveness of bulk characterization methodologies and simultaneously complicates the analysis of individual catalyst particles due to a lack of statistical significance. Hence, there is a pressing need for the development of refined techniques with high sensitivity capable of screening individual catalyst particles in a high-throughput manner. Recent advancements in the field of microfluidics have opened up new avenues for catalyst particle analysis, drawing inspiration from high-throughput techniques used in single-cell analysis[93,94]. For example, the on-chip encapsulation of particles in droplets allows for their individual analysis and eventual (passive or active) sorting based on specific properties (e.g. activity)[58]. Moreover, droplets can serve as individual reaction compartments of pico- to microliter scale, effectively functioning as micro-nanoreactors[95,49]. Another approach is the generation of (reactant, temperature, pH, …) gradients across a microchannel, to screen catalyst performance under different reaction conditions, following approaches used for drug screening[96]. Finally, different experiments can be performed in multiplexed devices having separate parallel channels/chambers, which can facilitate the comparison of the performance of a library of catalysts, having different sizes, porosity, etc., or the impact of different reactant concentrations or reaction conditions. The advent of Artificial Intelligence (AI) in the form of intelligent informatics tools, including advanced software and sophisticated algorithms, offers transformative potential in the realm of catalyst design. AI-driven tools can be used in combination with high-throughput methods to efficiently analyze large datasets and identify

correlations between structure and properties, which represents the fundamental aspect for a more rational catalyst design.

The future of lab-on-chip technologies in catalyst characterization lies in the development of integrated systems that combine multiple functionalities. This includes the integration of synthesis, characterization, and testing steps on the same chip, which would significantly accelerate the process of catalyst development. Looking ahead, the introduction of standardized microfluidic devices for catalyst characterization emerges as a critical focus. At present, the fabrication of devices tends to largely differ even for the same application and technique requirements. As a result, the interchangeability, reproducibility, and scalability of experimental results can be limited. The development and adoption of standardized microfluidic platforms would significantly simplify this process, enabling more robust and comparable results across different studies. It would also facilitate the wide-scale and commercial adoption of microfluidic technologies, thus saving time and resources and expanding the possibilities for *in situ* and *operando* studies. While significant challenges remain, particularly concerning the diversity of catalysts and reactions to be studied, the benefits of standardizing microfluidic devices for catalyst characterization are substantial, remaining a compelling goal for the scientific community in the years to come.

2

2.3 References

1. Xu, B. Bin, Zhang, Y. L., Wei, S., Ding, H. & Sun, H. B. On-Chip catalytic microreactors for modern catalysis research. *ChemCatChem* **5**, 2091–2099 (2013).

2. Mei, F. *et al*. Homogeneous, heterogeneous, and enzyme catalysis in microfluidics droplets. *Smart Mol.* **1**, e20220001 (2023).

3. Gemoets, H. P. L. *et al*. Liquid phase oxidation chemistry in continuous-flow microreactors. *Chem. Soc. Rev.* **45**, 83–117 (2016).

4. Amreen, K. & Goel, S. Review–Miniaturized and Microfluidic Devices for Automated Nanoparticle Synthesis. *ECS J. Solid State Sci. Technol.* **10**, 017002 (2021).

5. da Rosa, A. P. P. *et al*. H2O2-assisted photoelectrocatalytic degradation of Mitoxantrone using CuO nanostructured films: Identification of by-products and toxicity. *Sci. Total Environ.* **651**, 2845–2856 (2019).

6. Yue, J. Multiphase flow processing in microreactors combined with heterogeneous catalysis for efficient and sustainable chemical synthesis. *Catal. Today* **308**, 3–19 (2018).

7. Al-Rifai, N., Cao, E., Dua, V. & Gavriilidis, A. Microreaction technology aided catalytic process design. *Curr. Opin. Chem. Eng.* **2**, 338–345 (2013).

8. Zhao, S. *et al*. Operando Characterization of Catalysts through use of a Portable Microreactor. *ChemCatChem* **7**, 3683–3691 (2015).

9. Iwasawa, Y., Asakura, K., & Tada, M. *XAFS techniques for catalysts, nanomaterials, and surfaces*. (Cham: Springer International Publishing, 2017).

10. Ríos, Á. & Zougagh, M. Modern qualitative analysis by miniaturized and microfluidic systems. *TrAC Trends Anal. Chem.* **69**, 105–113 (2015).

11. Kalz, K. F. *et al*. Future Challenges in Heterogeneous Catalysis: Understanding Catalysts under Dynamic Reaction Conditions. *ChemCatChem* **9**, 17–29 (2017).

12. Tsakoumis, N. E., York, A. P. E., Chen, D. & Rønning, M. Catalyst characterisation techniques and reaction cells operating at realistic conditions; towards acquisition of kinetically relevant information. *Catal. Sci. Technol.* **5**, 4859–4883 (2015).

13. Nieuwelink, A. E. *et al*. Single catalyst particle diagnostics in a microreactor for performing multiphase hydrogenation reactions. *Faraday Discuss.* **229**, 267–280 (2021).

14. Stavitski, E. & Weckhuysen, B. M. Infrared and Raman imaging of heterogeneous catalysts. *Chem. Soc. Rev.* **39**, 4615–4625 (2010).

15.   Larkin, P. *Infrared and Raman Spectroscopy. Infrared and Raman Spectroscopy: Principles and Spectral Interpretation* (Elsevier, 2011).

16.   Bradley, M. S. Lineshapes in IR and raman spectroscopy: A primer. *Spectroscopy* **30**, 42–46 (2015).

17.   Anand, M., Farooqui, S. A., Singh, J., Singh, H. & Sinha, A. K. Mechanistic in-operando FT-IR studies for hydroprocessing of triglycerides. *Catal. Today* **309**, 11–17 (2018).

18.   Zhao, S. *et al.* Operando Characterization of Catalysts through use of a Portable Microreactor. *ChemCatChem* **7**, 3683–3691 (2015).

19.   Daniel, C. *et al.* Spatially resolved catalysis in microstructured reactors by IR spectroscopy: CO oxidation over mono- and bifunctional Pt catalysts. *J. Catal.* **272**, 55–64 (2010).

20.   Tan, C. K. C., Delgass, W. N. & Baertsch, C. D. Spatially resolved in situ FTIR analysis of CO adsorption and reaction on Pt/SiO2 in a silicon microreactor. *Appl. Catal. B Environ.* **93**, 66–74 (2009).

21.   Karabudak, E. Micromachined silicon attenuated total reflectance infrared spectroscopy: An emerging detection method in micro/nanofluidics. *Electrophoresis* **35**, 236–244 (2014).

22.   Perro, A. *et al.* Combining microfluidics and FT-IR spectroscopy: Towards spatially resolved information on chemical processes. *React. Chem. Eng.* **1**, 577–594 (2016).

23.   Birarda, G. *et al.* Microelectronic Engineering Fabrication of a microfluidic platform for investigating dynamic biochemical processes in living samples by FTIR microspectroscopy. *Microelectron. Eng.* **87**, 806–809 (2010).

24.   Hinsmann, P., Frank, J., Svasek, P., Harasek, M. & Lendl, B. Design, simulation and application of a new micromixing device for time resolved infrared spectroscopy of chemical reactions in solution. *Lab Chip* **1**, 16 (2001).

25.   Chan, K. L. A. & Kazarian, S. G. FT-IR Spectroscopic Imaging of Reactions in Multiphase Flow in Microfluidic Channels. *Anal. Chem.* **84**, 4052–4056 (2012).

26.   Srisa-art, M., Noblitt, S. D., Krummel, A. T. & Henry, C. S. IR-Compatible PDMS micro fl uidic devices for monitoring of enzyme kinetics. *Anal. Chim. Acta* **1021**, 95–102 (2018).

27.   Polshin, E. *et al.* Sensors and Actuators B : Chemical Integration of microfluidics and FT-IR microscopy for label-free study of enzyme kinetics. *Sensors Actuators B. Chem.* **196**, 175–182 (2014).

28.   Wagner, C., Buchegger, W., Vellekoop, M., Kraft, M. & Lendl, B. Time-

resolved mid-IR spectroscopy of (bio)chemical reactions in solution utilizing a new generation of continuous-flow micro-mixers. *Anal. Bioanal. Chem.* **400**, 2487–2497 (2011).

29. Aguirre, A., Kler, P. A., Berli, C. L. A. & Collins, S. E. Design and operational limits of an ATR-FTIR spectroscopic microreactor for investigating reactions at liquid-solid interface. *Chem. Eng. J.* **243**, 197–206 (2014).

30. Flaman, G. T. *et al.* Chemical Imaging of Mass Transport Near the No-Slip Interface of a Microfluidic Device using Attenuated Total Reflection–Fourier Transform Infrared Spectroscopy. *Anal. Chem.* **95**, 4940–4949 (2023).

31. Lozeman, J. J. A. *et al.* Modular microreactor with integrated reflection element for online reaction monitoring using infrared spectroscopy. *Lab Chip* **20**, 4166–4174 (2020).

32. Chan, K. L. A., Gulati, S., Edel, J. B., De Mello, A. J. & Kazarian, S. G. Chemical imaging of microfluidic flows using ATR-FTIR spectroscopy. *Lab Chip* **9**, 2909–2913 (2009).

33. Zaera, F. New advances in the use of infrared absorption spectroscopy for the characterization of heterogeneous catalytic reactions. *Chem. Soc. Rev.* **43**, 7624–7663 (2014).

34. Duncan, W. D. & Williams, G. P. Infrared synchrotron radiation from electron storage rings. *Appl. Opt.* **22**, 2914 (1983).

35. Bomers, M. *et al.* Microfluidic surface-enhanced infrared spectroscopy with semiconductor plasmonics for the fingerprint region. *React. Chem. Eng.* **5**, 124–135 (2020).

36. Kurouski, D., Dazzi, A., Zenobi, R. & Centrone, A. Infrared and Raman chemical imaging and spectroscopy at the nanoscale. *Chem. Soc. Rev.* **49**, 3315–3347 (2020).

37. Tycova, A., Prikryl, J. & Foret, F. Recent strategies toward microfluidic-based surface-enhanced Raman spectroscopy. *Electrophoresis* **38**, 1977–1987 (2017).

38. Mulvaney, S. P. & Keating, C. D. Raman Spectroscopy. *Anal. Chem.* **72**, 145–158 (2000).

39. Edwards, H. G. M. Modern Raman spectroscopy–a practical approach. *J. Raman Spectrosc.* **36**, 835–835 (2005).

40. Strehle, K. R. *et al.* A reproducible surface-enhanced Raman spectroscopy approach. Online SERS measurements in a segmented microfluidic system. *Anal. Chem.* **79**, 1542–1547 (2007).

41. Huang, J. A., Zhang, Y. L., Ding, H. & Sun, H. B. SERS-Enabled Lab-on-a-Chip Systems. *Adv. Opt. Mater.* **3**, 618–633 (2015).

42. Pu, H., Xiao, W. & Sun, D. W. SERS-microfluidic systems: A potential platform for rapid analysis of food contaminants. *Trends Food Sci. Technol.* **70**, 114–126 (2017).

43. Guo, J., Zeng, F., Guo, J. & Ma, X. Preparation and application of microfluidic SERS substrate: Challenges and future perspectives. *J. Mater. Sci. Technol.* **37**, 96–103 (2020).

44. Xu, B. Bin *et al.* On-chip fabrication of silver microflower arrays as a catalytic microreactor for allowing in situ SERS monitoring. *Chem. Commun.* **48**, 1680–1682 (2012).

45. Xie, W., Grzeschik, R. & Schlücker, S. Metal Nanoparticle-Catalyzed Reduction Using Borohydride in Aqueous Media: A Kinetic Analysis of the Surface Reaction by Microfluidic SERS. *Angew. Chemie - Int. Ed.* **55**, 13729–13733 (2016).

46. Cristobal, G. *et al.* On-line laser Raman spectroscopic probing of droplets engineered in microfluidic devices. *Lab Chip* **6**, 1140–1146 (2006).

47. Yan, S. *et al.* Rapid, one-step preparation of SERS substrate in microfluidic channel for detection of molecules and heavy metal ions. *Spectrochim. Acta Part A Mol. Biomol. Spectrosc.* **220**, 117113 (2019).

48. Mao, H. Y. *et al.* Silicon nanopillar-forest based microfluidic surface-enhanced Raman scattering devices. in *2011 IEEE 24th International Conference on Micro Electro Mechanical Systems* 968–971 (IEEE, 2011).

49. Vis, C. M., Nieuwelink, A. E., Weckhuysen, B. M. & Bruijnincx, P. C. A. Continuous Flow Pickering Emulsion Catalysis in Droplet Microfluidics Studied with In Situ Raman Microscopy. *Chem. - A Eur. J.* **26**, 15099–15102 (2020).

50. Lichtman, J. W. & Conchello, J. A. Fluorescence microscopy. *Nat. Methods* **2**, 910–919 (2005).

51. Schäferling, M. The art of fluorescence imaging with chemical sensors. *Angew. Chemie - Int. Ed.* **51**, 3532–3554 (2012).

52. Schermelleh, L., Heintzmann, R. & Leonhardt, H. A guide to super-resolution fluorescence microscopy. *J. Cell Biol.* **190**, 165–175 (2010).

53. Pennathur, S., & Fygenson, D. K. Improving fluorescence detection in lab on chip devices. *Lab Chip* **8**, 649–652 (2008).

54. Buurmans, I. L. C. *et al.* Catalytic activity in individual cracking catalyst particles imaged throughout different life stages by selective staining. *Nat. Chem.* **3**, 862–867 (2011).

55. Hendriks, F. C. *et al.* Integrated Transmission Electron and Single-Molecule Fluorescence Microscopy Correlates Reactivity with Ultrastructure in a

Single Catalyst Particle. *Angew. Chemie - Int. Ed.* **57**, 257–261 (2018).

56. Roeffaers, M. B. J. *et al.* Super-resolution reactivity mapping of nanostructured catalyst particles. *Angew. Chemie - Int. Ed.* **48**, 9285–9289 (2009).

57. Vollenbroek, J. C. *et al.* Droplet microreactor for high-throughput fluorescence-based measurements of single catalyst particle acidity. *Microsystems Nanoeng.* **9**, 39 (2023).

58. Nieuwelink, A. E. *et al.* High-throughput activity screening and sorting of single catalyst particles with a droplet microreactor using dielectrophoresis. *Nat. Catal.* **4**, 1070–1079 (2021).

59. Solsona, M., Papadimitriou, V. A., Olthuis, W., Van Den Berg, A. & Eijkel, J. C. T. Ion Concentration Polarization for Microparticle Mesoporosity Differentiation. *Langmuir* **35**, 9704–9712 (2019).

60. Seebacher, C., Rau, J., Deeg, F. W., Bräuchle, C., Altmaier, S., Jäger, R., & Behrens, P. Visualization of Mesostructures and Organic. *Adv. Mater.* **13**, 1374–1377 (2001).

61. Seebacher, C., Hellriegel, C., Bräuchle, C., Ganschow, M. & Wöhrle, D. Orientational Behavior of Single Molecules in Molecular Sieves: A Study of Oxazine Dyes in AlPO 4 -5 Crystals. *J. Phys. Chem. B* **107**, 5445–5452 (2003).

62. De Cremer, G. *et al.* The influence of diffusion phenomena on catalysis: A study at the single particle level using fluorescence microscopy. *Catal. Today* **157**, 236–242 (2010).

63. Gallagher, S. H., Schlauri, P., Cesari, E., Durrer, J. & Brühwiler, D. Silica particles with fluorescein-labelled cores for evaluating accessibility through fluorescence quenching by copper. *Nanoscale Adv.* **3**, 6459–6467 (2021).

64. Sato, T. & Nakatani, K. Analysis of distribution and intraparticle diffusion of a fluorescent dye in mesoporous silica gel by confocal fluorescence microspectroscopy. *Anal. Sci.* **33**, 179–183 (2017).

65. Pfenniger, M. & Calzaferri, G. Intrazeolite diffusion kinetics of dye molecules in the nanochannels of zeolite L, monitored by energy transfer. *ChemPhysChem* **1**, 211–217 (2000).

66. Whiting, G. T., Nikolopoulos, N., Nikolopoulos, I., Chowdhury, A. D. & Weckhuysen, B. M. Visualizing pore architecture and molecular transport boundaries in catalyst bodies with fluorescent nanoprobes. *Nat. Chem.* **11**, 23–31 (2019).

67. Kärger, J., Ruthven, D. M. & Valiullin, R. Diffusion in nanopores: inspecting the grounds. *Adsorption* **27**, 267–281 (2021).

68. Dong, B. *et al.* In situ quantitative single-molecule study of dynamic catalytic

processes in nanoconfinement. *Nat. Catal.* **1**, 135–140 (2018).

69. Hendriks, F. C. *et al.* Single-molecule fluorescence microscopy reveals local diffusion coefficients in the pore network of an individual catalyst particle. *J. Am. Chem. Soc.* **139**, 13632–13635 (2017).

70. Zürner, A., Kirstein, J., Döblinger, M., Bräuchle, C. & Bein, T. Visualizing single-molecule diffusion in mesoporous materials. *Nature* **450**, 705–708 (2007).

71. Attwood, D. *Soft x-rays and extreme ultraviolet radiation: principles and applications*. (Cambridge university press, 2000).

72. Chao, W., Harteneck, B. D., Liddle, J. A., Anderson, E. H. & Attwood, D. T. Soft X-ray microscopy at a spatial resolution better than 15 nm. *Nature* **435**, 1210–1213 (2005).

73. Cloetens, P. *et al.* Holotomography: Quantitative phase tomography with micrometer resolution using hard synchrotron radiation x rays. *Appl. Phys. Lett.* **75**, 2912–2914 (1999).

74. De Smit, E. *et al.* Nanoscale chemical imaging of a working catalyst by scanning transmission X-ray microscopy. *Nature* **456**, 222–225 (2008).

75. Grunwaldt, J.-D. & Schroer, C. G. Hard and soft X-ray microscopy and tomography in catalysis: bridging the different time and length scales. *Chem. Soc. Rev.* **39**, 4741 (2010).

76. Bleuet, P. *et al.* Probing the structure of heterogeneous diluted materials by diffraction tomography. *Nat. Mater.* **7**, 468–472 (2008).

77. Carmona, A., Cloetens, P., Devès, G., Bohic, S. & Ortega, R. Nano-imaging of trace metals by synchrotron X-ray fluorescence into dopaminergic single cells and neurite-like processes. *J. Anal. At. Spectrom.* **23**, 1083–1088 (2008).

78. Schroer, C. G. *et al.* Mapping the chemical states of an element inside a sample using tomographic x-ray absorption spectroscopy. *Appl. Phys. Lett.* **82**, 3360–3362 (2003).

79. Hémonnot, C. Y. J. & Köster, S. Imaging of Biological Materials and Cells by X-ray Scattering and Diffraction. *ACS Nano* **11**, 8542–8559 (2017).

80. Fonda, L. Synchrotron radiation sources. *Eur. J. Cancer Prev.* **5**, 417–419 (1996).

81. Balerna, A. & Mobilio, S. Introduction to Synchrotron Radiation. in *Synchrotron Radiation* 3–28 (Springer Berlin Heidelberg, 2015).

82. Shin, S. New era of synchrotron radiation: fourth-generation storage ring. *AAPPS Bull.* **31**, 21 (2021).

83. Coburn, D. S. *et al.* Design, characterization, and performance of a hard x-

ray transmission microscope at the National Synchrotron Light Source II 18-ID beamline. *Rev. Sci. Instrum.* **90**, (2019).

84. Andrews, J. C. & Weckhuysen, B. M. Hard X-ray spectroscopic nano-imaging of hierarchical functional materials at work. *ChemPhysChem* **14**, 3655–3666 (2013).

85. Gonzalez-Jimenez, I. D. *et al.* Hard X-ray Nanotomography of Catalytic Solids at Work. *Angew. Chemie* **124**, 12152–12156 (2012).

86. Cats, K. H. *et al.* X-ray nanoscopy of cobalt Fischer-Tropsch catalysts at work. *Chem. Commun.* **49**, 4622–4624 (2013).

87. Cats, K. H. *et al.* Active phase distribution changes within a catalyst particle during Fischer-Tropsch synthesis as revealed by multi-scale microscopy. *Catal. Sci. Technol.* **6**, 4438–4449 (2016).

88. Meirer, F. *et al.* Life and death of a single catalytic cracking particle. *Sci. Adv.* **1**, 1–13 (2015).

89. Meirer, F. *et al.* Mapping metals incorporation of a whole single catalyst particle using element specific X-ray nanotomography. *J. Am. Chem. Soc.* **137**, 102–105 (2015).

90. Veselý, M. *et al.* 3-D X-ray Nanotomography Reveals Different Carbon Deposition Mechanisms in a Single Catalyst Particle. *ChemCatChem* **13**, 2494–2507 (2021).

91. Vogt, E. T. C., Fu, D. & Weckhuysen, B. M. Carbon Deposit Analysis in Catalyst Deactivation, Regeneration, and Rejuvenation. *Angew. Chemie Int. Ed.* **62**, (2023).

92. Buurmans, I. L. C. & Weckhuysen, B. M. Heterogeneities of individual catalyst particles in space and time as monitored by spectroscopy. *Nat. Chem.* **4**, 873–886 (2012).

93. Sivaramakrishnan, M., Kothandan, R., Govindarajan, D. K., Meganathan, Y. & Kandaswamy, K. Active microfluidic systems for cell sorting and separation. *Curr. Opin. Biomed. Eng.* **13**, 60–68 (2020).

94. Solsona, M. *et al.* Magnetophoretic Sorting of Single Catalyst Particles. *Angew. Chemie - Int. Ed.* **57**, 10589–10594 (2018).

95. Sun, A. C. *et al.* A droplet microfluidic platform for high-throughput photochemical reaction discovery. *Nat. Commun.* **11**, 1–6 (2020).

96. Schuster, B. *et al.* Automated microfluidic platform for dynamic and combinatorial drug screening of tumor organoids. *Nat. Commun.* **11**, 1–12 (2020).
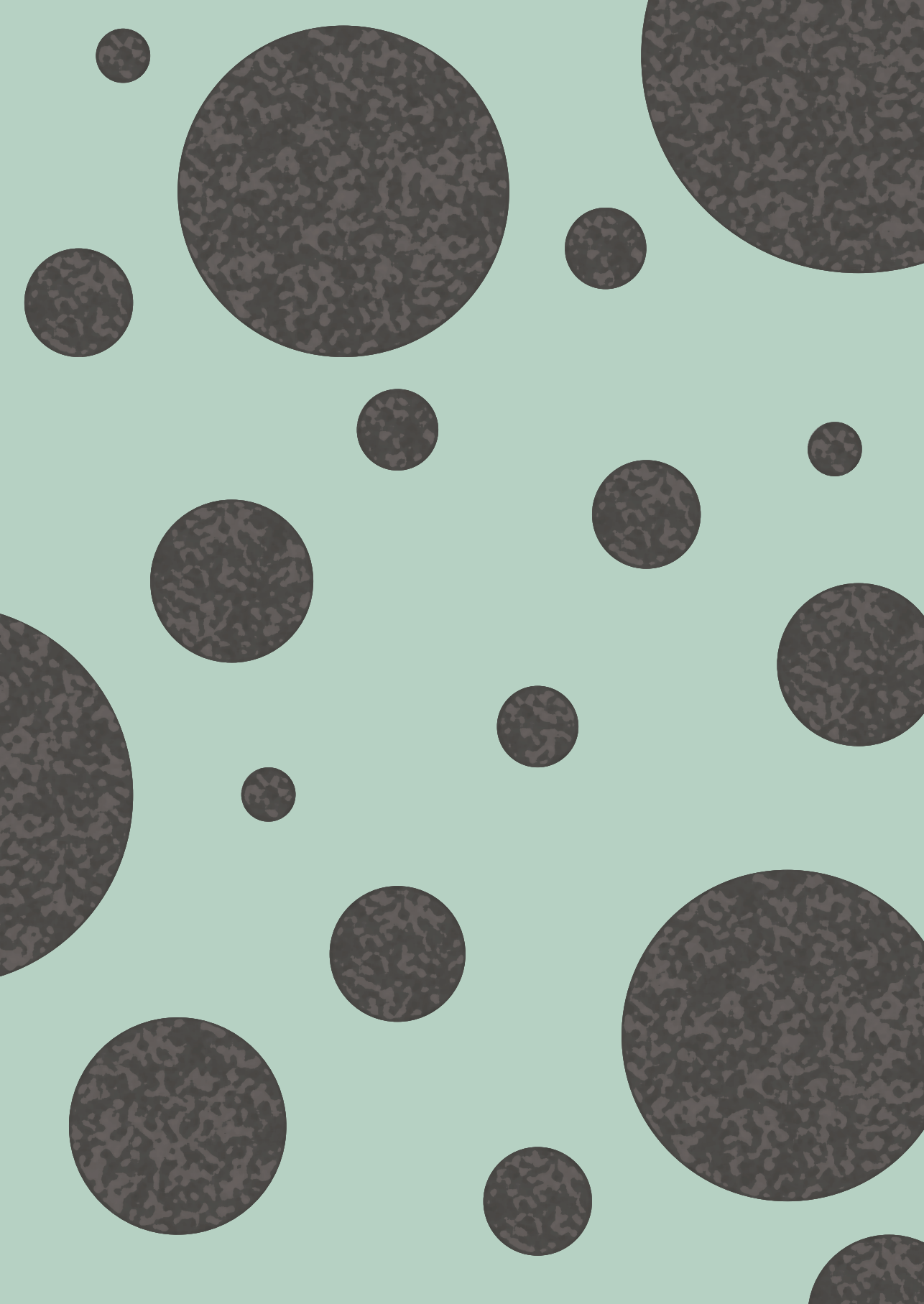
2

Chapter 3

Nanoparticle Printing for Microfluidic Applications: Bipolar Electrochemistry and Localized Raman Sensing Spots

The local integration of metal nanoparticle films on 3D-structured polydimethylsiloxane (PDMS)-based microfluidic devices is of high importance for applications including electronics, electrochemistry, electrocatalysis, and localized Raman sensing. Conventional processes to locally deposit and pattern metal nanoparticles require multiple steps and shadow masks or access to cleanroom facilities and are therefore relatively imprecise, or time and cost-ineffective. As an alternative, we present an aerosol-based direct-write method in which patterns of nanoparticles generated via spark ablation are locally printed with sub-mm size and precision inside microfluidic structures without the use of lithography or other masking methods. As proof of principle, films of Pt or Ag nanoparticles were printed in the chambers of a multiplexed microfluidic device and successfully used for two different applications: screening electrochemical activity in a high-throughput fashion, and localized sensing of chemicals via surface-enhanced Raman spectroscopy (SERS). The versatility of the approach will enable the generation of functional microfluidic devices for applications that include sensing, high-throughput screening platforms, and microreactors using catalytically driven chemical conversions.

3.1 Introduction

Polydimethylsiloxane (PDMS) is currently the most used material in the fabrication of micro-and nanoscale devices, due to its unique combination of properties including biocompatibility, easy fabrication via soft lithography, gas permeability, transparency, and inexpensiveness, making its use attractive in many fields of science. The integration of metal nanoparticle (NP) films on PDMS microfluidic chips provides flexibility in fabricating functional devices for applications such as stretchable electronics[1,2], chemical, and biological sensors[3].

However, an economically scalable and reproducible method to obtain and deposit NPs is still a fundamental roadblock. The precise implementation of NP films in specific regions of microfluidic chips is particularly interesting for example for the fabrication of devices for high-sensitivity analysis[4], in which the confinement of the detection spot improves the sensing performance or in the case of multiplexed chips. The direct deposition of NPs in pre-defined patterns or locations on PDMS remains a challenge, as in most cases either a masking layer or a local modification of the surface is needed prior to the NPs deposition on that area.

Conventional methods to perform a local deposition of NPs require vacuum processing and multiple lithographic steps, making the process complex and time-consuming. Metal films can indeed be deposited on PDMS-based substrates via e-beam evaporation or sputtering, which are contamination-free and highly productive methods, and then patterned by a lift-off process[5] or etching. These methods require a protective masking layer during the etching of the unwanted metal portions.

Alternatively, it is possible to directly inject and solidify a conductive solution into PDMS channels, although this technique is limited to metals with a low melting point (<300°C) and currently allows the fabrication of structures with cross-sections of 10 µm or bigger[6]. Inkjet printing of metal NPs[7,1] is an alternative additive method that enables the deposition and NPs patterning on PDMS without the use of any masks. However, it requires a surface modification of the substrate to optimize the wettability and adhesion of the metal ink on the PDMS to avoid the coalescence of adjacent

ink droplets. It also adds a carrier liquid that might cause unwanted interference with the application.

Metal deposition onto elastomeric substrates can also be obtained via direct metal transfer technology. This method usually requires a cleanroom working condition, as it is based on the fabrication of metal patterns on a rigid substrate (e.g., glass or silicon wafer) before their transfer onto PDMS substrates[8]. The control of the contact time and adhesion forces between the PDMS and the metal patterns plays a crucial role, and an intermediate layer (e.g. Ti[9], Cr[10]) is required to promote adhesion.

Recent advances in the fabrication of ordered arrays include bottom-up approaches based on the self-assembly of NPs, which represents a cost-effective method. Self-assembly involves the evaporation of a suspension on a solid surface[11]. To be able to obtain a local deposition of NPs, the self-assembly process should be performed on regions of the substrate with enhanced adhesion using physical, chemical, or biochemical bonding. Current approaches to fabricate ordered arrays include, for example, template-assisted self-assembly[12], dip-coating self-assembly[13], and directed self-assembly[14], in which patterned substrates are used to facilitate the periodic arrangement of NPs. However, such techniques require multiple steps (nanoparticles synthesis, template preparation and activation of the surface, assembly of the functionalized nanoparticles, and array transfer) and could therefore potentially be time-consuming and laborious.

An alternative approach to the abovementioned methods is offered by spark ablation, which represents a precise and versatile method to rapidly produce NPs in a gaseous environment. It enables a single-step manufacturing of metal or alloy NPs[15] with different properties[16] and has proven to be a simple, economical, and clean[17] method, as it doesn't require the use of any chemical precursors and doesn't generate any hazardous waste. The spark-discharge NP generator consists of a pair of (semi)conductive electrodes separated by a gap and a pulse-forming electrical circuit[18]. The spark discharge between the electrodes generates an aerosol of the electrode material, which is then carried away by a high-purity inert gas (e.g., Ar or N_2) and can potentially be deposited on any type

of substrate (e.g. Silicon[19], Poly(3,4-ethylenedioxythiophene): poly(styrenesulfonate) (PEDOT:PSS)[20], Nafion membranes [21]) by inertial impaction. In addition, size selection of the nanoparticles is possible by modifying an electric field.

So far, this method has not been used to integrate NPs on elastomeric substrates, specifically in PDMS microchips.
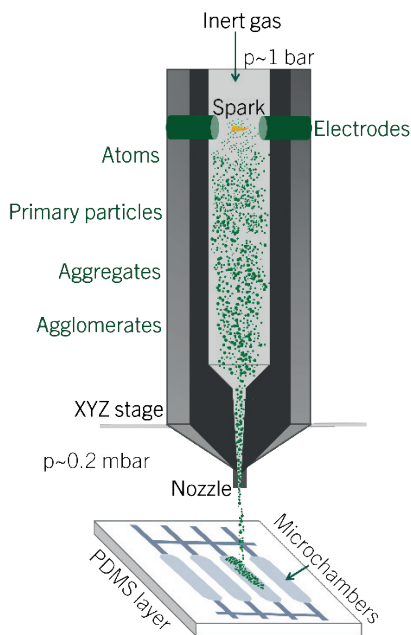
Figure 1: Schematic representation of the nanostructured material printer (VSP-P1 NanoPrinter) used for the deposition of nanoparticle films in the chambers of a multiplexed PDMS microfluidic device.

In this work, we present a novel method to locally deposit NPs generated by spark ablation in the chip chambers of a multiplexed PDMS microfluidic device using a nanomaterial 3D printer from VSParticle (Figure 1). It consists of a particle generator directly connected to a chamber in which the deposition of the nanoparticles on the substrate takes place through a nozzle via inertial impaction. The fabrication of nanoparticle patterns is performed by placing the substrate on an XYZ stage. The direct control of the deposition area and the fast process rate are among the main advantages of the technique compared to the existing methods. Moreover,

the adhesion of the nanoparticles on the substrate is obtained by inertial impaction, without requiring the use of any binder.

We report the effect of the printing parameters (speed of printing and nozzle-substrate distance) on the morphology of the deposited films of nanoparticles. Furthermore, microfluidic devices with integrated Pt and Ag NPs were tested for two different applications:

1. Pt NPs were used to generate potential and pH gradients via bipolar electrochemistry.

2. Ag NPs were used as the surface-enhanced Raman surfaces for the *in situ* detection of organic molecules, showing the potential and versatility of this new fabrication method.

3.2 Results and Discussion

3.2.1 Nanoparticle Film Characterization

The local deposition of nanoparticles was obtained using the experimental printing setup shown in Figure S1. The focusing nozzle allows the creation of the desired patterns of NPs on the substrate, in this case, PDMS. The range of feature sizes that can be obtained with the nanoparticle printer depends on the distance between the nozzle and the substrate, as well as on the dimension of the nozzle itself and the speed of printing. The minimum width of the printed features mostly depends on the nozzle throat, which is 100 µm in our case. We first studied the effect of the main printing parameters, the distance between the nozzle of the printer and the substrate, and the speed of printing. A first observation is that we see the formation of metal films, formed by agglomerates of nanoparticles unless really fast printing speeds are used. The distance between the nozzle and the substrate affects the morphology of the metal films, as shown in Table 1 with Pt and Ag NPs printed with nozzle-substrate (N-S) distances of 200 and 500 µm. The nozzle distance defines the width of the lines, as the closer the nozzle is to the substrate, the lower the expansion of the gas containing the NPs. Moreover, the speed of printing also influences the width of the lines as well as their thickness. The slower deposition speed corresponds to thicker lines, due to the higher amount of NPs focused on the substrate per unit of time.
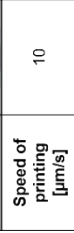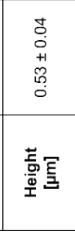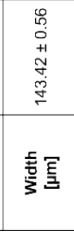
A

Pt NPs

Nozzle-substrate distance 200 µm					
Speed of printing [µm/s]	10	20	40	60	80
Height [µm]	0.53 ± 0.04	0.43 ± 0.01	0.34 ± 0.01	0.280 ± 0.003	0.250 ± 0.006
Width [µm]	143.42 ± 0.56	134.09 ± 1.08	126.22 ± 0.01	121.820 ± 0.003	118.73 ± 0.45
Nozzle-substrate distance 500 µm					
Speed of printing [µm/s]	10	20	40	60	80
Height [µm]	0.44 ± 0.02	0.32 ± 0.05	0.24 ± 0.01	0.22 ± 0.02	0.20 ± 0.02
Width [µm]	197.59 ± 0.07	193.17 ± 0.02	184.21 ± 0.45	175.58 ± 0.06	171.04 ± 0.44

B

Ag NPs

Nozzle-substrate distance 200 µm					
Speed of printing [µm/s]	10	20	40	60	80
Height [µm]	0.79 ± 0.01	0.500 ± 0.004	0.270 ± 0.005	0.170 ± 0.006	0.15 ± 0.01
Width [µm]	238.26 ± 0.55	198.49 ± 1.12	173.36 ± 0.03	151.07 ± 2.82	135.72 ± 1.05
Nozzle-substrate distance 500 µm					
Speed of printing [µm/s]	10	20	40	60	80
Height [µm]	0.56 ± 0.01	0.41 ± 0.06	0.24 ± 0.04	0.15 ± 0.02	0.11 ± 0.03
Width [µm]	317.82 ± 1.16	275.72 ± 3.34	222.93 ± 4.81	204.73 ± 3.07	201 ± 5

Table 1: Optical images and height and width values of Pt (A) and Ag (B) lines printed on PDMS with different N-S distances (200 and 500 µm) and speed of printing (10-80 µm/s). For each speed of printing, 3 lines of 1 mm were printed on PDMS substrates and the standard deviation of width and thickness was evaluated on 3 different points along each line. Slower deposition speeds result in thicker lines, as a higher amount of NPs is focused on the substrate per unit of time. All lines were printed using a nozzle throat of 100 µm, and the voltage and the current setting for the spark discharge were 1.3 kV and 10 mA respectively. Scale bars 100 µm.

It is therefore possible to control the morphology of the desired 3D pattern by controlling the printing parameters. The impact of the NPs beam on the elastomeric surface leads to local heating and expansion of the PDMS surface during the deposition[22], resulting in the formation of cracks on the metal films due to the difference in the coefficient of thermal expansion between the PDMS substrate and the metal nanoparticle films. As shown in the pictures of Table 1A, in the case of Pt, the cracks are more evident on the lines printed with the fastest speed. The slower printing speeds result in a thick and compact layer of NPs (Figure S2), which tend to better dissipate the heat involved in the printing process. In contrast, Ag printed with slower speeds shows a larger amount of cracks (Table 1B). We hypothesize this is due to the higher coefficient of thermal expansion of Ag compared to Pt, which could lead to more thermal stress of the silver film. For our experiments, we used printing parameters that didn't lead to crack formation.

Figure 3C shows an example of the typical morphology of the Pt film on the PDMS substrate, composed of a dense and rough layer of nanoparticles with a mean particle size of 33.7 ± 4.2 nm and larger aggregates of hundreds of nanometers. The nanoparticles generated via spark ablation are characterized by a diameter between 0 and 20 nm[23] and tend to agglomerate and form clusters due to collision and coalescence, which may occur on the way to the nozzle as well as directly on the substrate due to the clean surface of the particles and the favorable metal-metal contact[23].

Before the deposition of the nanoparticles, the PDMS surfaces were plasma-treated. During this process, the PDMS is exposed to the oxygen plasma which generates silanol functional groups and also increases the surface roughness of the material, enhancing the adhesion strength of the metal layer to the elastomeric surface[24]. Stability tests to check the adhesion of the printed NPs were performed on-chip, depending on the applications that will be discussed in the following sections. To check the stability of the NP films in the chambers, water was flushed in the chip for 48h. Samples were collected at the outlet periodically and investigated with UV/Vis analysis, which didn't reveal the presence of Pt/Ag NPs, thus confirming their stability on the PDMS substrate. Tape tests were also performed on

3

NPs printed on flat PDMS layers using a scotch transparent tape 3M, and the grade of adhesion was evaluated by optical analysis, inspecting any detachment of the metal film from the substrate. Also in this case, no Pt/Ag was released during the adhesion tests.

3.2.2 Application I. Bipolar electrodes in a multiplexed microfluidic chip

The possibility of locally printing metal NPs facilitates the integration of electrodes in microfluidic devices, which represent essential components for a broad range of applications including electrokinetic transportation or electrochemical detection. Particularly, electrochemical generation and control of gradients are widely used to create both static or dynamic solutions and surface gradients as well as to control pH and O_2 concentration[25]. Such gradients can be used to reproduce cellular environments and play an important role in the study of cell adhesion[26] or the control of protein conformation[27]. Gradients are also employed in the high-throughput generation and screening of materials[28], such as catalysts, or in the development of sensing platforms[29].

In this section, we propose an attractive alternative method to the current screening platforms, consisting of an array of individually addressable chambers embedding 3D-printed Pt electrodes which enable the generation and comparison of potential gradients over the electrodes.

A convenient configuration to integrate arrays of electrodes in a microfluidic device, thus increasing the processing throughput, relies on the use of bipolar electrodes (BPEs). A BPE consists of an isolated patch or strip of conductive material immersed in an electrolyte solution (Figure 2), between two external electrodes to generate an E-field. The main advantage of their use is the possibility to maintain control over single or multiple electrodes without direct electrical contact[30] facilitating their integration and parallelization in a chip. The polarization of a BPE derives from the interfacial potential difference between the solution and the surface of the electrode. This can be used to drive Faradaic reactions[31]. As shown in Figure 2B, the voltage difference is highest at the edges of the electrode that act as cathode and anode simultaneously.
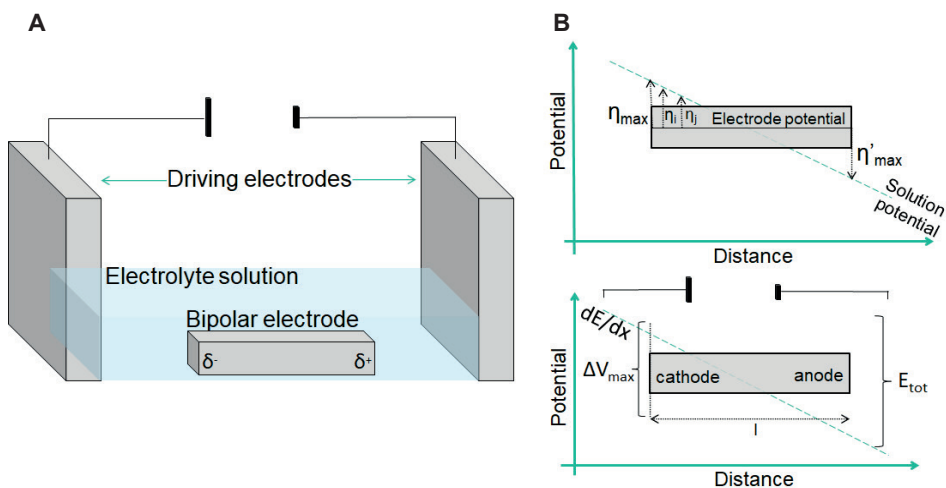
Figure 2: A) Schematic illustration of a bipolar electrode setup. **B)** Schematic of the magnitude of the interfacial potential difference between the BPE and the solution. The magnitude of the overpotentials varies along the length of the electrode, assuming the highest values at its extremities.

When a sufficient driving potential E_{tot} is applied in a channel, the fraction of E_{tot} dropped over the BPE depends on the distance between the driving electrodes ($l_{channel}$) and the length of the electrode itself ($l_{electrode}$), and can be estimated as follows[32]:

$$\Delta E_{elec} = E_{tot} \frac{l_{electrode}}{l_{channel}} \qquad (1)$$

It is also important to underline that since the polarization varies along the conducting BPE, a potential gradient is formed along the bipolar electrode which allows the screening of different thermodynamic conditions in one experiment[33].

The understanding of electrokinetic and electrochemical dynamics in microfluidic-based bipolar systems[34] led to their use for a wide range of applications, including the simultaneous enrichment and separation of analytes[35,36], as recently demonstrated with microplastics[37]. Arrays of BPEs have also been used for sensing, relying on electrochemiluminescence[38] or electrodissolution of the electrodes[39] themselves; or as screening platforms to study the activity of metal electrocatalysts[40].

Pt electrodes were 3D-printed in a PDMS microfluidic device with 4 independently addressable chambers and used as BPEs, which enable the generation and comparison of potential gradients. Each chamber results in a confined environment where the produced gradients can be tuned and monitored without affecting the activity of the nearby electrodes.

Figure 3 illustrates the microfluidic device consisting of two PDMS layers and a glass slide. We have previously reported a similar device for high-throughput cell culturing[41] and stem cell differentiation[42]. The top layer contains the fluidic channels and chambers, where the Pt electrodes are confined. The control channels and valves are placed on the bottom layer, which is directly attached to a glass slide. Pressurizing the control line will make the membrane bend into the flow channels, thereby blocking the flow as well as the electrical (ionic) current.
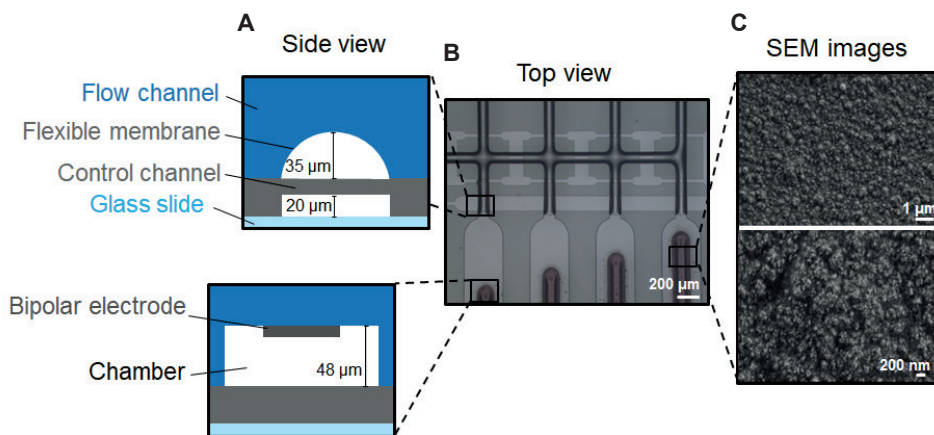
Figure 3: A) Schematic cross-section and B) Optical image of the multiplexed PDMS microfluidic device. Pt NPs are printed in the chip chambers (flow layer, in green). C) SEM images of the morphology of Pt NPs patterns deposited on the PDMS substrate. Voltage/current settings used for the deposition V=1.3 kV and I= 10 mA respectively, speed of printing of 10 µm/s and nozzle-substrate distance of 500 µm. Film thickness ~0.4 µm.

The operation of the microfluidic device was demonstrated by performing water electrolysis as a model reaction. When the externally applied electric field is sufficiently large (i.e. higher than the difference in the formal potentials for the two redox reactions[43]), the electrode is polarized enough to drive simultaneously redox reactions at its poles, which are given by[44]:

$$O_2 + 4H^+ + 4e^- \leftrightharpoons 2H_2O \qquad \text{water oxidation at acidic pH} \qquad (2)$$

$$O_2 + 2H_2O + 4e^- \leftrightharpoons 4OH^- \qquad \text{water oxidation at basic pH} \qquad (3)$$

$$2H^+ + 2e^- \leftrightharpoons H_2 \qquad \text{water reduction at acidic pH} \qquad (4)$$

$$2H_2O + 2e^- \leftrightharpoons H_2 + 2OH^- \qquad \text{water reduction at basic pH} \qquad (5)$$
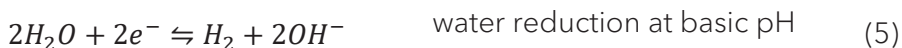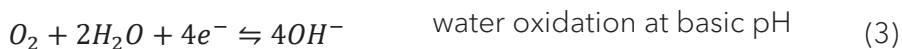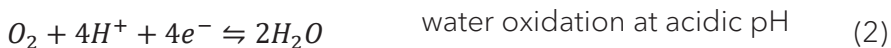
The listed reactions lead to changes in the pH and conductivity of the solution at the BPE poles, due to the consumption or generation of H^+ and OH^-. Specifically, the O_2 generation at the anodic pole of the BPE decreases the pH of the solution with OH^- consumption/ H^+ production; while the H_2 generation at the cathodic pole increases the pH due to the H^+ consumption/ OH^- production. To visualize the induced electric field on the BPE and follow the water electrolysis reaction, we monitored the changes in the fluorescence intensity of the pH-sensitive Fluorescein sodium salt (FL). FL exists in different forms (FL^+, FL^0, FL^-, FL^{2-}) so its fluorescence properties strongly depend on the pH of the electrolyte. Particularly, it exists in its cationic form at pH<2 and undergoes from $FL^{-1/-2}$ to FL^0 at pH<4. FL shows a strong fluorescence at a pH above 6.5[45]. During water electrolysis, a dynamic pH gradient is formed along the electrodes due to the aforementioned faradaic reactions, and hence it affects the charge and the fluorescence intensity of the tracer molecule FL. During water electrolysis, the O_2 generation and consequent decrease of the pH cause quenching of the fluorescence intensity, while the increase of the pH should increase/keep the intensity value constant, depending on the starting pH of the solution. The pK_a value of the FL is close to the pH of the electrolyte solution used in the experiments, so there is a quick change of the FL net charge and fluorescence intensity according to the induced pH profile[46] (Figure S3).

As already mentioned, the fraction of E_{tot} dropped over each BPE, depends on the ratio between the length of the electrode and the microchannel (Eq. 1). Figure 4 shows the microfluidic device with four Pt BPEs obtained using the same printing parameters (N-S=500 µm and speed of printing 10 µm/s) and thus having the same morphology (thickness, particle size), but

3

different lengths. The chambers containing the BPEs are filled with an aqueous solution of 100µM FL and 1.0 mM sodium phosphate buffer at pH 7.2. An external electric field was applied at two Pt wires used as driving electrodes, inserted into the inlet and outlet of the chip, and connected to a power supply to introduce a potential difference of 400 V between the electrodes (corresponding to an electric field of ~12 kV/m). The complete design of the chip used for the experiments and its equivalent circuit are shown in Figure S4.

Such high values of external potential are needed to visualize the O_2 and H_2 generations at the poles of the electrodes since the bipolar configuration is far from standards conditions (at which $E^0 = 1.23\,V$). The length of the channel (3 cm), corresponding to the distance between the driving electrodes, is an order of magnitude higher than the dimension of the bipolar electrodes (~1 mm) in the chambers.

Figure 4: A) Schematic (not to scale) of the experiments performed using the Pt electrodes in the chambers simultaneously. **B)** Fluorescence images showing the activity of BPEs used simultaneously upon the application of an external driving potential E= 400 V. **C)** Fluorescence emission intensity profile at the anodic poles of the electrodes. The change in fluorescence intensity reflects the decrease in the pH of the solution, due to the O_2 production via water splitting. The available overpotential for O_2 production is proportional to the length of the electrodes. Scale bars: 350 μm.

The application of a potential difference between the driving electrodes generates an electric field, which produces a linear change of the potential across the solution (Figure 2B) while the floating electrode is itself equipotential. The presence of a potential gradient in the solution results in the presence of a continuum of different driving forces along the electrode for electrochemical reactions, with a maximum value at the edges. In the

experiments, the length of the channel (3 cm) is the same for each electrode while their lengths are different (from chamber 1 to chamber 4, the lengths of the BPEs are 829, 1114, 1402, 1711 µm). This results in higher values of ΔE_{elec} on longer electrodes (Eq. 1), corresponding to a more pronounced quenching of the fluorophore as can be seen in Figure 4C. The fluorescence intensity of the dye drops starting from the anodic pole of the electrodes, due to the acidification of the solution. The different lengths of the electrodes result also in different portions of substrates polarized enough to drive the water oxidation; the longer electrode shows indeed a bigger portion active towards the O_2 generation. With these considerations, it is possible to design the electrodes for example according to the desired potential drop or screen the effect of different potentials on the reaction of interest.

One of the advantages of the proposed device is the confinement of the electrodes in parallel PDMS chambers, by which is it possible to avoid the influence of the electrodes nearby. The device allows the use of each electrode individually (Figure 5) thanks to the presence of pneumatically actuated valves in the "push-up" configuration, which can electrically insulate the electrodes in the path not in use.
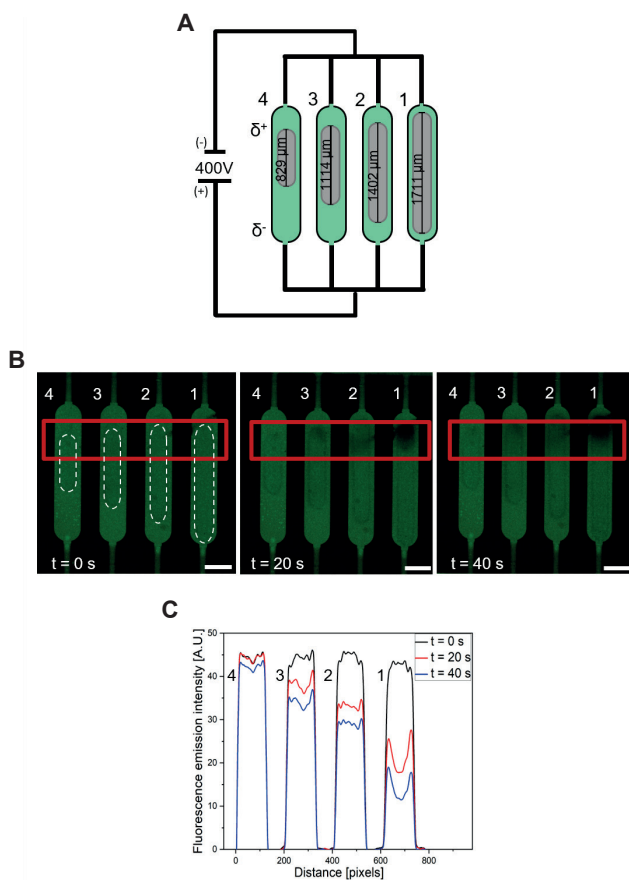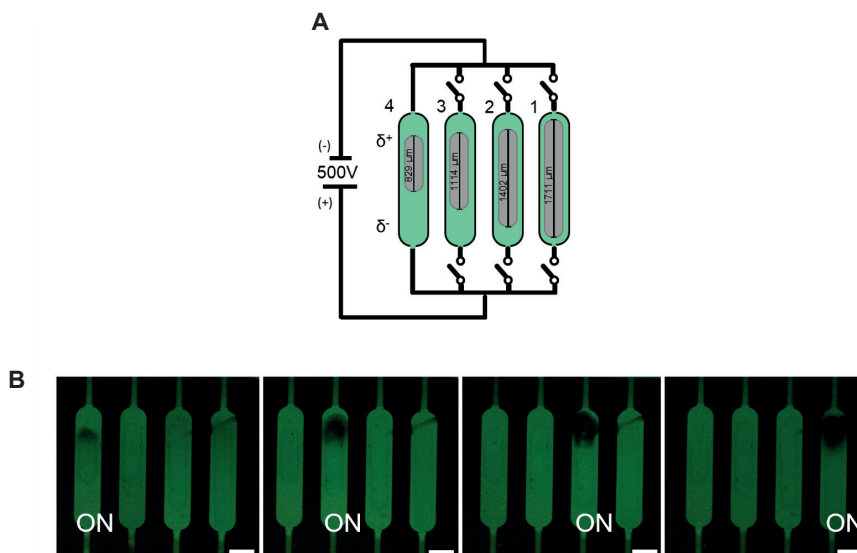
Figure 5: A) Schematic (not to scale) of the experiments performed using the Pt electrodes in the chambers independently. The PDMS valves are represented by switches. The open configuration of the valve corresponds to a closed switch, so the current can go through the chamber. **B)** Fluorescence micrographs showing the activity of the BPEs used individually upon the application of an external driving potential E_{tot}= 500 V. The change in the fluorescence intensity reflects the decrease in the pH of the solution, due to the O_2 production via water electrolysis reaction. The electrodes are used independently thanks to the presence of PDMS valves, which can act as insulators by closing the conductive path through the channels. Scale bars:350 µm.

3.2.3 Application II. SERS structures in a microfluidic device for organic molecule detection

Surface-Enhanced Raman spectroscopy (SERS) is nowadays an established and powerful analytical technique for the detection of low concentrated samples, and it's based on the amplification of the Raman signal of molecules adsorbed on nanostructured metallic surfaces. The improvement of the signal can be attributed to both electromagnetic and chemical enhancement[47], with the first being the dominant contributor. The electromagnetic enhancement mechanism is related to the amplification of the light by the excitation of localized surface plasmon resonances (LSPRs), while the chemical enhancement involves a charge-transfer mechanism[48],

in which the excitation wavelength is resonant with the metal-molecule charge-transfer electronic states. Noble metals such as gold, silver, or copper, are extensively used as SERS substrates, as all of them have LSPRs that cover most of the visible and near-infrared wavelength range, thus enhancing the measurement of the Raman signal. Among them, Ag exhibits the best optical absorption and scattering properties, and has been widely employed in chemical and biomedical detection.[49-50] The integration of Ag nanoparticles in a microfluidic device results in a promising approach as it can enable the static and dynamic liquid measurement of the samples, resulting in an in situ, real-time detection system[51]. The fabrication of SERS substrate in PDMS microfluidic devices is usually obtained from the reduction of Ag precursors injected in the channels[52], thus requiring precise control of the flow and heating conditions to obtain the homogeneous deposition of the metal along the channel. The spark ablation method and the use of a 3D nanoparticle printer provide an alternative, innovative, and convenient approach for the generation of local SERS-active patterns, as it represents a one-step process to obtain Ag NPs substrate in a microfluidic channel. To be able to study the possible Raman enhancement given by the Ag substrate, the NPs were deposited in the chip chambers of the microfluidic device reported in section 2.2 with a printing speed of 60 μm/s and nozzle-substrate distance of 500 μm. Table S1 reports the effects of different printing speeds and N-S distances over the Ag NPs printed on PDMS layers.

The performance of a SERS substrate is influenced by the size, density, and morphology of metal NPs, due to the influence of these factors upon the electromagnetic field. Particularly, the electromagnetic field can be highly enhanced in presence of nanogaps or hot spots between adjacent NPs[53], thus increasing the SERS intensity. On the other hand, when the NPs size and fill factor increase, the absorption of light is less effective and the absence of nanogaps decreases the electromagnetic enhancement. Moreover, aggregates of NPs of hundreds of nanometers have a low surface area compared to bare NPs, and thus lower adsorption of the target molecule. Figure 6C shows a film of Ag NPs deposited on the PDMS

surface, mainly consisting of particles with diameters ranging from 0-35 nm and some clusters of 40-50 nm, resulting in a suitable substrate for SERS.

To evaluate the SERS performance of the Ag NPs, a solution of methylene blue (MB) of $2.5 \cdot 10^{-5}$ M was used as a probe molecule. The characteristic Raman peaks of MB are shown in Figure S5, with the most intense highlighted in Figure 6B at 1623 cm^{-1} corresponding to C-C ring stretching[54].
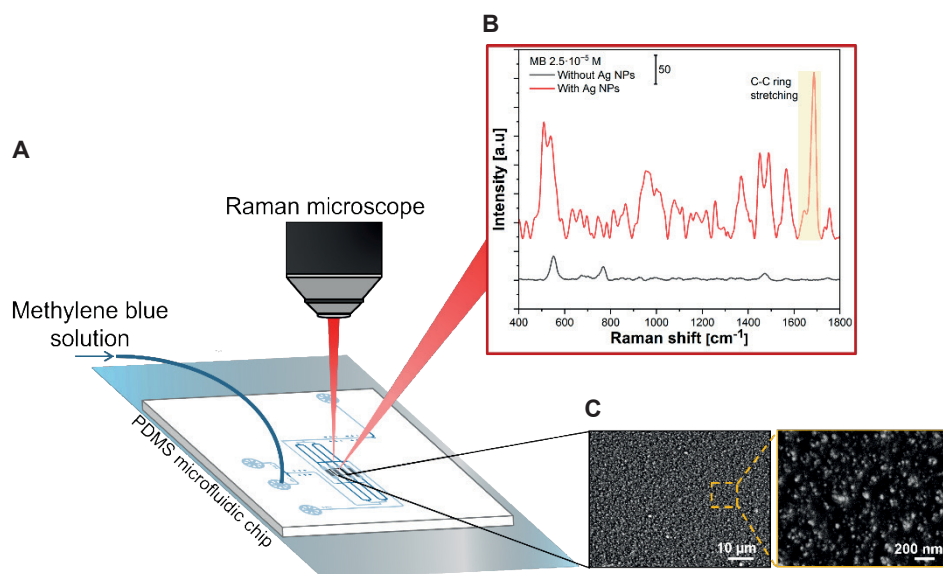
Figure 6: A) Schematic representation of the acquisition of the Raman signals from a PDMS chip with Ag NPs deposited in its chambers. B) Raman spectra of MB obtained by focusing the laser beam on areas of the chip chambers without (in black) and with Ag NPs (in red) deposited on the PDMS. The black curve only shows the PDMS peaks, while the red curve represents MB peaks. In both cases, the fluorescence background was subtracted. The highlighted peak refers to C-C stretching and it was used for the enhancement calculation. The additional MB characteristic peaks and vibrational modes are reported in Figure S5. C) SEM images of Ag NPs deposited on PDMS. Voltage/current settings used for the deposition V=1.3 kV and I= 10 mA speed of printing of 60 µm/s and nozzle-substrate distance of 500 µm.

Before the detection of MB on the Ag layer, the laser beam was focused on the bare PDMS and its Raman spectrum was collected to be able to distinguish its peaks (Figure S6) from the ones of the target molecule.

To investigate the reproducibility of the substrate, 5 points were randomly selected on the Ag substrate to collect the signal of the organic molecule (Figure S7). A comparison between the Raman spectra of MB obtained by focusing the laser in the chip chambers on the bare PDMS and areas with the Ag nanoparticles deposited on the PDMS is reported in Figure 6B. Moreover, the activity of the AgNPs towards the Raman enhancement was checked by using freshly prepared devices and with chips stored at ambient conditions for a week, and the results obtained showed the stability of the signal (Figure S8). For the experiments, the aqueous solution of MB was injected into the chip chambers and left in contact with the substrate for 1h, and the detection of the liquid was performed by focusing on the sensing spots. The Raman signals of the MB $2.5 \cdot 10^{-5}$ M were not detectable on the bare PDMS, as it only exhibits PDMS characteristic peaks (Figure 6B, black curve). On the other hand, the SERS signals of MB could be detected from the Ag substrate. In this case, the characteristic Raman peaks of MB resulted shifted by ~ 60 cm^{-1} compared to the typical MB spectra reported in the literature, suggesting chemisorption of the sample molecules on the Ag structure[55].

To quantify the SERS enhancement we referred to the analytical enhancement factor (AEF)[56], which is commonly used to relate the signal intensity to the analyte concentration. It provides information about the signal gain that the SERS substrate produces in comparison to a reference Raman experiment with the same analyte and under the same experimental conditions. The analytical enhancement factor (AEF) was evaluated by taking into account the most intense signal from the methylene blue spectrum (1623 cm^{-1}) and estimated using the equation:

$$AEF = \frac{C_{Raman}}{C_{SERS}} \cdot \frac{I_{SERS}}{I_{Raman}} \qquad (6)$$

C_{Raman} and C_{SERS} represents the concentrations of the aqueous MB solutions used for the Raman (0.11 M) and SERS ($2.5 \cdot 10^{-5}$ M) measurements, while I_{Raman} and I_{SERS} are the intensities of the corresponding peaks representative of the C-C ring stretching. A value of $(1.7 \pm 0.3) \cdot 10^5$ was obtained as AEF, comparable to a typical average EFs value reported in the literature[56] for Ag structures.

3.3 Conclusion and Outlook

In this work, we proposed a new, simple, and one-step process to locally print patterns of nanoparticles on PDMS. The nanoparticles are produced by spark ablation and directly deposited and patterned on the elastomeric substrate using a 3D printer which allows the control of the deposition area, resulting in particular interest for the integration of metal NP films in microfluidic devices.

The variation of printing parameters, such as the speed of printing and the distance between the nozzle of the 3D printer and the substrate, influence the morphology of the deposited layers. High speed of printing lead to a thin film of nanoparticles, while the distance between the nozzle of the 3D printer and the substrate influences the width of the lines. It is therefore possible to obtain full control over the desired NPs pattern.

We integrated Pt and Ag nanoparticles in a PDMS multiplexed microfluidic device used respectively to generate potential and pH gradients and as SERS sensors. In the first case, we confirmed the conductivity of the printed lines and obtained a device with parallel electrodes which can be used simultaneously and individually. The platform can be used for sensing or the high-throughput generation and screening of materials. The electrodes can indeed be used to control pH and O_2 concentration as well as to create both static or dynamic solutions and surface gradients.

In the second case, Ag films were used as SERS substrate and allowed the detection of a solution of MB $2.5 \cdot 10^{-5}$ M, with an AEF $\approx 1.7 \cdot 10^5$. This result can be further improved by screening the enhancement of the electric field of NPs obtained with different printing parameters or materials. The integration of SERS with microfluidics enables both the static and dynamic liquid measurements, offering more reliable and reproducible results than the static solid ones.

The results show the versatility of the method and its high potential for the functionalization of microfluidic structures. It is also possible to deposit metal alloys by using electrodes of different materials in spark ablation, or metal oxides by using air as a carrier gas, which further increases the

73

application fields. Preliminary experiments performed with TiO_2 show its possible use as photocatalyst.

The method allows the easy integration of metal nanoparticles in specific regions of microfluidic devices for the fabrication of functional devices for applications including sensing and screening platforms and microreactors.

3.4 Materials and Methods

3.4.1 Nanoparticle generation and printing

Pt and Ag NPs were produced and deposited on the PDMS substrates using a commercial particle generator (VSParticle- G1) and an aerosol printer (VSP- P1 NanoPrinter). The generation of NPs is obtained via spark ablation, which consists of an evaporation-condensation mechanism. The energy of the spark plasma leads to the evaporation and sublimation of a portion of the electrodes, and the metal vapor is then quenched and condensated via adiabatic expansion and mixing with the carrier gas[57], producing particles with diameters in 0-20 nm range. Subsequently, the particles tend to interact and agglomerate.

The particle generator was equipped with 2x Pt (99.9%) or Ag (99.9%) electrodes and 1 slm Ar (99.9%) was used as carrier gas. The voltage and current settings for the spark discharge were 1.3 kV and 10 mA. The deposition unit consists of a prototype nanomaterial printer, composed of a vacuum chamber (pressure in the chamber is 0.0002 bar) directly connected to the output of the particle generator, equipped with a nozzle (throat diameter 0.1 mm) for focusing and printing the beam of NPs on the substrate. The spot size of the nanoparticle beam depends on the nozzle-substrate distance, which can be adjusted between 200 and 1000 μm. To be able to see and control the deposition area, a camera is placed behind the nozzle. The PDMS substrate is placed and fixed perpendicularly to the particle beam on a motorized XYZ stage. NPs were therefore deposited by inertial impaction of the aerosol directly in the PDMS chip chambers.

3.4.2 Characterization of the nanoparticle films

NPs film thickness was measured by a Dektak Stylus optical profilometer and each line was checked on 3 different points along the length, to verify the uniformity of the printing method and evaluate the standard deviation of the value. The SEM measurements were performed using a Zeiss MERLIN HR-SEM.

3

3.4.3 Chip fabrication

The microfluidic devices consisted of PDMS chips with four independently addressable chambers. Their design and microfabrication are based on previous work[41]. Briefly, they were obtained by standard photolithography: SU8 (MicroChem, USA) was used for the control layer wafers, with 20 µm high channels, while for the flow layers wafers SU8 was used to first obtain channels with rectangular sections (~48 µm high) in the areas without valves, and AZ40XT (MicroChemicals, Germany) was used to create channels ~35 µm high with a rounded profile. In the area with valves, the rounded profile of the flow channels is needed to ensure their correct closing without leakage.

The chips were obtained by multilayer soft lithography. PDMS (RTV615, Permacol, The Netherlands) base and curing agent were mixed to obtain the flow (7:1 w/w base to curing agent) and control layers (20:1 w/w base to curing agent). The PDMS was degassed for about 2 hours.

A ~30 µm thick layer of PDMS was obtained on the control layer by spin coating, while the flow layer was obtained by pouring the PDMS on the mold. Both wafers were cured at 60°C for 45 min. Once cooled, the PDMS flow layer was cut from the wafer and the inlets and outlets were punched with a 1 mm hole puncher. The flow layer was then plasma treated and used as a substrate for nanoparticle printing. After the deposition of the NPs on the flow layer, it was aligned on the control wafer using a stereomicroscope (Olympus), and the layers were cured overnight at 60°C.

The chip was cut from the wafer and the control inlets were punched out with a 0.75 mm biopsy puncher. Finally, the chip was bonded to a microscope glass slide using a plasma cleaner (model CUTE, Femto Science, South Korea).

The valves of the microfluidic chip were driven by pneumatic actuation. The channels of the control layer were filled with water and pressurized with air (1.5 bar) by solenoid valves (Festo, the Netherlands), which can be controlled via a custom LabView program.

3.4.4   Bipolar experiments

For the bipolar electrode experiments, the driving electrodes consisted of Pt wires (99.9%, Sigma-Aldrich) located at the inlet and outlet of the chip. They were connected to a power supply (2401 Keithley Source Meter) via external contacts to apply a potential difference between the electrodes. The voltage/current settings used for the deposition of bipolar electrodes are V=1.3 kV and I= 10 mA respectively, speed of printing of 10 μm/s, and nozzle-substrate distance of 500 μm. Before the alignment with the control layer, the resistance of the Pt electrodes was measured using a multimeter (Fluke 179), providing a conductivity value $\approx 5.6 \cdot 10^6$ S/m.

The fluorescent experiments were carried out with a mixture of 100 μM Fluorescein sodium salt (FL) (Sigma-Aldrich) and 1.0 mM sodium phosphate buffer at pH 7.2. The solutions were prepared using deionized water (<18.2 MΩ cm, PURELAB flex). All solutions were kept away from light by covering the vials with aluminum foil when not in use. For the image acquisition, a microscope Olympus IX51 and a Grasshopper®3 (FLIR, U.S.) color camera were used with a pE300^{ultra} LED illumination system (CoolLED, U.K.).

3.4.5   SERS measurements

SERS measurements were carried out using a confocal Raman microscope (WITec Alpha300R, Germany). A He-Ne laser with a wavelength of 633 nm was used and focused on the substrate using a lens with a 100× magnification, and a numerical aperture of 0.9. The integration time was 1s, and the power applied was 10 mW. Higher power led to a massive heating of the PDMS and consequent detachment of the Ag substrate. The methylene blue (Sigma-Aldrich) solutions ($2.5 \cdot 10^{-5}$ M and 0.11 M) were prepared using DI water.

3.5 References

1. Abu-Khalaf, J. M., Al-Ghussain, L. & Al-Halhouli, A. Fabrication of stretchable circuits on polydimethylsiloxane (PDMS) pre-stretched substrates by inkjet printing silver nanoparticles. *Materials (Basel).* **11**, 1–17 (2018).

2. Ryspayeva, A. *et al.* A rapid technique for the direct metallization of PDMS substrates for flexible and stretchable electronics applications. *Microelectron. Eng.* **209**, 35–40 (2019).

3. He, J., Boegli, M., Bruzas, I., Lum, W. & Sagle, L. Patterned Plasmonic Nanoparticle Arrays for Microfluidic and Multiplexed Biological Assays. *Anal. Chem.* **87**, 11407–11414 (2015).

4. Zhou, J., Ren, K., Zhao, Y., Dai, W. & Wu, H. Convenient formation of nanoparticle aggregates on microfluidic chips for highly sensitive SERS detection of biomolecules. *Anal. Bioanal. Chem.* **402**, 1601–1609 (2012).

5. Jeong, J., Chou, N. & Kim, S. Fabrication of flexible electrode array based on PDMS for long-term in-vivo use. in *2013 6th International IEEE/EMBS Conference on Neural Engineering (NER)* 911–914 (IEEE, 2013).

6. Siegel, A. C., Bruzewicz, D. A., Weibel, D. B. & Whitesides, G. M. Microsolidics: Fabrication of three-dimensional metallic microstructures in poly(dimethylsiloxane). *Adv. Mater.* **19**, 727–733 (2007).

7. Kim, Y., Ren, X. & Noh, H. Direct printing of silver nano-particles based ink on polydimethylsiloxane (PDMS) for mems devices. in *2014 Solid-State, Actuators, and Microsystems Workshop Technical Digest* 191–194 (Transducer Research Foundation, 2014).

8. Byun, I., Coleman, A. W. & Kim, B. Transfer of thin Au films to polydimethylsiloxane (PDMS) with reliable bonding using (3-mercaptopropyl)trimethoxysilane (MPTMS) as a molecular adhesive. *J. Micromechanics Microengineering* **23**, (2013).

9. Loo, Y. L., Willett, R. L., Baldwin, K. W. & Rogers, J. A. Additive, nanoscale patterning of metal films with a stamp and a surface chemistry mediated transfer process: Applications in plastic electronics. *Appl. Phys. Lett.* **81**, 562–564 (2002).

10. Kim, D. H. *et al.* Materials and noncoplanar mesh designs for integrated circuits with linear elastic responses to extreme mechanical deformations. *Proc. Natl. Acad. Sci. U. S. A.* **105**, 18675–18680 (2008).

11. Kaneko, A. Surface Micro- / Nanostructuring Using Self- Assembly of Fine Particles. *Micro/Nano Fabr. Technol 2* **015001**, (2018).

12. Matricardi, C. *et al.* Gold Nanoparticle Plasmonic Superlattices as Surface-Enhanced Raman Spectroscopy Substrates. *ACS Nano* **12**, 8531–8539

(2018).

13. Kinnear, C. *et al.* Directed Chemical Assembly of Single and Clustered Nanoparticles with Silanized Templates. *Langmuir* **34**, 7355–7363 (2018).

14. Cerf, A. & Vieu, C. Transfer printing of sub-100 nm nanoparticles by soft lithography with solvent mediation. *Colloids Surfaces A Physicochem. Eng. Asp.* **342**, 136–140 (2009).

15. Tabrizi, N. S., Xu, Q., Van Der Pers, N. M. & Schmidt-Ott, A. Generation of mixed metallic nanoparticles from immiscible metals by spark discharge. *J. Nanoparticle Res.* **12**, 247–259 (2010).

16. Sun, J. *Open Aircraft Performance Modeling Based on an Analysis of Aircraft Surveillance Data. TU Delft University* (2019).

17. Guo, X. *et al.* Laboratory SWAXS combined with a low-pressure impactor for quasi-online analysis of nanoparticles generated by spark discharge. *J. Aerosol Sci.* **85**, 17–29 (2015).

18. Meuller, B. O. *et al.* Review of spark discharge generators for production of nanoparticle aerosols. *Aerosol Sci. Technol.* **46**, 1256–1270 (2012).

19. Aghajani, S., Accardo, A. & Tichem, M. Process and nozzle design for high-resolution dry aerosol direct writing (dADW) of sub-100 nm nanoparticles. *Addit. Manuf.* **54**, 102729 (2022).

20. Dong, J., Gerlach, D., Koutsogiannis, P., Rudolf, P. & Portale, G. Boosting the Thermoelectric Properties of PEDOT:PSS via Low-Impact Deposition of Tin Oxide Nanoparticles. *Adv. Electron. Mater.* **7**, (2021).

21. Sapountzi, F. M. *et al.* Spark Ablation for the Fabrication of PEM Water Electrolysis Catalyst-Coated Membranes. *Catalysts* **12**, 1–13 (2022).

22. Bowden, N., Brittain, S., Evans, A. G., Hutchinson, J. W. & Whitesides, G. M. Schmetterlinge der Alpen. *Nature* **393**, 146–149 (1998).

23. Tabrizi, N. S., Ullmann, M., Vons, V. A., Lafont, U. & Schmidt-Ott, A. Generation of nanoparticles by spark discharge. *J. Nanoparticle Res.* **11**, 315–332 (2009).

24. Baek, J. Y. *et al.* Stable Deposition and Patterning of Metal Layers on the PDMS Substrate and Characterization for the Development of the Flexible and Implantable Micro Electrode. *Solid State Phenom.* **124–126**, 165–168 (2007).

25. Xu, W., Foster, E., Ma, C. & Bohn, P. W. On-demand in situ generation of oxygen in a nanofluidic embedded planar microband electrochemical reactor. *Microfluid. Nanofluidics* **19**, 1181–1189 (2015).

26. Plummer, S. T., Wang, Q., Bohn, P. W., Stockton, R. & Schwartz, M. A. Electrochemically derived gradients of the extracellular matrix protein

3

fibronectin on gold. *Langmuir* **19**, 7528–7536 (2003).

27.   Wan, A. M. D. *et al.* Electrical control of protein conformation. *Adv. Mater.* **24**, 2501–2505 (2012).

28.   Termebaf, H., Shayan, M. & Kiani, A. Two-Step Bipolar Electrochemistry: Generation of Composition Gradient and Visual Screening of Electrocatalytic Activity. *Langmuir* **31**, 13238–13246 (2015).

29.   Mensack, M. M., Wydallis, J. B., Lynn, N. S., Dandy, D. S. & Henry, C. S. Spatially resolved electrochemical sensing of chemical gradients. *Lab Chip* **13**, 208–211 (2013).

30.   Fosdick, S. E., Knust, K. N., Scida, K. & Crooks, R. M. Bipolar electrochemistry. *Angew. Chemie - Int. Ed.* **52**, 10438–10456 (2013).

31.   Mavré, F. *et al.* Bipolar electrodes: A useful tool for concentration, separation, and detection of analytes in microelectrochemical systems. *Anal. Chem.* **82**, 8766–8774 (2010).

32.   Duval, J. F. L., Huijs, G. K., Threels, W. F., Lyklema, J. & Van Leeuwen, H. P. Faradaic depolarization in the electrokinetics of the metal-electrolyte solution interface. *J. Colloid Interface Sci.* **260**, 95–106 (2003).

33.   Munktell, S., Tydén, M., Högström, J., Nyholm, L. & Björefors, F. Bipolar electrochemistry for high-throughput corrosion screening. *Electrochem. commun.* **34**, 274–277 (2013).

34.   Dhopeshwarkar, R., Hlushkou, D., Nguyen, M., Tallarek, U. & Crooks, R. M. Electrokinetics in microfluidic channels containing a floating electrode. *J. Am. Chem. Soc.* **130**, 10480–10481 (2008).

35.   Laws, D. R., Hlushkou, D., Perdue, R. K., Tallarek, U. & Crooks, R. M. Bipolar electrode focusing: Simultaneous concentration enrichment and separation in a microfluidic channel containing a bipolar electrode. *Anal. Chem.* **81**, 8923–8929 (2009).

36.   Hlushkou, D., Perdue, R. K., Dhopeshwarkar, R., Crooks, R. M. & Tallarek, U. Electric field gradient focusing in microchannels with embedded bipolar electrode. *Lab Chip* **9**, 1903–1913 (2009).

37.   Davies, C. D. & Crooks, R. M. Focusing, sorting, and separating microplastics by serial faradaic ion concentration polarization. *Chem. Sci.* **11**, 5547–5558 (2020).

38.   Anderson, T. J., Defnet, P. A. & Zhang, B. Electrochemiluminescence (ECL)-Based Electrochemical Imaging Using a Massive Array of Bipolar Ultramicroelectrodes. *Anal. Chem.* **92**, 6748–6755 (2020).

39.   Chow, K. F., Chang, B. Y., Zaccheo, B. A., Mavré, F. & Crooks, R. M. A sensing platform based on electrodissolution of a Ag bipolar electrode. *J. Am.*

Chem. Soc. **132**, 9228–9229 (2010).

40. Fosdick, S. E. & Crooks, R. M. Bipolar electrodes for rapid screening of electrocatalysts. *J. Am. Chem. Soc.* **134**, 863–866 (2012).

41. Vollertsen, A. R. *et al.* Modular operation of microfluidic chips for highly parallelized cell culture and liquid dosing via a fluidic circuit board. *Microsystems Nanoeng.* **6**, 107 (2020).

42. Vollertsen, A. R. *et al.* Highly parallelized human embryonic stem cell differentiation to cardiac mesoderm in nanoliter chambers on a microfluidic chip. *Biomed. Microdevices* **23**, (2021).

43. Mavré, F. *et al.* A theoretical and experimental framework for understanding electrogenerated chemiluminescence (ECL) emission at bipolar electrodes. *Anal. Chem.* **81**, 6218–6225 (2009).

44. Pourbaix, M., Zhang, H. & Pourbaix, A. Presentation of an Atlas of chemical and electrochemical equilibria in the presence of a gaseous phase. *Mater. Sci. Forum* **251**–**254**, 143–148 (1997).

45. Martin, M. M. & Lindqvist, L. The pH dependence of fluorescein fluorescence. *J. Lumin.* **10**, 381–390 (1975).

46. Wei, W., Xue, G. & Yeung, E. S. One-step concentration of analytes based on dynamic change in pH in capillary zone electrophoresis. *Anal. Chem.* **74**, 934–940 (2002).

47. Yuen, C., Zheng, W. E. I. & Huang, Z. Surface-enhanced raman scattering: principles, nanostructures, fabrications, and biomedical applications. **1**, 267–284 (2008).

48. Pu, H., Xiao, W. & Sun, D. W. SERS-microfluidic systems: A potential platform for rapid analysis of food contaminants. *Trends Food Sci. Technol.* **70**, 114–126 (2017).

49. Alyami, A., Quinn, A. J. & Iacopino, D. Flexible and transparent Surface Enhanced Raman Scattering (SERS)-Active Ag NPs/PDMS composites for in-situ detection of food contaminants. *Talanta* **201**, 58–64 (2019).

50. Rao, S. *et al.* Single DNA molecule detection in an optical trap using surface-enhanced Raman scattering. *Appl. Phys. Lett.* **96**, (2010).

51. Choi, C. J., Wu, H. Y., George, S., Weyhenmeyer, J. & Cunningham, B. T. Biochemical sensor tubing for point-of-care monitoring of intravenous drugs and metabolites. *Lab Chip* **12**, 574–581 (2012).

52. Leem, J., Kang, H. W., Ko, S. H. & Sung, H. J. Controllable Ag nanostructure patterning in a microfluidic channel for real-time SERS systems. *Nanoscale* **6**, 2895–2901 (2014).

53. Wei, S., Zheng, M., Xiang, Q., Hu, H. & Duan, H. Optimization of the particle

3

density to maximize the SERS enhancement factor of periodic plasmonic nanostructure array. *Opt. Express* **24**, 20613 (2016).

54. Li, C., Huang, Y., Lai, K., Rasco, B. A. & Fan, Y. Analysis of trace methylene blue in fi sh muscles using ultra-sensitive surface-enhanced Raman spectroscopy. *Food Control* **65**, 99–105 (2016).

55. Niu, Z. & Fang, Y. Surface-enhanced Raman scattering system of sample molecules in silver-modified silver film. **66**, 712–716 (2007).

56. Le Ru, E. C., Blackie, E., Meyer, M. & Etchegoint, P. G. Surface enhanced raman scattering enhancement factors: A comprehensive study. *J. Phys. Chem. C* **111**, 13794–13803 (2007).

57. Pfeiffer, T. V., Feng, J. & Schmidt-Ott, A. New developments in spark production of nanoparticles. *Adv. Powder Technol.* **25**, 56–70 (2014).

3.6 Supporting Information

1. Equipment used for the nanoparticle deposition
2. SEM images
3. Calibration curve of Fluorescein sodium salt
4. Equivalent circuit of the microfluidic device
5. Raman spectra
6. Picture of the PDMS chip with nanoparticles in its chambers

1. Equipment used for the nanoparticle deposition
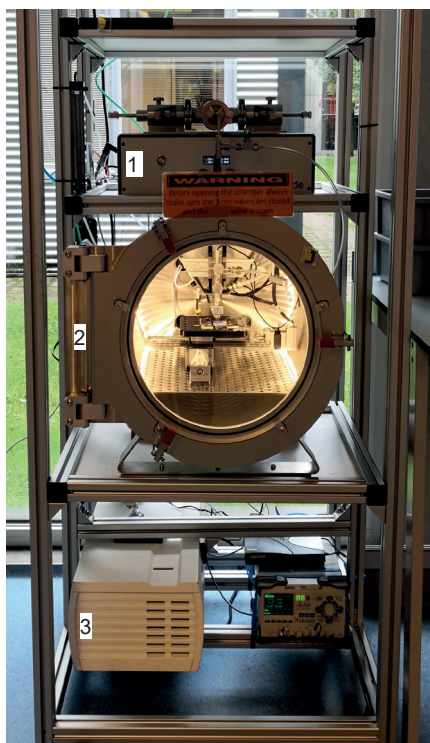
Figure S1: Picture of the prototype VSP-P1 nanostructured material printer setup. 1. VSP-G1 nanoparticle generator. 2. Vacuum chamber with deposition unit 3. Vacuum pump.

2. SEM images

A

B
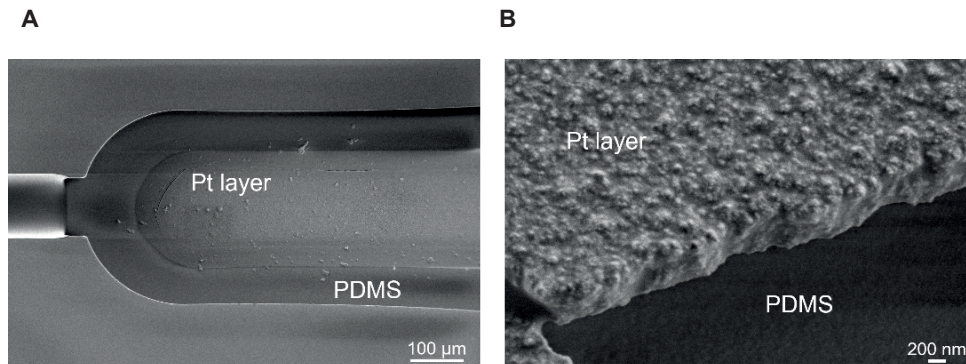
Figure S2: SEM image of **A)** top view and **B)** cross-section of Pt NP layer printed on a PDMS substrate at 10 µm/s, with a nozzle-substrate distance of 500 µm. The printing parameters define the morphology of the deposited material, which results in the formation of a dense layer of NPs in the case of printing speeds of 10 µm/s.

A

B

Nozzle-substrate distance 200 µm   Nozzle-substrate distance 500 µm

SEM images	Speed of printing [µm/min]	Mean particle size [nm]	Roughness average [nm]	SEM images	Speed of printing [µm/min]	Mean particle size [nm]	Roughness average [nm]
	10	30.5 ± 2.14	14.8		10	38.0 ± 1.2	15.8
	20	29.9 ± 2.9	14.8		20	37.9 ± 0.8	15.4
	40	29.5 ± 3.8	14.5		40	33.0 ± 1.6	15.2
	60	28.6 ± 1.7	14.3		60	33.1 ± 1.5	14.9
	80	28.0 ± 1.4	13.1		80	33.0 ± 1.5	14.4

Table S1: SEM images and average of the roughness profile of Ag NPs patterns deposited on PDMS at different printing speeds (10- 80 µm/min) using nozzle- substrate distances of **A)** 200 µm **B)** and 500 µm. With slower printing speeds, both the mean particle size and mean surface roughness values are higher compared to the results obtained with slower printing speeds. This can be explained by the higher amount of NPs deposited on the

substrate per unit of time, resulting in more collision and coalescence events between NPs. Scale bars 200 nm.

3. Calibration curve
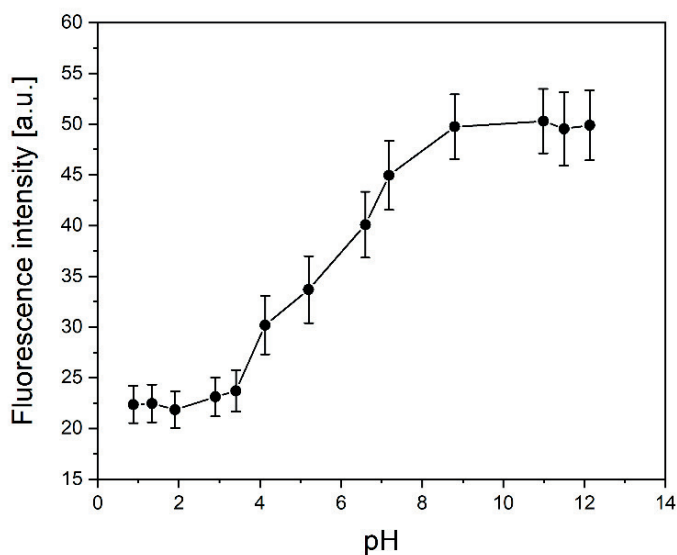
Figure S3: Effect of pH on the fluorescence emission intensity of solutions containing 100 µM fluorescein and 1.0 mM sodium phosphate buffer. The pH of the solutions varies from 0.9 to 12.1. Error bars correspond to the standard deviation of the average fluorescence emission intensity of the solutions in the 4 chambers of the device.

4. Equivalent circuit of the microfluidic device
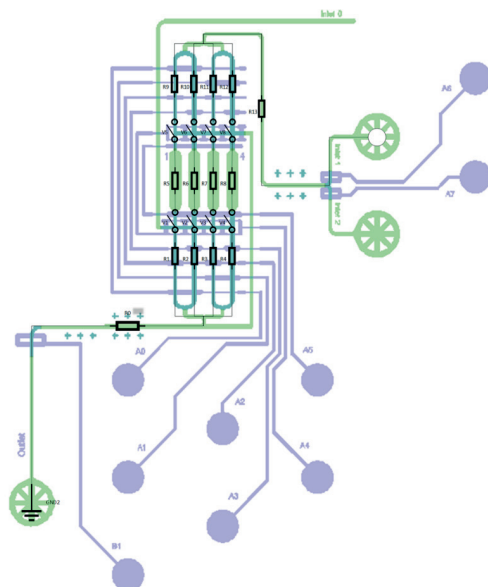
Figure S4: Design and equivalent circuit of the microfluidic device used for the bipolar experiments.

5. Raman spectra
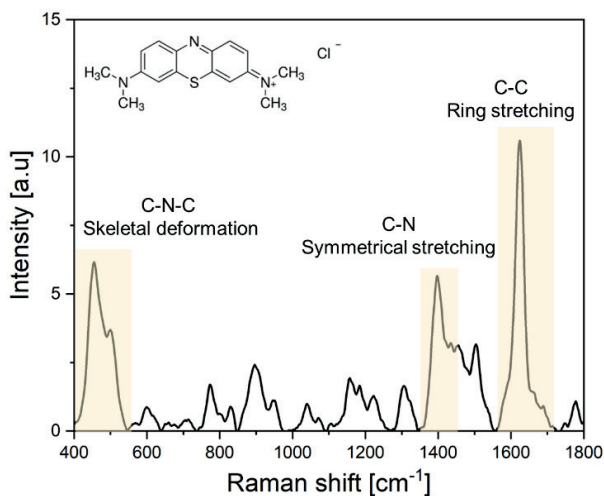
Figure S5: Raman spectrum of a solution of methylene blue 0.11M on PDMS. The most intense peaks and the corresponding vibrational modes are highlighted in the graph. The peak at 1623 cm^{-1} was used as a reference in the evaluation of the enhancement factor.
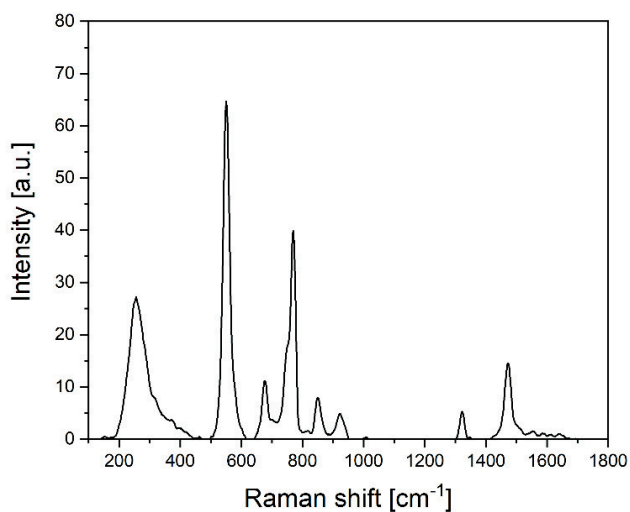
Figure S6: Raman spectrum of bare PDMS.
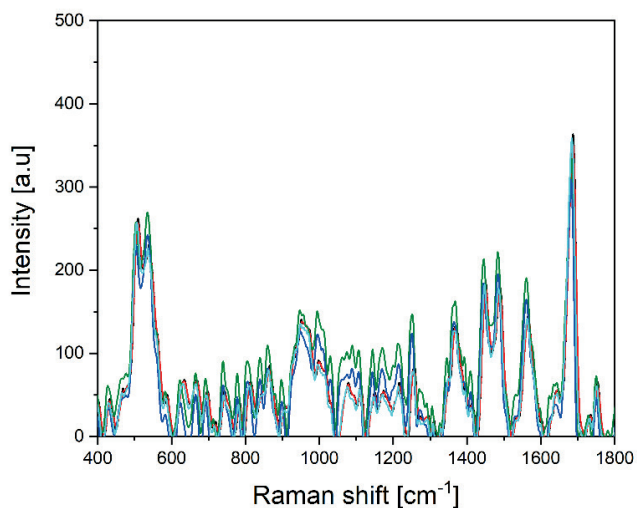
Figure S7: Raman spectra of 2.5·10^{-5} M methylene blue obtained on 5 points on the Ag NPs printed on PDMS. The printing conditions for the NPs are: writing speed of 60 μm/s, nozzle-substrate distance of 500 μm. Voltage/current settings used for the deposition V=1.3 kV and I= 10 mA.
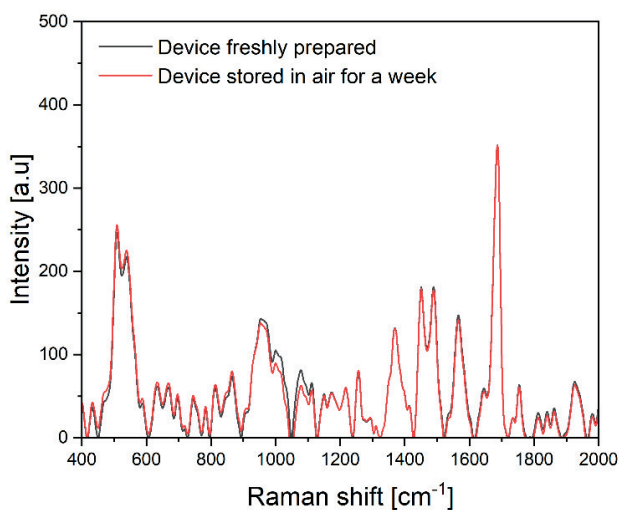
Figure S8: Comparison between the Raman spectra of 2.5·10^{-5} M methylene blue (MB) obtained by using a device with freshly printed Ag NPs patterns deposited in the chip chambers (in black) and with a device stored at ambient conditions for a week (in red).

6. Picture of the PDMS chip with nanoparticles in its chambers
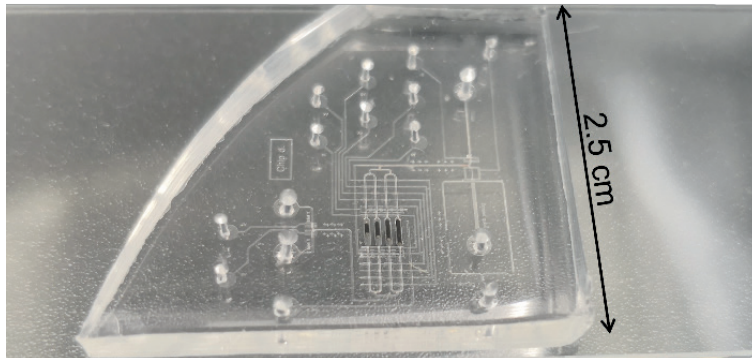
Figure S9: Picture of the multiplexed PDMS microfluidic device with Pt electrodes printed in its chip chambers.
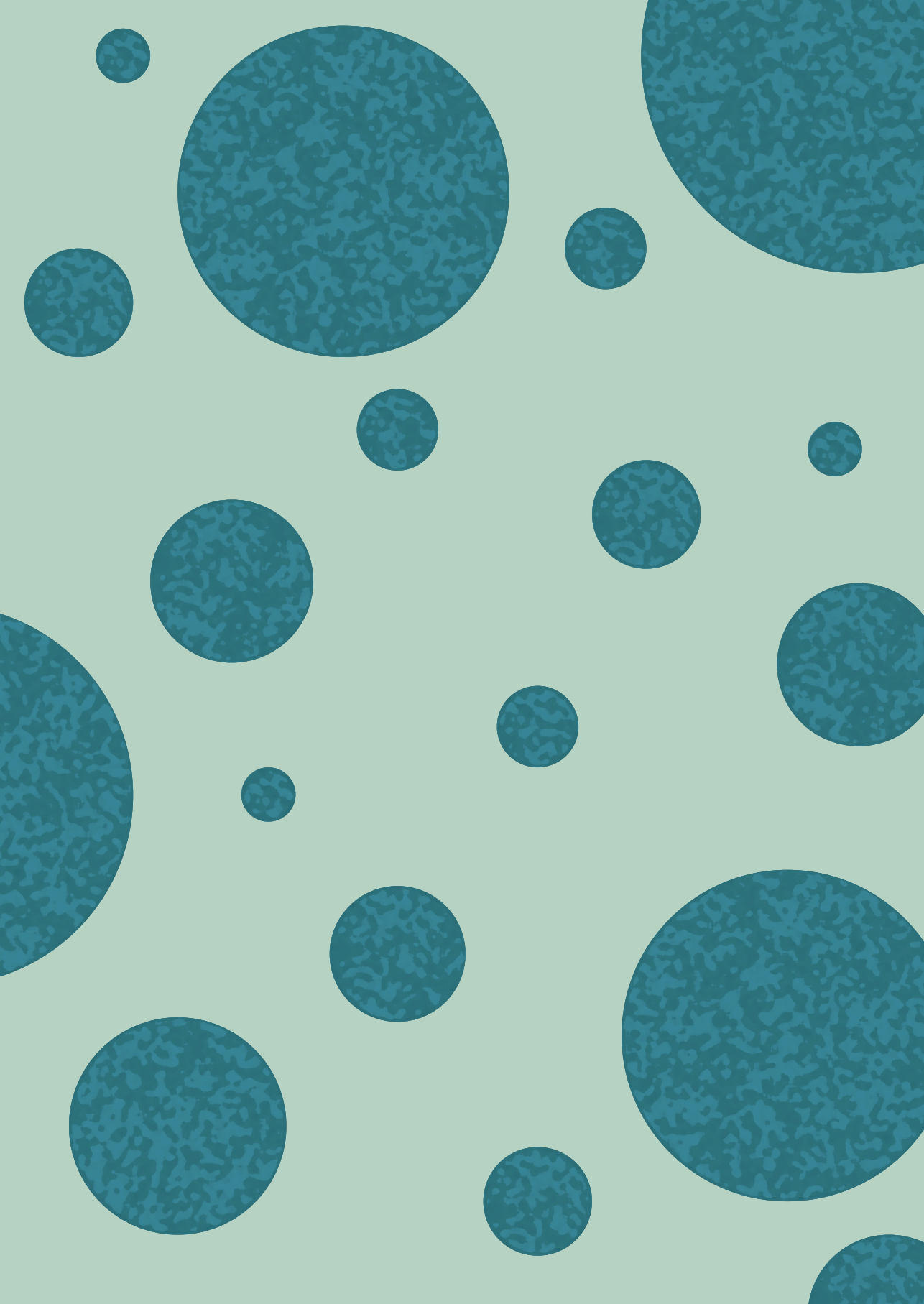
3

Chapter 4

Accessibility Study of Porous Materials at the Single Particle Level as Evaluated within a Multiplexed Microfluidic Chip with Fluorescence Microscopy

Understanding the mass transfer phenomena taking place in solid catalysts, batteries, fuel cells, and adsorbents is essential to improve their performances. Uptake experiments of ultraviolet-active or fluorescent probes represent a direct way to directly provide an accessibility measure of porous particles. We propose a new method to evaluate the accessibility of functional porous materials at the single-particle level. A multiplexed polydimethylsiloxane microfluidic device and a fluorescence microscope are employed to assess the uptake of fluorescent molecules in porous particles over time. The device allows for performing multiple uptake experiments in parallel, enabling the comparison of different particles under the same conditions. We showcase the method by studying the diffusion and adsorption properties of a dye in different silica model particles. The approach allows for probing interparticle heterogeneity in accessibility and accessible surface area as well as the dependence of these parameters on electrostatic interactions between the particle and the probe molecules.

4.1   Introduction

Molecular transport is a key aspect in the applications of most functional porous materials, as it determines their performances as adsorbents, batteries, fuel cells, and solid catalysts[1]. The efficiency of these materials depends on diffusion, adsorption, and desorption processes taking place inside their pores, which are in turn influenced by the physicochemical interactions between the pore walls and guest molecules[1-4]. Therefore, understanding these phenomena is essential for designing functional materials with much improved performances.

A direct way for elucidating mass transfer processes in porous materials is based on uptake and release experiments of ultraviolet (UV)-active[5,6] or fluorescent probes, directly providing a pore accessibility measure (i.e., how easily molecules enter the porous host). One example of such an approach is offered by the so-called Akzo Nobel Accessibility Index (AAI) test[4,7,8] introduced for Fluid Catalytic Cracking (FCC) particles, which is also used industrially. The method is based on measuring the uptake of UV-active molecules into catalyst particles by tracking the relative concentration of the molecules in solution over time (Figures 1A and 1B), providing a relative measure of the penetration rate. In this approach, it is assumed that the behavior of the entire system replicates the one of an individual particle. However, structural and compositional differences exist within a catalyst batch[9,10], that cannot be captured by ensemble-averaged analytical measurements.

Characterizing the uptake process of individual particles would be beneficial to supplement the data obtained from bulk methods, and also to capture heterogeneities among particles. This has been tried with different techniques. Recently, confocal laser scanning microscopy (CLSM) has proven to be a useful tool for visualizing the inner structure of materials. It has been applied to monitor the uptake and distribution of dyes[11-14] and dye-labeled particles[15,16] on the single-particle scale. The approach allowed a direct visualization of the particle's accessible porosity and the correlation between its structure and activity. This provides useful insight for the design of more efficient materials. Moreover, microimaging techniques based on

interference microscopy (IFM) and IR microscopy (IRM)[2,17,18] were successfully used for recording the evolution of guest molecule distributions in nanoporous host materials. Furthermore, advanced electron[19-25] and X-ray[26-31] microscopy techniques, have been applied to (partially) map the pore volume of individual particles in 3 dimensions and simulate mass transfer within them.

The mentioned analytical measurements require expensive equipment and sample preparation, and some of them are unfortunately destructive particularly due to the potential for ion, electron, and X-ray beam damage, as observed in electron microscopy and synchrotron-based techniques[9,32,33]. Furthermore, the number of particles that can be studied with these methods is very limited. Recently, microfluidic devices have been used to characterize catalysts at the single particle level in a high throughput fashion by isolating catalyst particles based on their activity[34] and metal loading[35]. However, this kind of approach has not yet been used to study intra-particle mass transport.

Here we propose a fast, cheap, and reproducible method (Figures 1C and 1D) to compare accessibility between and within different porous particles in a high throughput fashion. We used only a polydimethylsiloxane (PDMS) multiplexed microfluidic device and a LED-illuminated wide-field fluorescence microscope and we imaged and compared the uptake of fluorescent molecules by individual mesoporous silica particles. Moreover, we performed experiments using different solution conditions, to evaluate the influence of electrostatic interactions between guest molecules and host material on the overall uptake process. Furthermore, by suppressing these interactions the measured accessibilities were – for the tested samples – able to probe pore size accurately, obtaining a distribution comparable to the results from the N_2 physisorption method. Additionally, the saturation values of the uptake curves allowed us to study changes in accessible surface area as a function of guest-host interactions of individual particles, which cannot be distinguished with bulk and non-chemically sensitive techniques, such as gas physisorption. Finally, we investigated through simulations how internal diffusion, adsorption, and external mass transfer affected the shape of the uptake curves.

4
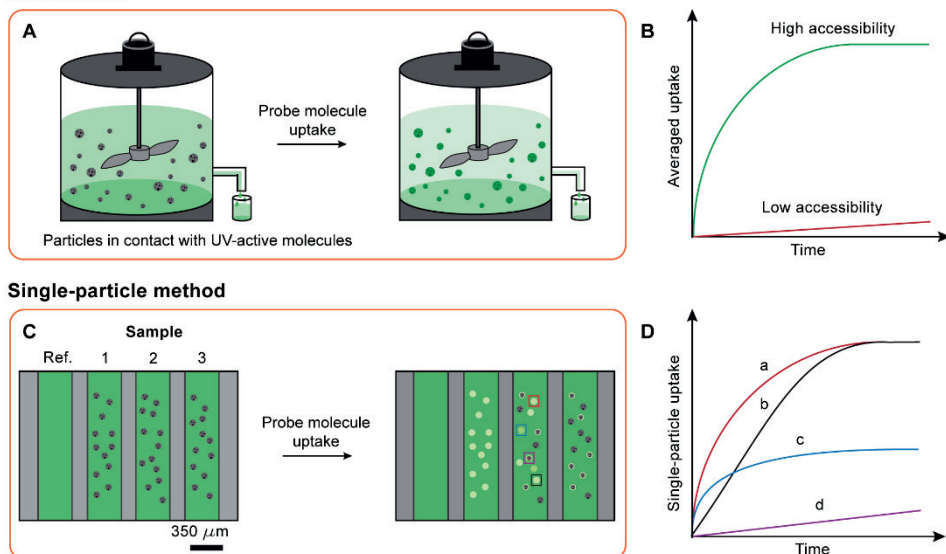
Figure 1: Schematic representation of the experimental methods to evaluate the accessibility of particles in bulk and at the single particle level A) A stirred tank contains both UV-active molecules and porous particles. The concentration in the solution decreases due to the uptake of the porous material. B) Based on the concentration change, the bulk uptake [mol/g(material)] is computed and used to characterize the material's accessibility. C) A multiplexed microfluidic device containing 4 chambers is filled with porous particles and a liquid containing a fluorescent dye. One reference chamber (left) is left empty to control for photobleaching. As fluorescent molecules enter the porous particles, their fluorescence increases. D) The fluorescence of individual particles (in the highlighted squares) is tracked over time to assess the uptake of fluorophores and in turn the accessibility of individual particles. Curves a and b correspond to particles with the same accessible adsorption capacity (both curves plateau at the same value), but different accessibilities (a>b). Particle c is rather accessible (saturation is reached quickly) but the total uptake of fluorophores is less than in particles a and b. Particle d corresponds to a particle with very low accessibility (saturation is not reached during the time of the experiment).

The experiments were performed using microfluidic devices consisting of two PDMS layers, and a glass slide (Figure S1), as previously reported[36,37]. The top layer contains four chambers, which allow the performance of three experiments in parallel under the same conditions while keeping a reference chamber to control for photobleaching (Figure 1C). In the experiments, each chamber is loaded with various porous SiO_2 particles. Then, all chambers are filled with water to first fill pores of the hydrophilic

material by capillary forces, this process takes place in less than a second[38]. Finally, the chambers are filled with a fluorescent dye solution. The mean fluorescence intensity, as a measure of dye concentration in each particle, is tracked individually as a function of time resulting in individual uptake curves (Figure 1D) constructed from the experimental data using a self-developed Matlab™ code. One can get information from the following features of these curves: 1) the final value of the curve contains information about the saturation state of the particle. If it is flat, the equilibrium in the uptake process has been reached (i.e., the particle surface is saturated with dye and there is no concentration change in the particle pore volume, Figure S2). Otherwise, uptake is still ongoing. 2) The intensity value reached after saturation contains information about the adsorption properties of the system. The higher this value, the more adsorption took place, which can be related to the surface area of the material. 3) The shape of the curve, i.e., how the curve's slope changes over time, contains information about the accessibility of the particle. The steeper the slope, the faster saturation is reached, and the more accessible the particle is.

4.2 Theoretical background

The interpretation of uptake data can be divided into two categories, based on the adsorption or diffusion as rate-limiting step. The latter represents the most common case for macroscopic adsorbent materials[39,40]. Several models have been developed to describe the experimentally obtained uptake curves[41]. However, most of these models require reaching a saturation state to extract the relevant parameters. The so-called intra-particle diffusion model[42] does not have this requirement and is therefore widely used for slow uptake experiments. Here the fractional uptake $q(t)$ usually expressed in mg(probe)/g(solid) is plotted as a function of $t^{0.5}$ [43-45,53-61, 62-66,45-51].

At low saturation values with an ideal mixing of the liquid phase (i.e., the dye concentration in solution is constant in space), this would initially result in a linear curve that eventually reaches a plateau, representing saturation of the sorbent material (Figure 2A). In the case of prominent external mass transfer effects (no ideal mixing), a stagnant layer, i.e. a concentration

gradient in the vicinity of the particle, is formed during uptake, slowing it down and resulting in a non-linear regime for small time values[41,61] (Figure 2B). Typically, linear regression is performed on the linear part of the uptake curve (Eq. 1) and its slope is used to quantify the so-called intra-particle diffusion rate constant[67] K_p (mg/g min$^{0.5}$), which we refer to as accessibility index:

$$q(t) = K_p \, t^{0.5} + C_y \tag{1}$$

The y-intercept C_y (mg/g) is typically used to evaluate the extent of the boundary layer thickness and therefore the external mass transfer effects. When the fitted line passes through the origin, the external mass transport is negligible. Otherwise, a non-zero y-intercept value indicates a relevant contribution of the boundary layer effects to the measured intra-particle diffusion. Both positive[43,44,53-58,45-52] and negative[59-61] C_y values have been reported in the literature. Positive values are interpreted as fast adsorption by the material; thus, it is not possible to capture the actual starting point of the adsorption process. Negative values are related to a diffusion process retarded by the boundary layer effects. Moreover, some studies use the intercept of the fitted line with the x-axis to evaluate external mass transfer effects[62-66]. Therefore, the exact physical meaning of the C_y parameter proposed in the aforementioned model remains unclear.
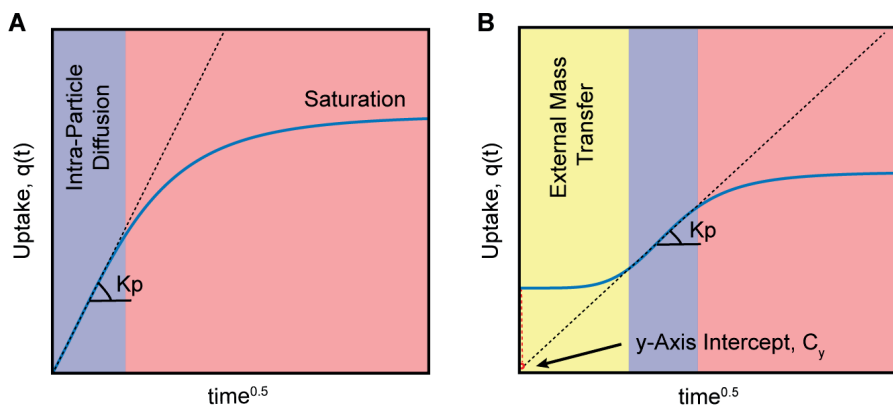
Figure 2: A) Ideal uptake curve with purely intraparticle diffusion and B) with external mass transfer contribution.

To investigate the significance of the accessibility index K_p and the y-intercept C_y, uptake simulations were performed by solving Fick's second law with the finite difference method. In our model (see SI 2), no flux at the center of the particle and external mass transfer effects at the particle surface were included in the boundary conditions. Moreover, adsorption was considered to be much faster than the diffusion process, which established diffusion to be the rate-limiting step. As a result, local equilibrium between the diffusing and adsorbed substance can be postulated. To simplify, we assumed a linear dependence between the concentration of the free and adsorbed substance.

The molecular uptake in porous particles is mostly dominated by three parameters: 1) the internal particle diffusion coefficient D (m^2/s), which increases with the pore size and pore interconnectivity; 2) the external mass transfer coefficient k (m/s), which depends on diffusion and convection outside the particle and correlates positively with D (SI 2, Eq. 7); and 3) the adsorption coefficient R (unitless proportionality constant expressing the ratio between adsorbed concentration and concentration in solution, SI 2, Eq. 2). The latter depends on the wall-molecule interactions as well as the number of accessible adsorption sites.

We performed a sensitivity analysis (Figure 3) to assess how these three parameters affect the uptake curve shape and its parameters K_p and C_y. Increasing the internal diffusion coefficient D of the particle resulted in a higher slope of the linear part of the uptake, i.e., higher accessibility index K_p, and a more negative y-axis intercept C_y (Figures 3A and 3D). A similar effect on K_p is observed by increasing k (reducing the external mass transfer limitations). However, it also shifts the linear regime of the uptake curve to shorter times, which results in a less negative y-intercept (Figures 3B and 3E). Finally, increasing the adsorption coefficient R increases the accessibility index K_p and decreases the y-intercept C_y (Figures 3C and 3F). It is worth noting that the external mass transfer coefficient k and the effective diffusion coefficient $D' = \frac{D}{1+R}$ which includes adsorption, are positively correlated due to the boundary conditions equating flow at the two sides of the solid-liquid interphase (SI 2, Eq. 7). Hence, increasing the internal particle diffusion coefficient D will result in higher external mass

transport (higher k) and vice-versa. However, both parameters contribute differently to the y-axis intercept C_y. Since the y-axis intercept is determined by several parameters, it should not be used to evaluate external mass transfer only.

In an uptake experiment, while using particles of the same material and pore volume, but different pore sizes, one varies the internal diffusion coefficient D and therefore the external mass transfer coefficient k as well as the adsorption coefficient R (as different surface areas are obtained). All of these values correlate positively with the amount of adsorbed material (uptake, $q(t)$) and the accessibility index K_p). Interestingly our experimental results show that the accessibility index and the y-axis intercept are correlated (Figure S3), proving the redundancy of using both parameters to characterize porous materials. Therefore, we will provide only the accessibility index K_p values obtained in the experiments to characterize and compare the processes.
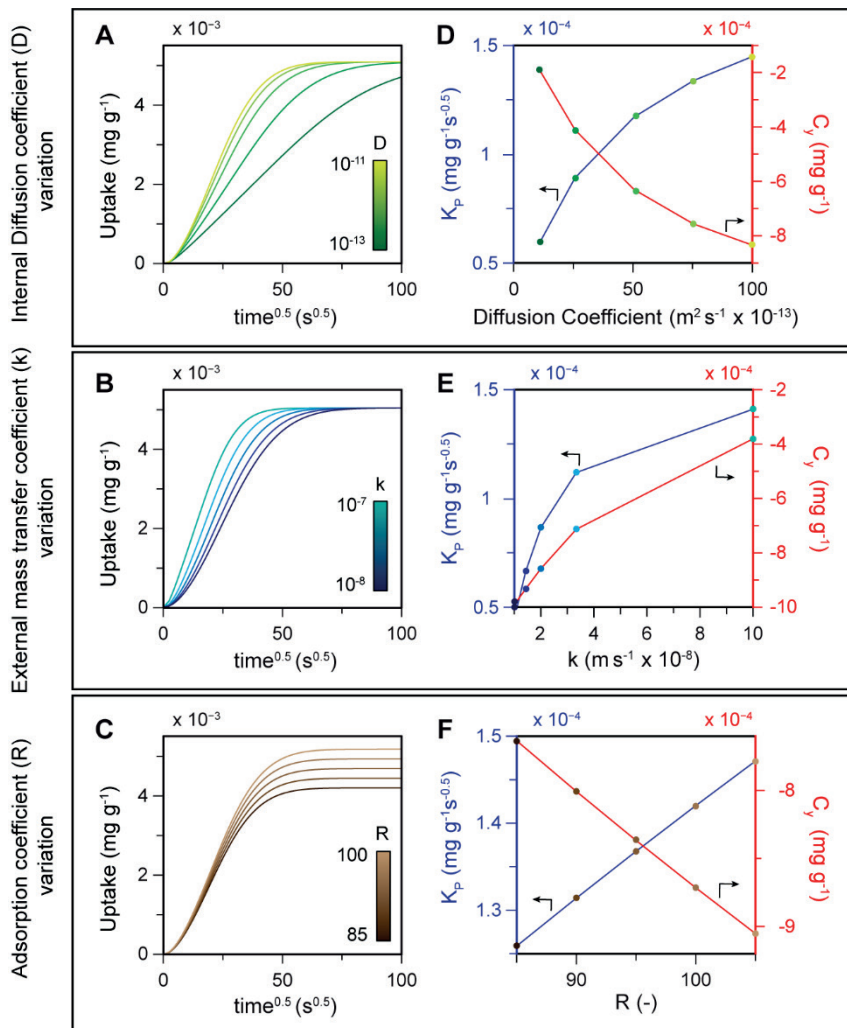
Figure 3: Simulations of uptake curves in a 35 μm spherical particle. **A)** Uptake curves obtained changing the internal diffusion coefficient D (k = 10-8 m/s and R = 100) **B)** the external mass transfer coefficient k (D = 10^{-12} m²/s and R = 100) and **C)** the adsorption coefficient R (D = 10^{-12} m²/s and k = 10^{-8} m/s). **D)**, **E)**, and **F)** show the slopes (accessibility indices) and y-intercepts of the inflection point tangents of the uptake curves shown in A), B), and C) respectively.

4.3   Results and Discussion

To showcase the developed method, we used SiO_2 particles with almost monodisperse pore size distributions (i.e., 50 nm, 35 nm, and 23 nm)

(Figure 5A and Figure S4) often used as catalyst supports (e.g., olefin polymerization catalysis). Rhodamine 110 (Rh110) (Figure 5B) was used as a fluorescent probe due to its photostability[68,69], high quantum yield, and fluorescent intensity being proportional to its concentration (Figure S5A). Therefore, particle fluorescent intensity values were directly used to obtain the uptake curves (Figure S5B and Figure S6), and the accessibility index was defined in min$^{-0.5}$ units. The particles were placed in the chambers leaving one empty that was used as a reference to check the photostability of the dye (Figure 1C). Uptake experiments were conducted for 5 h and images were acquired every minute. Figures 4A and 4B display a cropped version of the fluorescence microscopy images recorded at the beginning and end of the experiments using 50 nm pore-size particles showing an overall, but heterogeneous increase in intensity. Some particles of similar size display an intensity (i.e., concentration) gradient within them, whereas others show a more homogeneous dye distribution, hinting toward different pore connectivity. The final mean fluorescence intensity of the particles resulted higher than in the bulk solution, due to the adsorption of the probe molecules in the pore structure. Figure 4C shows the mean intensities of particles of the same sample as a function of time (the initial intensity of each particle was subtracted). Even particles that belong to the same batch, differ strongly in their uptake curves and therefore accessibilities. Traditional bulk experiments could not have measured this, which highlights the importance of the proposed method for elucidating inter-particle heterogeneity. Plotting the same uptakes versus $t^{0.5}$ results in a sigmoid-like (asymmetric sigmoid) curve (Figure 4D). The non-linear beginning of the curve suggests external mass transfer limitations. That is, a concentration gradient is formed outside the particle that slows the internal diffusion down. Moreover, the fact that the curves are reaching a plateau, means that, as expected, at some point in time the particles are starting to get saturated with dye.
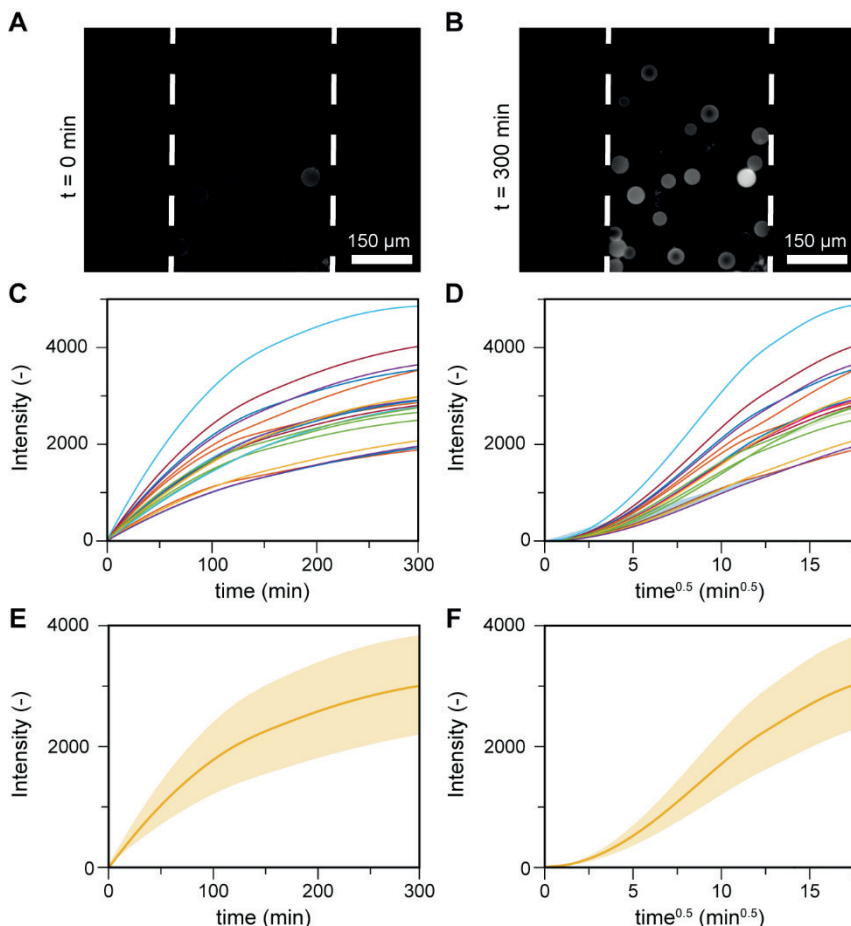
Figure 4: A) Zoomed-in and cropped fluorescence microscopy image of the microfluidic chamber containing silica particles with 50 nm pores at the beginning and **B)** end of the experiment. Scale bar 150 μm. **C)** Uptake curves of particles shown in Figures 4A and 4B. **D)** Uptake curves are linearized when plotted over $t^{0.5}$. **E)** and **F)** show the mean uptake curves obtained from the ones in Figures C and D. The shaded area represents the standard deviation of all particles considered (n=18).

Apart from varying the pore size of the particles to compare the uptake rates, we evaluated how the guest-host electrostatic interactions reflected upon the overall uptake process. These were tuned by using solutions at different ionic strength or pH. The pH affected the charge of the dye[70] and the pore-wall surface charge density, but its fluorescence properties remained unchanged (Figure S7). In the case of silica higher pH results in

more negative surface charge density[71]. The ionic strength of the solution influences the extent of the electrical double layer (EDL), a region where the liquid is not electroneutral because it contains a high concentration of counter-ions attracted by an oppositely charged surface[72]. If the characteristic length of the EDL (commonly called the Debye length) is greater than the pore radius, there is an overlap between EDLs extending from opposite surfaces in the pores (schematically shown in Figure 5C), which slows down or even prevents the entrance of (probe) molecules with the same charge as the counter-ions due to electrostatic repulsion.

We performed experiments using three different solutions: 1. pH = 4.3, 2. pH = 4.3, and 0.01M NaCl as supporting electrolyte, and 3. pH = 7 (Figures 5C, 5D, and 5E). Solution 1 and 2 have the same pH but different ionic strengths ($1.3 \cdot 10^{-4}$ and $9.4 \cdot 10^{-3}$ mol/L, respectively) which translate into different Debye lengths (26 nm in solution 1 and 3 nm in solutions 2 and 3) (SI 8). On the other hand, solutions 2 and 3 have the same ionic strength (Debye length), but different pH. The solutions used in the experiments have a pH above the silica isoelectric point (pH~2)[73]. Therefore, the oxide surface hydroxyls are deprotonated and the silica surface is negatively charged[74]. For all solutions, the uptake speed increased as a function of pore size and they all seem to be affected by external mass transfer as they show a non-linear regime at low $t^{0.5}$ values (Figures 5F, 5G, and 5H). However, mass transfer varied dramatically for the different conditions. Solution 1 (pH = 4.3) displayed the slowest uptake, with its linearized curve not reaching an inflection point and showing only small differences between samples with different pore sizes (Figure 5F). The linearized uptake curve of solution 2 (pH = 4.3, and 0.01M NaCl) reached the inflection point, showing moderate differences based on pore size (Figure 5G). Solution 3 (pH = 7) proved to be the fastest with respect to uptake and showed signs of saturation (i.e., the linearized uptake curve surpassed its inflection point) and the largest differences between the different porous silica samples (Figure 5H).

This behavior can be explained by the electrostatic interactions of the different systems: solution 1 (pH = 4.3) causes Rh110 and silica to be positively[70] and negatively charged[73] respectively. Moreover, due to the low

ionic strength of the system, an overlapping EDL (Debye length: 26 nm > r_{pore}) predominantly containing cations is formed in the vicinity of the pore walls, which interacts with the incoming Rh110(+) repulsively, slowing the diffusion process down (Figures 5C and 5F). Solution 2 (pH = 4.3, and 0.01M NaCl), with higher ionic strength, results in a smaller Debye length (3 nm) leading to milder repulsive electrostatic interactions between the EDL and the guest molecules as well as faster mass transport (Figures 5D and 5G). Similar Debye length effects of pore diffusion have been reported previously[75-77]. Solution 3 (pH = 7) has the same ionic strength as solution 2 (pH = 4.3, and 0.01M NaCl) and therefore a comparable Debye length. Moreover, at pH = 7, while silica has a higher negative surface density[72], Rh110 forms zwitterions due to the deprotonation of the carboxyl group and the amino group carries a positive charge[70]. Therefore, the guest-host electrostatic interactions are the lowest in this case, which results in a faster uptake and saturation (Figures 5E and 5H). As the strength of electrostatic interactions decreases (Figures 5C, 5D, and 5E), the pore size and structure become more dominant for the uptake process. This explains why we observe small, moderate, and large uptake differences between pore sizes in solutions 1, 2, and 3, respectively, in our experiments (Figures 5F, 5G, and 5H).

4
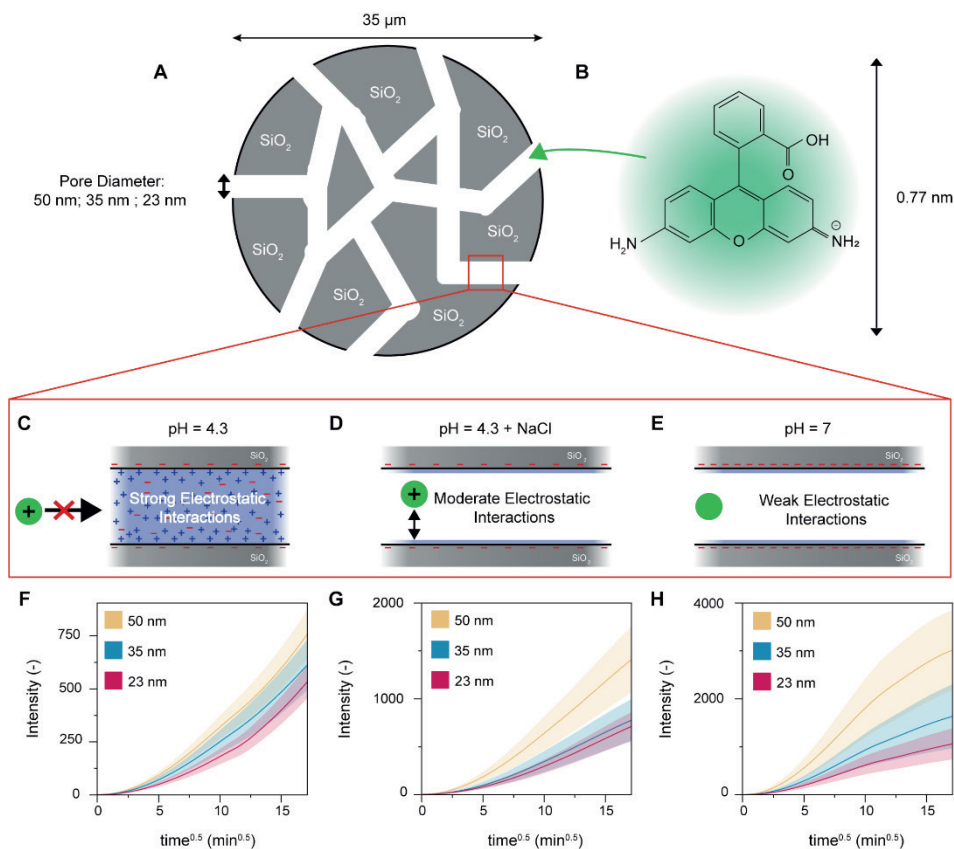
Figure 5: A) Silica particles (diameter: 35 μm) with almost uniform pore size distributions. Three pore sizes were used: 50, 35, and 23 nm. **B)** Rh110 chemical structure. Rh110 has a hydrodynamic diameter of 0.77 nm and is positively charged when solved in water[78]. C-E) Schematic of electrostatic interactions between Rh110 and the negatively charged pore-walls under different conditions. **C)** pH = 4.3: A cationic electric double layer overlap (blue-shaded area) is present inside the pore which repulses the Rh110(+). **D)** pH = 4.3 and 0.01M NaCl: Increasing the ionic strength reduces the Debye length and creates a neutrally charged region within the pore that allows Rh110(+) to enter the pore more easily. **E)** pH = 7: The surface charge density of the pore walls is more negative. However, Rh110(±) is neutrally charged so no main probe-wall electrostatic interactions are present. **F, G, H)** Uptake curves corresponding to the conditions described in C, D, and E, respectively. Decreasing the electrostatic interactions has 2 effects on the uptake curves: it speeds up the process and it also increases the differences between samples as the pore size gradually becomes more relevant (note the difference in the y-axis scale).

Figure 6A shows the obtained accessibility index distribution for different particles and wall-probe electrostatic interactions. The accessibility was evaluated from the slope of the uptake curve inflection point tangent (Figure S8). It is worth mentioning that this analysis approach cannot be used if the first derivative of the uptake curve does not reach a maximum during the experiment (i.e., the curve has no inflection point). The experiments performed with solution 1 (pH = 4.3) do not meet this criterion and cannot be analyzed in this fashion. As qualitatively described by the uptake curves, the accessibility index decreases with pore size, and the differences are more pronounced for solution 3 (weak electrostatic interactions). The difference between 35 nm and 23 nm for solution 2 (moderate electrostatic interactions) falls within the error bar of the measurement. At pH = 7 (weak electrostatic interactions), however, the measurement remains sensitive to these differences. Therefore, by suppressing the probe-wall electrostatic interactions, it is possible to probe accessibility as dominated by the pore structure (pore size and shape). This becomes clear if one compares the accessibility index distribution at pH = 7 (Figure 6B) with the pore size distribution obtained with N_2 physisorption (Figure 6C). Note that both distributions show a significant overlap of the 35 nm sample with both the 23 nm and the 50 nm samples. Further, the relative peak positions are similarly distributed with respect to each other.

4
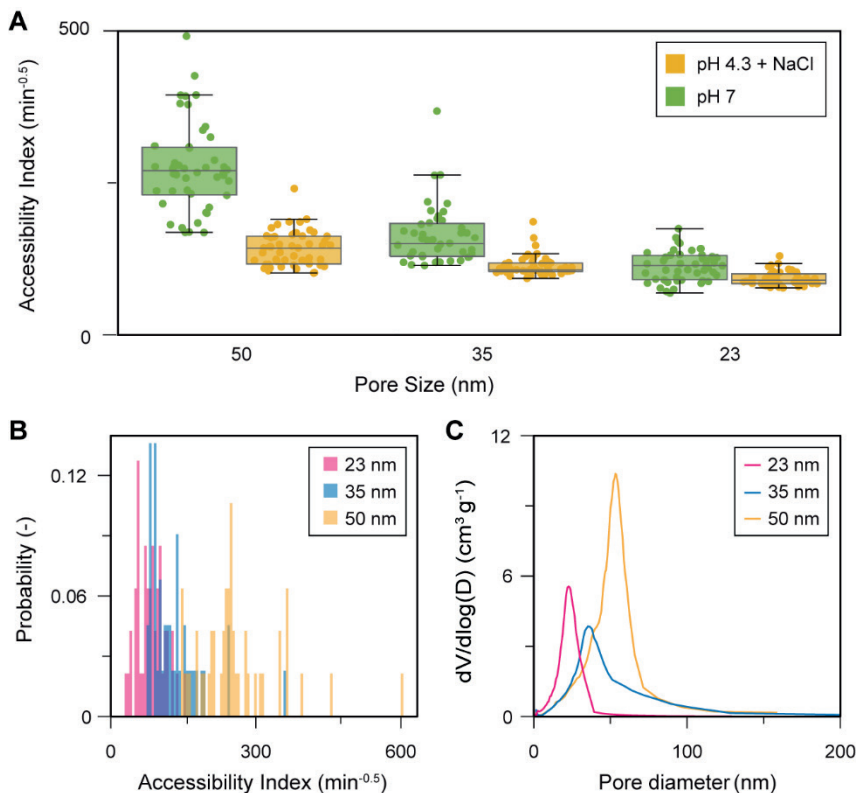
Figure 6: A) Comparison of accessibility index distribution of silica particles with different pore sizes (50, 35, and 23 nm) obtained by performing the experiments with fluorescent solutions at different pH but with the same ionic strength. The number of particles analyzed is ~ 50. At pH 7 the accessibility was higher as there are less electrostatic interactions. B) The accessibility index distribution at pH=7 and C) the pore size distribution exhibit similarities in terms of relative peak positions and overlapping features. The pore size distribution was determined through N_2-physisorption measurements, using Barrett-Joyner-Halenda (BJH) analysis of the desorption branch. The BET surface areas were ~ 523 m²/g (23 nm sample), ~ 439 m²/g (35 nm sample), and ~ 344 m²/g (50 nm sample). C) the pore size distributions obtained from N_2-physisorption

To investigate the adsorption behavior of the system, the fluorescence of individual particles was measured and compared after two weeks of uptake, to ensure that saturation was reached (Figure 7). For all evaluated conditions, the same trend could be observed for the pore size: the equilibrium intensity, and therefore the equilibrium concentration increases as the pore size decreases. All model particles have roughly the

same total porosity (~30%). If the total porosity is constant, the surface area available for adsorption decreases as a function of pore size. This explains why the amount of adsorbed Rh110 increases when particles with smaller pores are probed – intensity therefore directly correlates with surface area (BET results, SI 4). Nevertheless, the amount of adsorbed Rh110 also seems to depend strongly on the conditions used for the experiment. Interestingly, when Rh110 is neutrally charged (pH = 7, solution 3), the saturation intensity values are the lowest even though these conditions showed the fastest diffusion (Figure 5H and Figure 6A). This can be explained by the weak attractive electrostatic interactions between the probe and the walls. On the other hand, in the case of solution 1 (pH = 4.3), Rh110 and the silica walls have opposite charges, which results in a higher amount of probe electrostatically adsorbed on the walls after reaching equilibrium. Despite the repulsive electrostatic interactions between the EDL and Rh110 that slow diffusion down (Figure 5F), after long time periods, the Rh110 molecules eventually cross the predominantly positively charged EDL and adsorb on the negatively charged pore walls. If the Debye length is reduced by adding salt (solution 2, pH = 4.3 + NaCl), the interactions with the EDL are substantially reduced and the uptake is accelerated (Figure 5G). Interestingly, the final amount of adsorbed species in this case is even larger than for solution 1 (pH = 4.3). We assume that this is because some regions of the pore space of the particles remain inaccessible when a large EDL is present. This would be the case for regions connected through narrow bottle-necks where the EDL overlap is the highest, impeding Rh110 to access the whole particle void volume. Compared to N_2-physisorption which provides a single BET-surface area for an ensemble of particles, our method, on the other hand, delivers individual particle information. Furthermore, N_2-physisorption provides the accessible surface area under specific (inert) conditions, while our method can be applied under varying probe-host electrostatic interactions and is sensitive to them. This could be potentially exploited to determine the accessible surface area for a specific guest molecule (e.g., differently sized molecules within a catalyst particle). Moreover, the porous silica particles used in this study are, as mentioned above, commonly impregnated with metallocenes as active centers and used as olefin polymerization catalysts[79].

The chemosensitivity of our effective surface area measurements could be used to characterize silica support particles regarding their impregnation potential.
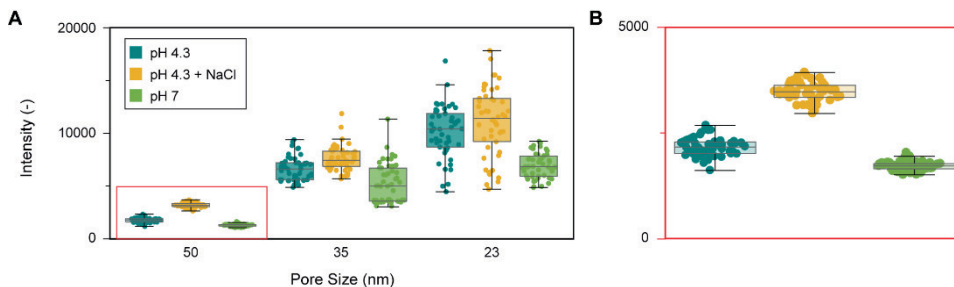
Figure 7: A) Distribution of mean fluorescent intensities of the silica model particles under different conditions after reaching saturation. Smaller pores result in higher saturation intensities, as they imply larger surface areas. At pH = 7, the equilibrium concentrations are the lowest since Rh110(±) is neutrally charged and less attracted to the silica walls. At pH 4.3 silica(-) and Rh110(+) have opposite charges resulting in higher saturation concentrations. Adding salt to the pH = 4.3 solution decreases the Debye length to the point where there is no EDL overlap. Pores connected through narrow bottle-necks with high EDL overlap become accessible as the pore entrance is no longer fully occupied by positively charged ions. Therefore, the total accessible porosity increases compared to the case of pH 4.3. As a result, the available surface area and the saturation concentrations increase as well. **B)** Zoom-in of red rectangle in A). The box plots display the median, the lower and upper quartiles as well as non-outlier minima and maxima.

4.4 Conclusion and Outlook

A novel analytical method to study the accessibility of individual porous particles in a high-throughput fashion was proposed and showcased using reference silica particles. From the conducted experiments, the following conclusions could be drawn: 1) Particles from the same batch showed great heterogeneity in terms of accessibility and number of accessible adsorption sites, which could not have been resolved with traditional bulk analytical methods. 2) The probe-wall electrostatic interactions proved to be of paramount importance for mass transfer and adsorption within mesoporous materials. 3) Therefore, conditions where these interactions are suppressed were employed to probe particles' accessibility as dominated by porosity. The pore-size probing sensitivity of our approach was similar to the one obtained with N_2-physisorption. 4) Evaluating the

saturation intensities proved to be suitable for studying surface area at the single particle level. Contrary to gas-physisorption methods, where the results are independent of the surface chemistry, our method can be used to study the changes in accessible surface area as a function of the probe-host interactions, which could be used to study catalyst support impregnation. 5) Two linearized uptake curve parameters were found to be relevant for this kind of experiment: the accessibility index and the saturation intensity. The y-axis intercept, typically reported in mass transfer studies, proved to be redundant, as it strongly correlated with the accessibility index. Our validated method should be used to conduct uptake experiments using different probes and complex porous materials. Moreover, modifications to the microfluidic device can be made in order to make it compatible with organic solvents, expanding the application to the use of hydrophobic dyes and particles.

4

4.5 Materials and Methods

4.5.1 Chip fabrication

The microfluidic devices were obtained by standard photolithography as previously reported by Vollertsen et al.[1]. For the fabrication of flow layers, we first used SU8 to generate rectangular channels (~48 µm high) in the areas without valves, while AZ40XT (MicroChemicals, Germany) was employed to form ~35 µm high channels with a rounded profile. For the sections with valves, such rounded channels are needed to ensure effective sealing without any leaks.

The chips were fabricated by multilayer soft lithography. A mixture of PDMS (RTV615, Permacol, The Netherlands) base and curing agent was used to form the flow (7:1 w/w base to curing agent) and control layers (20:1 w/w base to curing agent). The mixed PDMS was then degassed for an approximate duration of 2 hours. The PDMS was then degassed for ~ 2 h. For the creation of the control layer, a PDMS layer with a thickness of approximately 30 µm was developed using spin-coating. The flow layer was obtained by directly pouring PDMS onto the mold. Both wafers were cured at 60°C for 45 min. Upon cooling, the PDMS flow layer was removed from the wafer and the inlets and outlets were obtained by using a 1 mm hole puncher. The SiO_2 particles (SUNSPERA, AGC Si-Tech Co., Ltd) were manually deposited in the chip chamber of the flow layer by using a needle (SEIRIN J-type needle No.3) and a stereomicroscope (Olympus). Due to the sticky nature of PDMS, once placed on the layer the particles don't move. After the deposition of the particles on the flow layer, it was aligned on the control wafer, and the layers were cured overnight at 60°C. The chip was cut from the wafer and a 0.75 mm biopsy puncher was used to create the control inlet. The final step consists of bonding the chip to a microscope glass slide using a plasma cleaner (model CUTE, Femto Science, South Korea).

The valves of the microfluidic chip were driven by pneumatic actuation. The channel of the control layer was filled with water and pressurized with air (1.5 bar) by solenoid valves (Festo, Netherlands), controlled via a custom LabView program.

4.5.2 Uptake experiments

For the uptake experiments, the chip chambers were first filled with deionized water (PURELAB flex) so that the particles were soaked in the solvent. Rhodamine 110 Chloride (Sigma Aldrich) 100 µM in deionized water was used as fluorescent solution at pH 4.3 (solution 1) and ionic strength $1.3 \cdot 10^{-4}$ mol/L. Higher ionic strength ($9.4 \cdot 10^{-3}$ mol/L) of solution 2 and 3 was obtained by adding respectively NaCl (Sigma Aldrich) 0.01M as supporting electrolyte and NaOH (Sigma Aldrich) 0.01M to adjust the pH to 7. The solutions were injected from the inlet by using a pressure pump (Fluigent, Germany) regulating the flow from a fluid reservoir to the flow layer. After that, the chambers were closed by pressurizing the valve and the chip channels were filled with a fluorescent solution of Rhodamine 110 Chloride (Sigma Aldrich) 100 µM by using a bypass channel. Once the solution was uniformly present in the channels, the chambers were opened and filled with it. For image acquisition, a fluorescence microscope (Leica DMi 5000M) equipped with a Hamamatsu ORCA-Flash4.0 camera was used with a pE300ultra LED illumination system (CoolLED, U.K.). The fluorescent dye was excited with the blue LED light (450 nm center wavelength) combined with a BGR filter cube (dichroic mirror: 510 nm). The latter features an excitation band at 495 ± 7.5 nm and emission band at 530 ± 15 nm. The images were acquired every minute using the MicroManager microscope control software[80]. For the pH and conductivity measures, a Mettler Toledo SevenMulti Lab Meter was used.

4

4.6 References

1.   Kärger, J. & Ruthven, D. M. Diffusion in nanoporous materials: Fundamental principles, insights and challenges. *New J. Chem.* **40**, 4027–4048 (2016).

2.   Chmelik, C. & Kärger, J. In situ study on molecular diffusion phenomena in nanoporous catalytic solids. *Chem. Soc. Rev.* **39**, 4864–4884 (2010).

3.   Kärger, J., Chmelik, C., Heinke, L. & Valiullin, R. A new view of diffusion in nanoporous materials. *Chemie Ing. Tech.* **82**, 779–804 (2010).

4.   Jonker, R.J., O'connor, P., Wijngaards, H.N.J. Method and Apparatus for Measuring the Accessibility of Porous Materials with Regard to Large Compounds. U.S. Patent US2002187555A1, 2004.

5.   Cauda, V., Mühlstein, L., Onida, B. & Bein, T. Tuning drug uptake and release rates through different morphologies and pore diameters of confined mesoporous silica. *Microporous Mesoporous Mater.* **118**, 435–442 (2009).

6.   Andersson, J., Rosenholm, J., Areva, S. & Lindén, M. Influences of Material Characteristics on Ibuprofen Drug Loading and Release Profiles from Ordered Micro- and Mesoporous Silica Matrices. *Chem. Mater.* **16**, 4160–4167 (2004).

7.   Rainer, D. R., Rautiainen, E. & Imhof, P. Novel lab-scale deactivation method for FCC catalyst: Inducing realistic accessibility responses to iron poisoning. *Appl. Catal. A Gen.* **249**, 69–80 (2003).

8.   Psarras, A. C., Iliopoulou, E. F., Nalbandian, L., Lappas, A. A. & Pouwels, C. Study of the accessibility effect on the irreversible deactivation of FCC catalysts from contaminant feed metals. *Catal. Today* **127**, 44–53 (2007).

9.   Buurmans, I. L. C. & Weckhuysen, B. M. Heterogeneities of individual catalyst particles in space and time as monitored by spectroscopy. *Nat. Chem.* **4**, 873–886 (2012).

10.   Velthoen, M. E. Z., Meeldijk, J. D., Meirer, F. & Weckhuysen, B. M. Intra- and Interparticle Heterogeneities in Solid Activators for Single-Site Olefin Polymerization Catalysis as Revealed by Micro-Spectroscopy. *Chem. - A Eur. J.* **24**, 11944–11953 (2018).

11.   Buurmans, I. L. C. Ruiz-Martínez, J., Knowles, W. V van der Beek, Bergwerff, J. A., Vogt, E. T. C., Weckhuysen, B. M. Catalytic activity in individual cracking catalyst particles imaged throughout different life stages by selective staining. *Nat. Chem.* **3**, 862–867 (2011).

12.   Sato, T. & Nakatani, K. Analysis of distribution and intraparticle diffusion of a fluorescent dye in mesoporous silica gel by confocal fluorescence microspectroscopy. *Anal. Sci.* **33**, 179–183 (2017).

13.   Qian, Q. Ruiz-Martínez, J., Mokhtar, M., Asiri, A. M., Al-Thabaiti, S. A., Basahel, S. N., Van Der Bij, H. E., Kornatowski, J., Weckhuysen, B. M. Single-particle spectroscopy on large SAPO-34 crystals at work: Methanol-to-olefin versus ethanol-to-olefin processes. *Chem. - A Eur. J.* **19**, 11204–11215 (2013).

14.   Gartmann, N. & Brühwiler, D. Controlling and Imaging the Functional-Group Distribution on Mesoporous Silica. *Angew. Chemie Int. Ed.* **48**, 6354–6356 (2009).

15.   Whiting, G. T., Nikolopoulos, N., Nikolopoulos, I., Chowdhury, A. D. & Weckhuysen, B. M. Visualizing pore architecture and molecular transport boundaries in catalyst bodies with fluorescent nanoprobes. *Nat. Chem.* **11**, 23–31 (2019).

16.   Gallagher, S. H., Schlauri, P., Cesari, E., Durrer, J. & Brühwiler, D. Silica particles with fluorescein-labelled cores for evaluating accessibility through fluorescence quenching by copper. *Nanoscale Adv.* **3**, 6459–6467 (2021).

17.   Chmelik, C., Gläser, R., Haase, J., Hwang, S. & Kärger, J. Application of microimaging to diffusion studies in nanoporous materials. *Adsorption* **27**, 819–840 (2021).

18.   Kortunov, P. Chmelik, C., Kärger, J., Rakoczy, R. A., Ruthven, D. M., Traa, Y., Vasenkov, S., Weitkamp, J. Sorption kinetics and intracrystalline diffusion of methanol in ferrierite: An example of disguised kinetics. *Adsorption* **11**, 235–244 (2005).

19.   Mitchell, S., Michels, N. L., Kunze, K. & Pérez-Ramírez, J. Visualization of hierarchically structured zeolite bodies from macro to nano length scales. *Nat. Chem.* **4**, 825–831 (2012).

20.   Zečević, J., Gommes, C. J., Friedrich, H., Dejongh, P. E. & Dejong, K. P. Mesoporosity of zeoliteY: Quantitative three-dimensional study by image analysis of electron tomograms. *Angew. Chemie - Int. Ed.* **51**, 4213–4217 (2012).

21.   Friedrich, H., De Jongh, P. E., Verkleij, A. J. & De Jong, K. P. Electron tomography for heterogeneous catalysts and related nanostructured materials. *Chem. Rev.* **109**, 1613–1629 (2009).

22.   Díaz, I., Alfredsson, V. & Sakamoto, Y. Transmission electron microscopy in formation and growth of ordered mesoporous materials. *Curr. Opin. Colloid Interface Sci.* **11**, 302–307 (2006).

23.   Midgley, P. A. & Dunin-Borkowski, R. E. Electron tomography and holography in materials science. *Nat. Mater.* **8**, 271–280 (2009).

24.   Gommes, C. J., Friedrich, H., Wolters, M., De Jongh, P. E. & De Jong, K. P.

4

Quantitative characterization of pore corrugation in ordered mesoporous materials using image analysis of electron tomograms. *Chem. Mater.* **21**, 1311–1317 (2009).

25.   De Winter, D. A. M., Meirer, F. & Weckhuysen, B. M. FIB-SEM Tomography Probes the Mesoscale Pore Space of an Individual Catalytic Cracking Particle. *ACS Catal.* **6**, 3158–3167 (2016).

26.   Bossers, K. W. Valadian, R.*,* Zanoni, S., Smeets, R.*,* Friederichs, N.*,* Garrevoet, J.*,* Meirer, F.*,* Weckhuysen, B. M. Correlated X-ray Ptychography and Fluorescence Nano-Tomography on the Fragmentation Behavior of an Individual Catalyst Particle during the Early Stages of Olefin Polymerization. *J. Am. Chem. Soc.* **142**, 3691–3695 (2020).

27.   Liu, Y., Meirer, F., Krest, C. M., Webb, S. & Weckhuysen, B. M. Relating structure and composition with accessibility of a single catalyst particle using correlative 3-dimensional micro-spectroscopy. *Nat. Commun.* **7**, 1–8 (2016).

28.   Meirer, F., Kalirai, S., Morris, D., Soparawalla, S., Liu, Y., Mesu, G., Andrews, J. C., Weckhuysen, B. M.Life and death of a single catalytic cracking particle. *Sci. Adv.* **1**, e1400199 (2015).

29.   Veselý, M. Valadian, R., Lohse, L. M., Toepperwien, M., Spiers, K., Garrevoet, J., Vogt, E. T. C., Salditt, T., Weckhuysen, B. M., Meirer, F. 3-D X-ray Nanotomography Reveals Different Carbon Deposition Mechanisms in a Single Catalyst Particle. *ChemCatChem* **13**, 2494–2507 (2021).

30.   da Silva, J. C., J. C., Mader, K., Holler, M., *et al.* Assessment of the 3 D Pore Structure and Individual Components of Preshaped Catalyst Bodies by X-Ray Imaging. *ChemCatChem* **7**, 413–416 (2015).

31.   Mayorga-González, R., Rivera-Torrente, M., Nikolopoulos, N., Bossers, K. W., Valadian, R., Yus, J., Seoane, B., Weckhuysen, B. M., Meirer, F. Visualizing defects and pore connectivity within metal-organic frameworks by X-ray transmission tomography. *Chem. Sci.* **12**, 8458–8467 (2021).

32.   Bassim, N. D., De Gregorio, B.T., Kilcoyne, A.L.D., Scott, K., Chou, T., Wirick, S., Cody, G., Stroud, R.M. Minimizing damage during FIB sample preparation of soft materials. *J. Microsc.* **245**, 288–301 (2012).

33.   Zabilska, A., Clark, A. H., Ferri, D., Nachtegaal, M., Kröcher, O., Safonova, O. V Beware of beam damage under reaction conditions: X-ray induced photochemical reduction of supported VO x catalysts during in situ XAS experiments. *Phys. Chem. Chem. Phys.* **24**, 21916–21926 (2022).

34.   Nieuwelink, A. Vollenbroek, J. C., Ferreira De Abreu, A. C., Tiggelaar, R. M., Van Den Berg, A., Odijk, M., Weckhuysen, B. M. Single catalyst particle

diagnostics in a microreactor for performing multiphase hydrogenation reactions. *Faraday Discuss.* **229**, 267–280 (2021).

35. Solsona, M., Nieuwelink, A. E., Meirer, F., Abelmann, L., Odijk, M., Olthuis, W., Weckhuysen, B. M., van den Berg, A. Magnetophoretic Sorting of Single Catalyst Particles. *Angew. Chemie - Int. Ed.* **57**, 10589–10594 (2018).

36. Broccoli, A. Vollertsen, A. R., Roels, P., van Vugt, A., van den Berg, A., Odijk, M. Nanoparticle Printing for Microfluidic Applications: Bipolar Electrochemistry and Localized Raman Sensing Spots. *Micromachines* **14**, 453 (2023).

37. Vollertsen, A. R., De Boer, D., Dekker, S., Wesselink, B. A. M., Haverkate, R. Rho, H. S., Odijk, M. Modular operation of microfluidic chips for highly parallelized cell culture and liquid dosing via a fluidic circuit board. *Microsystems Nanoeng.* **6**, 107 (2020).

38. Haneveld, J., Tas, N. R., Brunets, N., Jansen, H. V. & Elwenspoek, M. Capillary filling of sub- 10 nm nanochannels. *J. Appl. Phys.* **104**, (2008).

39. Do, D. D. *Adsorption analysis: Equilibria and kinetics*. (World Scientific, 1998).

40. Klein, G. Principles of adsorption and adsorption processes. *Reactive Polymers, Ion Exchangers, Sorbents* **4**, 62 (1985).

41. Brandani, S. Kinetics of liquid phase batch adsorption experiments. *Adsorption* **27**, 353–368 (2021).

42. Weber, B. W. J. Proceedings of the American Society of Civil Engineers. **89**, 31–59 (1963).

43. Wu, F. C., Tseng, R. L. & Juang, R. S. Initial behavior of intraparticle diffusion model used in the description of adsorption kinetics. *Chem. Eng. J.* **153**, 1–8 (2009).

44. Teixeira, R. N. P., Sousa Neto, V. O., Oliveira, J. T., Oliveira, T. C., Melo, D. Q., Silva, M. A. A., Nascimento, R. F. Study on the use of roasted barley powder for adsorption of cu2+ ions in batch experiments and in fixed-bed columns. *BioResources* **8**, 3556–3573 (2013).

45. Pholosi, A., Naidoo, E. B. & Ofomaja, A. E. Intraparticle diffusion of Cr(VI) through biomass and magnetite coated biomass: A comparative kinetic and diffusion study. *South African J. Chem. Eng.* **32**, 39–55 (2020).

46. Ali, H. E., Nasef, S. M. & Gad, Y. H. Remediation of Astrazon blue and Lerui acid brilliant blue dyes from waste solutions using amphoteric superparamagnetic nanocomposite hydrogels based on chitosan prepared by gamma rays. *Carbohydr. Polym.* **283**, (2022).

47. Hashem, A. & El-Khiraigy, K. Bioadsorption of Pb (II) onto Anethum

graveolens from contaminated wastewater: Equilibrium and Kinetic studies. J. Environ. Prot. (Irvine,. Calif). 04, 108–119 (2013).

48. Largitte, L. & Pasquier, R. A review of the kinetics adsorption models and their application to the adsorption of lead by an activated carbon. Chem. Eng. Res. Des. 109, 495–504 (2016).

49. Özcan, A. S. & Özcan, A. Adsorption of acid dyes from aqueous solutions onto acid-activated bentonite. *J. Colloid Interface Sci.* **276**, 39–46 (2004).

50. Özcan, A. & Özcan, A. S. Adsorption of Acid Red 57 from aqueous solutions onto surfactant-modified sepiolite. *J. Hazard. Mater.* **125**, 252–259 (2005).

51. Kannan, N. & Sundaram, M. M. Kinetics and mechanism of removal of methylene blue by adsorption on various carbons - A comparative study. *ye. Pigment.* **51**, 25–40 (2001).

52. El Mouzdahir, Y., Elmchaouri, A., Mahboub, R., ElAnssari, A., Gil, A., Korili, S. A., Vicente, M. A.Interaction of stevensite with Cd2+ and Pb2+ in aqueous dispersions. *Appl. Clay Sci.* **35**, 47–58 (2007).

53. Önal, Y. Kinetics of adsorption of dyes from aqueous solution using activated carbon prepared from waste apricot. *J. Hazard. Mater.* **137**, 1719–1728 (2006).

54. Akmil-Başar, C., Önal, Y., Kiliçer, T. & Eren, D. Adsorptions of high concentration malachite green by two activated carbons having different porous structures. *J. Hazard. Mater.* **127**, 73–80 (2005).

55. Lorenc-Grabowska, E. & Gryglewicz, G. Adsorption of lignite-derived humic acids on coal-based mesoporous activated carbons. *J. Colloid Interface Sci.* **284**, 416–423 (2005).

56. El-Khaiary, M. I. Kinetics and mechanism of adsorption of methylene blue from aqueous solution by nitric-acid treated water-hyacinth. *J. Hazard. Mater.* **147**, 28–36 (2007).

57. Çiçek, F., Özer, D., Özer, A. & Özer, A. Low cost removal of reactive dyes using wheat bran. *J. Hazard. Mater.* **146**, 408–416 (2007).

58. Singh, K. K., Rastogi, R. & Hasan, S. H. Removal of cadmium from wastewater using agricultural waste 'rice polish'. *J. Hazard. Mater.* **121**, 51–58 (2005).

59. Huo, M. X. Jin, Y. L., Sun, Z. F., Ren, F., Pei, L., Ren, P. G. Facile synthesis of chitosan-based acid-resistant composite films for efficient selective adsorption properties towards anionic dyes. *Carbohydr. Polym.* **254**, (2021).

60. Yang, Y., Lin, X., Wei, B., Zhao, Y. & Wang, J. Evaluation of adsorption potential of bamboo biochar for metal-complex dye: Equilibrium, kinetics and artificial neural network modeling. *Int. J. Environ. Sci. Technol.* **11**, 1093–1100 (2014).

61.   Medley, J. A. & Andrews, M. W. The Effect of a Surface Barrier on Uptake Rates of Dye into Wool Fibers. *Text. Res. J.* **29**, 398–403 (1959).

62.   Cheung, W. H., Szeto, Y. S. & McKay, G. Intraparticle diffusion processes during acid dye adsorption onto chitosan. *Bioresour. Technol.* **98**, 2897–2904 (2007).

63.   Sze, M. F. F. & McKay, G. An adsorption diffusion model for removal of para-chlorophenol by activated carbon derived from bituminous coal. *Environ. Pollut.* **158**, 1669–1674 (2010).

64.   Alexander, F., Poofs, V. J. P. & McKay, G. Adsorption Kinetics and Diffusional Mass Transfer Processes during Color Removal from Effluent Using Silica. *Ind. Eng. Chem. Process Des. Dev.* **17**, 406–410 (1978).

65.   Sun, Q. & Yang, L. The adsorption of basic dyes from aqueous solution on modified peat-resin particle. *Water Res.* **37**, 1535–1544 (2003).

66.   Özer, D., Dursun, G. & Özer, A. Methylene blue adsorption from aqueous solution by dehydrated peanut hull. *J. Hazard. Mater.* **144**, 171–179 (2007).

67.   Weber, W. J. & Morris, J. C. Closure to "Kinetics of Adsorption on Carbon from Solution". *J. Sanit. Eng. Div.* **89**, 53–55 (1963).

68.   Beija, M., Afonso, C. A. M. & Martinho, J. M. G. Synthesis and applications of rhodamine derivatives as fluorescent probes. *Chem. Soc. Rev.* **38**, 2410–2433 (2009).

69.   Gendron, P. O., Avaltroni, F. & Wilkinson, K. J. Diffusion coefficients of several rhodamine derivatives as determined by pulsed field gradient-nuclear magnetic resonance and fluorescence correlation spectroscopy. *J. Fluoresc.* **18**, 1093–1101 (2008).

70.   Blom, H., Hassler, K., Chmyrov, A. & Widengren, J. Electrostatic interactions of fluorescent molecules with dielectric interfaces studied by total internal reflection fluorescence correlation spectroscopy. *Int. J. Mol. Sci.* **11**, 386–406 (2010).

71.   Behrens, S. H. & Grier, D. G. The charge of glass and silica surfaces. *J. Chem. Phys.* **115**, 6716–6721 (2001).

72.   Sen, T. & Barisik, M. Internal surface electric charge characterization of mesoporous silica. *Sci. Rep.* **9**, 1–9 (2019).

73.   Kosmulski, M. The pH dependent surface charging and points of zero charge. VIII. Update. *Adv. Colloid Interface Sci.* **275**, 102064 (2020).

74.   Bo, Z., McCullough, L. R., Dull, S., Ardagh, M. A., Wang, J., Notestein, J. Strong electrostatic adsorption of Pt onto SiO_2 partially overcoated Al_2O_3 - Towards single atom catalysts. *J. Chem. Phys.* **151**, (2019).

75.   Plecis, A., Schoch, R. B. & Renaud, P. Ionic transport phenomena in

4

nanofluidics: Experimental and theoretical study of the exclusion-enrichment effect on a chip. *Nano Lett.* **5**, 1147–1155 (2005).

76. Wu, H., Wang, D. & Schwartz, D. K. Connecting Hindered Transport in Porous Media across Length Scales: From Single-Pore to Macroscopic. *J. Phys. Chem. Lett.* **11**, 8825–8831 (2020).

77. Wu, H., Sarfati, R., Wang, D. & Schwartz, D. K. Electrostatic Barriers to Nanoparticle Accessibility of a Porous Matrix. *J. Am. Chem. Soc.* **142**, 4696–4704 (2020).

78. Alemdaroglu, F. E., Wang, J., Börsch, M., Berger, R. & Herrmann, A. Enzymatic control of the size of DNA block copolymer nanoparticles. *Angew. Chemie - Int. Ed.* **47**, 974–976 (2008).

79. Bolner, F. M., Blazzio, Y. R., Lara, B. R., Machado, F. & McKenna, T. F. L. Impact of silica pore structure on the performance of metallocene catalysts in ethylene gas-phase polymerization. *Can. J. Chem. Eng.* **101**, 4819–4831 (2023).

80. Edelstein, A. D. et al. Advanced methods of microscope control using µManager software. J. Biol. Methods 1, e10 (2014).

4.7 Supporting Information

1. Microfluidic Device

4
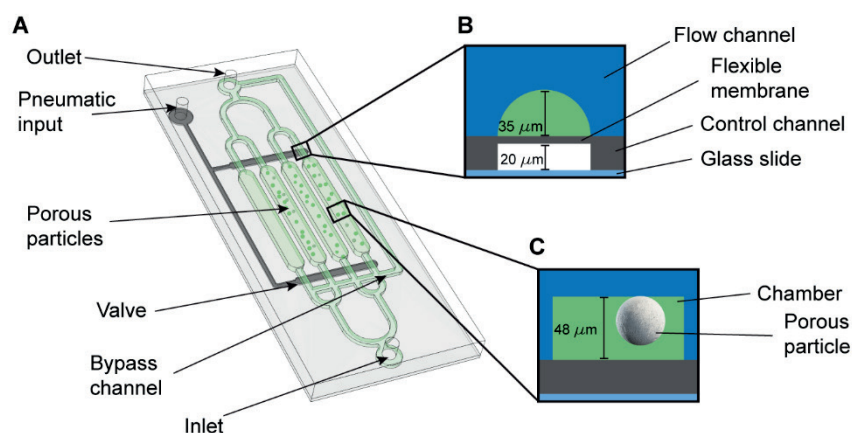
Figure S1: **A)** Schematic and **B, C)** cross-section of the microfluidic device used for the uptake experiments. **A)** shows the chip 4 chambers: one is empty and used as a reference chamber while the other 3 are filled with porous particle samples. The bypass channel is used to purge the channels without contaminating the chambers when switching liquids. **B)** Valve cross-section in open configuration. The channels in the flow layer are shown in green, while the control layer channel is shown in white. The rounded profile of the flow channel is needed to ensure the closing of the valve without leaking. **C)** Chamber cross section

showing the position of the particles. Due to the loading procedure and the sticky nature of PDMS, the particles tend to stay attached to the top layer.

2. Uptake Simulations

The concentration profile changes during the uptake process were simulated by solving Fick's second law in spherical coordinates with adsorption (Eq. 1). Therefore, the porous particle was modeled as a pseudo homogenous porous sphere with an internal liquid phase diffusion coefficient D (m²/s), an adsorption coefficient R (1), and an external mass transfer coefficient k (m/s). The uptake process as well as the variables used for the simulation are schematically depicted in Figure S2.

$$\frac{\partial C}{\partial t} = \frac{D}{r^2} \frac{\partial}{\partial r}\left(r^2 \frac{\partial C}{\partial r}\right) - \frac{\partial S}{\partial t} \tag{1}$$

A linear relationship between the adsorbed concentration S (mg/m³) and the concentration C (mg/m³) in the solution was considered, assuming diffusion as a limiting process in the sorption process.

$$S = RC \tag{2}$$

By combining equations (1) and (2) Fick's law can be rewritten to

$$\frac{\partial C}{\partial t} = \frac{D'}{r^2} \frac{\partial}{\partial r}\left(r^2 \frac{\partial C}{\partial r}\right) \tag{3}$$

where D' represents an effective diffusion (including adsorption):

$$D' = \frac{D}{1+R} \tag{4}$$

The initial dye concentration inside the particle's pores C_0 as well as the adsorbed concentration S_0 were assumed to be 0.

$$C = C_0 = 0 \qquad t = 0 \,\forall\, r \tag{5}$$

$$S = S_0 = 0 \qquad t = 0 \,\forall\, r \tag{6}$$

Further, the following conditions were implemented:

1) The molecular flow at both sides of the liquid-solid interface has to be the same (Eq. 7). This boundary condition at $r = R_p$ (particle radius) relates internal and external mass transfer through a positive correlation between the effective diffusion coefficient D' and the external mass transfer

coefficient k. Both of these parameters correlate positively with the accessibility index (Figure 3).

$$D' \left(\frac{\partial C}{\partial r}\right)_{r=R_p} = k \ (C_B - C) \qquad t > 0 \tag{7}$$

where C_B is the concentration in the bulk solution (constant over time) and

2) Due to the symmetry of the system the first derivative of the concentration profile should be zero at the center of the spherical particle.

$$D' \left(\frac{\partial C}{\partial r}\right)_{r=0} = 0 \qquad t > 0 \tag{8}$$

The partial differential equation including the initial and boundary conditions was solved with a homemade Matlab code using the finite difference method:

$$C_i^{n+1} = C_i^n + \frac{D'\Delta t}{\Delta r^2}[C_{i+1}^n - 2C_i^n + C_{i-1}^n] \tag{9}$$

The total probe molecule concentration profile consists of the sum of the concentration in the pore space of the particle (C), and the concentration adsorbed on the pore-walls (S):

$$C_{tot}(r) = S(r) + C(r) \tag{10}$$

This value was integrated over the whole radius of the particle for each time step n and used to calculate the uptake as:

$$q = \frac{(C-C_0)}{m_c}V_s \tag{11}$$

with m_c (g) the sorbent amount and V_s (mL) the volume of the solution. The so-calculated uptake plotted as function of $t^{0.5}$ results in the uptake curve of the particle (Figure 3). According to Eq. 4, if the adsorption increases, the effective diffusion coefficient decreases (steep and persistent concentration gradient). Nevertheless, the overall amount of material taken up by the particle increases (Figure 3C). Increasing D and/or k has the same effect on the accessibility.
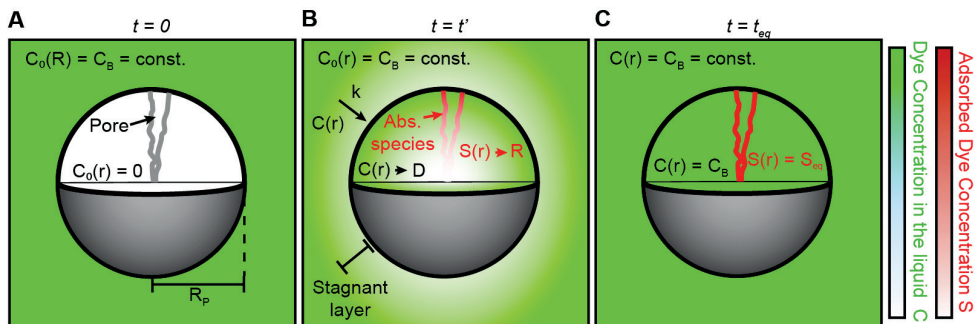
Figure S2: Schematic of the uptake process showing the variables used and assumptions made. **A)** Initial conditions: at the beginning of the process, we assume that the dye concentration outside of the particle is constant, C_B. Within the particle, the adsorbed concentration C_B, as well as the concentration in the liquid phase C0, are assumed to be 0. **B)** Uptake process: The concentration far away from the particle is assumed to be constant C_B. In the vicinity of the particle, a stagnant layer, i.e., a concentration gradient characterized by the external mass transfer coefficient k, is formed. Within the particle, the adsorbed and liquid concentrations are spatially dependent, these concentration profiles are characterized by the internal diffusion coefficient D and the adsorption constant R. **C)** Saturation: there are no concentration gradients on either the liquid or adsorbed phase. Since there are no concentration gradients, there is no driving force for diffusion or adsorption. The particle is in equilibrium and cannot take up more dye.

3. Uptake Curve Parameters

Interestingly, the experimentally obtained accessibility indices and y-axis intercepts are strongly correlated (Figure S3 A, B). Therefore, if one wants to quantify the pore space of a material through uptake experiments, one of these parameters would suffice. Preferably, the accessibility index should be used, as it is positively correlated with pore size, adsorption coefficient, and external mass transfer coefficient and all these parameters result in faster uptake rates as they grow.
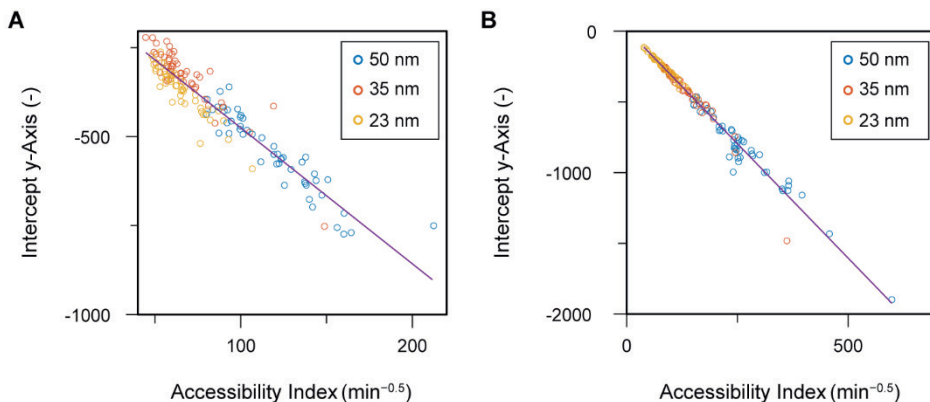
Figure S3: Experimental data- scatter plot to show the correlation of accessibility index and y-axis intercept. **A)** Solution 2 (pH= 4.3; 0.01M NaCl) **B)** Solution 3 (pH = 7). The accessibility index of solution 1 (pH 4.3) could not be calculated because the curves did not show an inflection point (Figure 5F).

4. Characterization of SiO$_2$ particles

Focused Ion Beam Scanning Electron Microscopy (FIB-SEM) and N$_2$ physisorption were performed on the SiO$_2$ particle samples to visualize and check their mesoporosity. Focused Ion Beam Milling Scanning Electron Microscopy (FIB-SEM) was performed on an FEI Helios NanoLab G3 UC microscope. Samples were loaded on Al stubs with carbon tape and sputter-coated with 10 nm of Pt, before the measurement. Beam currents of 0.1 nA and 2 kV were used to image particles with dwell times varying between 1 and 5 µs, depending on the imaging mode. External morphologies were imaged by collecting secondary electrons (SE) with an Everhart–Thornley detector (ETD), while cross-sections were imaged by collecting back scattered electrons (BSE) with a through-the-lens detector (TLD) with a dual scanning electron microscope focused-ion beam. Cross-sections were obtained with a Gallium FIB operating at 2.5 nA for milling, removing half of the particle material. Then, Pt deposition was performed with 0.77 nA for a protective layer on top of the surface of the particle and subsequent cleaning with precision milling operating at 2.5 nA the exposed cross-section. N$_2$ physisorption measurements of the SiO$_2$ particles were performed using a Micromeritics TriStar 3000 instrument operating at −196 °C. Before performing the measurements, the particles were dried for

15h at 200 °C under N_2. The resulting surface area values were 344 m²/g; 439 m²/g; 523 m²/g for the 50, 35, and 23 nm pore size particles, respectively.
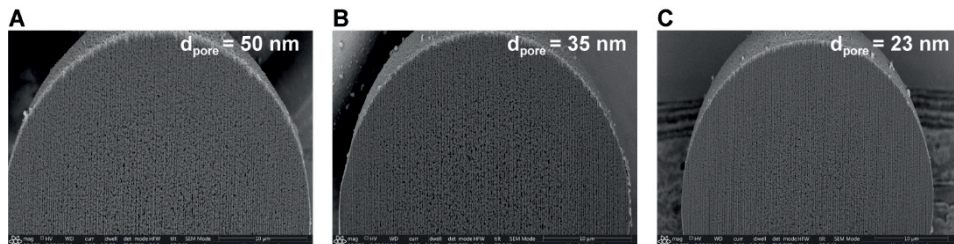
Figure S4: SEM image of FIB-cut particles showing mesopores of the different samples used for the experiments.

5. Calibration curves

To verify the correlation between the dye concentration and the fluorescence intensity both in bulk and in the particles, experiments were performed using solutions of Rhodamine 110 at pH 7 at different concentrations. The measured intensity grew linearly as a function of the concentration, suggesting that the fluorescence intensity can be used as a measure of concentration in the used concentration range.
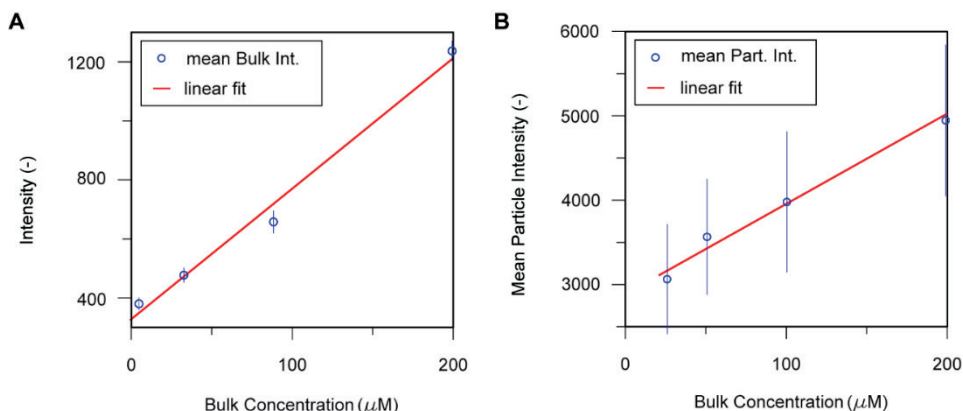
Figure S5: Calibration curves of Rhodamine 110 at pH 7 **A)** in the bulk solutions and **B)** in the particles with 35 nm pore size. In B) the particles were in contact with the solutions at different concentrations until they reached the equilibrium. The measured intensity grew linearly as a function of the bulk solution concentration, suggesting that the fluorescence intensity can be used as a measure of concentration in the used concentration range. The error bars in A) represent the standard deviation of the mean intensity over the 4 chambers

and in B) represent the standard deviation of the mean particle intensity. The number of particles analyzed is ~ 50.

6. Image Processing

The fluorescence microscopy images (Figure S5 A, B) were processed using custom Matlab code. The pixels that correspond to particles are segmented using the Segmentation Editor from ImageJ (Figure S5 C). The mean pixel intensity of each of these regions was calculated for each picture. Figure S5 D shows the intensity changes over $time^{0.5}$ for individual particles of the same batch. Note that the particles that were in contact with the lateral walls of the chambers were excluded from the analysis as their contact surface area with the liquid was reduced.
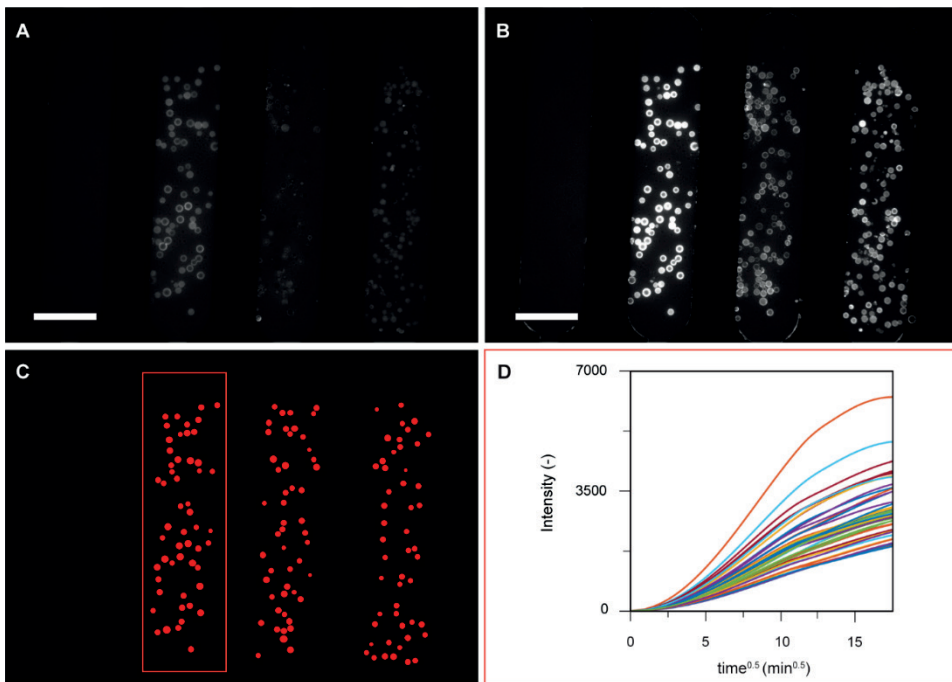
Figure S6: A) Fluorescence microscopy image recorded at the beginning of the uptake process. B) Fluorescence microscopy image recorded after 5 h of uptake displays higher intensities for each particle. C) The pixels that belong to particles were segmented. The mean intensity of each of these regions was calculated for each time. D) Mean intensity changes within the chamber on the left as a function of the $time^{0.5}$. The initial intensity values were subtracted so that the curves begin at an intensity equal to 0. Each uptake curve refers to an individual particle.

7. Reference Chambers and Photostability
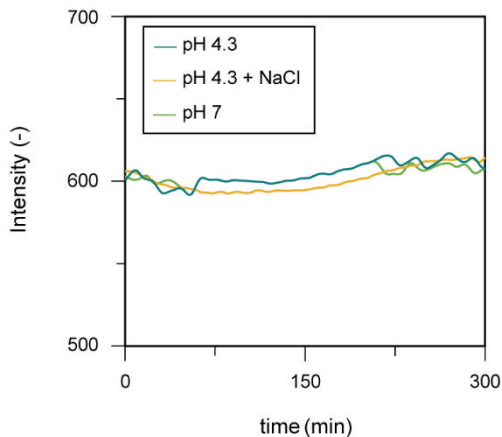
Figure S7: Mean intensities over time of the solutions of Rhodamine 110 used for the uptake experiments as evaluated from the reference chamber. In all the cases, the solutions show photostability within the 5 h of the experiment.

1. Debye length calculation

The Debye length was estimated as follows:

$$\lambda_D = \sqrt{\frac{\varepsilon K_B T}{2e^2 N_A I}}$$

where:

ε is the solvent dielectric constant [F/m]; K_B is the Boltzmann constant [C^2/J·m]; T is the temperature [K], e is the elementary charge [C], N_A is Avogadro's constant [mol^{-1}], and I is the ionic strength [mol/L].

8. Accessibility Index Determination

In order to quantify the speed of the uptake process, many published studies fit a line to a fraction of the uptake-$t^{0.5}$ curve. The resulting slope is used as a parameter to quantify the extent of the internal mass transfer[1,2,3]. Moreover, the intercept with the y-axis is usually used to evaluate the external mass transfer limitations[4]. However, to the best of our knowledge, no publication clarifies how the "linear part" of the curve was chosen.

Performing a linear regression on different, arbitrarily chosen, parts of the curve can lead to different slopes (and y-axis intercepts) on the same dataset. To quantify our data in a systematic way, we determined the inflection point of each uptake- $t^{0.5}$ curve as well as its first derivative. The inflection point tangent was used to replace the linear fit usually used in literature. Figure S8 displays an uptake curve together with its inflection point tangent used to approximate the "linear part of the curve".
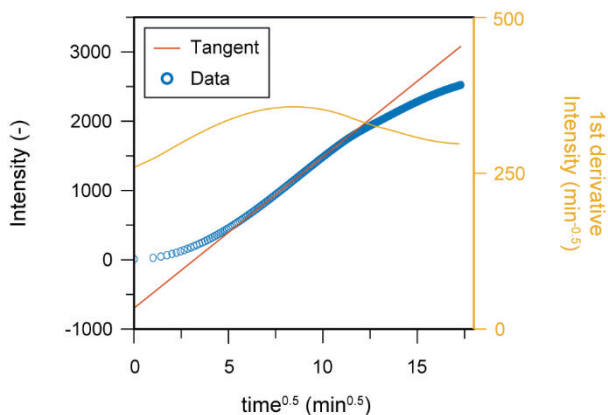
Figure S8: Experimental data of uptake of the solution at pH 7 from one silica particle with 50 nm pores.

Supporting References

1.   Rainer, D. R., Rautiainen, E. & Imhof, P. Novel lab-scale deactivation method for FCC catalyst: Inducing realistic accessibility responses to iron poisoning. *Appl. Catal. A Gen.* **249**, 69–80 (2003).
2.   Psarras, A. C., Iliopoulou, E. F., Nalbandian, L., Lappas, A. A. & Pouwels, C. Study of the accessibility effect on the irreversible deactivation of FCC catalysts from contaminant feed metals. *Catal. Today* **127**, 44–53 (2007).
3.   Connor, P. O. & NI, H. (12) United States Patent. **2**, (2004).
4.   Sze, M. F. F. & McKay, G. An adsorption diffusion model for removal of para-chlorophenol by activated carbon derived from bituminous coal. *Environ. Pollut.* **158**, 1669–1674 (2010).
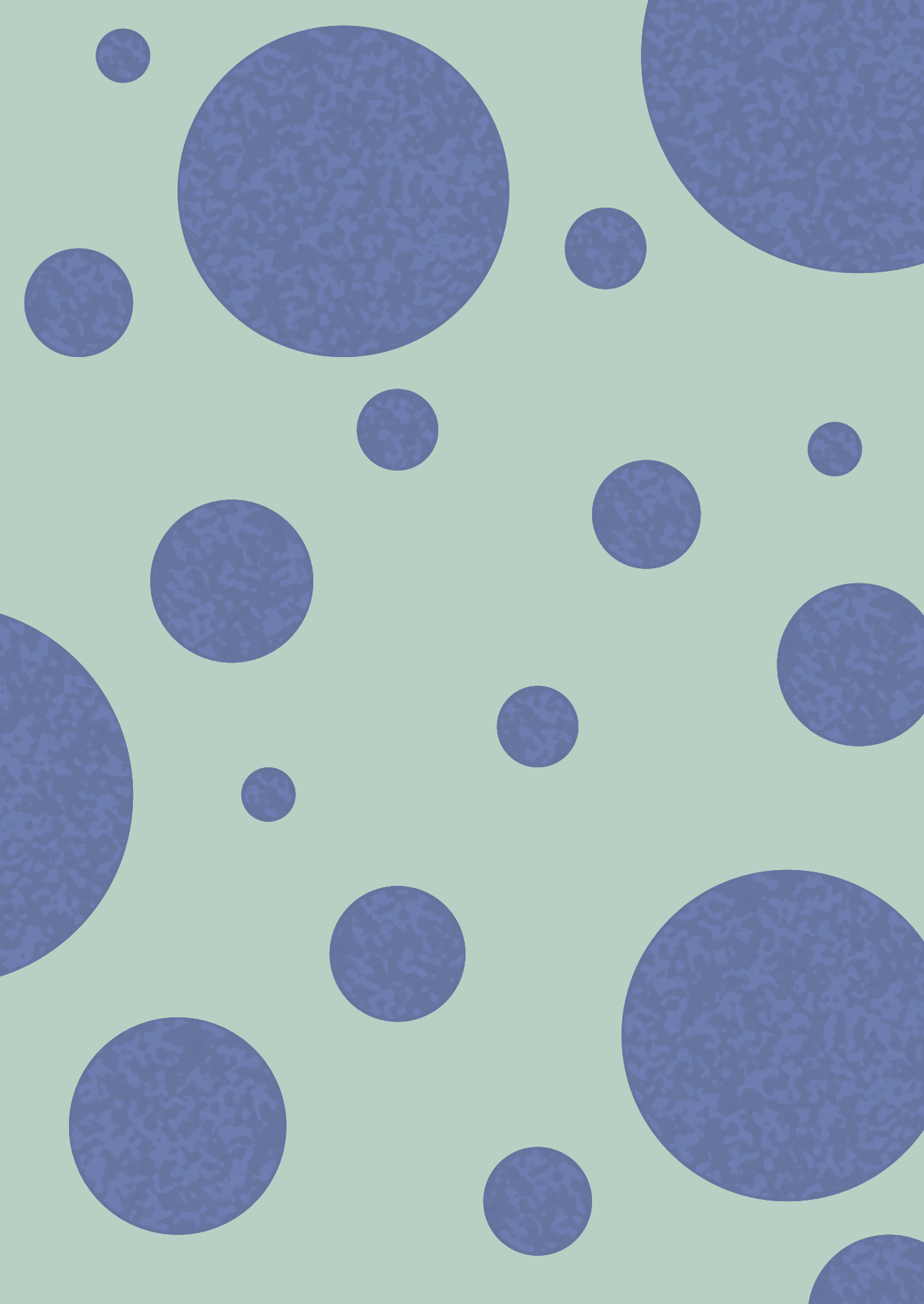
Chapter 5

High-Throughput Device for *In Situ* Studies and at Millisecond Spatiotemporal Resolution of Heterogeneous Catalytic Reactions at the Single Particle Level with Fluorescence Microscopy

Coke formation and deposition on catalyst surfaces are among the most common causes of their deactivation. A thorough understanding of the mechanisms and rate of coke deposition on heterogeneous catalyst particles under or approaching reaction conditions is essential for the prediction of their deactivation and can ultimately lead to the design of more robust and efficient catalysts.

In catalytic cracking of hydrocarbons, coke formation takes place in the initial catalyst-reactant contact, at a time frame below 50 ms. To investigate the process at the single particle level at high throughput, we designed and fabricated a device for *in situ* analysis providing millisecond resolution. The approach consists of using fluorescence microscopy to detect coke formation on the particles by focusing on different locations of the (continuous flow) reactor, which are representative of different residence times.

The device comprises a 3D-printed chamber for storing and releasing the particles, a glass capillary serving as the reaction chamber, and an in-house constructed setup for collecting and converting the particles' fluorescent signals. Preliminary experiments were performed using coked fluid catalytic cracking (FCC) particles with varying degrees of deactivation obtained by reactions with n-hexane for different reaction times. The results show that it is possible to detect and relate signal intensity with catalyst age, suggesting that the approach can provide information on their deactivation by coke formation.

5.1 Introduction

The deposition of carbonaceous species on catalyst particles, commonly referred to as coking, is a well-known cause of catalyst deactivation during industrial processes involving hydrocarbons (e.g. reforming, hydrotreating, or cracking). Coke byproducts are retained on the catalyst particles due to their low volatility, trapping, and adsorption on acid sites[1,2]. These deposits consist of a mixture of hydrocarbon species (high molecular weight polycyclic hydrocarbons, mixtures of aromatic hydrocarbons, methylbenzenes, branched long-chain aliphatics, aliphatic structures,…) and lead to a reduction of catalyst activity and selectivity, due to pore clogging (poisoning) and coverage of the active sites. Usually, this process is reversible and catalyst activity is restored by removing the coke through e.g. oxidation with air (O_2)[3].

Extensive research has been done to understand the coke formation mechanisms[4,5] and kinetic[6,7] at different length scales, to be able to predict catalyst lifetime and optimize the efficiency of catalyst utilization. Particularly, characterization methods focusing on individual catalyst particles revealed detailed information on coke composition and origin. Various techniques such as electron microscopy (EM)[8,9], atom probe tomography (APT)[10], and confocal fluorescence microscopy (CFM)[11,4] have been used to characterize carbon deposits and their distribution on the catalyst at length scales ranging from active sites to individual particles. Recently, X-ray holotomography[12] was also reported to retrieve 3D coke location on single particles at ca. 200 nm resolution. These methods often rely on spent samples and therefore lack temporal information. To be able to study the reaction *in situ,* techniques such as soft X-ray scanning transmission X-ray microscopy (STXM)[13], UV-Vis microspectroscopy[14,15], and Raman spectroscopy[16], together with microreactor technology can provide insights into the dynamic behavior of catalyst particles during the reaction and have been used to study both catalyst activation and deactivation mechanisms.

Although the study at the single-particle level with *in situ* techniques can lead to a detailed understanding of the rate of coke formation and catalyst

lifetime, there is still a loss of speed and statistical relevance. This is of particular importance in the case of systems with large interparticle heterogeneities, where the single-particle analyses could not be representative of the particle population. Therefore, techniques based on single-catalyst particle screening in a high-throughput fashion have been developed to characterize particle activity[17,18] providing statistically relevant results.

Fluid catalytic cracking (FCC) particles represent relevant examples of systems with both inter- and intraparticle heterogeneities[19,20], which has been a topic of extensive research due to their industrial relevance[21-23]. The FCC reaction traditionally represents the main industrial process in the oil refinery to produce gasoline and propylene from vacuum gas oil (VGO) and raw materials for important associated processes (synthesis of MTBE, alkylation, isomerization, etc.) that produce cleaner fuels[24]. Even though society is moving away from fossil fuels, the study of the FCC process is still relevant for the co-processing of alternative sources of fuel or chemical building blocks such as biomass[21] and plastic waste[25], contributing to a more circular society.

During the reaction, long-chain feedstock molecules are cracked into smaller fragments with the use of multicomponent spherical particles with an average diameter of 50-150 μm consisting of catalytically highly active phases (zeolite US-Y or ZSM-5) embedded in a matrix of alumina, silica, and clay. The cracking reaction is an endothermic process, which takes place in a riser reactor in a few seconds at temperatures of ~500 °C. The formed products are then separated from the catalyst using cyclones. During the process, carbonaceous species originating from side reactions can accumulate on the catalyst material[26], thereby reducing bulk accessibility to the active sites and lowering further cracking activity. The catalyst is therefore transported to the regenerator, in which the coke is burned off in an oxygen-rich environment at temperatures above 650 °C, making the catalyst particles available for a consecutive cycle of feedstock cracking. However, these harsh steaming conditions can results also in catalyst deactivation due to dealumination[27] of the embedded zeolite material, thus reducing the amount of acidic sites. Finally, feedstock impurities such as Ni,

5

Fe, V, and nitrogen- and sulfur-containing molecules irreversibly reduce the catalyst performance[28,29] and promote coke formation[30,31].

To preserve the overall activity in the reactor, part of the spent catalyst is constantly removed and replaced with fresh one, leading to a steady state catalyst lifetime distribution and it's called equilibrium catalyst (ECAT).
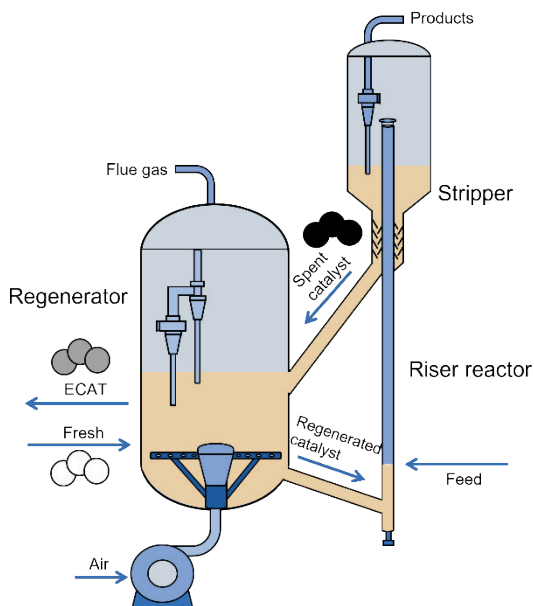
Figure 1: Schematic representation of the fluid catalytic cracking process. During the reaction, the catalyst is subjected to deactivation due to coke deposition and is therefore subjected to continuous regeneration and mixing with fresh catalyst. Image inspired by Vogt and Weckhuysen[21].

Over the years, various methods and approaches both on the bulk and single particle level have been used to investigate the effect of the FCC catalyst deactivation processes. In most cases, two-step cyclic deactivation (CD)[32] and Mitchell impregnation-steam deactivation (MI)[28] are used to mimic the conditions faced by the catalyst during operation. The CD approach is based on cyclic feedstock cracking and regenerations steps, while MI is used to first deposit metals on the catalyst particles via impregnation, followed by steaming of the catalyst. Those *ex-situ* approaches and further catalyst characterization at different stages of their lifetime with microscopic and spectroscopic approaches provided valuable

information on their irreversible deactivation due to metal loading or zeolite dealumination, as well as the location and nature of the deposited coke[33].

At the same time, a large body of literature deals with coke formation[11,25,34,35,36,37] which can occur through a combination of thermal cracking and coking reactions. The coke deposits on the outer surface of the catalyst particle blocking the pores, leading to a gradual decrease in the activity of the catalyst over time. The time scale of coke production on FCC catalyst particles is a crucial factor in determining the efficiency and lifespan of the FCC process. To get a picture of the actual deactivation rates during the direct cracking of hydrocarbons (*in situ*) different reaction systems at the laboratory scale have been proposed.

Reactor designs based on fixed beds[38,39] have been widely used to study the process. However, those systems have the drawback of an unrealistic amount of coke deposited on the catalyst, due to its long exposure to the feedstock[40] and the long catalyst residence time in the reactor leading to the development of temperature and coke profiles along the fixed catalytic bed. This was addressed with a catalytic fixed fluidized bed[41], in which the catalyst bed is fluidized in a gas stream. Also, in this case, the catalyst is exposed to the feed for a long duration, thus far from the conditions the catalyst experience in the commercial units. Down-scaled riser reactors represented the closest approximation to the actual process. Briefly, the designs proposed by Dupain et al.[42] and Corma et al.[40] consisted of coiled reactors of adjustable lengths (by adding or removing sections) in which contact times of seconds could be achieved.

It was shown that the deactivation by coke occurs at a very short time scale, in a time frame below 50 ms[43]. These results are based on the estimation of bulk product yields and catalyst selectivity at different residence times.

To obtain detailed insight into the rate of coke formation within individual FCC catalyst particles at the initial reaction stage, a method with a short acquisition time is needed to capture the carbon deposition, while studying the process under or approaching true reaction conditions. Moreover, depending on the nature of the feed, coke concentration on the catalyst

5

can be low[44] (<1 wt%), thus requiring analysis with high-sensitivity techniques.

With the aim to tackle the challenge of visualizing coke formation on catalyst particles during the process, we propose a method to evaluate *in situ* the activity of particles in heterogeneous gas phase catalytic reactions at the single-particle level at high-throughput and at different reaction times (ms). The approach consists of monitoring the formation of fluorescent coke on the particles during the reaction. The lifetime and progressive deactivation of the particle by coke deposition on the particles is followed with fluorescence-based measurements at different lengths of the reactor, as each position is representative of different residence times.

The system consists of a thin glass tube as the microreactor while releasing single catalyst particles using a 3D printed reservoir and valve, and subsequent falling of the particles down the tube due to gravity (Figure 2). Preliminary results focused on the fabrication of the device and detection setup and their validation. This was obtained by performing *ex situ* n-hexane cracking over FCC particles at 350°C as a model reaction, and the coked particle were analyzed with the developed setup.

5.2 Materials and Methods

5.2.1 Device design

The designed device for controlled particle release (Figure 2, Figure S1) is composed of a 3D printed part with an overall dimension of 40x25x13 mm and is used to store and control the particles' release. A glass capillary (GC15OTF-15, Clark Electromedical Instruments), with an OD of 1.5 mm and ID of 0.86 mm is partially inserted in the device and represents the reaction chamber. A picture of the device is reported in Figure S1. Detection windows along the capillary are representative of different particle residence times.

Carbon deposit formation is thermodynamically favored above 350 °C. Therefore, to obtain the elevated temperature range required from the reaction, the external control via Joule heating[45,46] effect was exploited. Joule heating has the advantage of fast temperature cycling, steep

gradients, and localized heating. By coiling Nichrome resistance wires (30 Ω/m) around the capillary, it can be heated efficiently via the Joule effect by applying a voltage over the extremities of the wires. Nichrome is among the most common resistance wire for heating purposes, due to its high resistivity and resistance to oxidation at high temperatures[47,48]. The simple heaters' design and approach allow for changes in the setup (e.g. position of the detection window, localization, and amount of released heat) without requiring any modification of the device. Nichrome wire was wrapped around the capillary, with spacing 4 mm long between the coils, representing the optical detection windows.

The particle reservoir is a 3D-printed device made up of a flow layer and a control layer. The first one contains a conic-shaped chamber to store the particles, which can be inserted from an inlet with a diameter of 3 mm. The inlet to introduce the gaseous reagent into the reaction system has a diameter of 1.5 mm to be able to connect it to 1/16'' PFA tubing. The channel for the gas crosses the device and intersects the glass capillary in an unheated area so that the reaction takes place in the proximity of the detection window.

The control layer has a pneumatically actuated Viton membrane (thickness 250 µm) to control the release of the particles. The valve design is derived from Quake's poly(dimethyl siloxane) (PDMS) valve design[49] in push-up configuration. These valves typically consist of a three-layer PDMS architecture. The design incorporates two microchannels arranged orthogonally, with a thin elastomeric membrane positioned between them. In operation, one microchannel serves as a control channel. When pressure is applied, it induces deflection of the membrane, leading to the interruption of flow within the orthogonal flow channel. The latter has a half-rounded profile to avoid leaking at the corners. We used a thin elastomeric membrane made of Viton as the actuated element in the valve to control the particle release from the reservoir to the glass capillary. On the control layer, the area where the valve is located includes raised ridges (0.2 mm) to locally clamp the membrane and define the valve geometry. The pneumatic routing is done via the channel through the control layer, shown in Figure 2A.

5

The opening and closing of the membrane are controlled by an external commercially available solenoid valve (Festo, The Netherlands), operated by a custom LabVIEW program (Figure S3). When the control channel is pressurized with 0.5 bar of N_2, the membrane can deform (Figure 2B) and close the chamber containing the particles. Once depressurized, the membrane restores to its undeformed state so that the chamber results open and particles are released in the glass capillary.

Four holes (diameter 3.1 mm) for screws were designed on the device edges, to allow clamping of the flow and control layers and to ensure proper membrane compression and positioning.
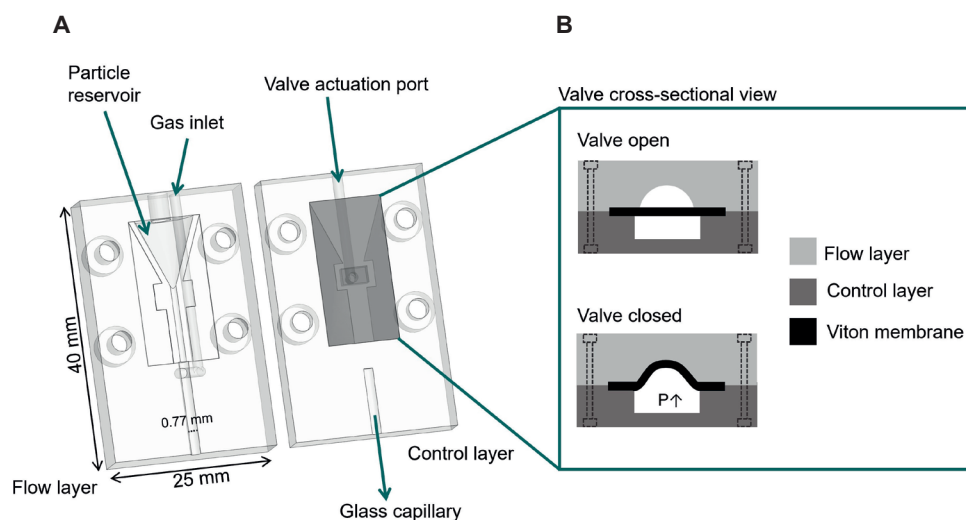
Figure 2: A) Design of the 3D printed part used to store and control the particle release in the glass capillary. The flow layer contains the inlet to introduce the particles in the conic chamber. The grey area represents the valve position. In the control layer, the valve actuation port is connected to the pneumatic actuator, which uses N_2 to control the valve closing and opening. **B)** Schematic side view of the pneumatically actuated push-up valve used to control the particle release.

5.2.1.1 Device holder

To focus and precisely move the device, a holder Figure 3 was fabricated with 3D printing and mounted on a manual linear XYZ stage (Figure S2). The translational stage allowed for movements on the axes with a step size of 10 µm, ensuring vertical stability and accurate control of the capillary

position. The capillary was positioned vertically on the holder in correspondence with the cavity and the device was then laterally fixed on the stage by using screws on two sides. By moving the device along the z-axis, it was possible to focus on different areas of the capillary and thus collect info on coke formation at different reaction stages.
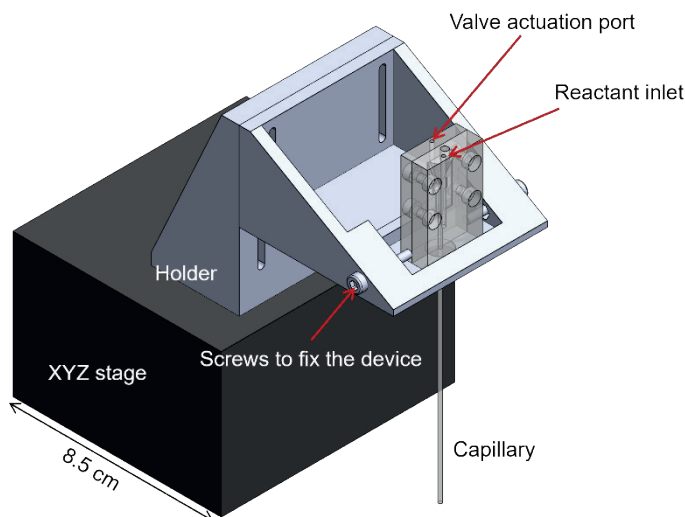
Figure 3: Assembly of the XYZ stage, holder, and device used for the *in situ* experiments. The holder is used to ensure a fixed position of the device and control the movement along the axes for focusing.

5.2.2   Device Fabrication

The 3D-printed device was designed by using SolidWorks and printed in ABS-like clear resin (Elegoo) on an Elegoo Mars 3 printer. The layer thickness was set to 50 µm and both parts were printed by orienting them at 55° with respect to the build platform to obtain flat surfaces to ensure proper clamping between the layers. Supports for printing were generated with the Chitubox software. After the printing, the layers were cleaned in IPA to remove resin residues and the curing step was performed by heating at 60°C and UV exposure for 1h.

250 µm thick Viton membrane was placed on the control layer and the glass capillary was mounted by friction in the designed mold. Clamping screws were tightened until any gaps between the flow and control layers were

seen to disappear. 1/16'' PFA tubing was connected to the reactant inlet on the flow layer, and 1/16'' Tygon® tubing was inserted in the control inlet and hooked up to the solenoid valve on the other end. The valve can switch between pressurized (approximately 0.5 bar relative pressure of N_2) and atmospheric pressure, which can be controlled via an EasyPort USB interface with a custom LabView program.

The capillary outlet was inserted and sealed into a glass vial, to be able to saturate the system with the reactant.

5.2.3 Fluorescence detection setup

The optical detection of the fluorescent particles was performed with an in-house constructed setup, which is based on previous works[17,50].

Figure 4 shows a schematic representation of the fluorescent particle detection system. Upon reaching the detection spot, the particles are excited with an LED light (center wavelength: 470 nm, M470L3, Thorlabs, Munich, Germany) with an optical power of 3.9 mW controlled by an LED driver (LEDD1B, Thorlabs). The emission signal (center wavelength: 600 nm) passed through a 20x objective (20x/0.4 HCX PL FLUOTAR, Leica), a dichroic mirror (DMLP505R, Thorlabs), and a long-pass filter (Edge Basic long wave pass 568, Semrock) to reduce the background signal caused by the scattering from the exciting light. 50% of the signal is then directed via a beam splitter (BS013, Thorlabs) to a Grasshopper 2 camera (FLIR) used to adjust the focus on the detection spot. The remaining 50% of the incoming optical signal is converted into a voltage through a PhotoMultiplier Tube (PMT H7422, Hamamatsu, Herrsching am Ammersee, Germany) and then amplified (10 $V\mu A^{-1}$, C7319, Hamamatsu) with an amplifier. The measurement of the output signal is performed by Analog Discovery 2 (Digilent, sampling rate 100Hz), and for the data readout, a custom MATLAB code was used. Those settings allowed for the detection of signals from single particles.

To be able to assign the signal to the particles passing the detection spot and account for their dimension in the data analysis, these were recorded by using a Photron FASTCAM SA3 camera at 1000 fps.
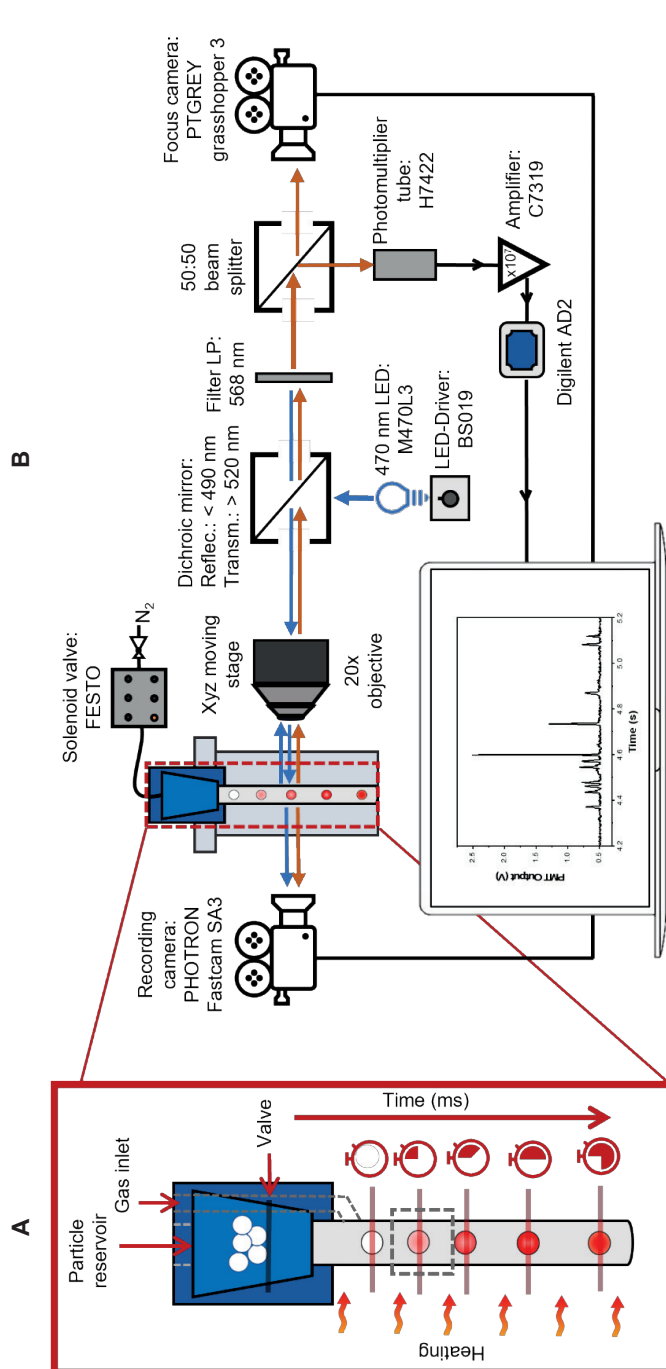
Figure 4: A) Conceptual image of the *in situ* monitoring of coke formation in the reactor. The particles are released in the glass capillary using a 3D-printed reservoir and valve. Upon contact with the reactant at the desired temperature, the reaction is started. The lifetime and progressive deactivation of individual particles by coke formation is imaged at fixed positions down the microreactor. **B)** Schematic of the optical setup used to detect fluorescent signal related to coke formation on the particles. The signal is converted to a voltage and amplified, resulting in a PMT output voltage over time where each peak corresponds to a fluorescent particle passing the detection spot.

5.3 Results and Discussion

5.3.1 Temperature simulation

The experimental setup for temperature control in the capillary, which served as the reaction chamber, involved the use of nichrome resistance wires. Six 8-mm long coiled wires (resistance of ~4Ω) were positioned in close proximity to the capillary, separated by detection windows of 2 mm. Efficient and localized heating was obtained via the Joule effect, induced by the application of a voltage at the wires.

To estimate the order of magnitude of the power needed to heat up the fluid in the capillary at the desired temperature (above 350°C) and the resulting temperature profile along the capillary, a simulation was performed using the Heat Transfer in Solids and Fluids module COMSOL Multiphysics®. The simulation was set up in an axisymmetric geometry, enabling the 2D modeling of the system's behavior. No bulk flow of the fluid in the capillary was assumed. Further details on the simulation are reported in the SI 5. The simulation result (Figure 5) shows the temperature profile inside the glass capillary. By considering a power of 0.6 W for each electrode, the temperature is in the range of 360-430°C, in agreement with the temperature needed for the reaction.
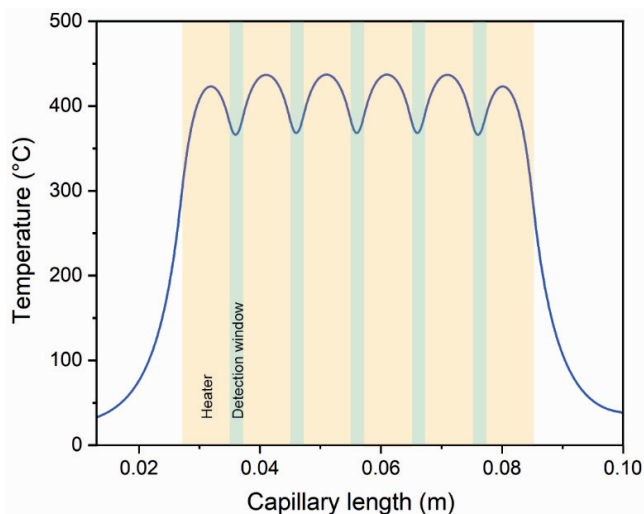
Figure 5: Temperature profile along the capillary vertical axis as obtained from the simulation performed using the Heat Transfer in Solids and Fluids module COMSOL Multiphysics®.

To experimentally calibrate the output temperature with different applied voltages, a thermocouple was inserted in the capillary in close proximity to a detection window. The heaters were connected in parallel and actuated by applying a potential difference (0.5, 0.75, 1, 1.25, 1.5 V) via an Agilent E3631A power supply. The temperature variations were monitored by means of a digital readout connected to the thermocouple. The power dissipated from each electrode was calculated from the total current and resistances:

$$i_n = \frac{i_{tot}}{6} \tag{5}$$

$$P = R \cdot i^2 \tag{6}$$
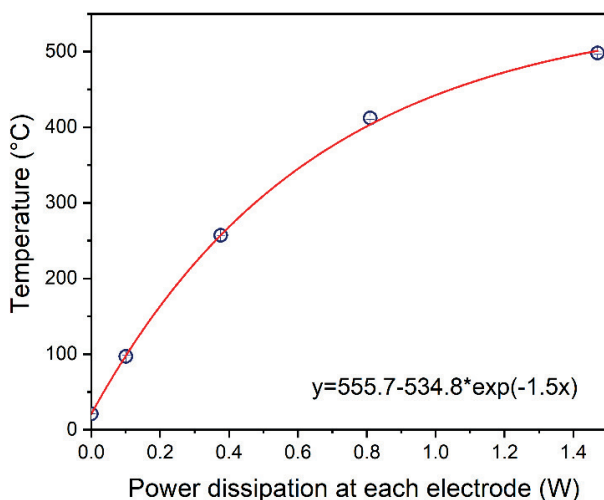
Figure 6: Correlation between the registered temperature in the capillary and the power dissipated at each electrode. For each applied voltage, the temperature measurements were repeated 3 times after cooling down the device.

An empirical exponential fit was used to estimate the power dissipated at different temperatures (Figure 6). Particularly, a power of 0.6 W resulted in a temperature of 345°C, which is close to the simulated temperature obtained at the detection window (360°C). The difference can be ascribed to variations in the thermal properties of the materials used in the experimental setup.

5.3.2 *Ex situ* reactions

The capability of the setup to detect particle fluorescence while passing the detection spot was tested by using catalyst particles with different amounts of coke. Those samples were obtained performing ex situ hexane cracking, used as a model reaction to mimic catalytic coke formation in (calcined) FCC Ecat particles. The particles were first calcined in air for 4h at 600°C with a ramp rate of 5°C per minute to guarantee the elimination of carbon deposits in the catalyst without compromising its internal structure or causing any phase changes. Then, they were sieved to a size range of 38-75 μm (Figure S4), which resulted in a theoretical terminal velocity distribution of the particles in free fall in the capillary ranging from 0.11-0.41 m/s (calculated using Stoke's law[51]). The actual particle velocities were determined by recording and tracking the particles in free fall along the capillary (Figure S5), resulting in velocities in the range of 0.05-0.7 m/s. This disparity in particle velocity enabled the single-particle diagnostic approach, as in most cases particles reach the detection spot at different times. This ensured that each particle's fluorescence signal could be recorded and analyzed separately, allowing for precise and accurate data collection.

To obtain information on particles at different reaction stages, the cracking was performed over four sample batches and stopped at different times. Next, each sample was characterized by using the described fluorescent detection setup to check any difference in their signals. Briefly, four samples of 35 mg of catalyst particles were preheated to 350°C. Each sample was then put in contact with 10μL of n-Hexane and the reaction was quenched respectively after ~0.5, 1, 2, and 5 s, obtaining particles of different reaction times and thus the amount of coke. Each of the samples was then introduced in the 3D printed device and released in the capillary, and the signal from the different particle batches was collected with the detection setup.

Figure 4B shows an example of the voltage peaks over time, observed when fluorescent particles pass the detection spot. Particles reached the detection spot by means of gravity, resulting in an average rate of ~19 particles per second. To ensure that the signals can be attributed to

individual particles and also to normalize their dimensions during data analysis, movies are recorded simultaneously to match the frames containing a particle with the recorded voltage signals.

Figure 7 shows the signals collected by checking the catalyst particles with different amounts of coke. In all the cases, it is possible to distinguish the particles' average signal from the background intensity value, which has an average value of 0.50197 and it's reported in the graph as a dashed line. The results suggest that the approach can be used to perform the reaction *in situ* and to detect the formation of fluorescent coke in time.
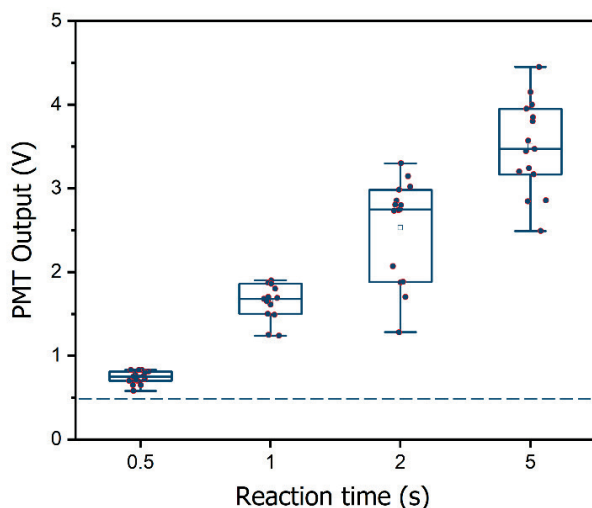
Figure 7: PMT output voltage of FCC Ecat particles that reacted with n-hexane for 0.5, 1, 2, and 5 s. In all of the cases, the signals are above the noise level. For longer reaction times, the signals result due to the higher amount of coke formed on the particles.

Particles with a longer reaction time show a higher signal, which is directly related to a higher amount of coke formed. Moreover, the standard deviation of the signals increases with the reaction time, suggesting that the inter-particle heterogeneity[20] plays a role at longer reaction stages, in which activity variations are related to a different amount of byproducts.

5.4 Conclusion and Outlook

To be able to study the deactivation process due to coke formation on catalyst particles at the single particle level and at different residence times,

we designed and fabricated a microreactor to detect the coke formation on particles *in situ* at a high-throughput rate of ~19 particles s^{-1} with millisecond timescale resolution. The device allows the performing of gas-phase catalytic reactions in a glass capillary, and a controlled release of particles. The amount of coke formed at initial reaction times can be evaluated through fluorescence-based measurements of individual particles, thus allowing for the study of deactivation kinetic and inter-particle heterogeneity.

N-hexane cracking was performed as a model reaction to showcase the method. The preliminary experiments showed that it is possible to detect and relate signal intensity with individual particles. Moreover, the higher amount of coke formed during longer reaction times resulted in a clear correlation between the signal intensity and catalyst age, suggesting that the method can be used to obtain information on catalyst deactivation rates by coke formation. Further, the proposed device and experimental setup could be used to assess calcination efficiency - a crucial process for catalyst activity restoration. Various factors, including temperature and duration, can impact calcination effectiveness, and this apparatus can offer real-time monitoring of signal changes throughout the procedure, enabling valuable insights into catalyst regeneration and interparticle heterogeneity post-calcination, elucidating how particle features affect the catalyst's regeneration. This information could inform the design of catalysts with superior deactivation resistance and enhanced regeneration efficiency.

The approach will be used in future work to study the cracking reaction *in situ*, using the reaction setup reported below.

The hexane cracking reaction setup was built by connecting the device to the gas line as schematically reported in Figure 8. The gas pressure and flow rate of the gas line were regulated by means of a pressure reducer and a mass flow controller respectively. All these components were connected via 1/8'' stainless steel gas lines. A gas bubbler containing 2 mL of n-hexane was mounted in an appropriate clamp stand, close to the reactor. Prior to the *in situ* reaction, the system can be saturated with N_2 and afterward with the reactant by connecting the inlet to a gas bubbler. Two gas lines connect the N_2 either to the bubbler or directly to the device by using 3-way valves

for the switch. The route to the reactant inlet on the device was obtained by using 1/16″ PFA tubing (Idex).

Components:
1. Nitrogen gas bottle
2. Pressure reducer
3. 2- ways ball valve
4. Mass Flow Controller
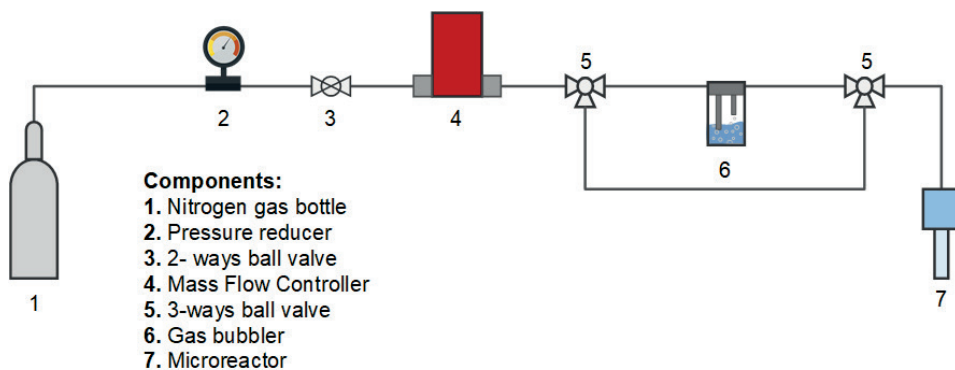5. 3-ways ball valve
6. Gas bubbler
7. Microreactor

Figure 8: Schematic of hexane cracking experiments. A pressure regulator and a flow meter control the N_2 in the gas line. N_2 is used to transport the hexane from the bubbler to the reactor.

5.5 References

1.   Cerqueira, H. S., Ayrault, P., Datka, J. & Guisnet, M. Influence of coke on the acid properties of a USHY zeolite. *Microporous Mesoporous Mater.* **38**, 197–205 (2000).

2.   Hopkins, P. D. *et al.* Acidity and cracking activity changes during coke deactivation of ultrastable Y zeolite. *Appl. Catal. A Gen.* **136**, 29–48 (1996).

3.   Trimm, D. L. The regeneration or disposal of deactivated heterogeneous catalysts. *Appl. Catal. A Gen.* **212**, 153–160 (2001).

4.   Gao, S. *et al.* Insight into the deactivation mode of methanol-to-olefins conversion over SAPO-34: Coke, diffusion, and acidic site accessibility. *J. Catal.* **367**, 306–314 (2018).

5.   Towfighi, J., Sadrameli, M. & Niaei, A. Coke formation mechanisms and coke inhibiting methods in pyrolysis furnaces. *J. Chem. Eng. Japan* **35**, 923–937 (2002).

6.   Wiehe, I. A. A Phase-Separation Kinetic Model for Coke Formation. *Ind. Eng. Chem. Res.* **32**, 2447–2454 (1993).

7.   Moustafa, T. M. & Froment, G. F. Kinetic modeling of coke formation and deactivation in the catalytic cracking of vacuum gas oil. *Ind. Eng. Chem. Res.* **42**, 14–25 (2003).

8.   Zhang, H., Shao, S., Xiao, R., Shen, D. & Zeng, J. Characterization of coke deposition in the catalytic fast pyrolysis of biomass derivates. *Energy and Fuels* **28**, 52–57 (2014).

9.   Wang, H. Z. *et al.* Coke Formation on Pt-Sn/Al2O3 Catalyst for Propane Dehydrogenation. *Ind. Eng. Chem. Res.* **57**, 8647–8654 (2018).

10.   Schmidt, J. E. *et al.* Coke Formation in a Zeolite Crystal During the Methanol-to-Hydrocarbons Reaction as Studied with Atom Probe Tomography. *Angew. Chemie - Int. Ed.* **55**, 11173–11177 (2016).

11.   Ruiz-Martínez, J. *et al.* Microspectroscopic insight into the deactivation process of individual cracking catalyst particles with basic sulfur components. *Appl. Catal. A Gen.* **419–420**, 84–94 (2012).

12.   Veselý, M. *et al.* 3-D X-ray Nanotomography Reveals Different Carbon Deposition Mechanisms in a Single Catalyst Particle. *ChemCatChem* **13**, 2494–2507 (2021).

13.   van Ravenhorst, I. K. *et al.* Capturing the Genesis of an Active Fischer–Tropsch Synthesis Catalyst with Operando X-ray Nanospectroscopy. *Angew. Chemie - Int. Ed.* **57**, 11957–11962 (2018).

14.   Mores, D., Kornatowski, J., Olsbye, U. & Weckhuysen, B. M. Coke formation during the methanol-to-olefin conversion: In situ microspectroscopy on

individual H-ZSM-5 crystals with different brønsted acidity. *Chem. - A Eur. J.* **17**, 2874–2884 (2011).

15. Suarnaba, E. G. T., Lee, Y. F., Yamada, H. & Tagawa, T. Ultraviolet-Visible (UV-Vis) Microspectroscopic System Designed for the in Situ Characterization of the Dehydrogenation Reaction over Platinum Supported Catalytic Microchannel Reactor. *Appl. Spectrosc.* **70**, 1806–1812 (2016).

16. Kuba, S. & Knözinger, H. Time-resolved in situ Raman spectroscopy of working catalysts: Sulfated and tungstated zirconia. *J. Raman Spectrosc.* **33**, 325–332 (2002).

17. Nieuwelink, A. E. *et al.* High-throughput activity screening and sorting of single catalyst particles with a droplet microreactor using dielectrophoresis. *Nat. Catal.* **4**, 1070–1079 (2021).

18. Vollenbroek, J. C. *et al.* Droplet microreactor for high-throughput fluorescence-based measurements of single catalyst particle acidity. *Microsystems Nanoeng.* **9**, 39 (2023).

19. Qie, Z. *et al.* Multiscale investigation of pore network heterogeneity and permeability of fluid catalytic cracking (FCC) particles. *Chem. Eng. J.* **440**, 135843 (2022).

20. Nieuwelink, A. E. *et al.* Single Particle Assays to Determine Heterogeneities within Fluid Catalytic Cracking Catalysts. *Chem. Eur. J.* **26**, 8546–8554 (2020).

21. Vogt, E. T. C. & Weckhuysen, B. M. Fluid catalytic cracking: recent developments on the grand old lady of zeolite catalysis. *Chem. Soc. Rev.* **44**, 7342–7370 (2015).

22. Bai, P. *et al.* Fluid catalytic cracking technology: current status and recent discoveries on catalyst contamination. *Catal. Rev. - Sci. Eng.* **61**, 333–405 (2019).

23. Meirer, F. *et al.* Life and death of a single catalytic cracking particle. *Sci. Adv.* **1**, 1–13 (2015).

24. Passamonti, F. J., de la Puente, G. & Sedran, U. Laboratory evaluation of FCC commercial catalysts. Analysis of products of industrial importance. *Catal. Today* **133**–**135**, 314–318 (2008).

25. Vollmer, I., Jenks, M. J. F., Mayorga González, R., Meirer, F. & Weckhuysen, B. M. Plastic Waste Conversion over a Refinery Waste Catalyst. *Angew. Chemie - Int. Ed.* **60**, 16101–16108 (2021).

26. Zhang, Y. S. *et al.* Fine structural changes of fluid catalytic catalysts and characterization of coke formed resulting from heavy oil devolatilization.

5

Appl. Catal. B Environ. **263**, 118329 (2020).

27.   Xu, B., Bordiga, S., Prins, R. & van Bokhoven, J. A. Effect of framework Si/Al ratio and extra-framework aluminum on the catalytic activity of Y zeolite. *Appl. Catal. A Gen.* **333**, 245–253 (2007).

28.   Mitchell, B. R. Metal Contamination of Cracking Catalysts. 1. Synthetic Metals Deposition on Fresh Catalysts. *Ind. Eng. Chem. Prod. Res. Dev.* **19**, 209–213 (1980).

29.   Liu, Y., Meirer, file:///C:/Users/Rafael/Desktop/PhD/literature/liu2016. pdfFloria., Krest, C. M., Webb, S. & Weckhuysen, B. M. Relating structure and composition with accessibility of a single catalyst particle using correlative 3-dimensional micro-spectroscopy. *Nat. Commun.* **7**, 1–8 (2016).

30.   Tangstad, E., Andersen, A., Myhrvold, E. M. & Myrstad, T. Catalytic behaviour of nickel and iron metal contaminants of an FCC catalyst after oxidative and reductive thermal treatments. *Appl. Catal. A Gen.* **346**, 194–199 (2008).

31.   Xu, M., Liu, X. & Madon, R. J. Pathways for Y Zeolite Destruction: The Role of Sodium and Vanadium. *J. Catal.* **207**, 237–246 (2002).

32.   Psarras, A. C., Iliopoulou, E. F., Kostaras, K., Lappas, A. A. & Pouwels, C. Investigation of advanced laboratory deactivation techniques of FCC catalysts via FTIR acidity studies. *Microporous Mesoporous Mater.* **120**, 141–146 (2009).

33.   Cerqueira, H. S., Sievers, C., Joly, G., Magnoux, P. & Lercher, J. A. Multitechnique Characterization of Coke Produced during Commercial Resid FCC Operation. 2069–2077 (2005).

34.   Jolly, S., Saussey, J., Bettahar, M. M., Lavalley, J. C. & Benazzi, E. Reaction mechanisms and kinetics in the n-hexane cracking over zeolites. *Appl. Catal. A Gen.* **156**, 71–96 (1997).

35.   Bleken, F. L. *et al.* Catalyst deactivation by coke formation in microporous and desilicated zeolite H-ZSM-5 during the conversion of methanol to hydrocarbons. *J. Catal.* **307**, 62–73 (2013).

36.   Guisnet, M. & Magnoux, P. Organic chemistry of coke formation. *Appl. Catal. A Gen.* **212**, 83–96 (2001).

37.   Qian, K. *et al.* Coke formation in the fluid catalytic cracking process by combined analytical techniques. *Energy and Fuels* **11**, 596–600 (1997).

38.   Sedran, U. A. Laboratory testing of fcc catalysts and hydrogen transfer properties evaluation. *Catal. Rev.* **36**, 405–431 (1994).

39.   Moorehead, E. L., McLean, J. B. & Cronkright, W. A. Chapter 7 Microactivity Evaluation of FCC Catalysts in the Laboratory: Principles, Approaches and

Applications. *Stud. Surf. Sci. Catal.* **76**, 223–255 (1993).

40.   Corma, A., Martínez, C., Melo, F. V., Sauvanaud, L. & Carriat, J. Y. A new continuous laboratory reactor for the study of catalytic cracking. *Appl. Catal. A Gen.* **232**, 247–263 (2002).

41.   Vieira, R. C., Pinto, J. C., Biscaia, E. C., Baptista, C. M. L. A. & Cerqueira, H. S. Simulation of catalytic cracking in a fixed-fluidized-bed unit. *Ind. Eng. Chem. Res.* **43**, 6027–6034 (2004).

42.   Dupain, X., Makkee, M. & Moulijn, J. A. Optimal conditions in fluid catalytic cracking: A mechanistic approach. *Appl. Catal. A Gen.* **297**, 198–219 (2006).

43.   Den Hollander, M. A., Makkee, M. & Moulijn, J. A. Fluid catalytic cracking (FCC): Activity in the (milli)seconds range in an entrained flow reactor. *Appl. Catal. A Gen.* **187**, 3–12 (1999).

44.   Schuurman, Y., Delattre, C., Pitault, I., Reymond, J. P. & Forissier, M. Effect of coke deposition on transport and sorption in FCC catalysts studied by temporal analysis of products. *Chem. Eng. Sci.* **60**, 1007–1017 (2005).

45.   Selva, B., Marchalot, J. & Jullien, M. C. An optimized resistor pattern for temperature gradient control in microfluidics. *J. Micromechanics Microengineering* **19**, (2009).

46.   Vigolo, D., Rusconi, R., Piazzaa, R. & Stone, H. A. A portable device for temperature control along microchannels. *Lab Chip* **10**, 795–798 (2010).

47.   Shannon, F. A. & Werler, J. E. Report on a Small Collection of Amphibians from Veracruz, with a Description of a New Species of Pseudoeurycea. *Herpetologica* **11**, 81–85 (1955).

48.   Im, D. H., Yoon, T. W., Min, W. S. & Hong, S. J. Fabrication of planar heating chuck using nichrome thin film as heating element for pecvd equipment. *Electron.* **10**, (2021).

49.   Melin, J. & Quake, S. R. Microfluidic large-scale integration: The evolution of design rules for biological automation. *Annu. Rev. Biophys. Biomol. Struct.* **36**, 213–231 (2007).

50.   Van Den Brink, F. T. G. *et al.* A miniaturized push-pull-perfusion probe for few-second sampling of neurotransmitters in the mouse brain. *Lab Chip* **19**, 1332–1343 (2019).

51.   Hartman, M. & Yates, J. G. Free-Fall of Solid Particles through Fluids. *Collect. Czechoslov. Chem. Commun.* **58**, 961–982 (1993).

5

5.6 Supporting Information

1. Picture of the device for the particle release
2. Fluorecence detection setup
3. Labview program
4. Velocity of particles in free fall
5. Simulationof heat transfer in the capillary
6. Estimation of heat transfer to the particle traveling in the capillary

1. 3D printed device
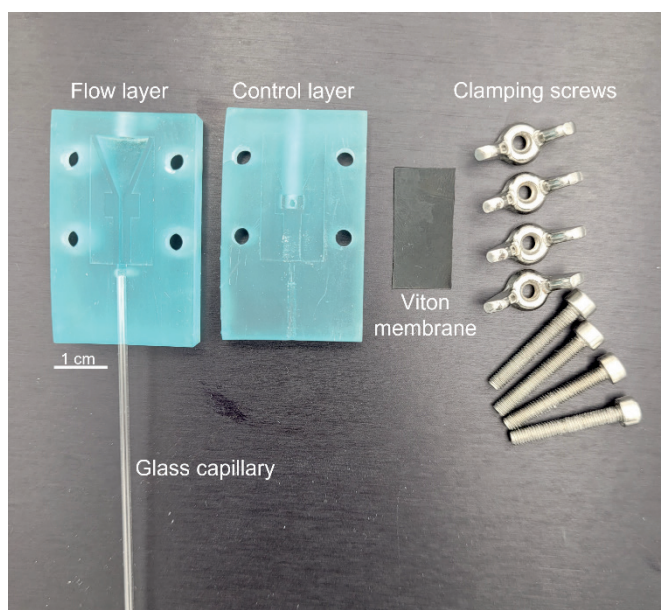
Figure S1: Picture of the 3D printed device used for the controlled release of the particles in the glass capillary.

2. Fluorescence detection setup
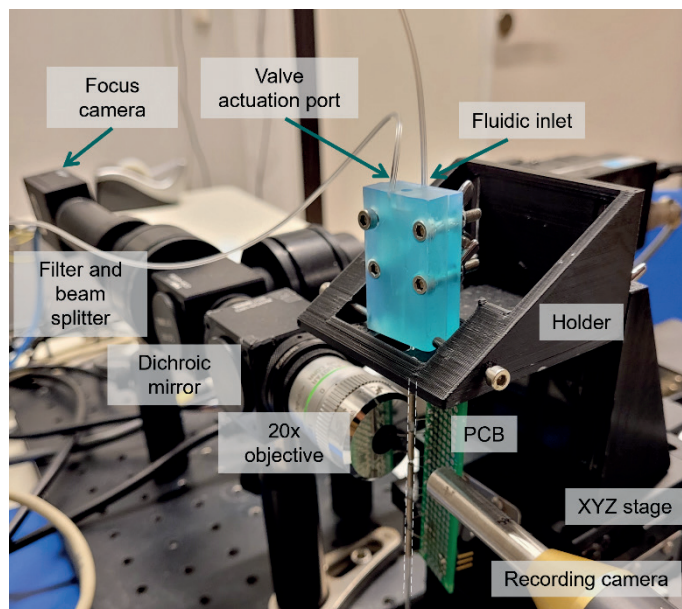
Figure S2: Picture of the fluorescence detection setup showing the focus camera, the filter, beam splitter and dichroic mirror for the emitted light detection. The device is shown in its holder, placed on a XYZ stage.

3. Labview program

The valve in the control layer was actuated mechanically by N_2 pressure. The control channel of the chip was connected to solenoid valves which switch between high and atmospheric pressure, whereby compressed N_2 is used as a high-pressure source. As the valve opens, the particles fall into the glass capillary and a Photron high-speed camera and PFV software were used to record movies from the particles as they reach the detection spot. Both the valve opening and camera triggering were controlled by a custom LabView program.

5
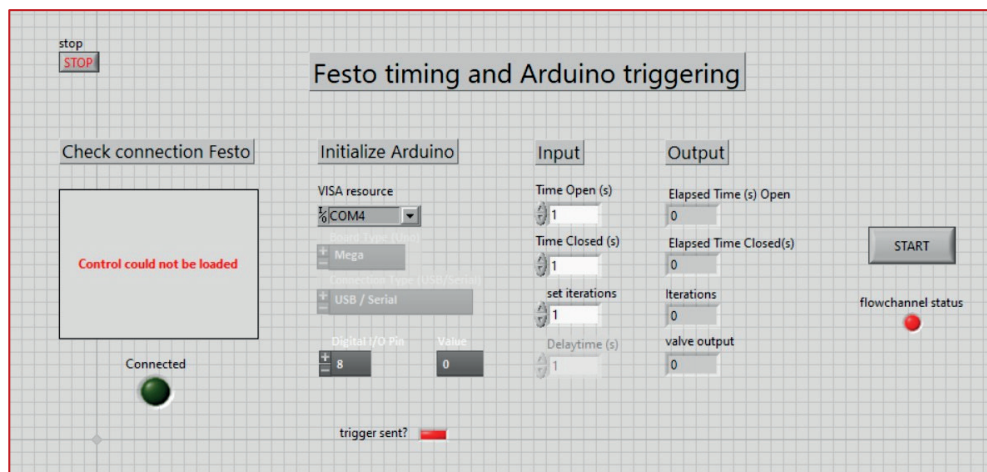
Figure S3: Graphical user interface of the custom LabView program to control the valve and the camera triggering and recording.

4. Velocity of particles in free fall

FCC ECAT particle size distribution of a 38-75 μm sieved fraction (300 particles in total) was determined by analyzing microscopy images using Image J. Particle diameter was evaluated by assuming a spherical shape, which is not always the case for ECAT. This results in the presence of some outliers, as shown in the box plot, and the median particle diameter is ~60 μm.
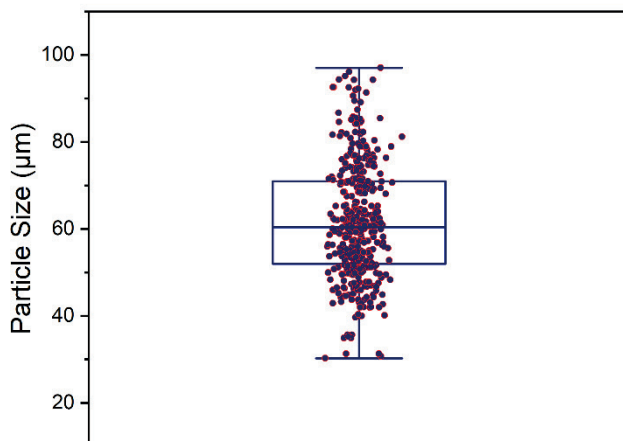
Figure S4: Boxplot of the FCC ECAT particle size distribution of the 38-75 μm sieved fraction. The sample contained 300 particles and the median value was 60.4 μm.
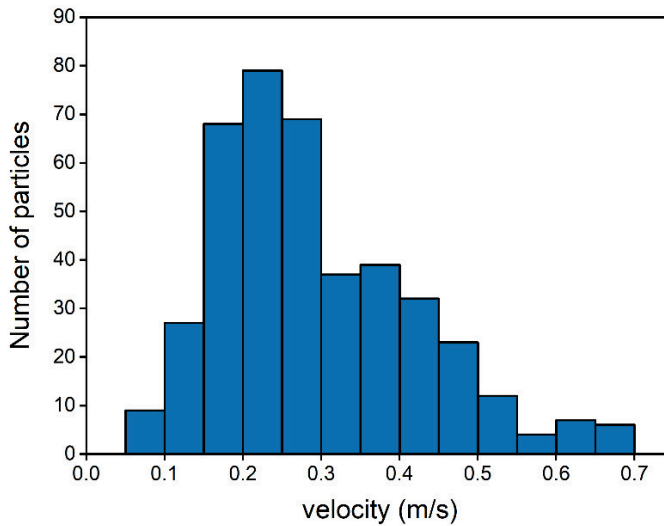
Figure S5: Histogram showing the FCC ECAT velocity distribution of the 38-75 µm sieved fraction.

The same sample used to evaluate particle size distribution was then inserted in the device to check the velocity of particles in free fall in the capillary. Movies were recorded at 1000 frames per second, with a travel length in the capillary of 5mm. A Matlab script for particle tracking was used to estimate the particle size and obtain the mean value for the particle velocity.

5. Simulation of heat transfer in the capillary

The power required for heating the capillary to temperatures above 350°C and the resulting temperature profile were simulated by using the Heat Transfer in Solids and Fluids module in COMSOL Multiphysics®. The simulation was configured with an axisymmetric 2D model.

5
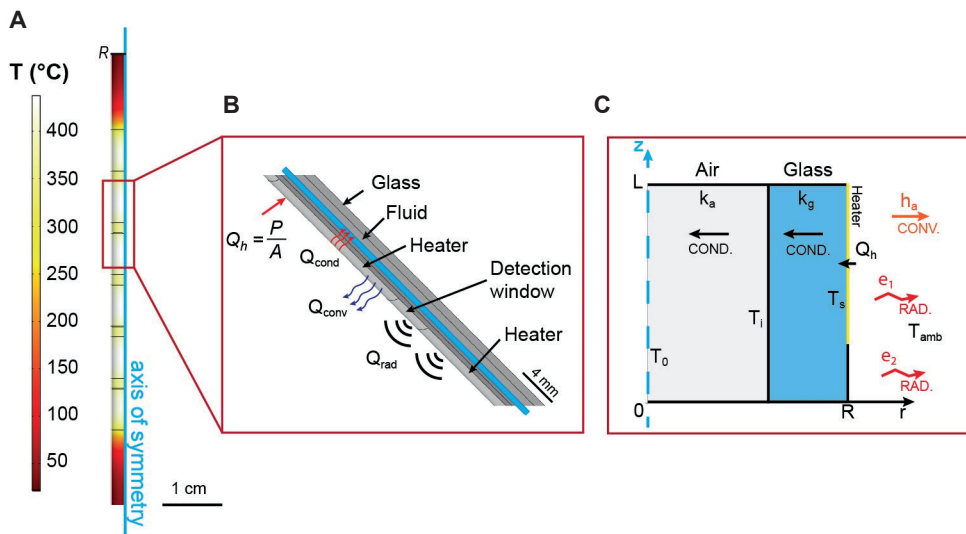
Figure S6: A) Simulated temperature profile along the glass capillary by considering a power of 0.6 W on the Nichrome heaters. **B)** Zoomed-in image of the capillary showing the geometry and materials used in the simulation. The input heaters' power is 0.6 W. **C)** Schematic of heat transfer through the system with boundary conditions.

The heat flux is the outflow of heat normal to the surface area. Assuming a stationary state and no bulk fluid flow within the capillary, the heat transfer within the system is governed by:

$$\nabla \cdot \mathbf{q} = Q \tag{1}$$

$$\mathbf{q} = -k\nabla T \tag{2}$$

Eq. 1 derives from the law of conservation of thermal energy in the specific case uder consideration, in which the rate of change of thermal energy ($\nabla \cdot \mathbf{q}$) equals the overall heat flux through the boundary (Q [W/m²]). Eq. 2 refers to the conduction through the system where k [W/m·K] represents the thermal conductivity of the materials, i.e. glass (k_g= 1.38 W/m·K) and air ($k_a(T) = -0.002 + 1.155 \cdot 10^{-4} * T - 7.903 * 10^{-8} * T^2 + 4.11702505 * 10^{-11} * T^3 - 7.439 * 10^{-15} * T^4$ W/m · K) confined in the capillary, in which the heat transfer occurs in series. These k values are obtained from the material library of Comsol. ∇T [K/m] is the temperature gradient.

The model was solved by considering the initial temperature of the system equal to the ambient temperature (T_{amb} = 293.15K), and the following boundary conditions:

$$\nabla \cdot \mathbf{q}|_{r=R} = Q_h = \frac{P}{A} \tag{3}$$

$$\nabla \cdot \mathbf{q}|_{r=R} = Q_{conv} = h(T_{amb} - T) \tag{4}$$

$$\nabla \cdot \mathbf{q}|_{r=R} = Q_{rad} = \varepsilon\sigma(T_{amb}^4 - T^4) \tag{5}$$

Nichrome elements were modeled as heat sources, and Eq. 3 represents the resulting heat rate Q_h as the ratio between the heater power P [W] and surface area A [m²]. Eq. 4 and 5 refer to convection and radiation at the capillary external wall R, in which h is the heat transfer coefficient of air [10 W/(m²·K)], T_{amb} (293.15K) and T are the temperatures outside and inside the device in [K]. εh=0.89, and ε=0.7 are the surface emissivities of nichrome and glass respectively, σ=5.67·10⁻⁸ W/m²°C ⁴ is the Stefan-Boltzmann constant.

6. Estimation of heat transfer to the particle traveling in the capillary

To estimate the time needed for the particle to heat up to the internal capillary mean temperature $T_a = 400°C$, the energy balance of the system was considered[1]:

$$\rho_p V_p C_p dT = h_a A_p (T_a - T)dt \tag{6}$$

Here, V_p [m³] and A_p [m²] are the volume and surface area of the spherical particle, respectively, which is assumed to have a diameter of 60 µm; and ρ_p [kg/m³] and C_p [J/kg·K] are the density and the specific heat capacity of the material of the sphere (silica); h_a [W/(m²·K)] is the heat transfer coefficient of air. Assuming that the particle is initially at room temperature and in free fall in hot air at 400°C (T_a) with a mean velocity of 0.25 m/s, the resulting Reynolds number Re approaches zero. In this case, the Nusselt number Nu is:

$$Nu = \frac{h_a d_p}{k_a} \sim 2 \tag{7}$$

And its definition can be used in Eq. 1 to estimate the time needed for the particle to reach the thermal equilibrium:

$$\tau = \frac{\rho_p C_p d_p^2}{12 k_a} \sim 0.01\ s \tag{8}$$

Those considerations together with the mean particle terminal velocity in the capillary allow for the estimation of the positioning of the first detection window along the capillary to obtain information on the reaction

at the desired temperature. A mean velocity of 0.25 m/s corresponds to a path length of 2.5 mm to have the particle at the equilibrium temperature, so the first detection window is positioned at 5 mm from the capillary inlet.

[1] We acknowledge prof. N. G. Deen for the suggestion.
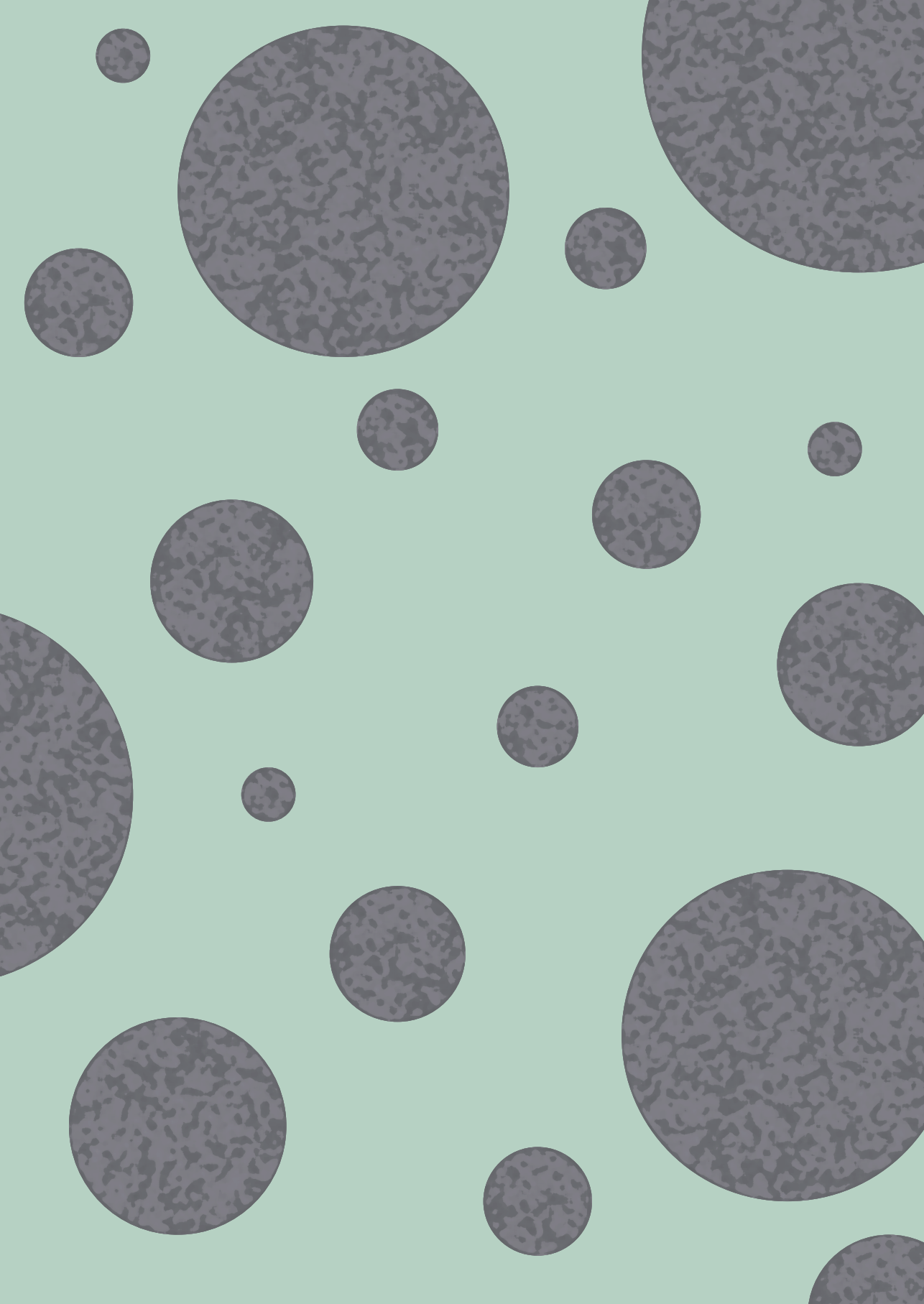
5

Chapter 6

In Situ Study of Mass Transfer Limitations in Plastic Waste Conversion over a Single Catalyst Particle using a MEMS-based Microreactor for High-Resolution X-ray Microscopy

Plastic waste disposal poses a significant environmental challenge due to its persistence and ability to accumulate in the food chain, impacting both human and ecosystem health. Catalytic pyrolysis represents an attractive technique to convert plastic waste into valuable products due to its flexibility towards feedstocks and utilization of existing oil refineries. To optimize plastic waste degradation over zeolite-based catalysts, mass transfer limitations and spatial changes in pore structure caused by polymer intrusion and coke formation after cracking need to be investigated. Characterizing the process in situ requires techniques and devices that allow for 3D imaging of catalyst particles during plastic melting and cracking. This study presents a new method to perform in situ 3D analysis of individual catalyst particles using synchrotron-based hard X-ray tomography imaging techniques. The combination of hard X-ray holotomography with an innovative micro-electromechanical system (MEMS)-based microreactor allowed for the first time the direct observation of polymer melting and cracking over a single catalyst particle, potentially providing spatially resolved information on the polymer intrusion and changes in the catalyst pore space. In this chapter, we describe the relevance of the proposed method and elaborate on the possible improvements in the measurements and data analysis.

6.1 Introduction

The widespread use of plastic materials has led to steady growth in their consumption due to their versatility and relatively low cost[1,2]. Despite these advantages, plastic waste disposal remains a significant environmental challenge because of the chemical inertness of most polymers. The accumulation of plastic waste in landfills and natural environments is a growing concern for both the environment and human health[3,4]. Particularly, the formation of micro- and nanoplastics poses a significant environmental threat[5] due to their persistence, ability to accumulate in the food chain, toxicity to aquatic life, and impact on human[4] and ecosystem health. Global production and disposal rates of plastic are on the rise, while current recycling rates are estimated at a meager 9 wt%[6,7,8]. Furthermore, about an estimated 12 wt% of plastic is incinerated, contributing to climate change due to the CO_2 emitted during incineration[9]. Therefore, there is an urgent need to develop sustainable solutions to limit the environmental and health consequences of plastic waste disposal.

To address this issue, innovative solutions are required to improve plastic waste management, reduce waste production, and promote recycling. Among the currently used strategies, mechanical recycling techniques[10,11] are attractive due to the low energy demand. The process typically involves plastic melting and re-extruding, but it often results in degraded plastic properties. On the other hand, chemical routes can convert plastic to its monomers or valuable products[12,13,14] through e.g. solvolysis, gasification, hydrocracking, and pyrolysis, which currently represent the most common conversion process for biomass and plastic waste[15,16]. Pyrolysis consists of a thermal treatment (400−700 °C) taking place under an inert atmosphere, either with or without the use of a catalyst. Particularly, catalytic pyrolysis can be considered an efficient technique due to its advantages such as the flexibility of feedstocks and the conversion of plastic waste into gasoline-like products[13,17]. Moreover, the approach involves the utilization of existing oil refineries, which can reduce the need for additional investment in new infrastructure and make use of the existing knowledge and expertise on the oil refinery process. The reaction mechanism of plastic waste catalytic pyrolysis is indeed similar to the well-known fluid catalytic cracking

(FCC)[18,19], in which vacuum gas oil (VGO) is converted into gasoline and propylene in the presence of a solid catalyst with acidic sites[20,21] (zeolites). FCC catalyst has been used to pyrolyze various forms of plastic waste[22,23,24,25,26,27], showing high liquid oil (>C_5 aromatic and aliphatic hydrocarbons) yields[28]. Recently, FCC catalysts have been used and compared for polypropylene cracking[29], identifying product distribution and possible limitations in the approach.[30,31,32] For instance, the high viscosity of plastic results in low contact with the catalyst surface, which can translate into reduced reaction efficiency. This aspect strongly influences the degradation process, as it hinders the direct entry of long-chain polymer molecules into the acid sites of the catalyst's micropores, resulting in restricted access and slow mass transfer.[25,33]

Therefore, to understand and optimize plastic waste degradation over zeolite-based catalysts, mass transfer limitations should be investigated. In addition, the spatial change of pore structure caused by polymer intrusion and coke formation related to catalytic performance remains to be revealed.

To gain those information 3D analysis would allow the observation of the catalytic process and changes in porous architecture. For this purpose, synchrotron-based hard X-ray tomography imaging techniques have emerged as important non-destructive tools for 3D studies for spatially resolved information on thick (tens of microns) and opaque materials[34,35,36,37,38].

As regards FCC catalysts, hard X-ray methods have been used to assess single-particle morphology[39] and composition, providing insights into the catalyst pore structure[40], activity, and deactivation mechanism[41,42,43]. Recently, Vesely *et al.* revealed the effects of carbon deposits within single catalyst bodies using hard X-ray holotomography[44]. The approach consisted of imaging a single (coked) catalyst particle before and after calcination to reveal the spatial distribution of coke within the pore space. The study opened up the possibility of visualizing weakly absorbing organic phases (low atomic number elements, i.e. carbonaceous species, polymers) at the macro-pore scale (>50 nm) by hard X-rays. To implement the technique for *in situ* studies, the main experimental challenges are related

6

to the design and fabrication of devices permeable to X-rays, additionally allowing for the control of the sample environment. In the literature, few devices have been proposed to address those requirements and investigate catalysts with hard X-ray microscopy techniques[38,45] with limitations in the precise control of the experimental conditions (temperature and pressure).

Herein, we combined the use of hard X-ray holotomography with an innovative micro-electromechanical system (MEMS)-based microreactor. This allowed us to perform and image *in situ* and in 3D for the first time the dynamics of polymer intrusion after melting and cracking over a single FCC catalyst particle. The developed device consists of a monolithic silicon chip with a free-standing silicon-rich nitride (SiRN) capillary equipped with heaters and vertical trenches as particles trap. The particle spatial confinement ensures its position is always in the field of view during the analysis. The thin SiRN capillary wall makes X-ray attenuation in the hard regime negligible, and the free-standing capillary configuration allows optical access to almost 180°. The presence of the heaters near the particle trap allows for precise local heating in the microreactor, so polymer melting and cracking temperatures could be obtained in the capillary. Polypropylene (PP) beads were loaded in the microreactor with a single FCC particle and imaged after *in situ* polymer melting and cracking. The current study confirms the applicability of the proposed device and method to potentially reveal insights regarding polymer to catalyst contact and changes in its pore space during the process. The preliminary data processing procedure is reported and follows the one proposed by Vesely *et. al.*[44], and further advances for both experimental approach and analysis are discussed to improve the image resolution and to get insightful data interpretation.

6.2 Materials and Methods

6.2.1 MEMS-based microreactor

The MEMS-based microreactor was developed by Carnevale[46] for *in situ/operando* X-ray microscopy, and the fabrication is reported in SI 1. The design with the main features is schematically reported in Figure 1. It

consists of a microchannel with 1-µm thick silicon-rich nitride (SiRN) walls (Figure 1A-C), which results in limited X-ray attenuation, a hydraulic diameter of 100 µm, and a length of 18 mm. The novel design allowed for optical access for tomography of 160° over 180° being part of the channel freely suspended outside the Si substrate. The microchannel presents a semicircular cross-section with a flat roof, providing a suitable location for electrodes. The microreactor can be operated under high pressures (up to ~ 30 bar) and temperatures (up to ~ 400 °C, see SI 2) due to its monolithic nature. Heating is enabled by platinum microheaters (H1 and H2 in Figure 1C-D) embedded in the channel above and below the detection window which can also function as temperature sensors. The external connection for their actuation is obtained through the electric pads positioned on the front side of the chip substrate. Furthermore, the microreactor is equipped with four SiRN vertical trenches 3 µm thick to trap the particle under study while allowing flow through the channel. The inlet and outlet (200 µm in diameter) are positioned on the chip's backside.

6
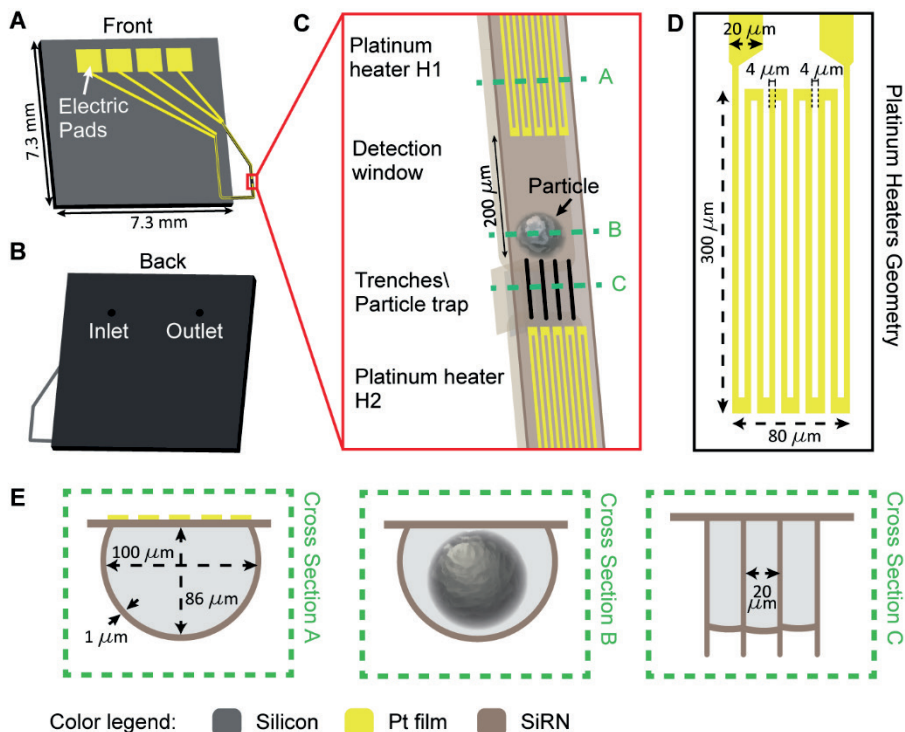
Figure 1: A) A 3D schematic of the front and **B)** back side of the MEMS-based microreactor. **C)** The microchannel's free-standing structure, which includes platinum microheaters H1 and H2 positioned above and below the particle trap, as well as a detection window. **D)** The geometry of the platinum microheaters (H1 and H2), which feature a meander shape and a thickness of 200 nm. **E)** Schematic cross-sectional views of the microchannel at various heights, revealing the semicircular shape of the microchannel with a particle inside, as well as the particle trap cross-section, in which the four vertical trenches are separated by 20 μm.

6.2.2 Microreactor holder

The microreactor was mounted on a stainless-steel holder for rotation as well as to enable access to the fluidic/electrical connections interfaces. Figure 2 shows the holder components. The top part features inlet and outlet fluidic connectors that are compatible with 360 μm fittings for fused silica tubing (VICI Cheminert fittings - Nanovolume), used to flush and saturate the system with N_2. To hold the microreactor firmly in place onto the stainless steel body, a plastic clamp made of PEEK with 4 screws is utilized, with Viton O-rings (OD 1.02mm - ID 0.74mm) ensuring compression and tightness at the interface.
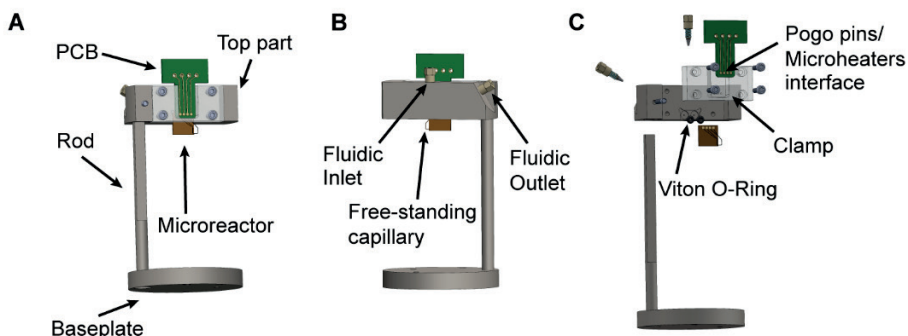
Figure 2: 3D rendering of the **A)** front and **B)** back view of the stainless steel holder for the MEMS microreactor. To enable optical access to the capillary during measurements, the top part of the holder partially clamps the chip. **C)** 3D view of the disassembled holder.

Conducting spring metal contact probes are present on the PEEK clamp which can contact the electrode pads on the chip and allow further interfacing with a microcontroller (myRIO 1900, National Instruments) for heaters actuation and control. A custom LabView program was used to set and measure the temperature inside the capillary during the reaction. The height of the system can be easily adjusted by the screws to fix the top part of the holder on the rod.

6.2.3 Preliminary test using Dark-field microscopy

Preliminary experiments were performed by using an optical microscope to assess the experiment's feasibility and efficacy. The microreactor was loaded with a single FCC catalyst particle and polypropylene beads (VISCOL 330P, Sanyo Chemical Industries) with a melting temperature of 152°C (Figure S2). The experiment was performed *in situ* by using dark field microscopy, to enhance the contrast of the specimen and to be able to distinguish the polymer beads in the capillary, otherwise transparent in bright field configuration. The microreactor was mounted in the holder and secured on the microscope stage, as shown in Figure 3.

6
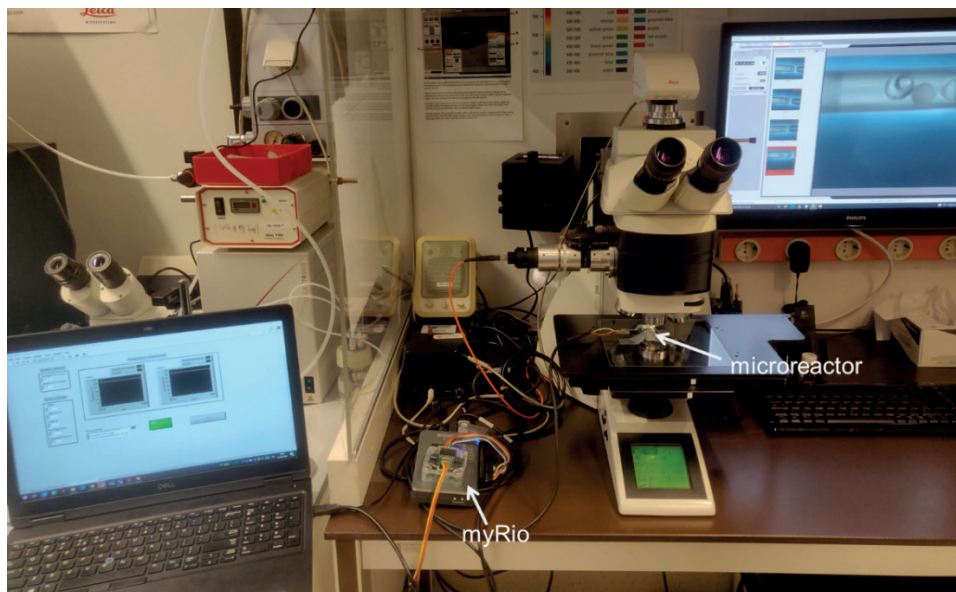
Figure 3: Picture of the experimental setup used to perform and image plastic (PP) melting and cracking over a single FCC catalyst particle. The microreactor was first saturated with N_2 and then the heaters were actuated up to the melting and cracking temperatures by using a microcontroller actuated via a custom LabView program.

Initially, the chip holder was connected to an N_2 gas line through a fused silica capillary to obtain an inert atmosphere in the capillary. To induce polymer melting, the sample was heated to a temperature of 150°C with a ramp rate of 10°C min^{-1}. By recording a movie as the temperature in the capillary gradually increased, we were able to capture the dilation of PP beads and their melting. The second step consisted of reaching the cracking temperatures. Therefore, the temperature was set to 300°C with a ramp rate of 20°C min^{-1}. As the temperature increased, the polymer's viscosity decreased, and once the system reached 300°C a change in the color of the FCC is observed (Figure 4). This is indicative of plastic conversion and consequent coke formation and deposition on the catalyst.
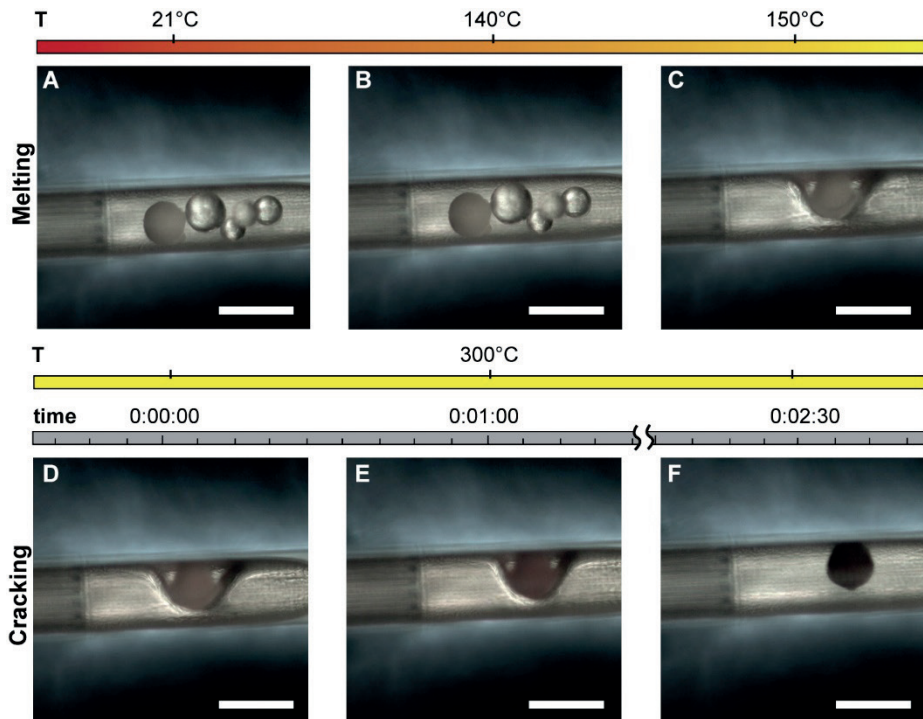
Figure 4: Optical images of polymer beads melting and cracking *in situ* over a single FCC catalyst particle using the MEMS-based microreactor. A-C) were recorded while heating the system to 150°C. A) is the initial step, in which it's possible to distinguish the heater, polymer, and catalyst particle in the chip capillary. In B) the polymer beads dilate due to the increased temperature and C) shows the molten polymer. D-F) Cracking step performed in the chip at 300°C. As the reaction proceeds, the particle color is turning to black due to the formation of carbonaceous species on the particle. Scale bar 100 μm.

The test revealed the applicability of the device to study the process, as both the melting and cracking of the polymer were successfully induced and visualized. Additionally, it was observed that the FCC particle was embedded in the molten polymer, resulting in restricted particle movement along the capillary during the reaction as compared to its initial position. This represents a convenient aspect of *in situ* imaging, ensuring that the particle stays in the field of view (FOV) throughout the process.

To visualize the polymer intrusion and particle changes in the pore network during the process, there's a need for 3D imaging to increase the spatial

6

resolution. This could be obtained utilizing X-ray microscopy (e.g., holotomography).

6.2.4 Holotomography

X-ray holotomography is a powerful full-field phase-contrast imaging technique, which relies on the phase shift of the X-ray beam induced by the object. Particularly, when X-ray beams interact with matter, the complex refractive index n for X-rays can be described as:

$$n = 1 - \delta + i\beta \tag{1}$$

The dispersion term, denoted by the symbol δ, is related to the phase contrast, and the electron density[47] of the sample ρ_e by the following:

$$\delta(r) = \frac{\rho_e(r)\lambda^2 r_e}{2\pi} \tag{2}$$

Where r_e corresponds to the classical electron radius, and λ is the wavelength of the incident X-rays. The absorption term, represented by the symbol β, is associated with the amplitude of the beam. The contribution of β leads to attenuation contrast imaging, which relies on the atomic numbers (Z) of the materials present in the sample. In the case of low-absorbing specimens such as carbonaceous species, or materials having similar Z, techniques based on phase contrast can provide better imaging quality.

The difference in magnitude between δ and β is an important factor that highlights the benefits of using X-ray phase information for the abovementioned cases. Figure 5 reports calculated δ and δ/β for different materials, including PP, as a function of X-ray energy.
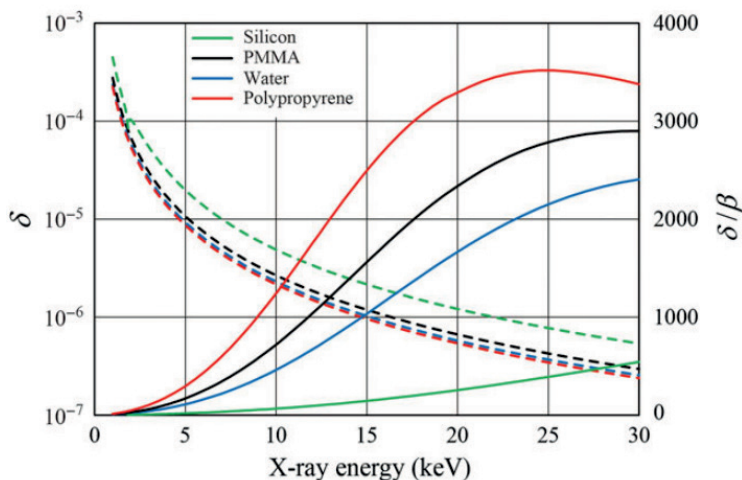
Figure 5: The figure displays the values of *δ* and the ratio *δ/β* for several materials. The dashed lines represent *δ*, while the solid lines correspond to the ratios. Figure reproduced with permission from Momose[48].

At high photon energies, materials that are primarily composed of low-Z elements exhibit a phase contrast *δ* that is approximately three orders of magnitude larger than the absorption contrast *β*. Therefore, using phase contrast imaging rather than absorption contrast imaging results is beneficial in our case. The phase *Φ* can be expressed as:

$$\Phi(x,y) = -\frac{2\pi}{\lambda} \int \delta(r) dz \qquad (3)$$

Where z is the propagation direction. By acquiring a series of holograms at different angular positions it is possible to obtain information about the 3D structure of the sample[49]. To ensure accurate tomographic reconstructions and remove any systematic error that may arise during the acquisition of tomographic data (e.g. non-homogeneous illumination), flat field and dark field images are acquired before and after each tomographic scan.

6.2.5 Setup holotomography

The imaging with hard X-ray holotomography was performed at the beamline P05 of the PETRA III storage ring at the Deutsches Elektronen Synchrotron (DESY, Hamburg), and the experimental setup is schematically shown in Figure 6[50,51]. For the measurements, the X-ray beam is first

monochromized using a Si-111 double crystal monochromator (DCM)[50] to an energy of 17 keV and then focused by a Fresnel zone plate (FZP)[52] determining the achievable spatial resolution. A scintillator-based fiber-coupled scientific detector with a pixel size of 6.5 µm and a resolution of 2048×2048 pixels from Photonic Science is utilized to capture the Fresnel diffraction patterns produced by the object. To ensure precise imaging, a beamstop was positioned near the FZP, blocking the unfocused beam. Additionally, order sorting apertures (OSA) were used to further refine the beam. The microreactor holder was mounted on a high precision rotation stage and could be moved along the optical axis on an air-bearing slider up to a defocus distance of 5 µm. The detector was placed in an adjacent experimental hutch at a maximum sample-to-detector distance of 22 m to obtain high image magnification without the use of optics and therefore limiting the introduction of further artifacts (e.g. aberrations)[50]. A field of view of 105 µm was used for the experiments, with a final voxel size of 102 nm. Approximately 2 h were required per sample for mounting, alignment and holotomography. The fast scan time and large working distance made the setup suitable for *in situ* experiments. At every source-to-sample distance, 1267 projections were acquired over an angular range of 180° resulting in a projection every 0.14°.
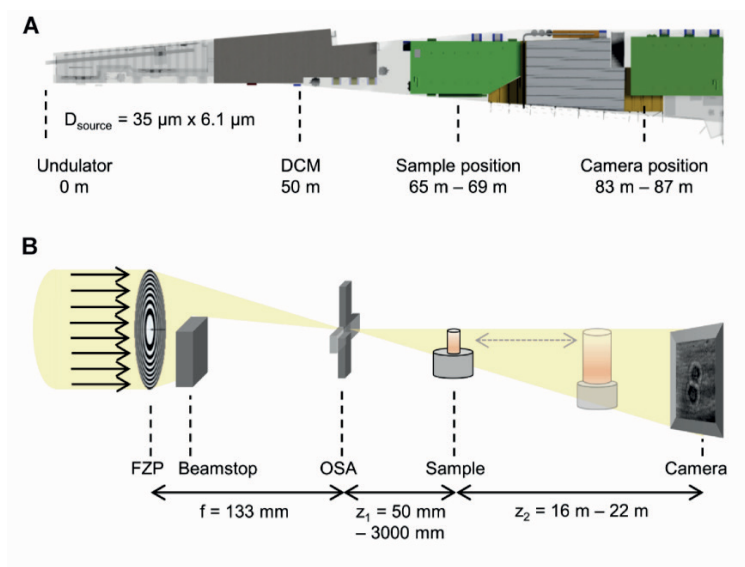
Figure 6: A) Overview of the beamline P05 with relevant hardware components and their distances to the source. B) experimental setup for the X-ray holotomography. Figure reproduced with permissions from Flenner *et al.*[51]

The microreactor with polymer beads and an FCC particle was secured in the holder and mounted on the rotational stage as shown in Figure 7.
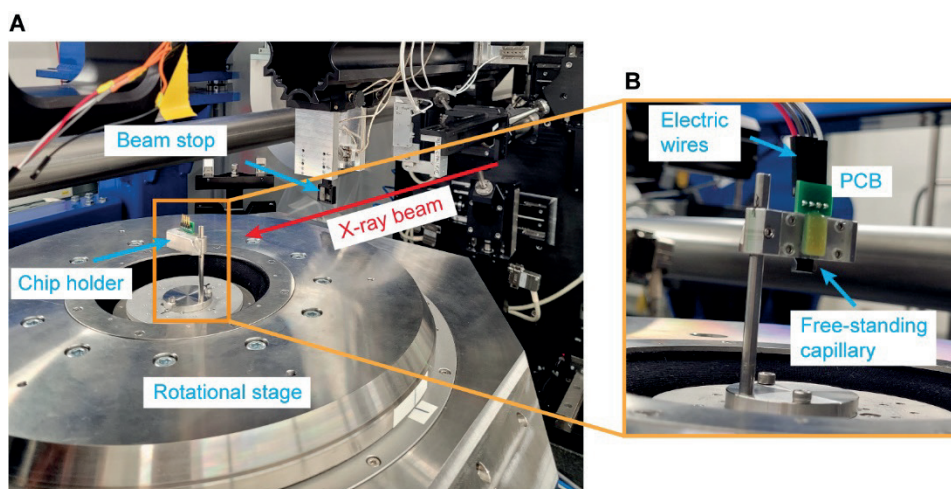
Figure 7: Pictures of the MEMS microreactor mounted on the nanotomography endstation for *in situ* measurements at beamline P05 of DESY. B) Zoom-in of the microreactor and free-standing capillary mounted in a stainless steel holder of adjustable height. The electrical connection to the heaters is obtained through a PCB.

Initially, the sample was roughly aligned in the X-ray beam path using an optical microscope with a large field of view. Then, the X-ray microscope was employed to achieve precise alignment of the sample with respect to both the center of rotation and the desired final FOV.

6.2.6   Polymer melting and cracking over FCC particle imaged via holotomography

Before the experiments, the microchannel was filled with N_2 to ensure an inert atmosphere needed for the pyrolysis. The first tomographic scan was performed at room temperature. Then, the temperature was increased to 150°C with a ramp of 10°C/min. After this, the heater was turned off and the reactor was cooled down to collect another tomography with the molten polymer.

Finally, the temperature was increased to 300°C to induce the catalytic cracking reaction and a tomographic scan was performed afterward. Images of the particle in the microchannel were acquired with a stereomicroscope at the beginning and the end of the experiment (see Figure S3), revealing that the particle color changed from white to black due to the presence of carbon deposits on the surface and thus confirming the success of the polymer cracking.

6.2.7 Phase Retrieval, Image Reconstruction, and Segmentation

Phase retrieval is an essential step in hard X-ray holotomography, as it refers to the reconstruction of the projected phase images from the collected diffraction patterns. Those 2D images of the projected phase shift of the sample represent the basis for the tomographic reconstruction of the 3D relative electron density distribution of the sample.

Holotomography can make use of various iterative phase retrieval algorithms, such as iterative alternating projections[53] providing the 2D projections as output. Those are aligned with respect to the center of rotation to account for any sample movement and motor errors. Following the phase retrieval procedure, tomographic reconstruction is carried out using the filter back projection (FBP) algorithm. This step enables the creation of a 3D model of the sample's electron density, providing detailed

insights into its structural composition and potentially allowing for quantitative mapping of the electron density and material composition. The resulting information is crucial in understanding the properties and behavior of the specimen under study. The electron density distribution of the sample was transformed into a 16-bit integer format for its 3D visualization, followed by additional processing. Data were also normalized with respect to the intensity capillary wall of the microreactor, to perform a direct comparison of the images over the different experimental steps.

Finally, the AvizoTM software package by Thermo Fisher Scientific Inc. was used for the post-processing of the reconstructed images. Typically, the images are represented using a grayscale color map, where lower electron density values are associated with white pixels (voxels), while higher electron density values are represented by black pixels. The images were masked and then segmented into their corresponding pore space and solid phase in MATLAB via k-means clustering algorithm[54], or manual thresholding in case of artifacts. Further data statistical analysis to assess polymer intrusion was performed using MATLAB.

6.3 Results and Discussion

The presented data elaboration is intended as preliminary, so it is important to recognize that further experiments are required to confirm and validate the reported findings and approach to data analysis. This study represents the first attempt at conducting *in situ* polymer melting and cracking in a microreactor coupled with hard X-ray holotomography, and both elaboration and data interpretation is not straightforward as there are no established findings to build upon and support the described methods. We report the steps for the data elaboration, which follows the approach reported by Vesely *et al.* [44]

6.3.1 Evaluation of plastic intrusion and cracking

The particle was imaged A) before, B) after the polymer melting, and C) after the cracking reaction (Figure 8). The experimental settings and setup remained unchanged during the holotomography data acquisition of the three steps and therefore, the changes in the greyscale values (electron

6

density) in the datasets compared to the initial step are due to the polymer intrusion and coke formation respectively.
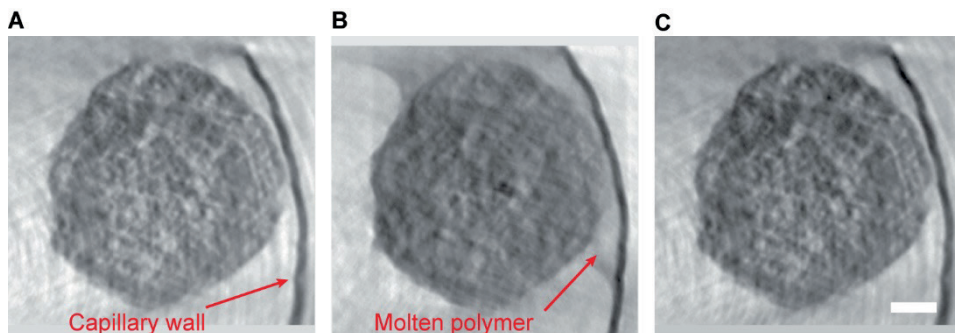
Figure 8: The same 2D virtual slice through the registered volume images of the FCC particle. **A)** at the beginning of the experiment, **B)** after the polymer melting, and **C)** after the polymer cracking. The white and black pixels (voxels) correspond to low and high electron density values, respectively. Despite the low contrast, it is possible to distinguish the molten polymer around the particle and the capillary. Scale bar is 10μm.

The achieved image resolution (see SI 5) allowed for the identification of particle macropores above 600 nm. In Figure 8B despite the low contrast, it is still possible to discern the presence of the molten polymer as it wets both the particle and the capillary while in the third step (Figure 8C), no plastic was detected hinting towards its conversion via catalytic cracking. The affinity between the polymer and the particle results in a good wetting of the catalyst surface.

By analyzing the mean particle intensity at each stage, one can qualitatively observe the progression of the cracking reaction. The shift towards more negative gray value intensities in steps B) (-0.0151 ± 0.0023) and C) (-0.0134 ± 0.0029) indicates an increase in electron density with respect to the step A) (-0.0116 ± 0.0030), ascribable to the presence of the polymer and carbonaceous species respectively.

To compare the different steps, the tomographies were first aligned (see SI 6), and the alignment quality was assessed using Scale-Invariant Feature Transform (SIFT) algorithm (see SI 7). This was performed to ensure that the mean displacement between the dataset after alignment lies within the achieved effective resolution. Then, to localize the polymer in the porous particle, differential contrast X-ray holotomography analysis was carried out

by subtracting the X-ray holotomography data sets of step B) and step A) (see SI 8). The values of the resulting difference were fitted with a Gaussian function, and the deviation from the Gaussian function for positive values ensured that we were above the noise level. A threshold was applied in correspondence to the deviation, to segment the particle matrix and polymer (see Figure 9).
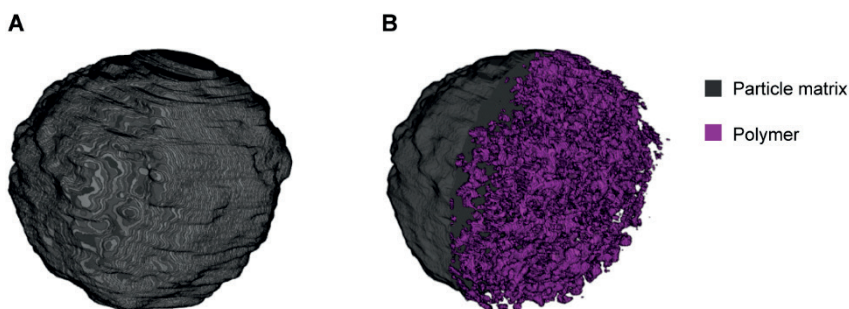
Figure 9: Reconstructed volumes of the entire FCC particle **A)** surface and **B)** cross-section after polymer melting and intrusion in the macro-pores. In the latter volume, the pores filled with the polymer are highlighted in purple.

To get information on the polymer intrusion in the catalyst pore space, we reported the distribution of plastic voxels relative to the fraction of pore voxels at different radial distances from the surface to the center of the particle (see SI 9). This radial distribution indicates that the plastic material is present along the whole particle, with 70% of the total pore volume being filled. Some empty pores are still present probably due to the scarce accessibility related to their geometry (connectivity) or surface wettability.

6.4 Conclusion and Outlook

The current study validates the potential of the proposed MEMS-based microreactor and hard X-ray holotomography for investigating polymer-catalyst interactions and pore space changes during the catalytic pyrolysis of plastic. PP melting and cracking over the FCC particle were successfully performed *in situ*, and the microreactor showed compatibility with imaging via hard X-ray holotomography. Despite small movements caused by the

6

plastic melting, the presence of the trap in the capillary allowed us to keep the particle always in the field of view and allowed for alignment over the 3 steps necessary for their direct comparison. The images' grayscale values were normalized with respect to the capillary wall which was always in the FOV and represents an additional internal standard (together with air outside the capillary) to make the comparison quantitative. The obtained phase contrast proves the capability of the method to distinguish different phases within the particle. Preliminary image processing and analysis provided qualitative insights into the polymer intrusion in the particle macropore space, resulting in 70% of pores filled with PP. The incomplete filling of the FCC particle pore space can be attributed to its complex, heterogeneous, and hierarchical nature, in which some pores may be isolated or poorly connected, leading to restricted diffusion. Due to the complex and heterogeneous structure of FCC particles, it would also be beneficial to test different combinations of polymers and catalysts (e.g. fresh, equilibrium) to assess how changes in surface wettability influence the overall process.

To further enhance the research outcomes, improvements in image resolution are needed from both experimental and data analysis perspectives. The presence of artifacts during the measurements decreases the resolution, introducing uncertainties in the analysis. To improve the overall quality of the measurements, tomographies should be acquired at different distances (i.e., magnifications) between the sample and the detector, improving the signal-to-noise ratio and reducing the impact of artifacts in the phase retrieval step. Moreover, performing two consecutive tomographies of the same sample under identical conditions facilitates the possibility of quantitative analysis and also provides reliable error evaluation as originated from the measurement. This evaluation of measurement errors enhances the accuracy and reliability of the tomographic data and enables a more comprehensive assessment of the sample and process.

6.5   References

1.   Payne, J., McKeown, P. & Jones, M. D. A circular economy approach to plastic waste. *Polymer Degradation and Stability* **165**, 170–181 (2019).

2.   Lebreton, L. & Andrady, A. Future scenarios of global plastic waste generation and disposal. *Palgrave Commun.* **5**, 1–11 (2019).

3.   Mofijur, M. *et al.* Source , distribution and emerging threat of micro- and nanoplastics to marine organism and human health : Socio-economic impact and management strategies. *Environ. Res.* **195**, 110857 (2021).

4.   Leslie, H. A. *et al.* Discovery and quantification of plastic particle pollution in human blood. *Environ. Int.* **163**, 107199 (2022).

5.   Kacprzak, S. & Tijing, L. D. Microplastics in indoor environment: Sources, mitigation and fate. *J. Environ. Chem. Eng.* **10**, 107359 (2022).

6.   Global Plastics Outlook: Plastic waste by end-of-life fate and region - projections. *OECD Environment Statistics (database)* (2023). Available at: https://doi.org/10.1787/e4e8c086-en. (Accessed: 4th August 2023)

7.   Geyer, R., Jambeck, J. R. & Law, K. L. Production, use, and fate of all plastics ever made. *Sci. Adv.* **3**, 25–29 (2017).

8.   MacLeod, M., Arp, H. P. H., Tekman, M. B. & Jahnke, A. The global threat from plastic pollution. *Science (80-.).* **373**, 61–65 (2021).

9.   Astrup, T., Fruergaard, T. & Christensen, T. H. Recycling of plastic: Accounting of greenhouse gases and global warming contributions. *Waste Management and Research* **27**, 763–772 (2009).

10.   Schyns, Z. O. G. & Shaver, M. P. Mechanical Recycling of Packaging Plastics: A Review. *Macromolecular Rapid Communications* **42**, 1–27 (2021).

11.   Ragaert, K., Delva, L. & Van Geem, K. Mechanical and chemical recycling of solid plastic waste. *Waste Manag.* **69**, 24–58 (2017).

12.   Thiounn, T. & Smith, R. C. Advances and approaches for chemical recycling of plastic waste. *Journal of Polymer Science* **58**, 1347–1364 (2020).

13.   Wong, S. L., Ngadi, N., Abdullah, T. A. T. & Inuwa, I. M. Current state and future prospects of plastic waste as source of fuel: A review. *Renew. Sustain. Energy Rev.* **50**, 1167–1180 (2015).

14.   Chen, H., Wan, K., Zhang, Y. & Wang, Y. Waste to Wealth: Chemical Recycling and Chemical Upcycling of Waste Plastics for a Great Future. *ChemSusChem* **14**, 4123–4136 (2021).

15.   Al-Rumaihi, A., Shahbaz, M., Mckay, G., Mackey, H. & Al-Ansari, T. A review of pyrolysis technologies and feedstock: A blending approach for plastic and biomass towards optimum biochar yield. *Renew. Sustain. Energy Rev.* **167**, 112715 (2022).

6

16. Mante, O. D., Agblevor, F. A. & McClung, R. Fluid catalytic cracking of biomass pyrolysis vapors. *Biomass Convers. Biorefinery* **1**, 189–201 (2011).

17. Rodríguez, E. *et al.* Fuel production by cracking of polyolefins pyrolysis waxes under fluid catalytic cracking (FCC) operating conditions. *Waste Manag.* **93**, 162–172 (2019).

18. Harding, R. H., Peters, A. W. & Nee, J. R. D. New developments in FCC catalyst technology. *Appl. Catal. A Gen.* **221**, 389–396 (2001).

19. Pinheiro, C. I. C. *et al.* Fluid catalytic cracking (FCC) process modeling, simulation, and control. *Industrial and Engineering Chemistry Research* **51**, 1–29 (2012).

20. Vogt, E. T. C. & Weckhuysen, B. M. Fluid catalytic cracking: recent developments on the grand old lady of zeolite catalysis. *Chem. Soc. Rev.* **44**, 7342–7370 (2015).

21. Bai, P. *et al.* Fluid catalytic cracking technology: current status and recent discoveries on catalyst contamination. *Catal. Rev. - Sci. Eng.* **61**, 333–405 (2019).

22. Lee, K. H., Noh, N. S., Shin, D. H. & Seo, Y. Comparison of plastic types for catalytic degradation of waste plastics into liquid product with spent FCC catalyst. *Polym. Degrad. Stab.* **78**, 539–544 (2002).

23. Olazar, M. *et al.* Influence of FCC catalyst steaming on HDPE pyrolysis product distribution. *J. Anal. Appl. Pyrolysis* **85**, 359–365 (2009).

24. De La Puente, G., Klocker, C. & Sedran, U. Conversion of waste plastics into fuels recycling polyethylene in FCC. *Appl. Catal. B Environ.* **36**, 279–285 (2002).

25. Dogu, O. *et al.* The chemistry of chemical recycling of solid plastic waste via pyrolysis and gasification : State-of-the-art , challenges , and future directions. *Prog. Energy Combust. Sci.* **84**, 100901 (2021).

26. Saeaung, K., Phusunti, N., Phetwarotai, W., Assabumrungrat, S. & Cheirsilp, B. Catalytic pyrolysis of petroleum-based and biodegradable plastic waste to obtain high-value chemicals. *Waste Manag.* **127**, 101–111 (2021).

27. Eschenbacher, A., Varghese, R. J., Abbas-Abadi, M. S. & Van Geem, K. M. Maximizing light olefins and aromatics as high value base chemicals via single step catalytic conversion of plastic waste. *Chem. Eng. J.* **428**, 132087 (2022).

28. Lee, K. H., Noh, N. S., Shin, D. H. & Seo, Y. Comparison of plastic types for catalytic degradation of waste plastics into liquid product with spent FCC catalyst. *Polym. Degrad. Stab.* **78**, 539–544 (2002).

29. Vollmer, I. *et al.* Beyond Mechanical Recycling: Giving New Life to Plastic

Waste. *Angew. Chemie - Int. Ed.* **59**, 15402–15423 (2020).

30.   Vollmer, I., Jenks, M. J. F., Mayorga González, R., Meirer, F. & Weckhuysen, B. M. Plastic Waste Conversion over a Refinery Waste Catalyst. *Angew. Chemie - Int. Ed.* **60**, 16101–16108 (2021).

31.   Palos, R., Rodríguez, E., Gutiérrez, A., Bilbao, J. & Arandes, J. M. Cracking of plastic pyrolysis oil over FCC equilibrium catalysts to produce fuels: Kinetic modeling. *Fuel* **316**, 123341 (2022).

32.   Huang, J., Veksha, A., Chan, W. P., Giannis, A. & Lisak, G. Chemical recycling of plastic waste for sustainable material management: A prospective review on catalysts and processes. *Renew. Sustain. Energy Rev.* **154**, 111866 (2022).

33.   Aguado, R. *et al.* Defluidization modelling of pyrolysis of plastics in a conical spouted bed reactor. *Chem. Eng. Process. Process Intensif.* **44**, 231–235 (2005).

34.   Das, S., Pashminehazar, R., Sharma, S., Weber, S. & Sheppard, T. L. New Dimensions in Catalysis Research with Hard X-Ray Tomography. *Chemie-Ingenieur-Technik* **94**, 1591–1610 (2022).

35.   Beale, A. M., Jacques, S. D. M. & Weckhuysen, B. M. Chemical imaging of catalytic solids with synchrotron radiation. *Chem. Soc. Rev.* **39**, 4656–4672 (2010).

36.   Bare, S. R. *et al.* Characterization of a fluidized catalytic cracking catalyst on ensemble and individual particle level by X-ray micro- and nanotomography, micro-X-ray fluorescence, and micro-X-ray diffraction. *ChemCatChem* **6**, 1427–1437 (2014).

37.   Grunwaldt, J. D., Wagner, J. B. & Dunin-Borkowski, R. E. Imaging Catalysts at Work: A Hierarchical Approach from the Macro- to the Meso- and Nano-scale. *ChemCatChem* **5**, 62–80 (2013).

38.   Gonzalez-Jimenez, I. D. *et al.* Hard X-ray Nanotomography of Catalytic Solids at Work. *Angew. Chemie* **124**, 12152–12156 (2012).

39.   Buurmans, I. L. C., Soulimani, F., Ruiz-martínez, J., Bij, H. E. Van Der & Weckhuysen, B. M. Microporous and Mesoporous Materials Structure and acidity of individual Fluid Catalytic Cracking catalyst particles studied by synchrotron-based infrared micro-spectroscopy. *Microporous Mesoporous Mater.* **166**, 86–92 (2013).

40.   Ruiz-Martínez, J. *et al.* Microspectroscopic insight into the deactivation process of individual cracking catalyst particles with basic sulfur components. *Appl. Catal. A Gen.* **419–420**, 84–94 (2012).

41.   Meirer, F. *et al.* Life and death of a single catalytic cracking particle. *Sci. Adv.*

6

1, e1400199 (2015).

42. Meirer, F. *et al.* Agglutination of single catalyst particles during fluid catalytic cracking as observed by X-ray nanotomography. *Chem. Commun.* **51**, 8097–8100 (2015).

43. Kalirai, S., Boesenberg, U., Falkenberg, G., Meirer, F. & Weckhuysen, B. M. X-ray Fluorescence Tomography of Aged Fluid-Catalytic-Cracking Catalyst Particles Reveals Insight into Metal Deposition Processes. *ChemCatChem* **7**, 3674–3682 (2015).

44. Veselý, M. *et al.* 3-D X-ray Nanotomography Reveals Different Carbon Deposition Mechanisms in a Single Catalyst Particle. *ChemCatChem* **13**, 2494–2507 (2021).

45. Andrews, J. C. & Weckhuysen, B. M. Hard X-ray spectroscopic nano-imaging of hierarchical functional materials at work. *ChemPhysChem* **14**, 3655–3666 (2013).

46. Carnevale, L. Microreactors for In Situ Single Catalyst Particle Characterization Using Advanced Imaging Techniques. (University of Twente, 2023).

47. Diaz, A. *et al.* Quantitative x-ray phase nanotomography. *Phys. Rev. B - Condens. Matter Mater. Phys.* **85**, 1–4 (2012).

48. Momose, A. Development toward high-resolution X-ray phase imaging. *Microscopy* **66**, 155–166 (2017).

49. Cloetens, P. *et al.* Holotomography: Quantitative phase tomography with micrometer resolution using hard synchrotron radiation x rays. *Appl. Phys. Lett.* **75**, 2912–2914 (1999).

50. Flenner, S. *et al.* Hard x-ray nanotomography at the P05 imaging beamline at PETRA III. **12242**, (Proceedings of SPIE, 2022).

51. Flenner, S. *et al.* Hard X-ray nano-holotomography with a Fresnel zone plate. *Opt. Express* **28**, 37514 (2020).

52. Kirz, J. Phase zone plates for X-rays and the extreme UV. *J Opt Soc Am* **64**, 301–309 (1974).

53. Wittwer, F., Hagemann, J., Brückner, D., Flenner, S. & Schroer, C. G. Phase retrieval framework for direct reconstruction of the projected refractive index applied to ptychography and holography. *Optica* **9**, 295 (2022).

54. Dasilva, J. C. *et al.* Assessment of the 3-D pore structure and individual components of preshaped catalyst bodies by X-ray imaging. *ChemCatChem* **7**, 413–416 (2015).

6.6   Supporting Information

1. Microreactor fabrication

2. Characterization of micro heaters

3. Differential scanning calorimetry of the polymers

4. Bright-field images of the PP beads and FCC particles in the microchannel before and after the reaction

5. X-ray holotomography spatial resolution estimation

6. Registration of datasets

7. Alignment Precision Assessment Using Scale-Invariant Feature Transform

8. Thresholding of Differential X-ray Holotomography Data to Determine the Polymer Distribution

9. Radial Analysis

1. Microreactor fabrication

The MEMS-based microreactor developed by Carnevale[1] was fabricated in the cleanroom of the MESA+ NanoLab at the University of Twente. The microreactor is made of a silicon wafer using photolithography and a Surface Channel Technology (SCT) process, involving a seven-mask process to achieve the desired features. The process includes depositing a layer of oxygen-rich alumina AlO_x layer (500 nm) on the silicon wafer via Low-Pressure Chemical Vapor Deposition (LPCVD). A photoresist layer containing the vertical trenches pattern (3 by 60 µm) was deposited on top of the AlOx layer, with the pattern transferred to the AlO_x using plasma etching. Anisotropic etching into the silicon substrate formed the grooves for the 4 vertical trenches that serve as the particle trap. Those are made out of Silicon-rich Nitride (SiRN), deposited via LPCVD.

Successively, a layer of 500 nm of SiRN using LPCVD is deposited on the silicon. Another layer of 100 nm AlO_x layer is then deposited on top of the SiRN layer to protect it while etching the microchannel into the substrate. A photoresist layer is deposited to transfer the pattern including etching slits for the microchannel with a dimension of 5 by 2 µm to the AlO_x and SiRN

layers using plasma etching. The microchannel is then etched isotropically into the silicon substrate by SF_6 plasma.

After the microchannels are formed, the process is followed by creating fluidic inlets. This involves depositing a layer of SiO_2 (1.2 µm, LPCVD) on top of the microchannels, which serves as an etch stop during the inlet/outlet etch and protects the microchannels during the backside processing. A pattern of fluidic inlets is then created by depositing photoresist on the backside of the wafer and developing it. The pattern is then transferred into the SiO_2 and SiRN layers using a directional plasma etch, and a deep reactive ion etch (DRIE, Bosch process) is performed to etch the fluidic inlet up to the SiO_2 channel wall. Once the fluidic inlets are formed, a thick layer of SiRN is deposited using LPCVD to create the channel wall. The layer must be thick enough to cover the 1 µm wide slits and provide a strong and structurally rigid channel roof.

After the SiRN microchannel is formed, electrodes are created to actuate and read the microheaters. A Pt layer of 200nm is deposited by sputtering, with a Ta adhesion layer of 10nm underneath. The electrodes are then patterned using a photoresist layer, and ion beam etching is used to etch the electrodes. A layer of (AlO_x) with a thickness of 400 nm is deposited onto the metal layer using electron beam evaporation to enhance the robustness of the metal layer against high temperatures.

The final step is to release the micro-channels from the silicon bulk, which involves several sub-steps. After the etching and patterning of the AlO_x layer, the next step involves the deposition of Cr/Au bondpads through evaporation, followed by patterning using resist and wet chemical etching. Subsequently, a new resist layer is applied to create release holes in the SiRN, enabling the etching of cavities and break grooves within the microdevice structure. The channels are then released by isotropic etching of the silicon bulk using SF_6 plasma. The silicon is etched to a depth of 250 µm, about halfway through the wafer, allowing the wafer to be broken along grooves etched between devices to separate it into chips.

2. Characterization of microheaters

To regulate the temperature inside the microreactor, we used the microheaters as both heating and sensing elements. Initially, the Pt microheater was characterized as Resistance Temperature Detector (RTD). This sensing mechanism relies on a metal resistor with a positive temperature coefficient (PTC), which causes its electrical resistance to increase as the temperature rises. The Temperature Coefficient of Resistance (TCR), representing the change in electrical resistance with temperature (RvsT), was obtained by calibrating the Pt microheater in the range of 50-280°C. The calibration was carried out by fixating the microreactor in the holder and submerging it in an oil bath (IKA RET control-visc C) with a stirring at 300 rpm. The resistance values at different temperatures were measured by using a multimeter (Fluke 770) after reaching equilibrium conditions. This process was performed for both microheaters present in the microreactor design to obtain the resistance at 0°C (R0) and TCR values. Then, the electrical resistance of the Pt microheaters was calibrated with the applied voltage by varying the voltage from 1 to 6 V with a 1V step size using a source meter (Keithley 2400) that allowed for voltage source and online resistance measurement. To determine the relationship between the microheater's temperature and the applied voltage, the RvsT was used to obtain the TvsV correlation, as shown in Figure S1 B.
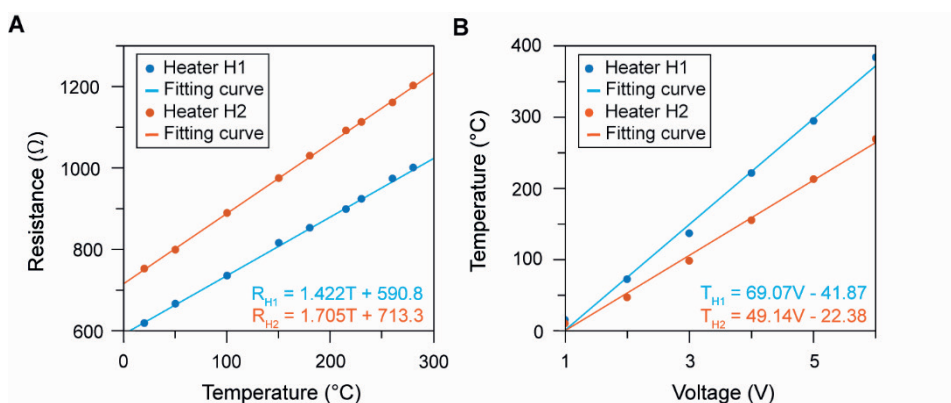

Figure S1: A) Calibration of microheater resistance with temperature using oil immersion. B) Calibration of the microheater temperature with the applied voltage.

3. Differential scanning calorimetry of the polymer

Differential scanning calorimetry (DSC) was conducted with the polypropylene sample using a Mettler Toledo DSC 3 STARe system. To examine the specific material properties and the thermal history of a sample, the sample was heated above the melting point at a defined heating rate. 5 ± 1 mg polymer was heated in aluminum sample pans from -60 °C or -30 °C to 250 °C, at 10 °C min^{-1} The melting points were determined as the first peak in the thermogram of the first heating cycle.
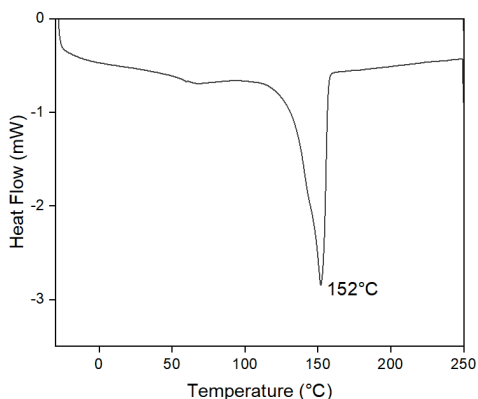
Figure S2: DSC curves of the two commercial polymers used in this study. The peaks in the curves correspond to the melting points, resulting at 144 °C for the 660P sample and 152 °C for the 330P sample respectively.

4. Bright-field images of the PP beads and FCC particles in the microchannel before and after the reaction
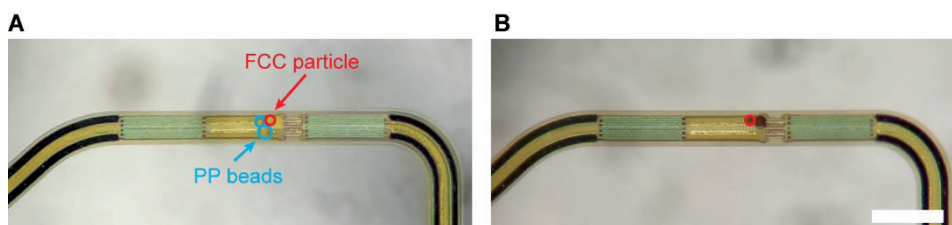
Figure S3: Optical images of the channel of the microreactor **A)** before and **B)** after cracking. The capillary contained 2 PP beads and 2 FCC particles, with the highlighted being the one imaged during the melting and cracking processes.

5. X-ray holotomography spatial resolution estimation

The X-ray holotomography resolution was estimated by following the workflow from Holler[2]. The approach consists of identifying distinctive features in the virtual 2D slice, choosing a line segment (red line in Figure S4 A), and generating an intensity plot along that line. The line analysis was performed on the capillary wall for all three samples. The intensity plot displays the 10%-90% criteria and determines the edge resolution by measuring the distance (indicated by vertical dashed lines). The resolution of the tomography 1) resulted to be equal to 568 nm, 2) to 557 nm, and 3) to 483 nm considering a voxel size of 102 nm.
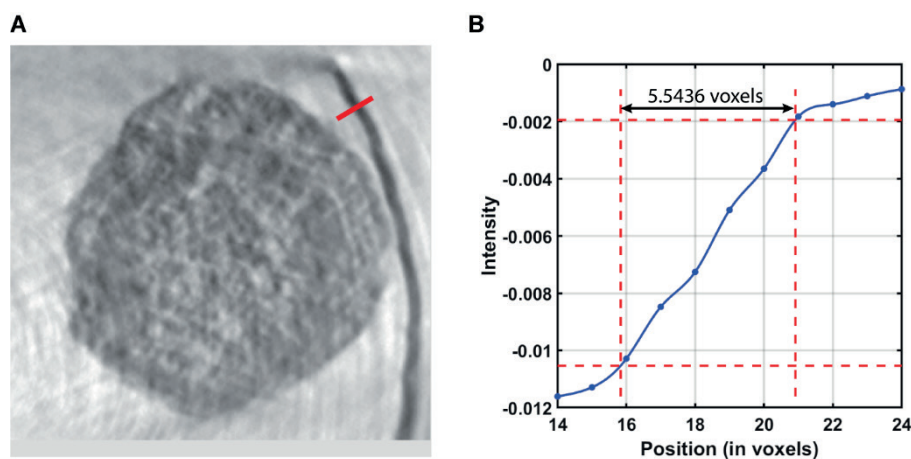
**Figure S4**: **A)** Example of a line scan used to evaluate the resolution of the recorded data. **B)** Intensity line plot showing the effective voxel resolution of 5.5436 resulting in a final resolution of 568 nm.

6. Registration of datasets

The volume images obtained from the holotomography measurements were aligned using the registration tool within the Avizo 9.4 software package (Thermo Fisher Scientific, UK). The volume image of the first step was used as a reference, and the volume data for the particle with the polymer and coke particle was adjusted for translation, rotation, shear, and scaling. To achieve precise alignment, a rough registration was initially carried out based on the binary total particle volume (TPV) of each particle, which includes both the particle volume and the pore space. In the next

step, a second alignment iteration was conducted starting from the grayscale volume images derived from the previous registration. The registration algorithm employed least squares minimization between corresponding pixels in the two images.

7. Alignment Precision Assessment

Scale-Invariant Feature Transform (SIFT) procedure is a widely used computer vision algorithm for extracting and matching distinctive features in images and is known for its robustness to various transformations, such as scaling and rotation. SIFT was used to find identical local features in 2D slices and to assess the alignment precision, a triplet of virtual slices was analyzed in the planes x-y. In total, the algorithm detected 20 pairs of distinctive features between the slice of the particle in steps A) and C). Among these, 14 were recognized in step B). The result is ascribable to the presence of the polymer inside the particle which influences the overall contrast and reduces the possibility to recognize the same features. Then, the mean square displacement for each pair was calculated. The average displacement value between A) and C) resulted to be 3.17 voxels, with a standard deviation of 2.24 voxels. Between slices A) and B), an average value of 3.83 voxels with a standard deviation of 2.75 voxels was found. Additionally, between slices B) and C), the average displacement value was 3.05 voxels, with a standard deviation of 2.90 voxels. Therefore, in each of the reported cases, the alignment precision as mean displacement is smaller than the achieved effective resolution. Figure S5 reports the positions of the identified features denoted by red squares.
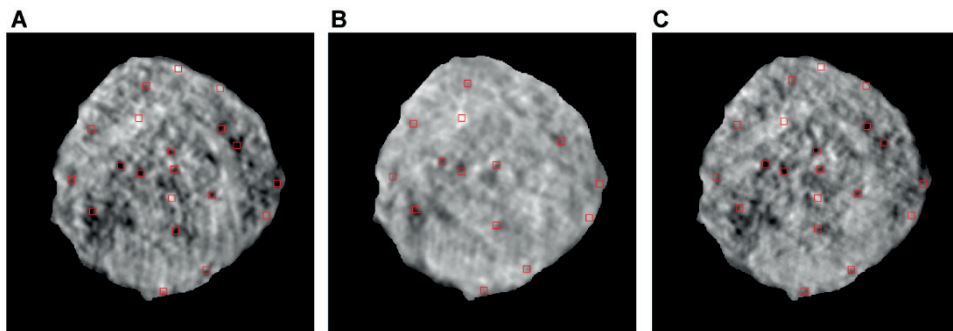
Figure S5 SIFT analysis results for the data alignment precision for a virtual slice in the plane x-y in the central position (slice=200). The features recognized are highlighted as red squares for the particle slice **A)** at the beginning of the experiment, **B)** after the polymer melting, and **C)** after the polymer cracking.

8. Thresholding of Differential X-ray Holotomography Data to Determine the Polymer Distribution

A direct comparison between the X-ray holotomography datasets of the step with the melted polymer and the initial step was obtained by direct subtraction. To do so, the inverted grayscale values of the particle tomography were used (positive values for high electron density, negative values for low electron density elements). This process results in a volumetric representation that includes both positive and negative values (Figure S6), ascribable to the noise in the data. The histogram of the difference values was then fitted with a Gaussian function optimizing the fit to the negative part of the histogram. The curve provided clear evidence that voxels exhibit positive values exceeding the noise level. Subsequently, this threshold was utilized to segment the data and recognize voxels containing polymer (voxels with values greater than or equal to 0.0044).

6
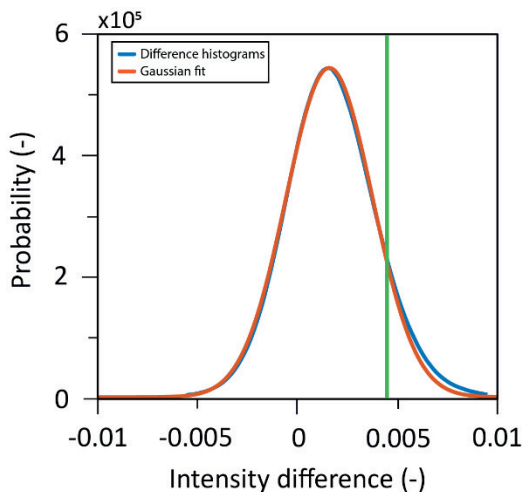
Figure S6: Distribution of gray value difference between the X-ray holotomography data sets of the measurements before and after polymer melting and intrusion. The histogram was fitted using a Gaussian function, with a focus on optimizing the fit to the negative portion of the distribution. The right panel of the figure highlights the deviation of the histogram from the noise distribution, specifically around the threshold value of X. This threshold value was employed to segment the data into two categories: empty voxels (with values below X) and voxels containing polymer.

9. Radial Analysis

The radial distribution[3,4] of the polymer within the catalyst pore structure was evaluated from the analysis of the PP melting step. Initially, the total particle volume (TPV) was generated, reporting the binarized image in which voxels belonging to the particle's volume have a value of 1. Then, the particle mask was divided into shells with a thickness of 1 voxel, obtained by subtracting the eroded mask of 1 voxel from the original mask. This erosion process is iterated until reaching the center of the particle. To obtain the number of voxels referred to as the pore space, the tomography of step 1) was segmented by using the k-means clustering algorithm[5], by which matrix and pore space were recognized. This allowed the evaluation of the voxels indicating the pores. Then, for each shell, the fraction of plastic voxels over the pore voxels was determined. The results suggest that the polymer is present all over the particle radius. However, caution should be exercised when interpreting the volume fraction in shells close to or at the

center, as they may contain only a few voxels and may not be statistically significant for accurate characterization of the particle's composition.
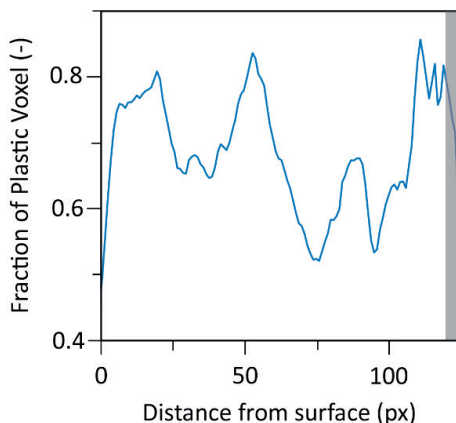
Figure S7: Radial distribution of the fraction of plastic voxels to the pore voxels. The graph indicates the distribution of the polymer within the particle and its presence across the entire radius. In the radial analysis, the last 5–10% (grey area) is usually ignored due to the minimal voxels per shell present at diminished particle volumes, which falls into a statistically non-significant range.

Supporting References

1. Carnevale, L. Microreactors for In Situ Single Catalyst Particle Characterization Using Advanced Imaging Techniques. (Doctoral dissertation, University of Twente, 2023)
2. Holler, M. *et al.* X-ray ptychographic computed tomography at 16 nm isotropic 3D resolution. *Sci. Rep.* **4**, 1–5 (2014).
3. Meirer, F. *et al.* Life and death of a single catalytic cracking particle. *Science Advances* **1**, e1400199 (2015).
4. Meirer, F. *et al.* Mapping metals incorporation of a whole single catalyst particle using element specific X-ray nanotomography. *J. Am. Chem. Soc.* **137**, 102–105 (2015).
5. Arthur, D. & Vassilvitskii, S. K-means++: the advantages of careful seeding. *Proceedings of the Eighteenth Annual ACM-SIAM Symposium on Discrete Algorithms,* 1027–1035 (2007).

6
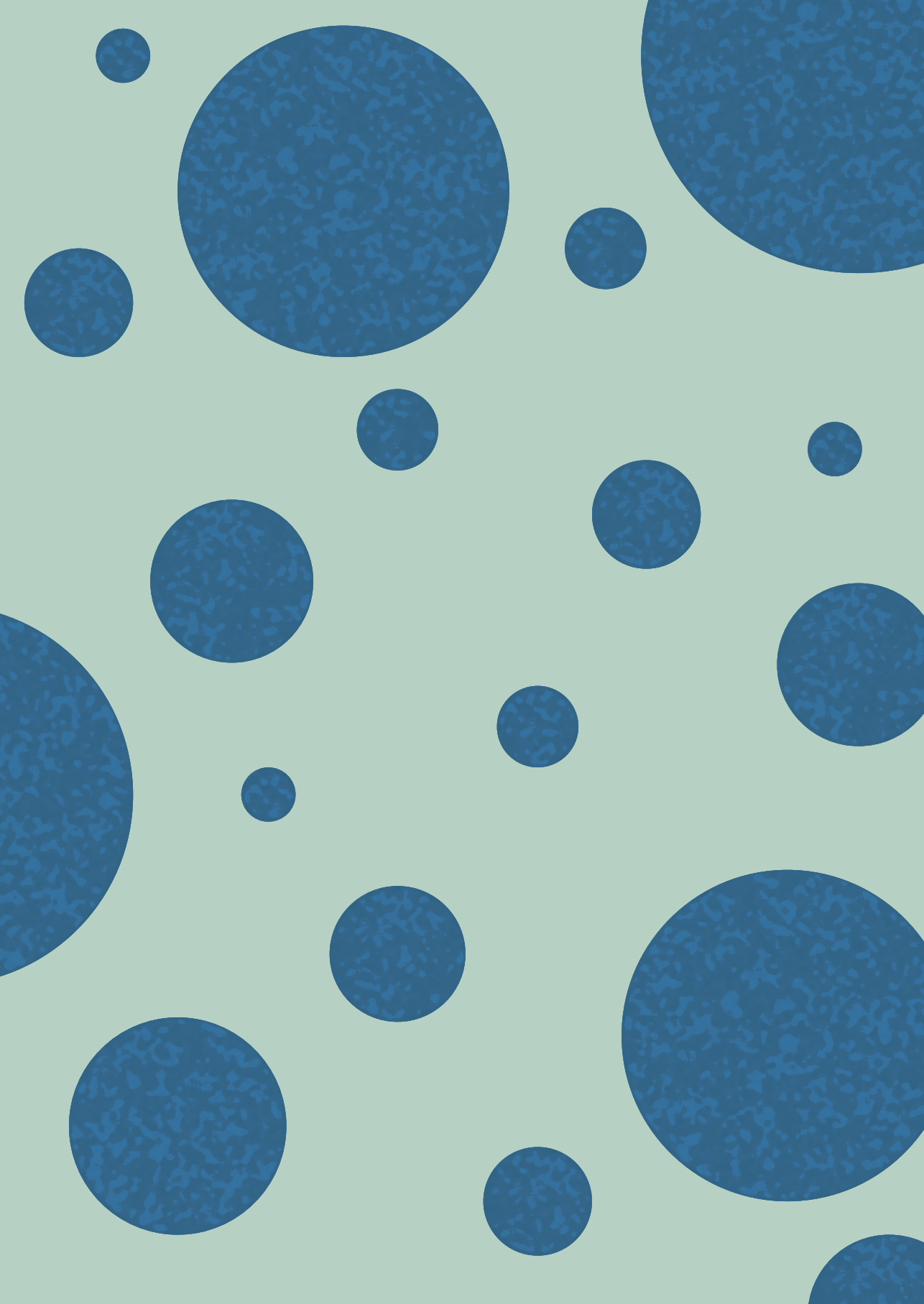
Chapter 7

Summary and Outlook

The ultimate goal of the research presented in this thesis is to develop microdevices to characterize individual catalyst particles. In this chapter, the main results and conclusions of the work presented in this thesis are summarized, together with suggestions for further applications and possible improvements.

7.1   Summary and Outlook

In the field of heterogeneous catalysis, a multiscale approach is indispensable for a comprehensive understanding of the dynamics of structurally complex catalytic materials. Spanning across diverse length scales, this approach addresses catalyst behavior from atomic-level interactions to macroscopic reactor operation. At the atomic and molecular scale, it probes the configuration of active sites, shedding light on catalyst structure and reactivity. The microscopic level enables the study of single catalyst particles, unveiling the heterogeneity and complexity among and within **individual particles**. At the macroscopic level, it captures how catalyst structure, distribution, and operation influence the overall reactor performance and efficiency. Therefore, each level of analysis contributes distinct perspectives, and their combination renders a comprehensive understanding of catalyst function. This, in turn, can guide the refinement of catalyst design and the fine-tuning of process conditions, paving the way for optimized catalytic performance.

Studies focused on catalyst particles on an individual level uncovered their significant **heterogeneity**[1-4], both interparticle (between different particles) and intraparticle (within a single particle), related to properties like active site distribution, particle size, pore network, and composition. This complexity fundamentally challenges the way we interpret traditional bulk characterization methods, which, on the other hand, intrinsically presume sample homogeneity. Furthermore, for an accurate understanding of how catalysts operate, it is desirable to observe them under or approaching operational conditions, ideally capturing the dynamic of the process under study.

In this context, the advent of **microfluidic technology** offers promising opportunities. Its ability to replicate operational conditions on a small scale, while maintaining precise control over the environment, paves the way for more accurate and informative catalyst characterization. Importantly, microfluidic systems hold a unique advantage in their inherent capability for high-throughput analysis[3,5-7]. This aspect allows for rapid testing and

comparison of a vast array of catalyst particles or conditions in a time-efficient manner.

The integration of microfluidic technology is the central theme throughout this thesis, in which we explored the possibilities of *in situ* analyses and **high throughput** strategies for catalyst particle characterization.

Chapter 1 introduces the research topic, providing the motivation and background of this thesis on the implementation of microfluidic technology for catalyst particle screening.

In **Chapter 2**, we provided an overview of the current state of the art of the use of microfluidic devices in traditional microscopy and spectroscopy catalyst characterization techniques. A theoretical background is presented, discussing the basics of selected analytical techniques, including the ones used in this research. Furthermore, we considered future trajectories in this field, with high-throughput platforms being the central pivot in shaping future advancements and innovations in catalyst analysis. The high-throughput testing can facilitate the collection of databases detailing relationships between physical, chemical, and structural parameters and catalytic performance. This vast information can serve as a library to predict catalytic activity through computational modeling and machine learning. Finally, the introduction of standardized microfluidic devices for catalyst characterization would lead to the streamlining of catalyst analysis, enabling more efficient and repeatable experiments.

Chapter 3 reports a novel method to locally deposit nanoparticles generated via spark ablation on 3D-structured microfluidic devices using a nanomaterial 3D printer. The approach consists of a cleanroom-free direct-write method to integrate metal (oxide) nanoparticle patterns in microfluidic structures, offering a new approach to catalyst design and screening. Moreover, the intrinsic ability to finetune the film morphology, based on the printing parameters, opens up new opportunities for the fabrication of screening and sensing platforms.

The potential of the approach was showcased through two distinct applications. Functional devices were obtained by depositing either Pt or Ag nanoparticles in the chambers of a multiplexed polydimethylsiloxane

7

(PDMS) microfluidic device. In one case, Pt films were used as bipolar electrodes, which allow for the creation of distinct electrochemical potentials along the electrodes. This was tested through the electrochemical generation of pH gradients in the chambers via water electrolysis, detected using a pH-sensitive dye.

Leveraging spatial electrochemical potential gradients, it's possible to create electrodes of which the composition changes along its length (i.e. compositional gradient) within a single deposition run. By using mixed-metal solutions, the variation of potential across the electrode length leads to selective metal electrodeposition at distinct locations. This results in a continuous range of material compositions, creating various alloys with different metal ratios over the electrode. The inherent high-throughput nature of the use of these bipolar electrodes is further increased when paired with multiplexed microfluidic devices. This combination provides a highly efficient system for generating and screening a wide range of materials, making it an efficient approach in the fields of catalysis or advanced materials research.

In the second application, the efficacy of Ag nanoparticles as Surface-Enhanced Raman Spectroscopy (SERS) substrates was tested. The chip chambers were filled with a solution of methylene blue used as a probe molecule, leading to an analytical enhancement factor of $1.7 \cdot 10^5$. The technique could allow for the simultaneous detection of multiple analytes in a single test, optimizing both diagnostic and analytical processes.

In **Chapter 4** we propose a new method to evaluate the accessibility of porous particles at the single-particle level, a parameter that determines their efficiency as adsorbents and catalysts. The approach consists of the use of a multiplexed PDMS microfluidic device to assess the uptake of fluorescent molecules in individual porous particles over time in a high-throughput fashion.

To demonstrate the method, mesoporous SiO_2 particles with uniform pore sizes and similar porosities were used. Interestingly, particles from the same batch, i.e., with the same pore size, showed great heterogeneity in terms of accessibility, that could not be resolved via traditional bulk methods.

Furthermore, by modulating the electrostatic interactions between the probe molecule and the SiO_2 surface through adjustments in system pH and ionic strength, we noticed substantial changes in mass transfer, thus resulting in a chemically-sensitive method to probe the accessible porosity and surface area. When these probe-host interactions are minimized, the uptake process is primarily influenced by the pore structure. In this case, the method provides a pore-size probing sensitivity similar to the one obtained with N_2-physisorption.

The concentration fronts identified within the porous particle could be fitted with a mass transfer model to provide spatially resolved insights and eventual intra-particle heterogeneities. Further, the fabrication of a device compatible with organic solvents would enable also the use of hydrophobic dyes, broadening the understanding of the material accessibility and interactions.

Chapter 5 presents the design and fabrication of a high-throughput device for *in situ* study of gas-phase catalytic reactions at the single particle level. The proposed setup has the potential to track the real-time progression of catalyst deactivation due to the deposition of carbonaceous species (coke) on its surface, which is relevant in industrial processes involving the conversion of hydrocarbons (e.g. cracking).

The concept is based on following the lifetime and progressive deactivation of the particle by coke formation by imaging at fixed positions down the microreactor, as each position is representative of different residence times. The amount of coke formed can be evaluated through fluorescence-based measurements of individual particles, thus allowing for the study of deactivation kinetic and interparticle heterogeneity. As for now, the capability of the setup to detect particle fluorescence while passing the detection spot was tested by using catalyst particles with different amounts of coke. Those were obtained via cracking experiments with fluid catalytic cracking (FCC) particles and n-hexane performed *ex-situ* and quenched at different times. The measurements revealed a clear correlation between the signal intensity and catalyst age, suggesting that the method has the potential for determining the rate of catalyst deactivation and intraparticle

7

heterogeneities, which become more pronounced at longer reaction stages.

The device and setup could also be used to assess the efficiency of calcination, which is the process used for restoring the catalytic activity of the particles. The effectiveness of this process can be influenced by numerous factors, including temperature and duration. By employing this apparatus and experimental setup, one could potentially monitor the changes in signal intensity throughout the calcination process, providing real-time insights into the regeneration of the catalyst. This could help in optimizing the calcination parameters to ensure maximum catalyst recovery while minimizing energy consumption and process time. Lastly, the device could also provide information about interparticle heterogeneity after calcination. It could reveal how different particles respond to the same calcination conditions, unveiling the role of particle characteristics in catalyst regeneration. This could pave the way for the design of catalysts with improved resistance to deactivation and enhanced regeneration performance.

In **Chapter 6** we introduce an innovative method that enables *in situ* 3D analysis of individual catalyst particles by leveraging synchrotron-based hard X-ray tomography imaging techniques. More specifically, the approach combines hard X-ray holotomography with a micro-electromechanical system (MEMS)-based microreactor developed by Luca Carnevale (BIOS/UT), consisting of a monolithic silicon chip with a free-standing capillary equipped with vertical trenches as particles trap and heathers for the precise control of the temperature at the particle location. This setup allows for the performance and direct observation of catalytic processes over individual particles.

It was used to study the catalytic pyrolysis of polypropylene using fluid catalytic cracking (FCC) particles, which represents an effective strategy and an active area of research for plastic waste conversion. By recording tomographies at different stages, specifically after polymer melting and cracking, it was possible to identify the polypropylene, the particle matrix, and macropores. Therefore, the approach is suitable for providing spatially resolved insights into the polymer intrusion within the catalyst's pore space,

which significantly influences the process efficiency. Preliminary results regarding the penetration of the polymer within the particle lead to an estimated 70% of macropores filled with polypropylene. The incomplete pore space filling is likely due to its complex structure, with some pores being disconnected or poorly accessible. Improvements in image resolution are needed to enhance the research outcomes, and different combinations of polymers and catalysts (e.g. fresh, equilibrium) to assess how changes in polymer viscosity and catalyst surface wettability influence the overall process.

7

Dutch Summary/Samenvatting

In het veld van heterogene katalyse is een multischaal benadering onmisbaar voor een alomvattend begrip van de dynamiek van katalytische materialen met een complexe structuur. Deze benadering bestrijkt uiteenlopende lengteschalen en adresseert zowel het gedrag van de katalysator, als van interacties op atomair niveau tot aan de macroscopische reactorbediening. Op atomair en moleculair niveau wordt onderzoek gedaan naar de configuratie van actieve katalytische sites, waardoor inzicht wordt verkregen in de structuur en reactiviteit van de katalysator. Onderzoek op deze microscopische schaal maakt de studie van enkele katalysatordeeltjes mogelijk, waarbij heterogeniteit en complexiteit binnen en tussen **individuele deeltjes** wordt onthuld. Op macroscopische schaal wordt vastgelegd hoe de structuur, de distributie en de werking van de katalysator van invloed is op de algehele reactorprestaties en efficiëntie. Elk analyse niveau draagt dus bij aan verschillende perspectieven en hun combinatie leidt tot een alomvattend begrip van de katalysatorfunctie. Dit kan vervolgens de verfijning van katalysatorontwerp en het fijnafstemmen van procescondities begeleiden, waardoor geoptimaliseerde katalytische prestaties worden bereikt.

Studies gericht op katalysatordeeltjes op individueel niveau hebben de aanzienlijke **heterogeniteit** van de katalysator deeltjes aangetoond[1-4], zowel tussen verschillende deeltjes (interdeeltjes) als binnen een enkel deeltje (intradeeltje). Dit is gerelateerd aan eigenschappen zoals de verdeling van actieve sites, deeltjesgrootte, poriënnetwerk en samenstelling. Deze complexiteit vormt een fundamentele uitdaging voor de interpretatie van traditionele bulk karakteriseringstechnieken, die anderzijds intrinsiek homogeniteit van het monster veronderstellen. Verder is het wenselijk om katalysatoren te observeren onder operationele reactor omstandigheden om een zo nauwkeurig mogelijk begrip te krijgen van hoe ze functioneren. Hierbij wordt idealiter de dynamiek van het onderzochte proces vastgelegd.

In deze context biedt de opkomst van **microfluïdicatechnologie** veelbelovende mogelijkheden. De mogelijkheid om operationele

omstandigheden te repliceren en tegelijkertijd precieze controle over de omgeving te behouden, opent de weg naar nauwkeurigere en informatievere karakterisering van katalysatoren. Een belangrijk voordeel van microfluïdische systemen is dat ze een uniek voordeel hebben in hun inherente mogelijkheid voor high-throughput analyse[3,5-7]. Dit aspect maakt snelle testen en vergelijkingen mogelijk van een groot aantal katalysatordeeltjes en/of omstandigheden op een tijdefficiënte manier. De integratie van microfluïdicatechnologie is het centrale thema in deze scriptie, waarin we de mogelijkheden hebben onderzocht van in-situ analyses en **high-throughput** strategieën voor karakterisering van katalysatordeeltjes.

Hoofdstuk 1 introduceert het onderzoeksonderwerp en biedt de motivatie en achtergrond van deze thesis over de toepassing van microfluïdicatechnologie voor het screenen van katalysatordeeltjes.

In **Hoofdstuk 2** hebben we een overzicht gegeven van de huidige stand van de techniek met betrekking tot het gebruik van microfluïdica-apparaten in traditionele microscopie- en spectroscopietechnieken voor katalysator karakterisering. We presenteren een theoretische achtergrond waarin we de basisprincipes van geselecteerde analytische technieken bespreken. Dit is inclusief de technieken die in dit onderzoek worden gebruikt. Bovendien hebben we toekomstige trajecten in dit vakgebied overwogen, waarbij high-throughput platformen centraal staan in het vormgeven van toekomstige ontwikkelingen en innovaties in katalysatoranalyse. Door middel van high-throughput testen kunnen databases worden verzameld die de relaties tussen fysische, chemische en structurele parameters en katalytische prestaties in kaart brengen. Deze uitgebreide informatie kan dienen als een bibliotheek om katalytische activiteit te voorspellen via computationele modellering en machine learning. Tot slot zou de introductie van gestandaardiseerde microfluïdica-apparaten voor katalysator karakterisering leiden tot vereenvoudiging van katalysatoranalyse, waardoor efficiëntere en herhaalbare experimenten mogelijk worden.

In **Hoofdstuk 3** wordt een innovatieve methode beschreven om lokaal gegenereerde nanopartikels via vonk-ontlading te deponeren op

driedimensionale microfluïdische systemen met behulp van een nanomateriaal 3D-printer. Deze benadering gebruikt een directe schrijfmethode waarbij geen cleanroom process nodig is. Met deze methode kunnen wij metalen (oxide) nanopartikel-patronen integreren in/op microfluïdica-structuren. Dit biedt een nieuwe aanpak voor katalysatorontwerp en screening. Bovendien biedt dit de intrinsieke mogelijkheid om de filmmorfologie fijn af te stemmen, gebaseerd op de printparameters. Hiermee verkrijgen we nieuwe mogelijkheden voor het vervaardigen van screening- en sensing-platforms.

De potentie van deze benadering werd gedemonstreerd aan de hand van twee onderscheidende toepassingen. Functionele systemen werden verkregen door het neerzetten van Pt- of Ag-nanodeeltjes in de kamers van een gemultiplext microfluïdicsche chip die is gemaakt van polydimethylsiloxane (PDMS). In één geval werden Pt-films gebruikt als bipolaire elektroden, die zorgen voor de generatie van verschillende elektrochemische potentialen langs de elektroden. Dit werd getest door middel van de elektrochemische generatie van pH-gradiënten in de kamers via water-elektrolyse, gedetecteerd met behulp van een pH-gevoelige kleurstof.

Door het benutten van ruimtelijke elektrochemische potentiaalgradiënten is het mogelijk om elektrodes te maken waarvan de samenstelling veranderd over de lengte van de elektrode (samenstellingsgradient) binnen één depositierun. Door verschillende metaaloplossingen te gebruiken, leidt de variatie van potentiaal over de lengte van de elektrode tot selectieve metalelektrodepositie op specifieke locaties. Dit resulteert in een continue reeks materiaalsamenstellingen, waarbij verschillende legeringen met uiteenlopende metaalverhoudingen over de elektrode worden gevormd. Het inherent high-throughput vermogen door het gebruik van deze bipolaire elektroden wordt verder verhoogd wanneer ze worden gecombineerd met gemultiplexte microfluïdische apparaten. Deze combinatie biedt een zeer efficiënt systeem voor het genereren en screenen van een breed scala aan materialen. Hierdoor is het een efficiënte benadering in de onderzoeksvelden aangaande katalyse of geavanceerd materiaalonderzoek.

In de tweede toepassing werd de effectiviteit van Ag-nanodeeltjes als Surface Enhanced Raman-spectroscopie (SERS) substraat getest. De kamers van de microfluidische chip werden gevuld met een oplossing van methyleenblauw dat dient als een probe-molecuul. Dit resulteerde in een analytische versterkingsfactor van $1.7 \cdot 10^5$. De techniek zou het gelijktijdig detecteren van meerdere analyten in één test mogelijk kunnen maken, waarbij zowel diagnostische als analytische processen worden geoptimaliseerd.

In **Hoofdstuk 4** stellen we een nieuwe methode voor om de toegankelijkheid van poreuze deeltjes op het niveau van individuele deeltjes te evalueren, een parameter die hun efficiëntie als adsorbentia en katalysatoren bepaalt. De benadering omvat het gebruik van een gemultiplexte PDMS-microfluïdica-apparaat om in een high-throughput mode de opname van fluorescente moleculen in individuele poreuze deeltjes in de loop van de tijd te beoordelen.

Om de methode te demonstreren, werden mesoporeuze SiO_2-deeltjes met uniforme poriegroottes en vergelijkbare porositeit gebruikt. Interessant genoeg vertoonden deeltjes uit dezelfde partij, dat wil zeggen met dezelfde poriegrootte, grote heterogeniteit qua toegankelijkheid. Dit kon niet worden opgelost via traditionele bulkmethoden. Bovendien merkten we door de elektrostatische interacties tussen het probe-molecuul en het SiO_2-oppervlak te moduleren door aanpassingen in de pH en ionsterkte van het systeem, aanzienlijke veranderingen op in massatransport, wat resulteerde in een chemisch-gevoelige methode om de toegankelijke porositeit van het oppervlakte onderzoeken. Wanneer deze probe-deeltje interacties worden geminimaliseerd, wordt het opnameproces voornamelijk beïnvloed door de poriestructuur. In dat geval biedt de methode een gevoeligheid voor poriegrootteverkenning die vergelijkbaar is met de resultaten verkregen metN_2-fysisorptie.

De geïdentificeerde concentratieprofielen binnen het poreuze deeltje konden worden aangepast met behulp van een massatransportmodel om ruimtelijke inzichten, en uiteindelijk data over de intra-deeltjes heterogeniteiten te verschaffen. Verder zou de fabricage van een apparaat dat compatibel is met organische oplosmiddelen ook het gebruik van

hydrofobe kleurstoffen mogelijk maken, waardoor het begrip van de toegankelijkheid en interacties van het materiaal wordt vergroot.

Hoofdstuk 5 presenteert het ontwerp en de fabricage van een high-throughput apparaat voor in-situ studie van gasfase katalytische reacties op het niveau van individuele deeltjes. De voorgestelde opstelling heeft het potentieel om de real-time voortgang van katalysatordeactivatie te volgen als gevolg van de afzetting van koolstofhoudende substanties (coke/roet) op het oppervlak ervan, wat relevant is in industriële processen die de omzetting van koolwaterstoffen (bijvoorbeeld bij het kraakprovess) omvatten. De deeltjes reizen door de chip op dezelfde snelheid, waardoor iedere positie overeenkomt met een bepaalde verblijf en reactietijd.

Het concept is gebaseerd op het volgen van de levensduur en progressieve deactivering van het deeltje door koolstofafzetting(coke/roet). Door de katalysatoren op vaste posities in de microreactor te bekijken krijgen we een beeld van hoe de deactivatie zich ontwikkelt over tijd. Elke positie representatief is dus voor verschillende verblijftijden. De hoeveelheid gevormde coke/roet kan worden geëvalueerd via fluorescentie-gebaseerde metingen van individuele deeltjes, waardoor de studie van deactivatie-kinetiek en interdeeltjes-heterogeniteit mogelijk is. Tot nu toe is de mogelijkheid van de opstelling om de fluorescentie van de deeltjes te detecteren tijdens het passeren van de detectieplek getest door gebruik te maken van katalysatordeeltjes met verschillende hoeveelheden coke/roet. Deze werden verkregen via kraak-experimenten met katalytische kraakdeeltjes (FCC) en n-hexaan. Deze reactie is ex-situ uitgevoerd en op verschillende tijdstippen gestopt om verschillende hoeveelheden coke/roet te hebben . De metingen onthulden een duidelijke correlatie tussen de signaalintensiteit en de leeftijd van het katalysator deeltje, wat suggereert dat de methode het potentieel heeft om het deactivatietempo van de katalysator en de intradeeltjes-heterogeniteit te bepalen.

Het apparaat en de opstelling kunnen ook worden gebruikt om de efficiëntie van calcinatie te beoordelen. Calcinatie is het proces dat wordt gebruikt om de katalytische activiteit van de deeltjes te herstellen. De effectiviteit van dit proces kan worden beïnvloed door tal van factoren,

waaronder temperatuur en tijdsduur. Door gebruik te maken van dit apparaat en experimentele opstelling, zou men in potentie de veranderingen in signaalintensiteit gedurende het calcinatieproces kunnen monitoren, waardoor real-time inzichten in de regeneratie van de katalysator worden verkregen. Dit kan helpen bij het optimaliseren van de calcinatieparameters om een maximaal katalysatorherstel te waarborgen. Tegelijkertijd kunnen het energieverbruik en de procesduur voor dit optimale herstel worden geminimaliseerd. Ten slotte kan het apparaat ook informatie verstrekken over interdeeltjes-heterogeniteit na calcinatie. Het kan onthullen hoe verschillende deeltjes reageren op dezelfde calcinatieomstandigheden, waarbij de rol van deeltjeseigenschappen bij de regeneratie van de katalysator wordt onthuld. Dit zou de deur kunnen openen voor het ontwerpen van katalysatoren met verbeterde weerstand tegen deactivering en verbeterde regeneratie/herstellings prestaties.

In **Hoofdstuk 6** introduceren we een innovatieve methode waarmee in-situ 3D-analyse van individuele katalysatordeeltjes mogelijk wordt gemaakt door gebruik te maken van synchrotron-gebaseerde harde röntgen-tomografie. Meer specifiek combineert de benadering harde röntgen holotomografie met een op micro-elektromechanische systemen (MEMS) gebaseerde microreactor ontwikkeld door Luca Carnevale (BIOS/UT). Deze microreactor bestaat uit een monolithische siliciumchip met een vrijstaande capillair uitgerust met verticale pincet structuren om een deeltje te vangen. Ook bevat de microreactor verwarmingselementen voor de nauwkeurige controle van de temperatuur op de locatie van het deeltje. Deze opstelling maakt het mogelijk om katalytische processen van individuele deeltjes direct te observeren.

Deze methode werd gebruikt om de katalytische pyrolyse van polypropyleen te bestuderen met behulp van fluid catalytic cracking (FCC) deeltjes, wat een effectieve strategie is en een actief onderzoeksgebied voor de omzetting van plastic afval. Door tomografieën op te nemen op verschillende momenten, met name na het smelten en kraken van het polymeer, was het mogelijk om het polypropyleen, de deeltjesmatrix en macroporiën te identificeren. Hierdoor bleek de benadering geschikt om ruimtelijke inzichten te verschaffen in de intrusie van het polymeer in de

poriën van de katalysator. Het is aangetoond dat dit aanzienlijk invloed heeft op de procesefficiëntie. Voorlopige resultaten met betrekking tot de penetratie van het polymeer binnen het deeltje wezen op een geschatte vulling van 70% van de macroporiën met polypropyleen. De onvolledige vulling van de poriënruimte is waarschijnlijk te wijten aan de complexe structuur, waarbij sommige poriën niet met elkaar verbonden zijn of slecht toegankelijk zijn. Verbeteringen in de beeldresolutie zijn nodig om de onderzoeksresultaten te verbeteren. Verschillende combinaties van polymeren en katalysatoren (bijv. verse deeltjes, en deeltje die na gebruik in een evenwichtstoestand zijn) kunnen worden getest om te beoordelen hoe veranderingen in de viscositeit van het polymeer en de affiniteit van het katalysatoroppervlak de algehele procesefficiëntie beïnvloeden.

7.2   References/ Referenties

1.   Dong, B. *et al.* In situ quantitative single-molecule study of dynamic catalytic processes in nanoconfinement. *Nat. Catal.* **1**, 135–140 (2018).
2.   Qie, Z. *et al.* Multiscale investigation of pore network heterogeneity and permeability of fluid catalytic cracking (FCC) particles. *Chem. Eng. J.* **440**, 135843 (2022).
3.   Nieuwelink, A. E. *et al.* High-throughput activity screening and sorting of single catalyst particles with a droplet microreactor using dielectrophoresis. *Nat. Catal.* **4**, 1070–1079 (2021).
4.   Buurmans, I. L. C. & Weckhuysen, B. M. Heterogeneities of individual catalyst particles in space and time as monitored by spectroscopy. *Nat. Chem.* **4**, 873–886 (2012).
5.   Sun, A. C. *et al.* A droplet microfluidic platform for high-throughput photochemical reaction discovery. *Nat. Commun.* **11**, 1–6 (2020).
6.   Solsona, M. *et al.* Magnetophoretic Sorting of Single Catalyst Particles. *Angew. Chemie - Int. Ed.* **57**, 10589–10594 (2018).
7.   Beugré, R., Dorval, A., Lavallée, L. L., Jafari, M. & Byers, J. C. Local electrochemistry of nickel (oxy)hydroxide material gradients prepared using bipolar electrodeposition. *Electrochim. Acta* **319**, 331–338 (2019).

Scientific output

Journal articles

Broccoli, A., Vollertsen, A. R., Roels, P., van Vugt, A., van den Berg, A., & Odijk, M. (2023). Nanoparticle Printing for Microfluidic Applications: Bipolar Electrochemistry and Localized Raman Sensing Spots. *Micromachines*, *14*(2), 453.

Broccoli, A.*, Carnevale, L.*, Mayorga González, R.*, Dorresteijn, J.M., Weckhuysen, B.M., Olthuis W., Odijk M., and Meirer F. (2023). Accessibility Study of Porous Materials at the Single Particle Level as Evaluated within a Multiplexed Microfluidic Chip with Fluorescence Microscopy. *In press in Chem Catalysis*
*equal contribution

Carnevale, L., **Broccoli, A.**, Mayorga González, R., van Swieten, T., Groenesteijn, J., Ma, K., Wiegerink, R. J., Weckhuysen, B. M., Meirer, F., Olthuis, W., and Odijk, M. MEMS-Based Microreactor for *In Situ/Operando* High-Resolution 3D X-Ray Microscopy of Single Catalyst Particles. *In preparation*

Conference contributions

Broccoli, A., Carnevale, L., Mayorga González, R., Dorresteijn, J.M., Weckhuysen, B.M., Olthuis W., Odijk M., and Meirer F. Chemically-Sensitive Accessibility Study of Porous Materials at the Single Particle Level as Evaluated within a Multiplexed Microfluidic Chip with Fluorescence Microscopy. *Mesa+ Annual Meeting,* September 25, 2023 (*invited talk*)

Carnevale, L., **Broccoli, A.**, Mayorga González, R., van Swieten, T., Groenesteijn, J., Ma, K., Wiegerink, R. J., Weckhuysen, B. M., Meirer, F., Olthuis, W., and Odijk, M. MEMS-Based Microreactor for *In Situ/Operando* High-Resolution 3D X-Ray Microscopy of Single Catalyst Particles, *28th North American Catalysis Meeting,* June 18 – 23, 2023, Providence, RI, USA. (*oral presentation*)

Broccoli, A., Ahlers, D., Wijnperle D., Carnevale, L., Vogt, E. T. C., Weckhuysen, B. M., High-Throughput Device For *In situ* Study at

Millisecond Spatiotemporal Resolution of Heterogeneous Catalytic Reactions at the Single Particle Level with Fluorescence Microscopy. *23rd Netherlands' Catalysis and Chemistry Conference,* March 6 – 8, 2023, Noordwijkerhout, The Netherlands. (*poster presentation*)

Broccoli, A., Carnevale, L., Mayorga González, R., Weckhuysen, B.M., Olthuis W., Odijk M., and Meirer F. Diffusion Phenomena at the Single Catalyst Particle Level, *Catalysis Connected*, September 15 – 16, 2022, Eindhoven, The Netherlands. (*poster presentation*)

Broccoli, A., Carnevale, L., Mayorga González, R., Weckhuysen, B.M., Olthuis W., Odijk M., and Meirer F. Diffusion Phenomena at the Single Catalyst Particle Level As Evaluated within a Multiplexed Microfluidic Chip with Fluorescence Microscopy, *27th North American Catalysis Meeting*, May 22 – 27, 2022, New York, NY, USA. (pp. 68). (*oral presentation*)

Broccoli, A., Carnevale, L., Mayorga González, R., Weckhuysen, B.M., Olthuis W., Odijk M., and Meirer F. Accessibility Study of Porous Materials at the Single Particle Level, *MCEC annual meeting*, June 15 – 16, 2022, Utrecht, The Netherlands. (*invited talk*)

Broccoli, A., Vollertsen, A.R., Roels, P., van Vugt, A., van den Berg, A., Odijk, M. Local Deposition of Nanoparticles on a PDMS Microfluidic Device. *25th International Conference on Miniaturized Systems for Chemistry and Life Sciences.* October 10 – 14, 2021, Palm Springs, CA, USA (pp. 1381-1382), online. (*poster presentation*)

Broccoli, A., Vollertsen, A.R., Roels, P., van Vugt, A., van den Berg, A., Odijk, M. Integration of Bipolar Electrodes and Raman Sensing Spots via Local Deposition of Nanoparticles on a PDMS Microfluidic Device, *MCEC annual meeting,* June 21-22, 2021, online and in Utrecht, The Netherlands. (*poster presentation*)

Broccoli, A., Vollertsen, A R., Papadimitriou, V. A., van den Berg, A., Odijk, M. Bipolar Electrochemistry On Chip, *MCEC annual meeting,* April 9, 2020, online. (*poster presentation*)

Broccoli, A., Odijk, M., van den Berg, A. Bijels Design On chip for Heterogeneous Catalysis, *MCEC annual meeting*, June 18-20, 2019, Enschede, The Netherlands. (*poster presentation*)

Funding and contributions

Funding

Contributions

Throughout the entire project, both Prof. Dr. Ir. Mathieu Odijk from the BIOS Lab on a Chip group (UT) and Dr. Florian Meirer from Inorganic Chemistry and Catalysis group (UU) supervised the research. Their constructive discussions and assessments contributed significantly to each chapter of the work presented.

Chapter 1: Introduction

Chapter 1 is written by Alessia Broccoli with critical input from Mathieu Odijk.

Chapter 2: Heterogeneous catalyst characterization in microfluidics

Chapter 2 is written by Alessia Broccoli. Mathieu Odijk provided his feedback regarding structure and writing.

Chapter 3: Nanoparticle printing for microfluidic applications: bipolar electrochemistry and localized Raman sensing spots

Mathieu Odijk, Bastian Mei, and Alessia Broccoli conceptualized the project. Aaike van Vugt kindly provided access to the prototype nanomaterial 3D printer, and Alessia Broccoli and Pauline Roels used it to deposit the nanoparticles on the devices. Alessia Broccoli performed the experimental work, data analysis and wrote the manuscript with critical input from Mathieu Odijk and Albert van den Berg.

Chapter 4: Chemically-Sensitive Accessibility Study of Porous Materials at the Single Particle Level as Evaluated within a Multiplexed Microfluidic Chip with Fluorescence Microscopy

This project is the result of the collaboration between Alessia Broccoli, Luca Carnevale, and Rafael Mayorga González (UU). Alessia Broccoli and Luca Carnevale conceptualized and initiated the work. Alessia Broccoli performed the experiments. Luca Carnevale and Rafael Mayorga González wrote the MATLAB scripts for the data analysis and performed the simulations. Florian Meirer (UU), Yadolah Ganjkhanlou (UU) Erik Maris (UU) contributed to fruitful discussions on experimental methods and data analysis. Alessia Broccoli, Luca Carnevale, and Rafael Mayorga González wrote the chapter with critical input from, Florian Meirer, Mathieu Odijk, Wouter Olthuis, and Bert Weckhuysen.

Chapter 5: High-throughput device for *in situ* studies at millisecond spatiotemporal resolution of heterogeneous catalytic reactions at the single particle level with fluorescence microscopy

The project was conceptualized by Mathieu Odijk, Bert Weckhuysen, Eelco Vogt, and Florian Meirer. This chapter started as an internship assignment for David Ahlers (University of Münster), who performed the preliminary experiments and took care of the optimization of the optical setup and signal acquisition. Alessia Broccoli designed and fabricated the device and performed the COMSOL simulations with input from Luca Carnevale. Daniël Wijnperle wrote the LabView program for the camera and valve triggering and assisted David Ahlers in optimizing the optical setup, which was adapted from an earlier work by Floris van den Brink, Ashish Asthana, and Mathieu Odijk.

Chapter 6: Accessibility Study of Porous Materials at the Single Particle Level as Evaluated within a Multiplexed Microfluidic Chip with Fluorescence Microscopy

This project is the result of the collaboration between Alessia Broccoli, Luca Carnevale, and Rafael Mayorga González (UU). The device used in this chapter is part of the PhD work of Luca Carnevale. The reported experiments were performed at DESY, PETRAIII beamline P05 by Luca

Carnevale, Alessia Broccoli, Rafael Mayorga González (UU), and Sebastian Rejman (UU), with supervision from Imke Greving and Silja Flenner (DESY). Luca Carnevale and Alessia Broccoli performed preliminary experiments using optical microscopy and microreactor characterization. Luca Carnevale, Rafael Mayorga Gonzaléz, and Florian Meirer wrote the proposal for the beamtime. The data analysis reported in the chapter was performed by Luca Carnevale, with input from Rafael Mayorga González and fruitful discussions with Florian Meirer and Alessia Broccoli. The chapter was written by Alessia Broccoli and Luca Carnevale, with critical input from Florian Meirer, Wouter Olthuis, and Mathieu Odijk.

Chapter 7: Summary and Outlook

Chapter 7 is written by Alessia Broccoli with critical input from Mathieu Odijk.

Words of Gratitude

As I prepare to cross the finish line and conclude this academic adventure, I carry with me not only a sense of accomplishment but also a profound sense of gratitude that runs deeper than words can express. Having had the opportunity to pursue a PhD has been an incredible privilege, and I am thankful for every part of this journey, including the unique experiences and the wonderful people I met who have contributed to its success.

This journey has been filled with challenges, discoveries, moments of self-doubt, tons of data and theories, and a collection of memories that I'll treasure forever. Each achievement has been the result of not just my individual efforts, but the contributions and collaborations of people that have enriched this academic experience. I believe the richness of the PhD it's not just about the knowledge I've gained, the experiments I've conducted, or the papers I've written – it's about the people who stood by my side, providing inspiration, encouragement, advice, and even a shoulder to lean on when things got tough. Their presence and support have been a guiding light in helping me navigate the twists and turns of the PhD but also the complexities of life itself.

I want to take a moment to thank the people who played a part in this remarkable story.

Mathieu and Guido, you were the first to believe in my potential during our initial phone calls and interviews, and for this, I want to begin by thanking both of you for setting the foundation of this Ph.D. journey. Thanks a lot for your trust and support.

Mathieu, your creativity and enthusiasm for science are contagious, and you can make your students curious and excited about it. You've turned the most daunting challenges into thrilling adventures. Thanks for helping me step out of my comfort zone and move from the industrial-scale processes to the world of microchips – a transition that once seemed so distant and challenging. Thanks a lot for your guidance and constant encouragement, which helped me to reach new heights and exceed my own expectations. Our meetings had always a friendly and positive atmosphere where we

could brainstorm on devices, new projects, and out-of-the-box concepts and openly talk about everything. Our cultural differences quickly turned into a source of curiosity and fun (except when you asked me to supervise the spaghetti bridge competition…thrice). I really enjoyed working with you and hope that the same goes for you despite my (over)management tendencies.

Florian, I'm so grateful for your support and mentorship throughout these years. The Pore Space Exploration meetings were one of the highlights of the week and even when our research didn't go as planned, you always managed to keep us motivated. You have the ability to turn our conversations into thought-provoking exchanges that have greatly enriched my research. Thanks for being a source of inspiration, and for always being there whether it was for academic advice, meetings during the beamtrip at any time of the week, or a friendly chat to lighten the mood.

Albert, your vision in scientific research provides essential guidance at BIOS. Your dedication, mentorship, and commitment to fostering a collaborative environment of shared knowledge within the group have been truly inspiring and reinforced my belief in the power of teamwork. Thanks for the memorable annual BBQs, workweeks, and mountain biking adventures and for making BIOS an exceptional place to learn and grow.

I would like to thank the graduation committee for taking the time to review my thesis, provide feedback, and for the willingness to discuss it during the defense. I'm sure it'll be a valuable moment for learning and exchanging opinions on the various topics presented in the thesis.

To the BIOS professors, Loes, Wouter, Jan, Tim, and Sergii: I am grateful for the opportunities to learn from you, whether through discussions or insightful feedback. Your different expertises have broadened my horizons in the lab on a chip field. And Loes, a special thanks to you for those sweets from Italy! That really made my day.

Johan, Eddy, and Daniël, you are the backbone of our group. Your skills and hard work are what keep BIOS research moving forward. Thanks a lot for helping me build setups and analyzing samples.

Hermine, Lisette, and Paul your management and support ensure that everything runs smoothly, from handling reservations to managing chemical orders and maintaining lab safety. Thanks for all the support and smiles, even during moments of frustration with bureaucracy. Paul, I've always had the impression that you were Italian, and after all these years, this impression has almost become a reality. When I look back on this doctoral period, I'll definitely have your ''Hey Alessia, Buongiorno!'' in my mind, the first thing I heard (very loudly) when I arrived at work.

A huge thank you to my officemates: Jeroen, Rob, Lanhui, Aniruddha, Koen, and Loes–you've been my rock through it all.

(Prof.) Jeroen, sharing an office with you right from day 1 felt like it was meant to be, and if I had a choice, I'd choose it all over again. You've been my guide in the world of microfluidics and catalysis, always ready with a joke and a helping hand, even with your crazy schedule. You deserve nothing but the best, and I'm sure you'll be an amazing professor.

Lanhui, you've been more than just a colleague; you've been a true and indispensable friend during the early years of my PhD. We've had so much fun in the lab, and you've always shared your genuine passion for research. You've also taught me how to handle challenging situations with maturity and dignity. I'll forever cherish our weekend trips, dinners, birthday surprises, and the Christmas we spent together during the lockdown. With you, I've always felt understood, and you had a knack for saying the right things at the right moments. I hope you'll always be happy, and I look forward to our reunion in China.

Rob, Aniruddha, Koen, and Loes, I've enjoyed sharing the office with you and all the serious and less serious conversations we had. I wish you a lot of success in everything you do, now and in the future! You've been a big part of making this journey special. I hope that I've been able to do the same for you during our time together. Also, a huge thank you to the office next door for always being so welcoming. Jamal, Dasha, and Jiyuan, I appreciate our chats about work, travel, our dreams, and just life in general. You've seen me in my super-stressed mode and managed to comfort me with kind words or a snack. Thanks a lot! And I extend my thanks to my second office

with Stella, Nienke, and Jasper. Thank you, guys, for all the advice, laughter, and discussions!

Anke, you have been an essential figure in my PhD, which started thanks to you and your chips. From the very beginning, you generously shared your knowledge, always willing to teach me everything about chip fabrication and working with valves. You shared precious tips and tricks that made my work much smoother. Thank you for being such a great team player and source of inspiration.

David, I really enjoyed supervising you. Even though the assignment was challenging and far from your expertise, you picked things up fast and were a huge help in building and testing the setup together with Daniël. Your positive spirit and can-do attitude made the daily challenges feel much lighter. You're going to be an awesome PhD candidate, no doubt about it!

To all my current and past colleagues at BIOS, with whom I've shared many wonderful moments, and a few challenging ones too. Every experience has contributed to my professional and personal growth. While I wish I could write a paragraph for each one of you, what truly matters is that I'm grateful to have met you all. Thanks for all the memories in the lab, during the workweeks, meetings, Friday afternoon activities and so much more.

I'd also like to thank the MCEC consortium and in particular Anne-Eva, Sabine, and Daan for all the meetings, summer schools, and fun events. These experiences made my research journey a lot more enjoyable and I had a lot of fun arranging activities with the C-team. And within the MCEC community, I'd like to extend a special thanks to Ainoa for the lovely time we spent together during all the MCEC events. And also a big thank you to Arvin, my favorite CFD engineer (the bar isn't set too high). But seriously, you're one of the most fun-loving people I know, and you've always been available, whether it was for brainstorming sessions or simply sharing a good laugh.

One of the most unforgettable experiences of these years has been the beamtrips. Having the opportunity to work in such facilities has been incredible, and sharing it with such great colleagues was the cherry on the cake. Luca, Rafael, Adrian, Jelle, and Sebastian, you have been fantastic

teammates, and I'll always carry with me the funniest (but also the most challenging) moments we've shared.

Rafito (Rafito, suave suavecito) quante esperienze bbbbbbellissime abbiamo condiviso? Dalle conferenze ai beam trips, dai meetings agli after-meetings per chiarire concetti e capire come dividere il lavoro. Anche se tu e Luca (il particle guru) non sempre mi ascoltavate (that's insane!), alla fine di questo percorso posso dire che lavorare con voi due é stata, contro ogni aspettativa, una delle esperienze piú belle che avrei potuto desiderare. Oltre al lavoro, sono felice per la nostra amicizia, per tutte le risate, i viaggi e i consigli. Ti meriti il meglio e ti auguro un futuro pieno di avventure straordinarie e soddisfazioni. Spero che le nostre strade si incrocino di nuovo nei prossimi capitoli della vita.

Ketki, Aniruddha, Luca, Martin, and Masha, the "Hola chicos!". Thank you for all the laughter, evenings, food, and gossip we've shared over these past few years. Thanks for always being open to answering my lab and off-lab interviews, for our lunch walks, and for sharing/watching nonsense videos. Although at times I felt more like a "project mom" than a friend, I loved every moment spent with all of you. You made one of my (bbbbbbbbbb)best birthdays ever, and for that, I'm immensely grateful. Aniruddha and Martin, your sarcasm, occasional disorganization, and unique personalities have added unforgettable flavors to our time together, making it all the more memorable. Ketki, you've always been a tornado of emotions and words, and your enthusiasm never fails to brighten my days. I'm sure you'll achieve all your plans and aspirations, and I wish you all the best in life.

Masha (bella!), we've been through so much together. Thank you for all the small and big gestures, for all the emotions we've shared, and for welcoming me into your life. You being by my side on this special day means the world to me.

E per la mia fantastica paraninfa italiana Anna: 10 anni di amicizia sono troppi per poter racchiudere in poche parole quanto tu sia importante per me. Nonostante la distanza sei stata il mio porto sicuro, sempre presente nei momenti più importanti e nelle sfide della vita. La tua presenza al mio

fianco è stata un regalo prezioso, e non vedo l'ora di condividere le prossime avventure che ci aspettano.

Alessandro (Desiderius), da dove cominciare? Forse dalle nostre prime e-mail, quando ti chiedevo informazioni sul gruppo e tu rispondevi in modo formale, mantenendo le distanze. E poi, siamo diventati come fratello e sorella. Insieme abbiamo vissuto tante esperienze, e sono felice di aver condiviso questa parte di vita con te. Sei la persona piú buona, sincera e altruista che io conosca e meriti tutto il meglio che la vita può offrire (senza dimenticare che hai già la miglior moglie e i migliori amici che si possano desiderare).

Carmela, sei stata la prima persona che ho incontrato ad Enschede e con la quale mi sono sentita da subito a casa. Se sono riuscita ad arrivare a questo punto lo devo anche a te e al tuo aiuto incondizionato. Grazie per tutti i consigli, le risate e le esperienze che abbiamo condiviso (e anche i bidoni). Ti voglio bene Mela!

Nel ringraziare tutti coloro che hanno contribuito al mio percorso, vorrei dedicare un pensiero speciale alla mia famiglia. Non ci si abitua a vivere lontano da voi, ma il vostro supporto e la vostra fiducia in me hanno fatto sentire la vostra vicinanza ogni giorno. Grazie per aver sempre sostenuto le mie scelte, per la vostra pazienza e comprensione nei momenti piú duri e per aver condiviso e celebrato i miei successi.

Luca, il mio ringraziamento piú grande va senza dubbio a te. È stato un viaggio incredibile, condividendo non solo la stessa strada ma anche sogni, difficoltá e momenti speciali. Il tuo supporto costante è stato un faro nella mia vita, e la tua presenza ha reso ogni sfida più gestibile e ogni gioia più intensa. Grazie per la tua capacitá di capirmi, per il tuo sostegno nei momenti in cui volevo mollare, per la tua comicitá che mi fa ridere di cuore, per le tue attenzioni, e per essere semplicemente la persona straordinaria che sei. Guardo con entusiasmo al futuro, e non vedo l'ora di continuare a condividere le gioie della vita insieme a te.

To all those whose contributions may have been more subtle but equally significant, I appreciate your influence in shaping my path. Whether it was a conversation that sparked inspiration, a piece of advice that helped me

navigate challenges, or a simple act of kindness that brightened my day, your presence has been felt and deeply appreciated.

So, here's to the conclusion of this chapter and the beginning of new ones. I carry your support and friendship with me into the next stage of my professional and personal journey. Thank you for being a part of these incredible years, and I can't wait to see where our paths lead next.

Alessia